

**The Effect of Urban Geometries and Roof Shapes
on Airflow and Pollutant Dispersion:
A CFD Investigation**



Hui Wen

Department of Civil, Environmental and Geomatic Engineering
University College London

A thesis submitted for the degree of *Doctor of Philosophy*

I, Hui Wen confirm that the work presented in this thesis is my own. Where information has been derived from other sources, I confirm that this has been indicated in the thesis.

Acknowledgements

I would like to express my deepest gratitude to all the people who have supported me in the past five years. Without them, I would never be possible to reach the destination of my PhD journey.

My gratitude goes first and foremost to my supervisor Dr. Liora Malki-Epshtein, for constant illuminating guidance for my PhD project and great concerns of my career and life. Every time I face difficulty in my research, it is she who gives me useful suggestion, shares her PhD experience and encourages me to carry on.

I would like to thank Dr. Kastner-Klein for providing her experimental data, which are used as the bases for benchmarking.

I would like to express my heartfelt gratitude to my fellows and the staff in our department, especially my second supervisor Dr. Philippe Duffour who gives me great help at the primary stage of my PhD, Dr. Nina Glover who guides me into the world of CFD and shares all her knowledge and experience in CFD modelling, Dr. Styliani Karra who shares her valuable experimental measurements with me, Les Ansdell who teaches me to use the equipment for field measurement and assists me to set it up.

I would like to thank everybody in GM16, especially Yanfei Yue, Xuan Zhang, and Shi Shi. The good atmosphere in the office makes me feel less alone and is an impulse to keep me moving. It is my good fortune to be a member of the lovely office.

I would also like to thank to my landlord Lewis Wong for providing good places to stay and sharing his life experience in the UK. They save me much effort from hunting house and enrich my life.

Finally, my sincere appreciation goes my parents, my relatives and my girlfriend for their continuous concern and support in both material and spiritual perspectives. You are always the paramount part of my life.

Abstract

Street canyons, where long narrow streets are bordered by a continuous row of buildings on both sides, are a typical urban geometry which leads to problems of high pollution and heat accumulation. With the trend of modernization and urbanization, it is inevitable to have more street canyons and those will become deeper. This compels scholars to research detailed building designs and urban planning, in order to mitigate the problems of street canyons.

This thesis uses Computational Fluid Dynamics (CFD) to study the impacts of several urban geometries on ventilation and pollutant removal, including pitched roofs, surrounding tall buildings, heterogeneous buildings and T-junctions. Before carrying out the study, benchmarking is performed to determine optimal CFD settings and to guarantee model accuracy.

The impacts of pitched roofs are studied separately through a parametric approach. In general, the pitched roofs produce similar flow patterns compared to the flat roofs, but they reduce velocity and turbulence and increase pollutant concentration in the street. Moreover, it should be noted that high pitch rise and pitched roof(s) on the leeward building are two designs that are likely to cause even higher pollutant concentrations in the street and at pedestrian level.

The area around Gloucester Place, London, is selected to be modelled in detail, in order to investigate the impacts of other typical urban geometries on airflow and pollutant dispersion. It is found that the downstream tall building and the T-junction between the windward buildings have profound impacts. The tall building produces along-street flow that does not normally form in consecutive homogenous street canyons, leading to significant improvement in ventilation and pollutant removal. This finding implies the great potential of isolated tall buildings to improve local air quality. The T-junction weakens the ventilation around it by breaking vortex flow. For this reason, the position of T-junctions should be carefully designed to avoid any unexpected pollution hot-spots.

Contents

1	Introduction.....	1
1.1	Objectives	3
1.2	Thesis structure.....	5
2	Literature Review	7
2.1	Typical flow patterns in street canyons	8
2.2	Turbulent transfer between a street canyon and the atmosphere.....	10
2.3	The impacts of background wind condition	11
2.4	The impacts of street and building geometries.....	13
2.4.1	Street length	13
2.4.2	Asymmetrical street canyon	16
2.4.3	Heterogeneous street canyon.....	17
2.4.4	Roof structure.....	19
2.4.5	Gap and junction	24
2.5	The effects of local parameters	27
2.5.1	The effect of trees.....	27
2.5.2	The effect of traffic	27
2.5.3	The effect of heating	28
2.6	CFD modelling of street canyon flow	30
2.6.1	Advantages and limitations	30
2.6.2	Performance and accuracy	31
3	Introduction of Computational Fluid Dynamics	34
3.1	Navier-Stokes equations.....	35
3.2	Turbulence model.....	36
3.2.1	The standard k- ϵ model.....	36
3.2.2	The RNG k- ϵ model	38
3.3	Wall treatments.....	40

3.4	Modelling pollutant dispersion.....	43
4	Methodology	44
4.1	General processes for CFD modelling	45
4.2	Selecting turbulence model	46
4.3	Selecting the wall function	48
4.4	Specifying boundary condition.....	49
4.4.1	Boundary type	49
4.4.2	Boundary position	50
4.4.3	Inlet boundary profile.....	50
4.5	CFD solver settings	53
5	Benchmark—validation of CFD models	54
5.1	Objectives	55
5.2	Experiments used for benchmarking	56
5.2.1	Descriptions of experimental setup.....	56
5.2.2	Wind condition for approaching flow	57
5.2.3	Traffic emission information	58
5.3	CFD models.....	60
5.3.1	Inlet boundary condition	61
5.3.2	Turbulence model and the wall function.....	63
5.3.3	Turbulent Schmidt number	64
5.3.4	Mesh sensitivity test.....	64
5.3.5	Data used for comparison.....	67
5.4	Results and analyses—benchmark case 1	69
5.4.1	Mesh sensitivity test on middle line.....	69
5.4.2	Mesh sensitivity test on two side lines	72
5.4.3	Comparison of flow pattern	74
5.4.4	Comparisons of flow properties and concentration	76
5.4.5	Assessment of model accuracy	81

5.5	Results and analyses—benchmark case 2	84
5.5.1	Comparison of flow pattern	84
5.5.2	Comparison of concentration	86
5.5.3	Assessment of model accuracy	88
5.6	Results and analyses—benchmark case 3	89
5.6.1	Mesh sensitivity test on middle line	89
5.6.2	Mesh sensitivity test on two side lines	91
5.6.3	Comparison of flow pattern	93
5.6.4	Comparisons of flow quantities and concentration	96
5.6.5	Assessment of model accuracy	101
5.7	Concluding remarks	103
6	A Parametric Study of Two-dimensional Street Canyons with Pitched Roofs	105
6.1	Model geometry	106
6.2	Parameters and nomination rule	107
6.3	CFD modelling settings	110
6.4	Results and Analyses	111
6.4.1	The effect of aspect ratio and roof structure on flow pattern	112
6.4.2	The effect of roof structure on flow properties	114
6.4.3	The effect of roof structure on concentration	120
6.4.4	Assessment of ventilation	127
6.4.5	Assessment of pollutant removal	130
6.5	Summary of main findings	138
7	A Case Study of Airflow and Pollutant Dispersion in Gloucester Place and Its Surrounding Area	140
7.1	Background information	141
7.2	Model geometry and CFD modelling settings	144
7.3	Airflow around the city blocks	148
7.4	Airflow in the test street canyon	154

7.4.1	Airflow in Zone 1	160
7.4.2	Airflow in Zone 2	160
7.4.3	Airflow in Zone 3	161
7.4.4	Airflow in Zone 4	162
7.5	Pollutant concentration distribution	164
7.6	Summary of main findings	168
8	Analyses of the Effects of Three Urban Geometries	170
8.1	Model geometries	171
8.2	Flow structures	174
8.2.1	Heterogeneous buildings	174
8.2.2	Pitched roofs	175
8.2.3	T-junction	180
8.3	Assessment of ventilation	182
8.3.1	Ventilation efficiency for whole test street	183
8.3.2	Ventilation efficiencies for different cross-sections	186
8.4	Assessment of pollutant removal	191
8.4.1	Pollutant removal performance for whole test street	192
8.4.2	Pollutant removal performance for different cross-sections	195
8.5	Summary of main findings	199
9	Conclusion and Discussion	201
10	References	206
11	Appendix	218
11.1	The similarity law for street canyon flow	218
11.2	Bulk Parameter Data for Chapter 6	220

List of Figures

Figure 1.1: A typical two-dimensional street canyon and a typical flow pattern in the street when background wind is perpendicular to the street.	2
Figure 2.1: Three flow regimes for flow over buildings: (a) isolated roughness flow, (b) wake interference flow, and (c) skimming flow. Adapted from Oke (1988).	9
Figure 2.2: Divisions of three flow regimes as a function of building height H/W and building length L/H . Adapted from Oke (1988).	9
Figure 2.3: Velocity vectors on two horizontal planes at $z=0.25H$ in two isolated street canyons with different street lengths, (a) $L/H=5$ and (b) $L/H=10$. Replotted following Kastner-Klein et al. (2004).	14
Figure 2.4: Streamlines in a building array, top: array layout and the test region (red circle), (a) the horizontal plane at height $z=0.12H$ and (b) the horizontal plane at height $z=0.73H$. Adapted from Coceal et al. (2014).	15
Figure 2.5: The geometry of a heterogeneous street canyon in Nicosia. Adapted from Karra (2012).	17
Figure 2.6: Flow patterns and pollutant distributions on (a) west side section of heterogeneous street, $H/W=1.0$, (b) homogeneous street, $H/W=1.25$, (c) middle section of heterogeneous street, $H_{lee}/H_{wind}=1.92$, (d) homogeneous street, $H_{lee}/H_{wind}=2.0$, (e) east side section of heterogeneous street, $H_{lee}/H_{wind}=1.28$ and (f) homogeneous street, $H_{lee}/H_{wind}=1.42$. Adapted from Karra (2012).	18
Figure 2.7: The layouts of four heterogeneous configurations, building heights $H_1=30\text{m}$ (white) and $H_2=45\text{m}$ (grey) and street width $W=30\text{m}$. Adapted from Gu et al. (2011).	19
Figure 2.8: Sketch of typical pitched roof and definition of its run, rise and span.	20
Figure 2.9: Streamlines around isolated buildings with different pitches: (a) 3.6:12, (b) 6:12 and (c) 9:12. Adapted from Tominaga et al. (2015).	20
Figure 2.10: Velocity vectors in a street canyon with 12:12 pitched roofs on the adjacent buildings. Adapted from Theodoridis and Moussiopoulos (2000).	21

Figure 2.11: Velocity vectors on the mid vertical plane of an isolated street canyon with 8:12 pitched roofs on the adjacent buildings, $L/H=10$. Replotted following Kastner-Klein et al. (2004).....	22
Figure 2.12(a)–(g): Streamlines in seven street canyons with different pitched roof configurations. Adapted from Xie et al. (2005a).	23
Figure 2.13(a)–(p): Velocity vectors in sixteen street canyons with different slanted roof configurations. Adapted from Huang et al. (2009).	24
Figure 2.14: Flow at a cross-junction, background wind direction of (a) 0° , (b) 15° and (c) 45° . Adapted from Soulhac et al. (2009).	25
Figure 2.15: Velocity vectors on a horizontal plane ($z=5\text{m}$), background wind direction of (a) 270° and (b) 90° . Adapted from Dixon et al. (2006).....	26
Figure 2.16: Streamlines on the mid vertical plane of a street canyon with heating on the windward wall, left $Ri=-8.0$, right $Ri=-10.6$. Adapted from Cheng et al. (2009).	29
Figure 2.17: Vertical velocity profiles evaluation against wind tunnel data, on the leeward and windward quarter lines. Solid symbols: wind tunnel data, hollow symbols: LES, and line plots: RANS models. Adapted from Koutsourakis et al. (2012).	32
Figure 2.18: TKE profile evaluation against wind tunnel data, on the mid vertical line. Solid: the standard k- ϵ model, dash: the same model with modified model constants, star: the wind tunnel data in Kastner-Klein et al. (2004). Adapted from Solazzo et al. (2009).	33
Figure 4.1: The wrong flow pattern predicted by the SST k- ω turbulence model.....	47
Figure 5.1: A sketch of Kastner-Klein’s experimental setup. Replotted following Kastner-Klein (1999).....	56
Figure 5.2: Measured R.M.S. of each velocity component. Adapted from Kastner-Klein (1999).	58
Figure 5.3: A sketch of the modelling domain of benchmark case 2 and the boundary conditions.	61

Figure 5.4: The velocity profile at the inlet boundary: red circle—experimental measurements, blue solid line—specified by a power law and used in CFD models. Replotted following Kastner-Klein (1999).....	62
Figure 5.5: TKE for approaching flow. Red circle: experimental measurements from Kastner-Klein, and blue solid line: the TKE profile obtained by fitting the measurements and used for the inlet boundary.	63
Figure 5.6: The nested mesh for benchmark case 3.	67
Figure 5.7: The positions for data comparison, magenta $x=-0.053\text{m}$ (or $-0.45H$), red $x=-0.03\text{m}$ (or $-0.25H$), blue $x=0\text{m}$, green $x=0.03\text{m}$ (or $0.25H$) and cyan $x=0.053\text{m}$ (or $0.45H$).	68
Figure 5.8: Mesh independence tests on the middle line ($x=0$): (a) U , (b) W , (c) k , (d) c for Emission case A, (e) c for Emission case B, and (f) c on the lowest point (ground) of the middle line for both emission cases vs mesh resolution.	71
Figure 5.9: Mesh independence tests on the leeward and windward side lines ($x=-0.45H$, magenta; $x=0.45H$, cyan): (a) U , (b) W , (c) k , (d) c for Emission case A, and (e) c for Emission case B.....	73
Figure 5.10: Velocity vectors on the mid vertical plane of an isolated street canyon with $L=15H$, experimental results. Replotted following Kastner-Klein et al. (2004).	74
Figure 5.11: Velocity vectors on the mid vertical plane of an isolated street canyon with $L=15H$, modelled by (a) the standard $k-\varepsilon$ model, and (b) the RNG $k-\varepsilon$ model.	75
Figure 5.12: Horizontal velocity U on the middle line and on the leeward and windward quarter lines. Solid line: CFD model results for benchmark case 1, and circle: Kastner-Klein’s experimental measurements.....	77
Figure 5.13: Vertical velocity W on the middle line and on the leeward and windward quarter lines. Solid line: CFD model results for benchmark case 1, and circle: Kastner-Klein’s experimental measurements.....	78
Figure 5.14: Turbulent kinetic energy k on the middle line and on the leeward and windward quarter lines. Solid line: CFD model results for benchmark case 1, and circle: Kastner-Klein’s experimental measurements.....	79

Figure 5.15: Concentration c on the leeward and windward side lines, (a) Emission case A and (b) Emission case B. Solid line: CFD model results for benchmark case 1, and circle: Kastner-Klein's experimental measurements.	80
Figure 5.16: Velocity vectors on the mid vertical plane of an isolated street canyon with $L=10H$, modelled by (a) the standard k- ϵ model, and (b) the RNG k- ϵ model.	85
Figure 5.17: Concentration c on the leeward and windward side lines, (a) Emission case A and (b) Emission case B. Solid line: CFD model results for benchmark case 2, and circle: Kastner-Klein's experimental measurements.	87
Figure 5.18: Mesh independence tests on the middle line ($x=0m$): (a) U , (b) W , (c) k , (d) c for Emission case A, (e) c for Emission case B, and (f) c on the lowest point (ground) of the middle line for both emission cases vs mesh resolution.	90
Figure 5.19: Mesh independence tests on the leeward and windward side lines ($x=-0.45H$, magenta; $x=0.45H$, cyan): (a) U , (b) W , (c) k , (d) c for Emission case A, and (e) c for Emission case B.	92
Figure 5.20: The iteration history for benchmark case 3, modelled by the RNG k- ϵ model.	93
Figure 5.21: Velocity vectors on the mid vertical plane of an isolated street canyon with $L=10H$, experimental results. Replotted following Kastner-Klein et al. (2004).	94
Figure 5.22: Velocity vectors on the mid vertical plane of an isolated street canyon with $L=10H$, modelled by the standard k- ϵ model.	94
Figure 5.23: Velocity vectors on the horizontal plane at $z=0.25H$, experimental results. Replotted following Kastner-Klein et al. (2004).	96
Figure 5.24: Velocity vectors on the horizontal plane at $z=0.25H$, modelled by the standard k- ϵ model.	96
Figure 5.25: Horizontal velocity U on the middle line and on the leeward and windward quarter lines. Solid line: CFD model results for benchmark case 3, and circle: Kastner-Klein's experimental measurements.	97

Figure 5.26: Vertical velocity W on the middle line and on the leeward and windward quarter lines. Solid line: CFD model results for benchmark case 3, and circle: Kastner-Klein's experimental measurements.....	98
Figure 5.27: Turbulent kinetic energy k on the middle line and on the leeward and windward quarter lines. Solid line: CFD model results for benchmark case 1, and circle: Kastner-Klein's experimental measurements.....	99
Figure 5.28: Concentration c on the leeward and windward side lines, (a) Emission case A and (b) Emission case B. Solid line: CFD model results for benchmark case 3, and circle: Kastner-Klein's experimental measurements.....	100
Figure 6.1: A sketch of the computational domain and street canyons for a typical case.	106
Figure 6.2: A sketch of the geometries of thirteen studied cases, $AR=1.0$	108
Figure 6.3: The flow patterns in the third (test) and the fourth street canyons: (a) AR080_6F_R0, (b) AR080_6P_R3, (c) AR100_6F_R0 (case A), (d) AR100_6P_R3 (case M), (e) AR133_6F_R0, and (f) AR133_6P_R3.	112
Figure 6.4: Three vertical lines in the test canyon for plotting flow properties.....	114
Figure 6.5: Horizontal velocity U on the middle line for Cases A to M.....	115
Figure 6.6: Vertical velocity W on the leeward side line for Cases A to M.....	115
Figure 6.7: Turbulent kinetic energy k on the leeward side line for Cases A to M.	116
Figure 6.8: Vertical velocity W on the windward side line for Cases A to M.	116
Figure 6.9: Turbulent kinetic energy k on the windward side line for Cases A to M..	117
Figure 6.10: Schematic diagram of the relationship between flow properties and roof arrangement.....	118
Figure 6.11 (b)–(g): The deviation of concentration from the reference case, cases B–G, the third street canyon.	122
Figure 6.12 (b)–(g): The deviation of concentration from the reference case, cases B–G, the fourth street canyon.	125
Figure 6.13: The scatter plot of normalized U_{mix} vs normalized U_{ex} , the third (test) street canyon. Triangle: $AR=0.8$, circle: $AR=1.0$ and square: $AR=1.33$. Large	

symbol represents high pitch rise, and the same colour scheme in Figure 6.2 is used to distinguish different roof arrangements.	128
Figure 6.14: The scatter plot of normalized c_{ped} vs normalized c_{can} , the third (test) street canyon. Triangle: AR=0.8, circle: AR=1.0 and square: AR=1.33. Large symbol represents high pitch rise, and the same colour scheme in Figure 6.2 is used to distinguish different roof arrangements.	131
Figure 6.15: The deviation of the concentration for AR133_6P_R3 from the reference case, the 3 rd street canyon.....	133
Figure 6.16: 'Heat-map' of volume-average concentration for eight parts of the third (test) street canyon.....	136
Figure 6.17: 'Heat-map' of volume-average concentration for eight parts of the fourth street canyon.....	137
Figure 7.1: Gloucester Place in central London and the city blocks surrounding it. Map downloaded from Google Earth on 28 th Nov, 2014. Red arrow—one of the prevailing wind directions, yellow frame—Gloucester Place, and blue frame—the model area.	142
Figure 7.2: A schematic diagram of the geometry of Gloucester Place.....	142
Figure 7.3: The wind rose for London Heathrow measured at 25 metres. Adapted from Met Office (2015). (Note: 1 knot=0.514m/s).....	143
Figure 7.4: Sketches of computational domain and the building blocks in it.	144
Figure 7.5: Sketches of a horizontal plane viewed from top (top) and two cross sections viewed from south (bottom).	145
Figure 7.6: The nested mesh viewed from the south.	147
Figure 7.7: Streamlines around the building blocks.....	148
Figure 7.8: A vertical plane across the north section of the test street and the tall building (72m away from the north street end) and the velocity vectors on it.	149
Figure 7.9: A vertical plane across the south section of the test street and the space between two short parallel buildings (32m away from the south street end) and the velocity vectors on it.	149

Figure 7.10: Horizontal velocity profiles above the five building rows (measured at 72m away from the north street end).....	149
Figure 7.11: Velocity vectors on the horizontal plane at $z=21\text{m}$ (near roof level).	151
Figure 7.12: Velocity vectors on the horizontal plane at $z=5\text{m}$ ($0.25H$).	152
Figure 7.13: Velocity W on five equally spaced vertical lines in the test street (each line is 10m away from the leeward building and the windward building).	153
Figure 7.14: A typical streamline in the non-uniform stream canyon. Adapted from Gu et al. (2011).	153
Figure 7.15(a)-(c): Streamlines in Gloucester Place, (a) overall view and relative positions of nine across-street vertical planes, (b) enlarged view for the north section, and (c) enlarged view for the south section.	155
Figure 7.16: Velocity vectors on nine across-street vertical planes, (a)–(i): v-plane1 to v-plane 9.	157
Figure 7.17: Velocity vectors across the T-junction plane.	162
Figure 7.18: A sketch of flow structures in Zone 1(red), Zone 2 (pink), Zone 3 (green) and Zone 4 (yellow).	163
Figure 7.19: Pollutant concentration on the horizontal plane at height $z=10\text{m}$ ($0.5H$).	164
Figure 7.20: Pollutant concentration on the horizontal plane at height $z=2\text{m}$ ($0.1H$ and pedestrian level).	165
Figure 7.21: Pollutant concentration on nine across-street vertical planes: v-plane1 to v-plane 5 (top) and v-plane6 to v-plane9 (bottom).	166
Figure 8.1: Velocity vectors on v-plane4. Top: Case 4, middle: Case 8 (heterogeneous buildings, $H_{lee}=H_{wind}=16\text{m}$ in that cross-section), and bottom: Case 6.	175
Figure 8.2: Velocity vectors on v-plane3, top: Case 9, and bottom: Case 10.	177
Figure 8.3: Tangential velocity vectors on six planes in the south section, Case 7.	178
Figure 8.4: Tangential velocity vectors on six planes in the south section, Case 8.	179
Figure 8.5: Tangential velocity vectors on six planes in the south section, Case 10.	181
Figure 8.6: Mixing velocities for whole street canyon, Cases 1–10.	185
Figure 8.7: Exchange velocities for whole street canyon, Cases 1–10.	185

Figure 8.8: The mixing velocities for the nine across-street vertical planes in Cases 3–10, and the mixing velocities for Cases 1 and 2.....	187
Figure 8.9: The exchange velocities for the nine across-street vertical planes in Cases 3–10, and the exchange velocities for Cases 1 and 2.	188
Figure 8.10: Percentage changes of the mixing velocities for nine across-street vertical planes in Cases 3–10.	190
Figure 8.11: Percentage changes of the exchange velocities for nine across-street vertical planes in Cases 3–10.	190
Figure 8.12: Overall canyon concentrations for Cases 1–10.	194
Figure 8.13: Overall pedestrian concentrations for Cases 1–10.	194
Figure 8.14: The canyon concentrations for the nine across-street vertical planes in Cases 3–10, and the canyon concentrations for Cases 1 and 2.	196
Figure 8.15: The pedestrian concentrations for the nine across-street vertical planes in Cases 3–10, and the pedestrian concentrations for Cases 1 and 2.	197
Figure 8.16: Percentage changes of the canyon concentrations for nine across-street vertical planes in Cases 3–10.	197
Figure 8.17: Percentage changes of the pedestrian concentrations for nine across-street vertical planes in Cases 3–10.	198

List of Tables

Table 3.1: The model constants for the standard k- ϵ model, proposed by Launder and Sharma (1974).....	38
Table 3.2: The model constants of the RNG k- ϵ model, proposed by Yakhot et al. (1992).	39
Table 4.1: The CFD software used in the thesis.	45
Table 4.2: A summary of the turbulence models used in the literature for modelling street canyon flow.	46
Table 4.3: Typical boundary conditions for a CFD model that simulates flow around street canyon.....	49
Table 4.4: Minimum distances between the boundaries and the buildings for modelling street canyon flow. Recommended by the COST best practice guideline (Franke et al., 2007) and the AIJ guidelines (Tominaga et al., 2008).....	50
Table 4.5: The default values for the under-relaxation factors in FLUENT.....	53
Table 5.1: Summary of three benchmark cases.	60
Table 5.2: Mesh information for each benchmark case.	67
Table 5.3: Model error statistics for benchmark case 1. $Q_{hit} < 66\%$ marked by red.....	83
Table 5.4: Model error statistics for benchmark case 2. $Q_{hit} < 66\%$ marked by red.....	88
Table 5.5: Model error statistics for benchmark case 3. $Q_{hit} < 66\%$ marked by red.....	102
Table 6.1: Full list of the model cases and the roof structures on the buildings adjacent to the third street.....	109
Table 6.2: Normalized volume-average concentrations in the 3 rd and 4 th street canyons, and deviations from reference case. Reference cases marked by coral, increase $>10\%$ marked by red, and decrease marked by green.....	135
Table 7.1: Nine across-street vertical planes which are used to present velocity vectors and concentration contours.	155
Table 8.1: A summary of the characteristic urban geometries in ten studied cases.....	172
Table 8.2: Momentum fluxes on the top of nine across-street vertical planes (Case 5), which are used for calculating exchange velocity.....	187

Table 11.1: The canyon velocities, mixing velocities, and exchange velocities for all the cases in Chapter 6.....	220
Table 11.2: The canyon concentrations and pedestrian concentrations for all the cases in Chapter 6.....	221

Nomenclature

Symbol	Description
A_{ex}	area of exchange plane
$C_{1\varepsilon}$	model constant in the standard k- ε model and the RNG k- ε model
$C_{2\varepsilon}$	model constant in the standard k- ε model and the RNG k- ε model
C_μ	model constant in the standard k- ε model and the RNG k- ε model
E	empirical constant in the logarithmic law for velocity
F_i	i components of additional source term of momentum (i=1,2 and 3)
G_k	the production of turbulent kinetic energy
H	building height of homogeneous buildings or characteristic building height of heterogeneous buildings
H_1	the height of lower building in a row of buildings
H_2	the height of taller building in a row of buildings
H_{lee}	leeward building height
H_{wind}	windward building height
I	turbulent intensity
L	building length
L_{mid}	length of mid vertical line
L_q	length of emission source
Q_{hit}	hit rate Q
R	pitch rise
Re	Reynolds number calculated by free-stream velocity
Re_L	turbulent Reynolds number calculated by turbulent kinetic energy
Re_τ	Reynolds number calculated by friction velocity
S	characteristic mean strain rate
S_k	additional source term of turbulent kinetic energy
S_m	additional source term of mass
S_ε	additional source term of turbulent dissipation
S_ϕ	additional source term of passive scalar
Sc	Schmidt number
Sc_t	turbulent Schmidt number
T_{ref}	reference temperature

Symbol	Description
T_{wall}	wall temperature
U	velocity magnitude or x component of velocity
U_0	free-stream velocity
U_{can}	canyon velocity
U_{ex}	exchange velocity
U_i	i components of velocity (i=1,2 and 3)
U_{mix}	mixing velocity
U_p	velocity at point p
U_{ref}	velocity at reference height
U_τ	friction velocity
U^*	dimensionless velocity near the wall
V	y component of velocity
V_{can}	street canyon volume
V_{ped}	volume below pedestrian level
W	street width or z component of velocity
c	pollutant concentration
c_{can}	canyon concentration
c_{ped}	pedestrian concentration
c^*	normalized concentration
d_0	displacement height
dl, dS, dV	line integral, surface integral and volume integral
g	gravity
k	turbulent kinetic energy
k_p	turbulent kinetic energy at point p
n	local coordinate normal to the wall
p	static pressure
u_i	i components of fluctuating velocity (i=1,2 and 3)
$u_i u_j$	Reynolds stress
$u'v'$	Reynolds stresses (another presentations for $u_i u_j$)
$u'w'$	
$v'w'$	
x	Cartesian coordinate, free-stream direction

Symbol	Description
y	Cartesian coordinate, street axis direction; wall distance
y_p	wall distance at point p
y^+	dimensionless wall distance calculated by dimensionless velocity near the wall
y^*	dimensionless wall distance calculated by turbulent kinetic energy
z	Cartesian coordinate, normal to ground
z_0	roughness length
z_{ref}	reference height
α	power-law index
β	model constant in the RNG k- ϵ model
η	intermediate quantity in the RNG k- ϵ model
η_0	model constant in the RNG k- ϵ model
σ_k	turbulent Prandtl number in k-equation
σ_ϵ	turbulent Prandtl number in ϵ -equation
δ	boundary layer height
δ_{ij}	Kronecker delta
ρ	density
ϵ	turbulent dissipation
ϵ_p	turbulent dissipation at point p
κ	Von Karman constant
μ	dynamic viscosity
ν	kinematic viscosity
ν_t	turbulent kinematic viscosity
τ_w	wall shear stress
Φ	passive scalar (representing pollutant concentration in this thesis)
Γ	molecular diffusion coefficient
Γ_t	turbulent diffusion coefficient
Γ_{eff}	effective diffusion coefficient
2D	Two-dimensional
3D	Three-dimensional
ABL	Atmospheric Boundary Layer
AR	Aspect Ratio

Symbol	Description
BP	Bulk Parameter
CFD	Computational Fluid Dynamics
DNS	Direct Numerical Simulation
TKE	Turbulent Kinetic Energy
LDA	Laser Doppler Anemometry
LES	Large Eddy Simulation
N-S	Navier-Stokes
RANS	Reynolds-Averaged Navier-Stokes
R.M.S.	Root Mean Square
RNG	Re-Normalization Group
RSM	Reynolds Stress Model
SIMPLE	Semi-Implicit Method for Pressure Linked Equations
SIMPLEC	Semi-Implicit Method for Pressure Linked Equations Consistent
SST	Shear Stress Transport

1 Introduction

Air pollution around the world has become more severe since the industrial revolution. Poor air quality is a huge threat to human health. Exposure to high levels of pollutants significantly increases the risk of respiratory, lung and cardiovascular diseases, and cancer (Blum, 2013; World Health Organization, 2014b). According to the statistics provided by World Health Organization (2014a), air pollution exposure caused around 7 million premature deaths in 2012, which is 1/8 of the total global deaths of that year. In the UK, it is estimated that poor air quality causes around 29,000 premature deaths every year (Johnston, 2014) and decreases their life expectancy by an average of 11 years (Fitzpatrick, 2014).

In order to provide public health protection and public welfare protection, environment agencies around the world, such as United States Environmental Protection Agency and European Environment Agency, have established regional air quality standards. These standards limit the exceedance of daily and annual levels of several principal pollutants (i.e., carbon monoxide, lead, nitrogen dioxide, ozone and sulphur dioxide) and particulate matters. However, they are not met in many member countries. For example, the UK has been facing up to £300m fines due to failing to meet a key air quality directive for a long time (Johnston, 2014).

Street canyons, where long narrow streets are bordered by a continuous row of buildings on both sides (illustrated in Figure 1.1 below), are known to lead to problems of high pollution and heat accumulation (Oke, 1988). The narrow space between the buildings hinders background wind from penetrating into the street and causes lower wind speed in the street than outside, especially when the background wind is perpendicular to the street (Oke, 1988). Moreover, vortex flow typically forms under the perpendicular wind condition (see Figure 1.1), causing higher concentration in the leeward side than in the windward side (Kastner-Klein et al., 2004).

According to the pioneer work of Oke (1988), the aspect ratio of building height to street width has the most significant effect on airflow in street canyons: when background wind is oblique or perpendicular to the street, the larger aspect ratio is, the lower velocity is in the street, thus the poorer ventilation is. However, following the trend of urbanization and population growth, it is inevitable to construct taller buildings, resulting in more street canyons and deeper street canyons. Thus, recent researches have

focused on studying street geometries, building geometries and local parameters (e.g., traffic motion, tree planting and solar radiation), in order to minimize the problems of high pollution and heat accumulation in street canyon by optimizing detailed building designs and urban planning (Buccolieri et al, 2011; Cheng and Liu, 2011; Sini et al., 1996). Moreover, the recent progress made in the research contributes to improving the accuracy of predicting models (Kastner-Klein et al, 2001).

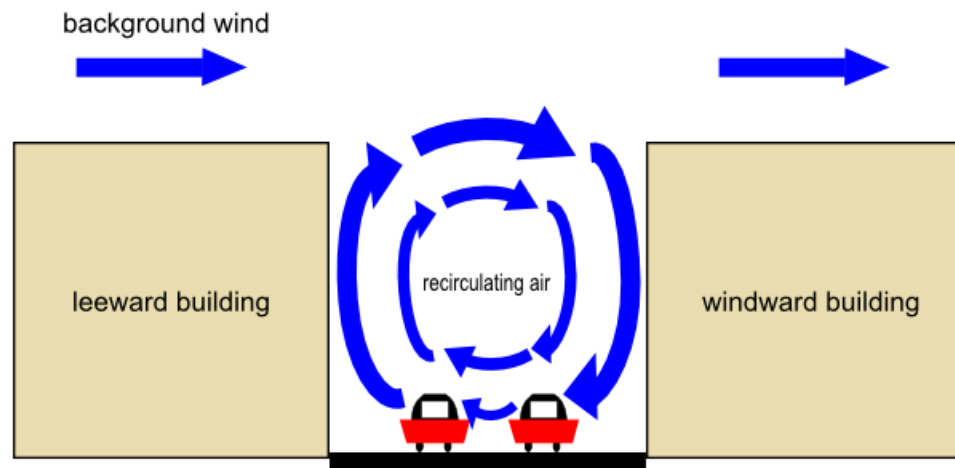


Figure 1.1: A typical two-dimensional street canyon and a typical flow pattern in the street when background wind is perpendicular to the street.

1.1 Objectives

This thesis studies the impacts of several typical urban geometries on airflow and dispersion, namely pitched roofs, tall surrounding building, heterogeneous buildings and T-junction. It is mainly motivated by three considerations. First, many previous researches in the literature assume ideal street canyon configurations that are made up of several consecutive street canyons with identical building geometries and flat roofs on the buildings. Ignoring typical urban geometries in the real world is one of the main sources of errors for makes the previous experimental models and numerical models less representative of the real situation for airflow and pollutant dispersion. Second, although typical urban geometries have been considered or studied in some literature, many of these geometries are not commonly seen in the real world. For example, it will be mentioned later that all the pitched roofs studied in the literature have a sharp roof angle, which might over-state the impacts of pitched roofs. Third, the results in the previous studies are difficult to be understood by people without fluid dynamics knowledge. It is important to make people not only know the conclusion of research but also understand how the conclusion is derived from the research data.

Based on the three considerations, four main objectives come into being before or during the research. They are explained below.

The first objective is to establish a reliable and economic method to model street canyon flow. This should be accomplished by choosing reliable experiment(s) with acceptable data resolution, creating CFD model(s) based on the experimental setup and validating the model results against the experimental measurements. In addition, it is expected to test several modelling settings. The optimal settings found in the validation will be used in this thesis as well as in future work.

The second objective is to study the impact of pitched roofs on airflow and pollutant dispersion in street canyons. Most of previous experiments and models assume flat roofs on all the buildings, which does not represent typical roof structures in many cases. Although a few studies have taken pitched roofs into account and have highlighted their profound effects on airflow, all of those studies are based on sharp roof angles which are not commonly seen in the real world. Therefore, it is useful to examine additional pitched roofs based on realistic roof angles and quantify their impacts on ventilation and pollutant removal. In addition, it is planned to test whether pitched roofs make consistent impacts under different urban geometries.

The third objective is to make a case study of airflow and pollutant dispersion in a real urban area. This study is aimed to investigate the special flow structures that only exist in this case but do not exist in any ideal street canyon and understand which elements of urban geometries cause these flow features. The study will help to identify the pollution issue in this urban area and provide useful guidance for future urban planning.

The fourth objective is to present modelling results in concise and readable ways. CFD results are usually difficult to read and understand for people without professional knowledge of fluid dynamics. It is hoped to use several simple bulk parameters to assess ventilation efficiency and pollutant removal performance, so people can easily judge which case or design has higher efficiency and better performance. Moreover, it is hoped to use graphical presentations to effectively display a group of data.

1.2 Thesis structure

The content of this thesis is outlined as follows:

Chapter 2 reviews previous research findings about airflow and pollutant dispersion in street canyons. The review focuses on three parts: the regimes of airflow, the effects of street and building geometries and the effects local parameters. Then, the state of the art in CFD simulation is briefly discussed by comparing with experimental model and field measurement.

Chapter 3 introduces the fundamental of CFD modelling, including Navier-Stokes equations, turbulence models, wall treatments and how to model pollutant dispersion.

Chapter 4 introduces the general procedures for modelling street canyon flow and pollutant dispersion by using commercial CFD software ANSYS FLUENT. In addition, this chapter discusses how to specify key CFD modelling settings, such as turbulence model, wall function, boundary conditions and solver settings. A few of them have been agreed in the literature, so those agreed settings are followed; while the others will be tested in the next chapter.

Chapter 5 validates three CFD models against Kastner-Klein's wind-tunnel experimental measurements. The errors between the model results and the experiment measurements are analysed through both graphical comparison and statistical approach. Moreover, the model settings that are not determined in the previous chapter, including mesh resolution, turbulence model, wall function and turbulent Schmidt number, are tested and optimized in this chapter. They will be used in the following chapters and will be used as initial settings in future work.

Chapter 6 carries out a parametric study of pitched roofs. The aspect ratio of building height to street width, pitch rise and roof arrangement are defined as three parameters. Variations of them give a total of 39 cases. Quantitative analyses are made across some of the cases, in order to understand how different roof structures affect mean flow, turbulence and pollutant concentration in the test street. Furthermore, four bulk parameters are proposed to assess the ventilation efficiency and pollutant removal performance of each case. Innovative graphical presentations (e.g. Figure 6.11 and Figure 6.16) are utilised to illustrate concentration difference between the cases.

Chapter 7 performs a case study of airflow and pollutant dispersion in a real urban area. Flow structures in the area and in the test street are visualized by 2D vector plots and

3D streamline plots. Pollutant distributions on several horizontal and vertical planes are visualized by 2D contour plots. This chapter focuses on discussing how the specific urban geometries result in special flow structures and pollutant distributions, which do not exist in an ideal street.

Chapter 8 studies three typical urban geometries that appear in the model in Chapter 7, namely heterogeneous buildings, pitched roofs and T-junction. This is accomplished by modifying the previous geometries to create seven additional CFD models and taking into account two CFD models in Chapter 6. The bulk parameters proposed in Chapter 6 are used to assess the ventilation efficiency and pollutant removal effect of each case. The assessments are made for both whole test street canyon and different sections of the street.

2 Literature Review

This chapter reviews recent progress made in studying street canyon flow. The review covers a few topics that are closely relevant to this thesis. After the review, the state of the art in CFD simulation is briefly discussed from two respects: its advantages and its performance. The structure of this chapter is given as below.

Section 2.1 introduces typical patterns of street canyon flow under perpendicular wind conditions. Section 2.2 explains the process of turbulent air exchange between street canyon and the atmosphere. Sections 2.3 and 2.4 discuss how background wind conditions and street canyon geometries influence airflow and pollutant dispersion. Section 2.5 summarizes the previous research findings about three local parameters—trees, traffic and heating. Section 2.6 discusses general advantages and limitations of CFD modelling and evaluates its performance and accuracy according to previous researches.

2.1 Typical flow patterns in street canyons

There are numerous researches studying street canyon flow. Most of them examine the case of a street subjected to perpendicular background wind condition(s), as this is the worst scenario for ventilation and pollutant removal. Oke (1988) conducted a pioneer work to summarize typical flow under this condition. He classified the flow into three basic regimes (see Figure 2.1 below) according to the aspect ratio of building height to street width H/W and the aspect ratio of building length to building height ratio L/H . The following three paragraphs make a summary of his findings in association with the famous schematic diagrams in his work as shown in Figure 2.1 and Figure 2.2 below.

As can be observed from Figure 2.2 below, the transitions between three basic flow regimes are mainly dependent on the aspect ratio H/W . For wide street canyons ($H/W < 0.3$), the flow behind the leeward building does not interact with the flow in front of the windward building, as illustrated in Figure 2.1(a) below. This type of flow is termed isolated roughness flow. When the street width is intermediate ($0.3 < H/W < 0.7$), the wake behind the leeward building interferes with the recirculation flow in front of the windward building (see Figure 2.1(b) below). This type of flow is termed wake interference flow. When the street is narrow ($H/W > 0.7$), the flow in the street canyon is characterised by a persistent large vortex, as shown in Figure 2.1(c) below. Since the background wind does not easily travel across the narrow space between the buildings, this type of flow is termed skimming flow.

On the other hand, Figure 2.2 below shows that the aspect ratio L/H has a minor effect on the transitions. In general, the critical aspect ratios (H/W) for the transitions are slowly increased with increasing street length.

Amongst the three flow regimes, skimming flow has been confirmed to be the most detrimental for ventilation and pollutant removal. Under this flow regime, the typical velocity in street canyon is usually an order of magnitude lower than the free-stream velocity in the atmosphere. Furthermore, the vortex flow pattern flushes pollutants upwards along the leeward building, causing higher pollutant concentration in the leeward side than in the windward side.

It should be mentioned that skimming flow regime also exists in deeper street canyons ($H/W > 2.0$). However, in this case, the flow inside the street canyon is not stable and is sensitive to background wind condition, street canyon geometries and local parameters. For example, Eliasson et al. (2006) found both single vortex and double counter-

rotating vortices (in the upper and lower parts of the street respectively) could exist in the same deep street canyon but at different times. The former persisted in most time, and the latter formed and broke in short terms (Eliasson et al., 2006).

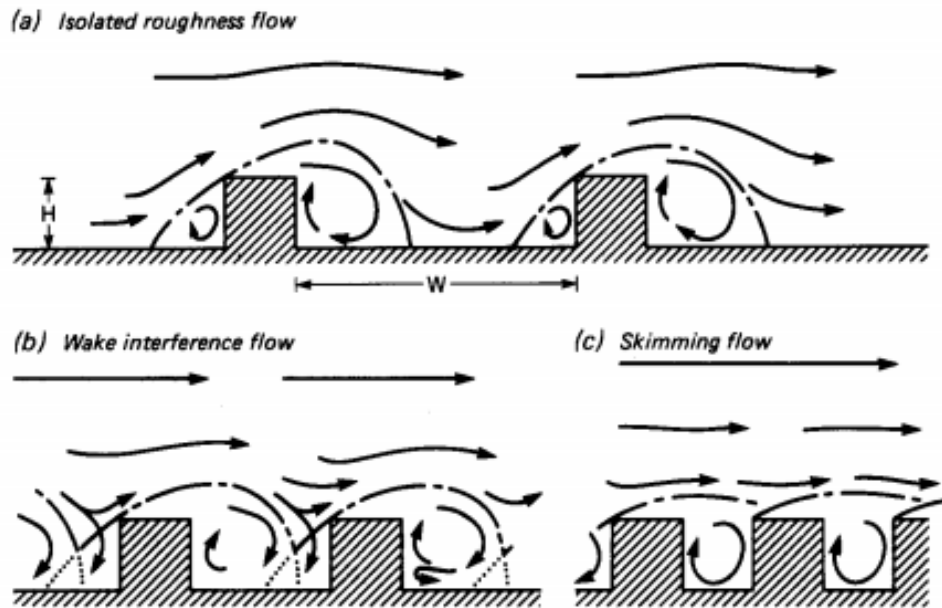


Figure 2.1: Three flow regimes for flow over buildings: (a) isolated roughness flow, (b) wake interference flow, and (c) skimming flow. Adapted from Oke (1988).

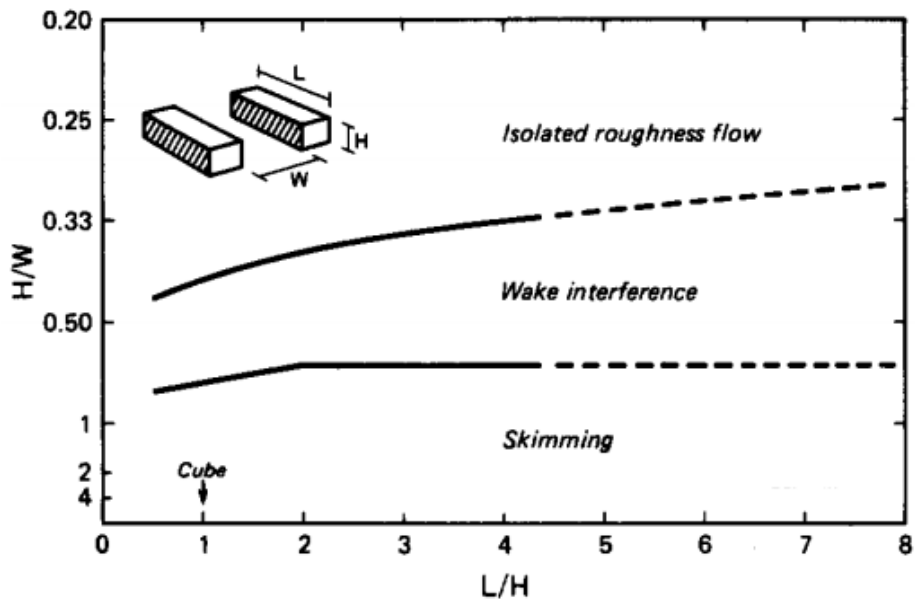


Figure 2.2: Divisions of three flow regimes as a function of building height H/W and building length L/H . Adapted from Oke (1988).

2.2 Turbulent transfer between a street canyon and the atmosphere

The ventilation efficiency of a street canyon relies on not only mean flow but also fluctuating flow or turbulence. The previous section has introduced typical flow patterns under perpendicular background wind condition(s), and this section explains turbulent transfer between street canyon and the atmosphere

For long street canyons, previous studies have demonstrated that the velocity difference between the external flow and the cavity flow will produce a shear layer above the buildings and the street canyons (Salizzoni et al., 2011). The flow in the shear layer is unstable, promoting air exchange between the street canyon and the atmosphere through an intermittent process of turbulent transfer (Cui et al., 2004; Salizzoni et al., 2011).

The turbulent transfer efficiency hinges on the dynamics of the shear layer, which are determined by the local production of turbulence and the turbulent flux from the external flow (Salizzoni et al., 2011). A good illustration is that the turbulent transfer for an isolated street canyon is usually very efficient, as the flow separation above the first building produces a large amount of turbulence (Kastner-Klein et al., 2001). In this case, air is continuously discharged from the isolated street canyon, and the flow pattern in the street changes over time (Meroney et al., 1996). In contrast, the turbulence transfer for a non-isolated street canyon (e.g., one of consecutive street canyons) is usually much weaker, because flow separation does not happen above the adjacent buildings to the street (Kastner-Klein et al., 2001). This results in stable vortex flow in the street and an intermittent discharge of air from the street (Meroney et al., 1996).

For short street canyons or building arrays, Salizzoni et al. (2011) found that the unstable shear layer did not form at the roof level. Thus, turbulent transfer plays a less important role compared to long street canyons. According to this finding, it should be made a reconsideration of the representativeness of physical and numerical models, as modelling work usually assume long streets and homogeneous buildings, while real urban geometries are always made up of short streets, heterogeneous buildings and other complicated geometries.

2.3 The impacts of background wind condition

Background wind condition directly affects airflow in street canyon. According to the similarity law of flow (given in Appendix 11.1), an increase of background wind velocity will lead to proportional increases of velocity components and turbulence statistics in the same street. This is the most straightforward effect made by different background wind velocities.

Background wind direction has profound effects on airflow and pollutant dispersion. Generally, street canyon is more efficiently ventilated when background is parallel or oblique to the street than when background is perpendicular to the street (Soulhac et al., 2008). Under a parallel background wind condition, street canyon flow shares a similar regime to channel flow (Louka et al., 2000; Yamartino and Wiegand, 1986). As a result, pollutants can be effectively flushed away along the street. For various oblique background wind conditions, Soulhac et al. (2008) showed that the general flow patterns were characterised by complicated combinations of vortex flow and channel flow. Kastner-Klein and Plate (1999) further investigated pollutant distribution under seven wind directions, which had angles of 0° , 15° , 30° , 45° , 60° , 75° , and 90° to the street axis. They confirmed that the perpendicular wind was the worst condition for pollution, and the 30° and 45° winds caused the second-highest concentrations in the street canyon. The parallel wind produced the best pollutant removal performance, as the concentrations at most measuring points were only around 1/3 of those measured concentrations under the perpendicular wind (Kastner-Klein and Plate, 1999).

Once the effects of steady background wind speed and direction were well understood, researchers started to study the effects of time-variant wind conditions.

The variation of background wind velocity mainly affects turbulence in street canyon. Castro and Robins (1977) and Kim and Baik (2003) claimed that the turbulent kinetic energy in street canyon was positively related to the turbulent kinetic energy in the background flow. When the background wind is critically unstable, the flow pattern in the street canyon will become unstable. A good illustration of this type of unstable flow is the existence of both single vortex flow and double counter-rotating vortices in the same deep street canyon but at different times, which has been mentioned before in Section 2.1. In addition, Eliasson et al. (2006) attributed these flow features to the relatively low mean background velocity and the strong fluctuation of background wind condition.

The variation of background wind direction is possible to induce the switch between different flow regimes. Balogun et al. (2010) found that a small change of the background wind direction altered the in-street flow angle substantially, and the flow near the cross-junction was the most sensitive to the change. With respect to pollutant dispersion, Karra et al. (2011) found more efficient vertical mixing of pollutants during a period that had large changes of wind direction.

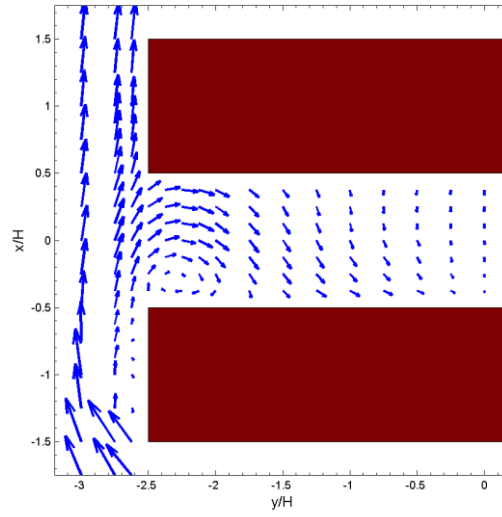
The simultaneous variations of background wind velocity and background wind direction have been taken into account in a limited number of studies. Zhang et al. (2011) modelled such effect by importing a real-time wind profile. By using this technique, they found some unique time-variant flow features, such as time-variant expansion and compression of the vortex flow, the flapping of the shear layer above the vortex and the detachment of the shear layer. These features were not found in the control model with the same geometries but modelled by a steady wind profile.

2.4 The impacts of street and building geometries

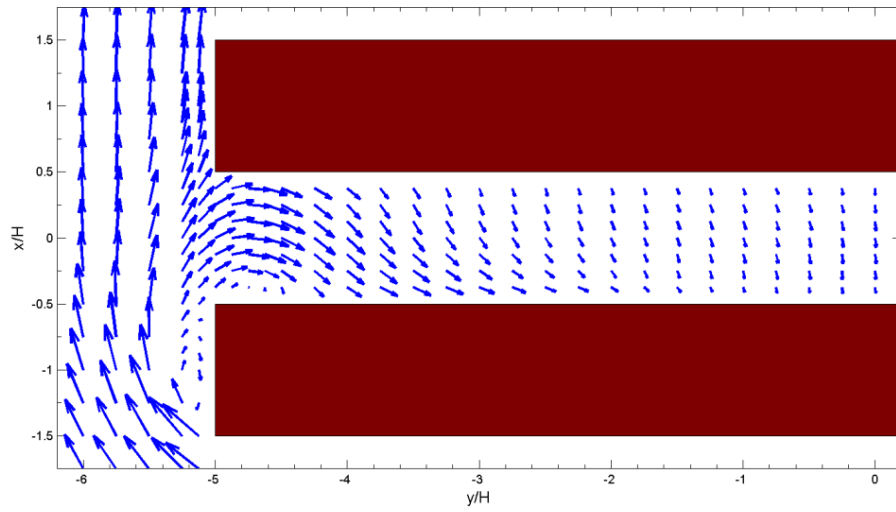
Various street and building geometries are the main reason (other than different background wind conditions) for different flow structures and pollutant distributions. The importance of the aspect ratio of building height to street width has been discussed in detail in Section 2.1. This section summarizes the effects of other geometries, including street length, asymmetric street canyon, heterogeneous street canyon, roof structure, and the presence of gaps and junctions. The summaries give useful suggestion and guidance for urban planning to improve air quality.

2.4.1 Street length

Kastner-Klein et al. (2004) studied the flow structures in short, medium and long street canyons ($L/H=5, 10$ and 15), aimed to understand how street length affected the flow approaching from street ends. They found that the short street had more complete vortex structure at two street ends and stronger flow along the street compared to the other two streets (compare Figure 2.3(a) and (b) below). After having compared the along-street flow between the three cases, they claimed that the case with $L/H=15$ had a two-dimensional vortex flow pattern in the region of $y=-4.5H$ to $y=4.5H$ (here y means along-street direction); the case with $L/H=5$ had three-dimensional flow features in the entire street (see the non-zero velocity vectors in Figure 2.3(a)). They further found that the case with $L/H=10$ had the highest pollutant concentrations on the mid vertical plane. It happened because the case with $L/H=15$ had weak along-street flow which transported fewer pollutants from the street ends to the centre, and the case with $L/H=5$ had strong three-dimensional flow which made more efficient air exchange between the street canyon and the atmosphere.



(a)



(b)

Figure 2.3: Velocity vectors on two horizontal planes at $z=0.25H$ in two isolated street canyons with different street lengths, (a) $L/H=5$ and (b) $L/H=10$. Replotted following Kastner-Klein et al. (2004).

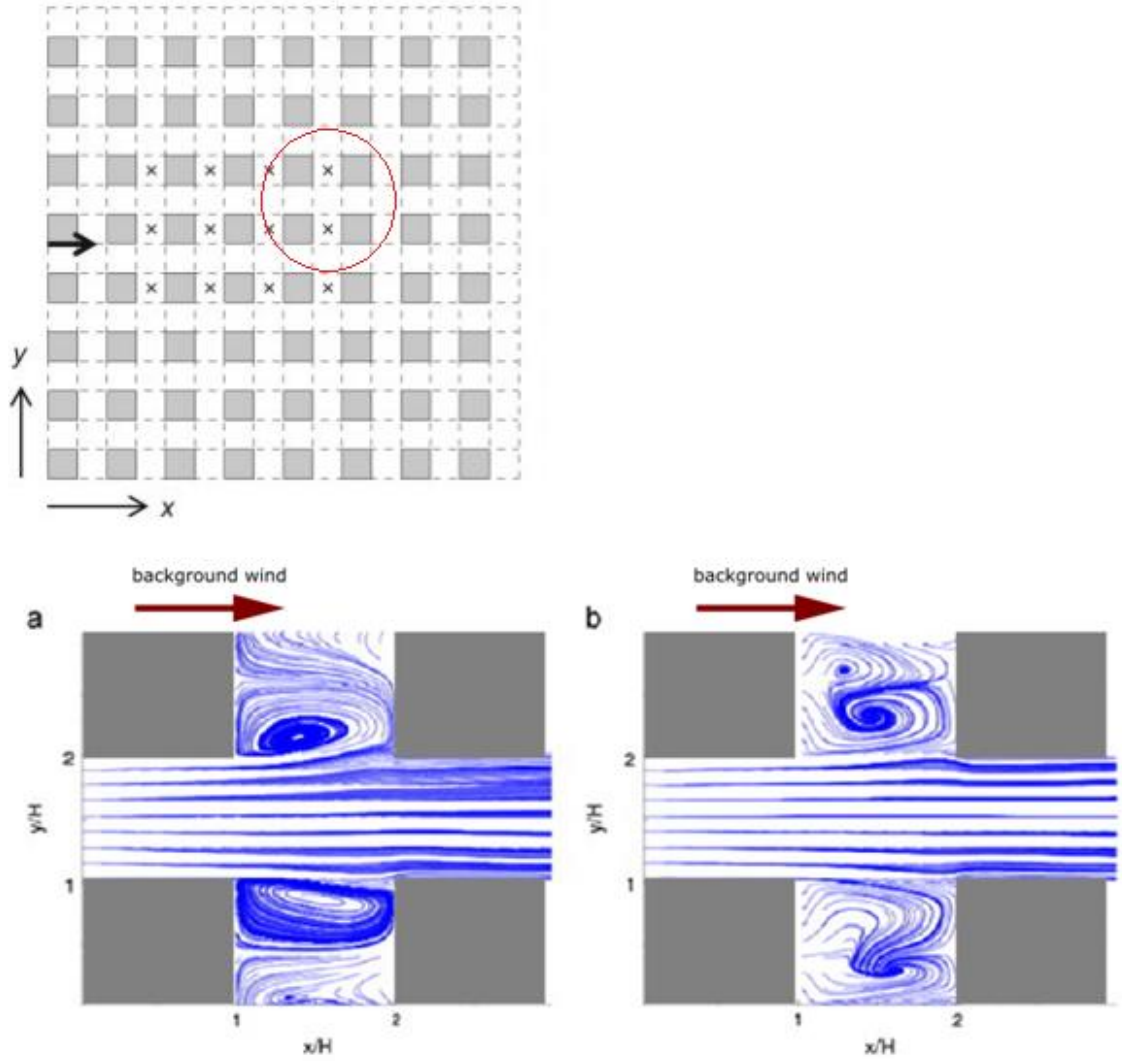


Figure 2.4: Streamlines in a building array, top: array layout and the test region (red circle), (a) the horizontal plane at height $z=0.12H$ and (b) the horizontal plane at height $z=0.73H$. Adapted from Coceal et al. (2014).

Coceal et al. (2014) used Direct Numerical Simulation (DNS) to model flow around a building array with $H/W=1$ and $L/H=1$. They found that two horizontal vortices formed behind the leeward building, as indicated in Figure 2.4 above. However, due to the short street length, the vortices contacted each other and had very different shapes than those found in long streets (compare Figure 2.4 above with Figure 2.3 above). Moreover, the streamlines in Figure 2.4(b) show that the flow at the middle of that horizontal plane travelled from the windward side to the leeward side. Since the horizontal plane is in the upper part of the street ($z=0.73H$), this flow direction was opposite to the typical flow direction in the upper part of a long street. It reveals disparate flow patterns between typical long street canyon and building array, and implies the existence of complicated three-dimensional flow around the building array.

2.4.2 Asymmetrical street canyon

For homogeneous step-up street canyon, the taller windward building has an effect in lifting airflow at the roof level. Accordingly, the vortex flow in the street is stretched at the windward roof corner, and the air motions near the ground are suppressed (Erell et al., 2012). Therefore, the mean flow in step-up street is generally weaker than in symmetrical street. On the other hand, the step-up configuration enhance the turbulent transfer between the street and the atmosphere, as the flow at the roof top impinges on the windward building and produces a large amount of turbulence (Erell et al., 2012; Miao et al., 2014). Miao et al. (2014) has found lower concentration in the step-up street canyon than in the symmetrical street. This is because the enhanced turbulent transfer outweighed the weakened mean flow with respect to pollutant removal.

The flow pattern in homogeneous step-down street canyon is determined by height difference between the leeward building and the windward building. When the leeward building is slightly taller than the windward building, vortex flow pattern still exists, but the vortex will extend upwards up to the height of the leeward building (see Figure 2.6(f) below in Section 2.4.3) (Karra, 2012). The extended vortex brings pollutants above the height of the windward building, so most pollutants are flushed downstream rather than entrained into the street from the windward side. Thus, compared to symmetrical street canyon, overall concentration is relatively low in this type of step-down street (Karra, 2012).

When the leeward building is critically taller than the windward building, an elliptical vortex flow forms behind the leeward building and above the height of the windward building (Zeman, 2012). The elliptical vortex has a longer axis in the horizontal direction than in the vertical direction, and it drives a weak counter-rotating vortex below the roof level (see Figure 2.6(d) below in Section 2.4.3) (Karra, 2012). Owing to the weak secondary vortex, overall concentration is higher in this type of step-down street canyon than in symmetrical street canyon. Owing to the double-vortex structure, pollutant concentration in this type of step-down street canyon is higher in the windward part than in the leeward part, which is opposite to the distribution for symmetric street.

2.4.3 Heterogeneous street canyon

Karra (2012) used experimental model to study airflow and pollutant dispersion in a heterogeneous street canyon and in three homogeneous street canyons (symmetrical $H/W=1.25$, step-down $H_{lee}/H_{wind}=1.92$ and step-down $H_{lee}/H_{wind}=1.42$) respectively. She compared flow pattern and pollutant distribution between on three cross-sections of the heterogeneous model and on the middle sections of the three homogeneous models. The positions and the dimensions of the three cross-sections are shown in Figure 2.5 below.

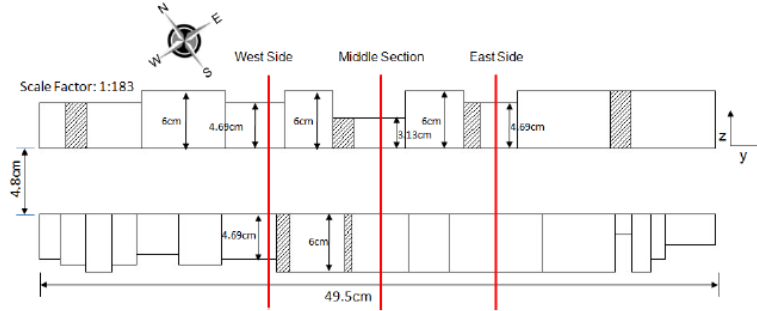


Figure 2.5: The geometry of a heterogeneous street canyon in Nicosia. Adapted from Karra (2012).

The flow pattern in the west side cross-section with $H/W=1.0$ was similar to that the flow pattern in the symmetrical homogeneous street canyon with $H/W=1.25$ (see Figure 2.6(a) and (b) below). The similar pattern under different aspect ratios was because Since the neighbour buildings to the west side cross-section were 25% taller than the buildings in this section, it is believed that the taller neighbouring buildings had a dominate effect on the flow in this section rather than the local buildings. Overall pollutant concentration was slightly lower in the west side cross-section than in the homogeneous street, because fewer pollutants accumulated at the ground level (compare Figure 2.6(a) with Figure 2.6(b)).

The flow pattern in the middle cross-section was very different from the flow pattern in the homogenous street canyon with $H_{lee}/H_{wind}=1.92$ (see Figure 2.6(c) and (d) below), due to the presence of step-down street configuration and highly heterogeneous windward buildings. Thus, both overall concentration and pollutant distribution were very different between the middle cross-section and the homogeneous street.

The flow pattern in the east side cross-section was similar to the flow pattern in the homogenous street canyon with $H_{lee}/H_{wind}=1.42$ (see Figure 2.6(e) and (f) below). A vortex flow pattern formed in the east side cross-section, but the vortex centre was

slightly lower compared to the homogeneous street. Compared to the homogeneous street, the mixing of pollutants was poor in the east side cross-section, and more pollutants accumulated above the ground.

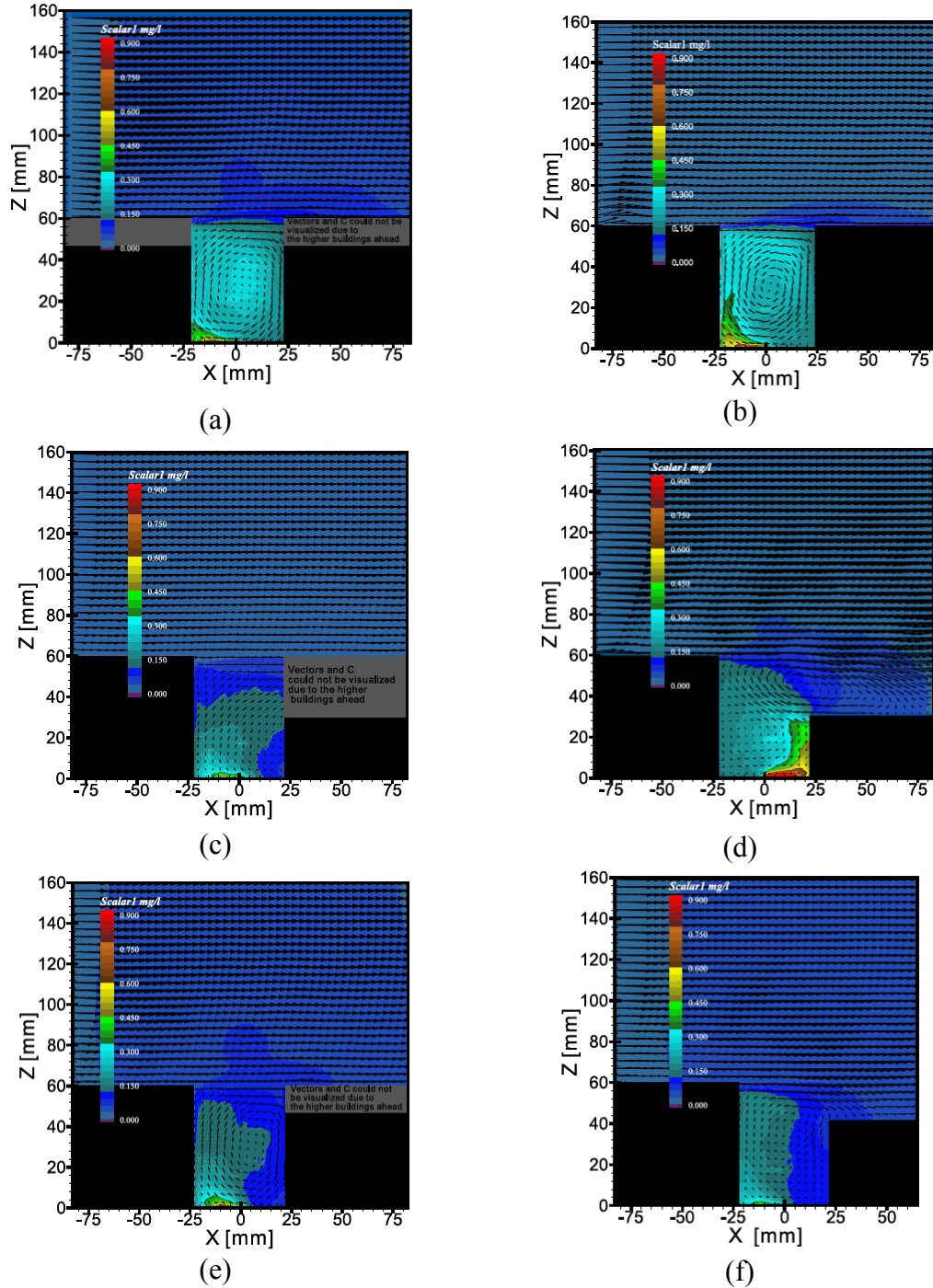


Figure 2.6: Flow patterns and pollutant distributions on (a) west side section of heterogeneous street, $H/W=1.0$, (b) homogeneous street, $H/W=1.25$, (c) middle section of heterogeneous street, $H_{lee}/H_{wind}=1.92$, (d) homogeneous street, $H_{lee}/H_{wind}=2.0$, (e) east side section of heterogeneous street, $H_{lee}/H_{wind}=1.28$ and (f) homogeneous street, $H_{lee}/H_{wind}=1.42$. Adapted from Karra (2012).

Gu et al. (2011) modelled airflow and pollutant dispersion in three street canyons that had different three-dimensional step-up and step-down street configurations (uneven building layouts) (see Figure 2.7 below). They compared these cases with a reference case which had a homogeneous symmetrical street. They found different three-dimensional flow features in the three studied case, while airflow always approached the street end with a step-up configuration and exited from the other end with a step-down configuration. The presence of this type of along-street flow caused lower overall concentrations and uneven pollutant distributions compared to the reference case. Amongst the three studied cases, the case with separation of step-up and step-down notches (Case 2 in Figure 2.7) had the strongest along-street flow and therefore had the lowest concentration in the street. In this case, the average and maximum concentrations were reduced by 70% and 60% respectively from the reference case.

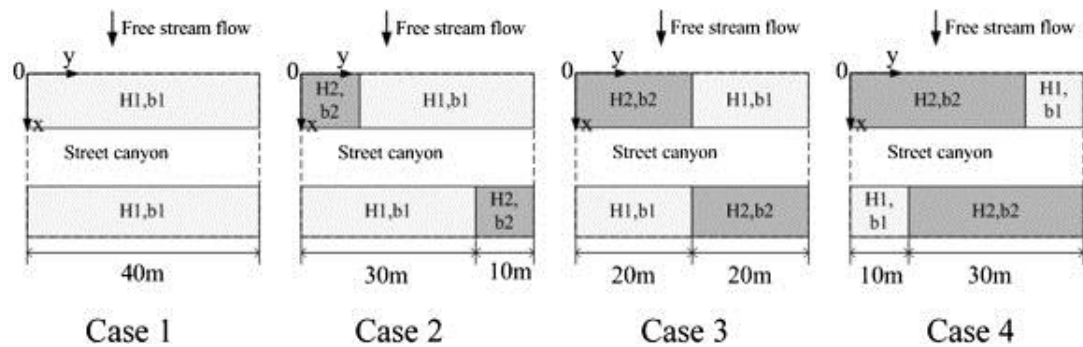


Figure 2.7: The layouts of four heterogeneous configurations, building heights $H_1=30\text{m}$ (white) and $H_2=45\text{m}$ (grey) and street width $W=30\text{m}$. Adapted from Gu et al. (2011).

2.4.4 Roof structure

The roof of a building envelope is a building structure that covers the uppermost part of the building. Pitched roof is a common type of roof, designed for the purpose of keeping out rain and snow. Besides this purpose, the detailed appearance of a pitched roof is further determined by available material, structural factors, roof space usage, walkability, aesthetic factors and native customs.

The pitch (or the angle) of a roof is usually defined by its run divided by its rise, as illustrated in Figure 2.8 below. It is conventionally expressed as a ratio of a whole number in the numerator to 12 in the denominator. According to the ratio, pitched roof can be classified into non-perfect flat roof (less than 2:12), low-slope roof (2:12 to 4:12), conventional roof (4:12 to 9:12) and steep-slope roof ($>9:12$) (Schmid, 2014). Pitched roofs on large buildings usually have low rises, considering the costs of material and

labour and space usage (Reid, 2000). Conventional roof is more commonly seen on residential buildings rather than large commercial buildings; steep-slope roof is a typical design in northern regions for redirecting snow (Reid, 2000).

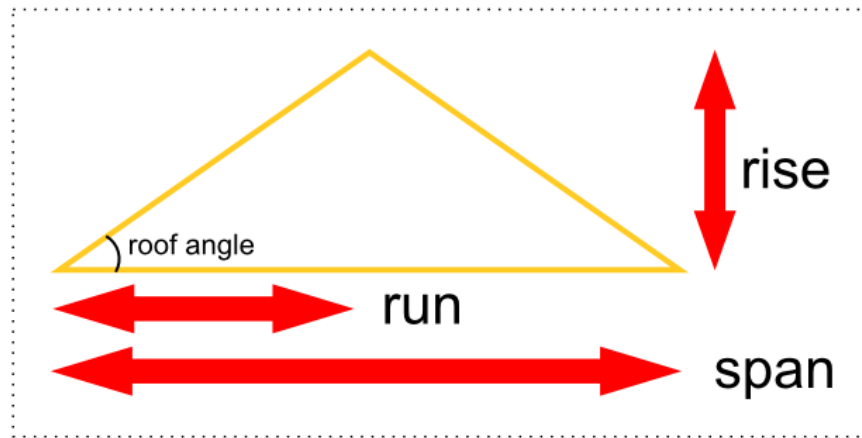


Figure 2.8: Sketch of typical pitched roof and definition of its run, rise and span.

Roof structure has been found to have a significant impact on airflow and pollutant dispersion around a building. Amongst all the roof types, pitched roofs have been studied relatively frequently, since they have very different aerodynamic performance to flat roofs.

Tominaga et al. (2015) studied airflow around an isolated building with three different pitched roofs of rise-to-run ratios 3.6:12, 6:12 and 9:12. Since the 3.6:12 pitched roof was relatively blunt, the approaching flow separated behind the ridge. As a consequence, vortex flow formed behind the building (see Figure 2.9(b) below). The 6:12 and 9:12 pitched roofs were critically sharp to engender flow separation on the ridge. As a consequence, vortex flow also formed behind the building, but the centre of the vortex was lifted higher (see Figure 2.9(c) and Figure 2.9(d) below). Based on these findings, Tominaga et al. (2015) claimed that the flow pattern around a pitched-roof building changed critically at an angle around 20° .

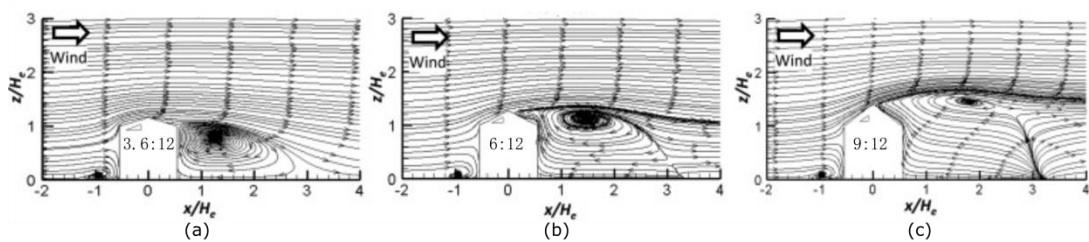


Figure 2.9: Streamlines around isolated buildings with different pitches: (a) 3.6:12, (b) 6:12 and (c) 9:12. Adapted from Tominaga et al. (2015).

Salizzoni et al. (2008) studied the impact of small-scale roughness on the flat roofs of consecutive street canyons. They found that the roughness contributed higher turbulence above the roofs but had limited influence on the velocity profile in the urban boundary layer.

Pitched roof with a rise-to-run ratio of 12:12 is found to be a relatively frequently studied roof prototype in the literature. Rafailidis (1997) modelled consecutive street canyons with this specific roof structure in his experiments. He found that the pitched roofs significantly retarded the flow $2-3H$ above the buildings. As a result, mean vertical velocity (V), fluctuant vertical velocity (v) and the Reynolds stress (uv) at the roof level were increased, causing more efficient turbulent transfer between the streets and the atmosphere. Theodoridis and Moussiopoulos (2000) and Leidl and Meroney (1997) used CFD models to simulate one of Rafailidis' experiments. They found that a strong vortex formed between the adjacent pitched roofs, and a weak counter-rotating vortex occupied the lower $3/4H$ of the street canyon (see Figure 2.10 below). These two vortices explain why the concentrations on the windward wall were much higher than on the leeward wall.

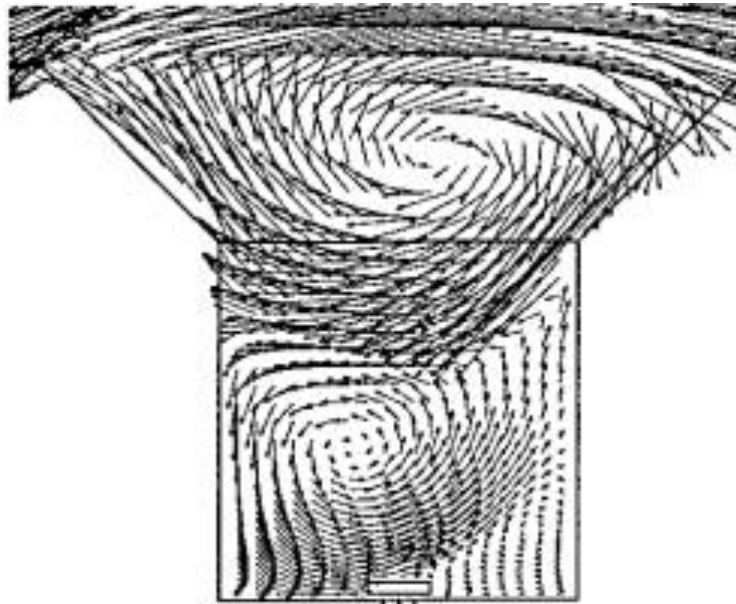


Figure 2.10: Velocity vectors in a street canyon with 12:12 pitched roofs on the adjacent buildings. Adapted from Theodoridis and Moussiopoulos (2000).

Kastner-Klein et al. (2004) carried out an experimental model which had a smaller rise-to-run ratio (8:12) and a shorter street length ($10H$) compared to Rafailidis' experiments. They observed a flow pattern different from Theodoridis and Moussiopoulos (2000) and Leidl and Meroney (1997). As shown in Figure 2.11 below, no vortex formed on the mid

vertical plane. Instead, air flowed from the windward wall to the leeward wall and from the bottom to the top, which indicates that three-dimensional flow existed in the street. The unique flow pattern implies that the slope or the rise of a pitched roof is a key factor to affect flow structure in street canyon.

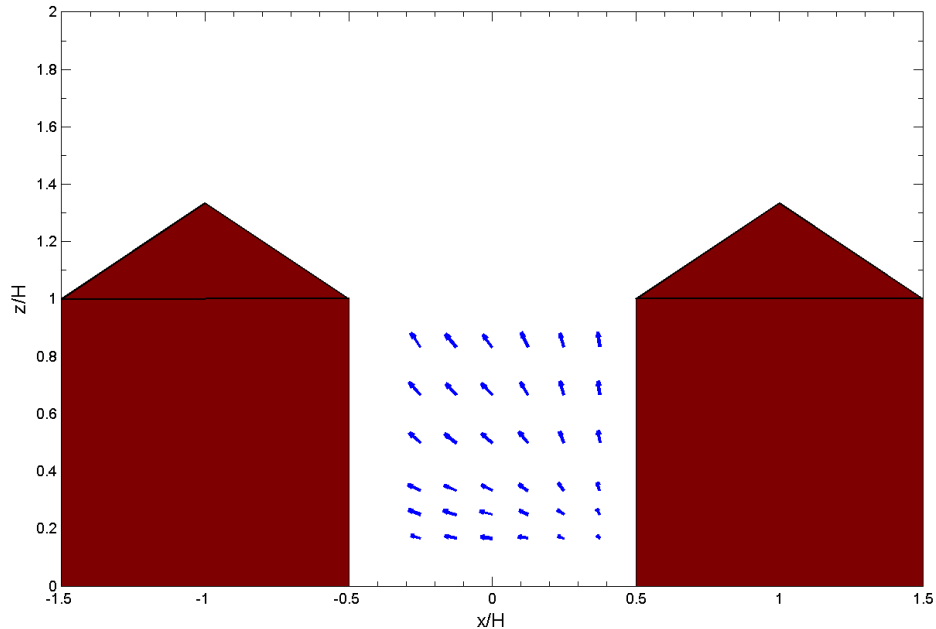


Figure 2.11: Velocity vectors on the mid vertical plane of an isolated street canyon with 8:12 pitched roofs on the adjacent buildings, $L/H=10$. Replotted following Kastner-Klein et al. (2004).

Xie et al. (2005a) studied different roof arrangements that were based on flat roof and 12:12 pitched roof. The modelled flow patterns are shown in Figure 2.12 below. For the cases that have the same eave heights for the leeward and windward buildings, the presence of a pitched roof on the leeward building resulted in two counter-rotating vortices which are similar to the vortices found in Theodoridis and Moussiopoulos (2000) and Leidl and Meroney (1997) (compare Figure 2.12(c) and Figure 2.12(d) below). On the other hand, the presence of a pitched roof only on the windward building caused the stretch of the vortex flow (see Figure 2.12(b) below). When the eave of flat-roof building was as tall as the ridge of pitched-roof building, double-vortex flow pattern only existed in the case that has a flat roof on the leeward building and a pitched roof on the windward building (see Figure 2.12(e) below).

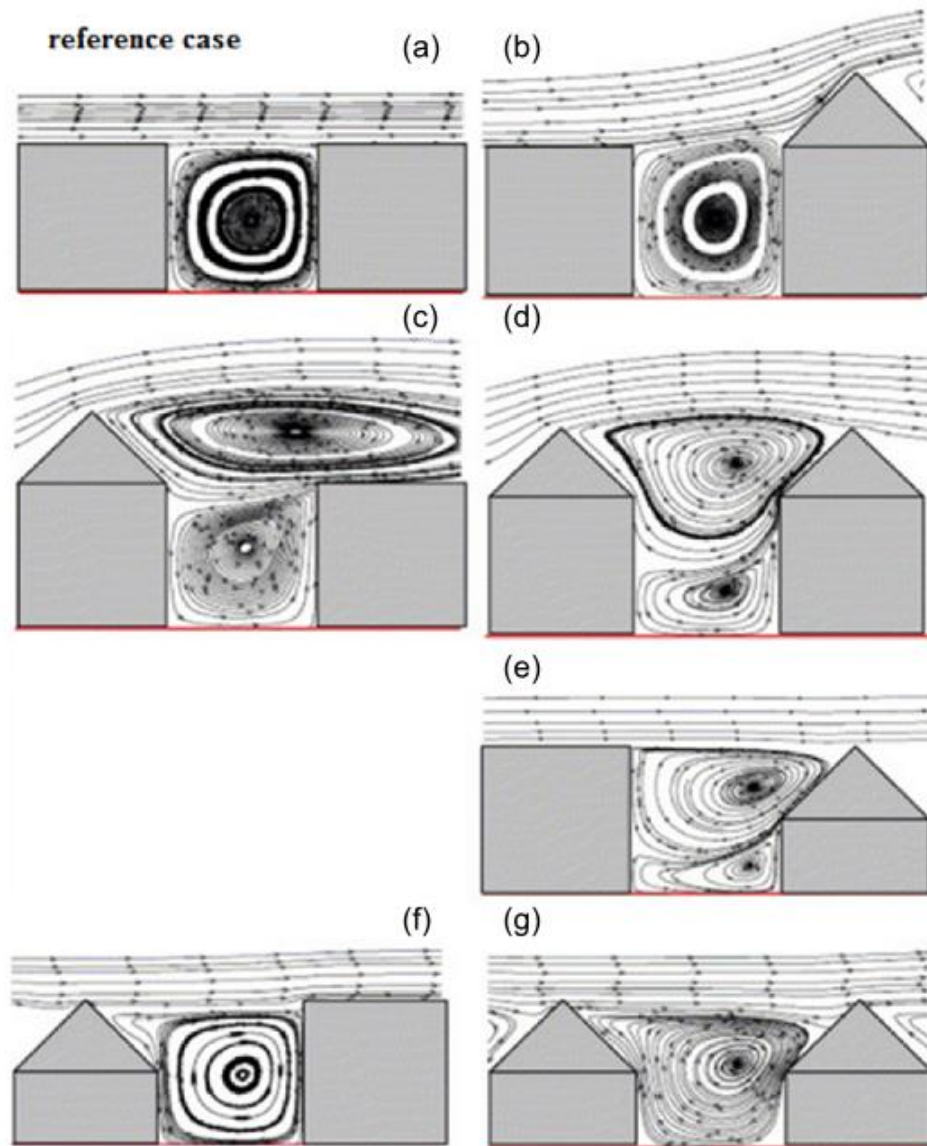


Figure 2.12(a)–(g): Streamlines in seven street canyons with different pitched roof configurations. Adapted from Xie et al. (2005a).

Huang et al. (2009) studied different roof arrangements. The modelled flow patterns are shown in Figure 2.13 below. The upward slanted roof on the leeward building produced two counter-rotating vortices in three cases (see Figure 2.13(b), (h) and (p) below). In these cases, the leeward wall was all taller than the corresponding windward wall, which gave configurations equivalent to step-down street canyons and therefore explained the double-vortex flow. The downward slanted roof on the leeward building caused the vortex flow extend above the eave level in three cases (see Figure 2.13(c), (g) and (o) below). On the other hand, the roof shape on the windward building had a weak effect on the airflow.

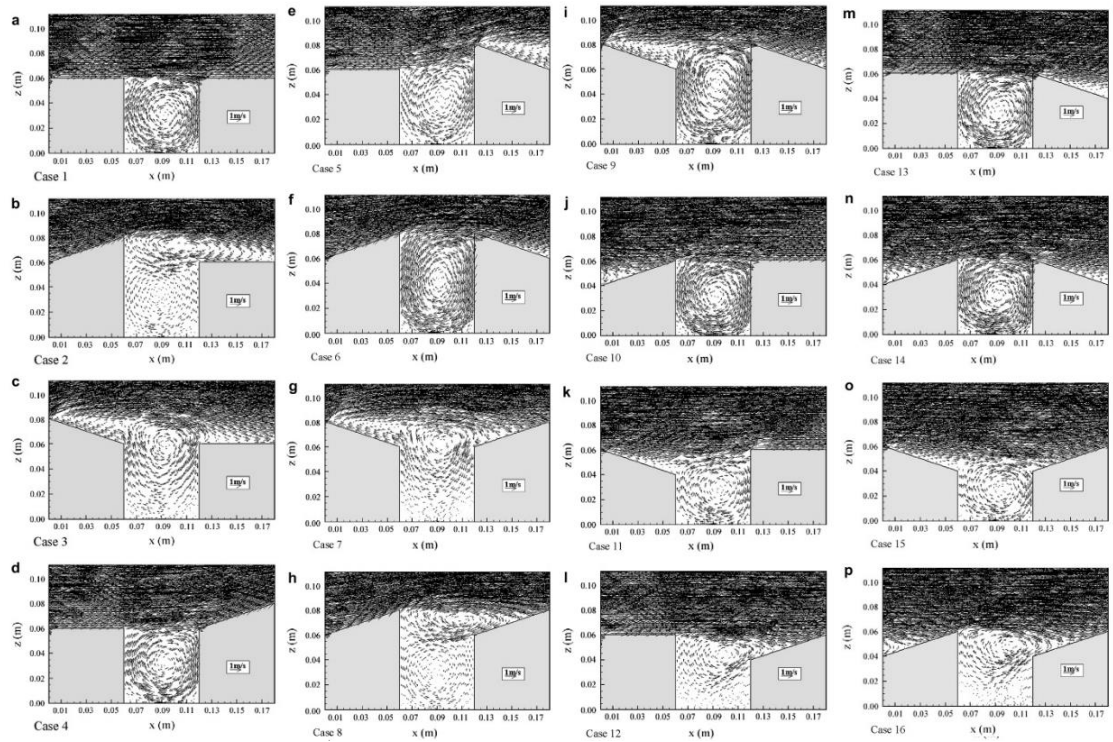


Figure 2.13(a)–(p): Velocity vectors in sixteen street canyons with different slanted roof configurations. Adapted from Huang et al. (2009).

After reviewing the above literature, it is found that the previous studies have four limitations. First, there is clear evidence that pitched roofs with different roof angles have different impacts on airflow in street canyon. However, only two roof angles were tested, namely the run-to-rise ratios of 8:12 and 12:12. Second, the 12:12 pitched roofs are very sharp and belong to steep-slope roof, which means they are not commonly seen in the real world. Third, the previous studies are all based on a fixed street canyon configuration that has consecutive street canyons with the aspect ratio of building height to street width of 1.0. Fourth, pollutant concentration is only studied in a few positions close to the building walls. All of the four limitations indicate that the previous studies are not enough or representative to comprehensively show the effects of pitched roofs.

2.4.5 Gap and junction

Karra (2012) found that the presence of gaps between the leeward buildings helped to reduce local pollutant concentration. This was because additional flow approached the street canyon through the gaps and enhanced vertical air motions near the leeward buildings. On the other hand, increases of concentrations were found in the case that had gaps between the windward buildings. This was because the flow from the gaps weakened downward motions near the windward buildings.

Soulhac et al. (2009) studied flow near a cross-junction under different background wind directions. Under a perpendicular background wind condition, they found that two symmetrical horizontal vortices formed in the same street but on different sides of the junction, as shown in Figure 2.14(a) below. Pollutants were trapped by these vortices, creating two hot-spots of high pollution near the junction. When the background wind had an angle of 15° to one of the streets, only one horizontal vortex formed (see Figure 2.14(b) below). Under a 45° background wind condition, airflow came from two branches of the streets, converged at the junction and bifurcated after passing the junction (see Figure 2.14(c) below). Meanwhile, two horizontal vortices formed at different streets and had compressed shapes. Compared to the vortices formed under the perpendicular background wind, the two vortices in this case also produced pollution hot-spots, but at different locations.

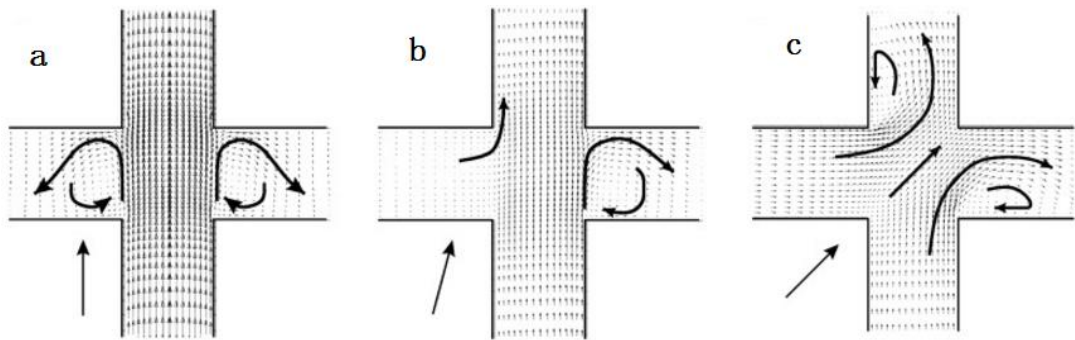


Figure 2.14: Flow at a cross-junction, background wind direction of (a) 0° , (b) 15° and (c) 45° . Adapted from Soulhac et al. (2009).

Dixon et al. (2006) modelled airflow in an urban configuration with a T-junction. They found bifurcated flow at the junction when the background wind came from the T-end (see Figure 2.15(a) below) and converged flow at the junction when the background wind travelled over the T-top first (see Figure 2.15(b) below). Owing to the asymmetrical building layouts, both the bifurcated flow and the converged flow were not perfectly symmetrical about the T-junction.

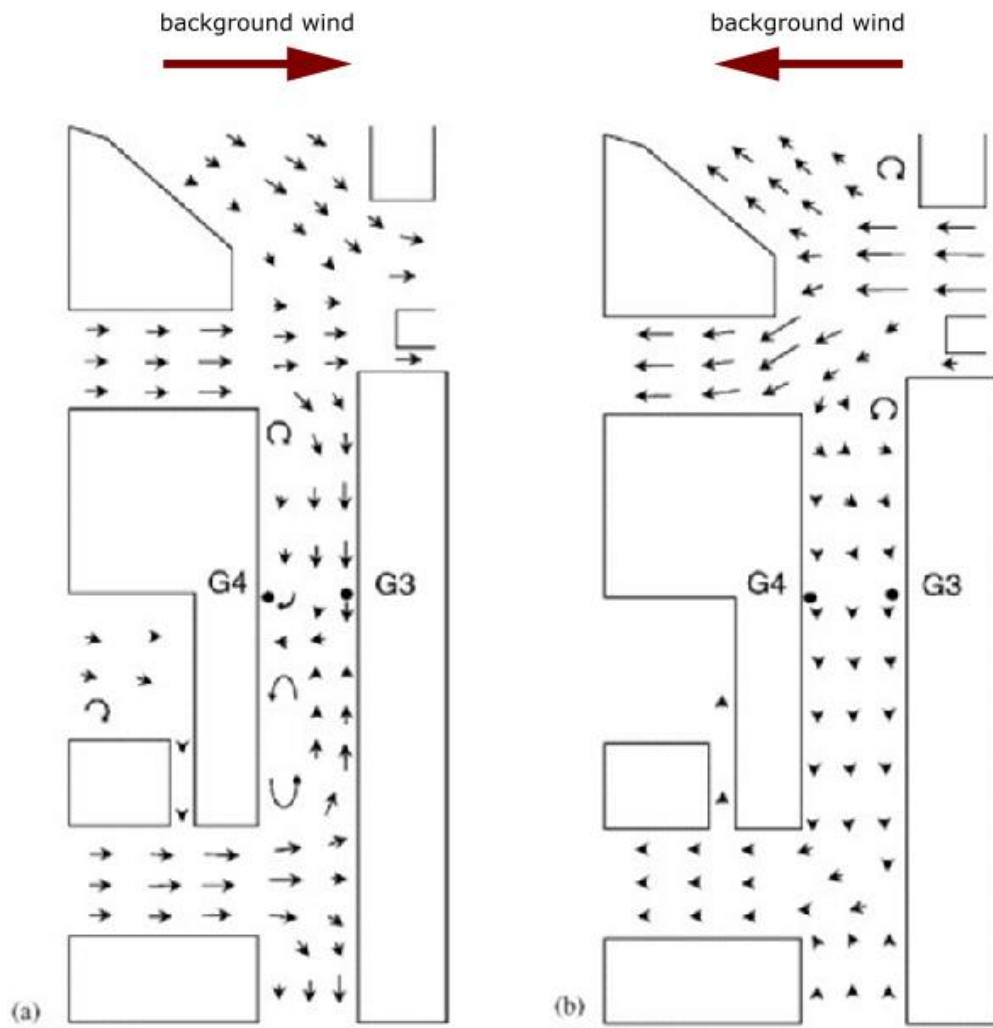


Figure 2.15: Velocity vectors on a horizontal plane ($z=5\text{m}$), background wind direction of (a) 270° and (b) 90° . Adapted from Dixon et al. (2006).

2.5 The effects of local parameters

In the real world, flow in street canyons is further complicated by local parameters. With the development of experimental and computational technologies, it is feasible to embed these parameters into physical and numerical models and then study their impacts in controlled conditions. This section reviews the findings about three local parameters: trees, traffic and heating.

2.5.1 The effect of trees

The deleterious effects of tree planting on ventilation have been highlighted in many studies (Buccolieri et al., 2011; Di Sabatino et al., 2007; Gromke et al., 2008). Individual trees act as obstacles to fully block or weaken the flow across and around them (Endalew et al., 2009). In addition, tree branches can break large-scale turbulence into small scales that dissipate rapidly (Glover, 2015), which leads to weaker turbulence around trees. Based on the understanding of the tree effects on local airflow, Vos et al. (2013) suggested that city planners and policymakers should consider “how urban vegetation can be used without significantly deteriorating the local air quality” rather than “how to use urban vegetation to improve local air quality”.

Detailed impacts of trees have been explored in a few experimental models and numerical models. Salmond et al. (2013) found that rows of trees caused the increase of pollutant concentration in most positions of the street canyon, and the increment is especially large near the street ends where the trees significantly suppressed lateral flow. Gromke and Ruck (2007) studied a few tree arrangements and suggested three favourable rules for tree planting: (1) small volume of tree crowns, (2) sufficient space between crowns and (3) tree height not exceeding building height. Amorim et al. (2013) tested how tree planting affected pollutant concentration under different wind directions. They found that the overall concentration was increased under the 45° background wind condition but was decreased under the parallel background wind condition.

2.5.2 The effect of traffic

Previous studies have found that the presence of traffic had two main impacts on airflow in street canyon—(1) increasing turbulence and (2) changing flow pattern.

Moving vehicles generate chaotic air motions in and around traffic lanes, whatever moving directions and moving speeds are. These motions have a macro effect in enhancing air exchange between street canyon and the atmosphere and mixing

performance in the street. Therefore, the presence of traffic is regarded as a favourable condition for ventilation and pollutant removal. The improvement made by traffic is especially significant at the leeward bottom corner, since the air motions in this region are always very weak if traffic is not considered (Vachon et al., 2002).

The impact of traffic motion on flow pattern is highly dependent on traffic arrangement. Kastner-Klein et al. (2001) tested three traffic arrangements—one-way traffic, two-way traffic and no traffic. The one-way traffic caused a piston effect along the street direction and contributed to highly skewed pollutant distribution about the mid vertical plane. For the other two arrangements, the along-street flow was relatively weak. For all the arrangements, the wake generated by vehicles had limited impacts on the cross-street flow.

2.5.3 The effect of heating

Uniform temperatures in street canyons and on building surfaces and road surfaces are usually assumed in modelling work but rarely happen in the real world, due to uneven solar radiation and different heat capacities of air and building materials. The presence of temperature difference induces buoyancy force which has certain impacts on airflow in street canyon (Allegrini et al., 2013; Sini et al., 1996; Uehara et al., 2000; Xie et al., 2005b), whereas the detailed effects due to heating hinge on heating intensity and heating position.

Heating intensity is usually described by Richardson number ($Ri = -gH(T_{wall} - T_{ref})/U_0^2 T_{ref}$, where g is the gravity, H is building height, U_0 is free-stream velocity, T_{wall} and T_{ref} are wall temperature and reference temperature) or other non-dimensional numbers (e.g. bulk Richardson number and Froude number) (Allegrini et al., 2014; Cheng et al., 2009; Uehara et al., 2000). When the Richardson number (Ri) is small, the thermal effect can be neglected (Kovar-Panskus et al., 2002). On the other hand, airflow in street canyon will be suppressed under large positive Richardson numbers (Ri), which stand for very stable conditions (Uehara et al., 2000). Under large negative Richardson numbers (Ri) which stand for highly unstable conditions, airflow in street canyon is found to be greatly enhanced with changed flow patterns (Allegrini et al., 2014; Cheng and Liu, 2011; Xie et al., 2005b).

Effects of heating position have been systematically studied by Cheng et al. (2009), Cheng and Liu (2011) and Allegrini et al. (2013). They found that windward heating was the worst scenario for ventilation. This was because the buoyancy force

counteracted the downward motion near the windward wall and led to the formation of a secondary vortex at the windward bottom corner (see Figure 2.16 below). Heating on leeward building and ground were found to be a favourable condition, since both mean flow and turbulence in the street were enhanced by the heating. For the case with heated air, the upward motion near the leeward building was weakened due to the cooler building surfaces and ground. Thus, air heating was adverse for ventilation.

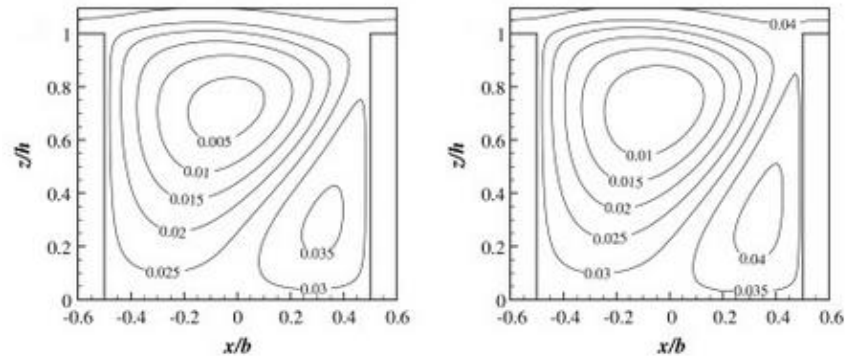


Figure 2.16: Streamlines on the mid vertical plane of a street canyon with heating on the windward wall, left $Ri=-8.0$, right $Ri=-10.6$. Adapted from Cheng et al. (2009).

2.6 CFD modelling of street canyon flow

Computational Fluid Dynamics (CFD) has been widely used as research and design tool since last century. This section first summarizes the general advantages of CFD modelling over physical model and field measurement and points out its limitation. Then, this section reviews the application of CFD modelling in studying street canyon flow and discusses its performance and accuracy in association with a few modelling cases.

2.6.1 Advantages and limitations

With the rapid development of computer technology, CFD is serving as an important tool for studying fluid dynamics. It possesses a few attractive advantages over experimental and theoretical fluid dynamics. Fletcher (1991) summarized five main advantages of CFD over experimental fluid dynamics as follows:

- Lead time in design and development is significantly reduced.
- CFD can simulate flow conditions not reproducible in experimental model tests (e.g., full-scale geometry).
- CFD provides more detailed and comprehensive information.
- CFD is increasingly more cost-effective than wind-tunnel testing
- CFD produces lower energy consumption.

The uppermost advantage of CFD modelling is good cost-effectiveness. A typical CFD model takes a few hours to set up and another few hours or days to run. In contrast, a field measurement typically takes days or months, and requires much more manual effort (Glover, 2015). An experimental model usually does not take such long time in the measuring stage, but it requires much time and effort in preparing and testing stages (Karra, 2012).

CFD modelling is able to simulate many flow conditions which are unable or difficult to realise in wind tunnels or water channels. For example, the full-scale geometry of an urban area, which is unable to be constructed in lab environment, can be easily reproduced and modelled by CFD software (Glover, 2015). Another good example is that making systematic changes of model geometry are straightforward in CFD modelling (Gu et al., 2011); whereas in experimental model, a small change of model

geometries means additional efforts for repositioning measuring device and further tests and calibration (Kastner-Klein, 1999).

Another outstanding advantage of CFD modelling is that high-resolution data are available in whole computational domain. In contrast, many field measurements have issues of low spatial and temporal resolutions, and high-resolution experimental measurements are usually limited to a few measuring positions (Meroney, 1996). Owing to the availability of high-resolution data, many secondary quantities, such as drag coefficient over a surface and mass flux through an area, can be directly calculated in the post-process stage of CFD modelling, while making further assumption and analysing measuring error are usually required to obtain such quantities from experimental measurements (Tao, 2001).

On the other hand, CFD modelling has certain limitations. The most concern is about modelling itself. It is always considered that CFD modelling has lower accuracy than experimental measurements, and that is why experiments are used to validate CFD models (Solazzo et al., 2009). Although computer technology has been rapidly developed, CFD modelling is still not an economic means for research at current stage. The license for CFD software and strong knowledge of fluid dynamics are essential for conducting modelling work. Moreover, performing accurate and reliable CFD modelling further requires not only high performance hardware but also plenty of computing time (Le et al., 1997).

2.6.2 Performance and accuracy

After review the literature that uses CFD to study street canyon flow, it is found that most of these studies assume perpendicular background wind conditions, homogeneous building geometries along street direction and flat roofs on the buildings. These studies have demonstrated that CFD models can predict reasonable flow patterns (Di Sabatino et al., 2008; Guillas et al., 2014; Hunter et al., 1992; Kim and Baik, 2003; Salim et al., 2011).

Horizontal velocity profile in street canyon is usually reasonably predicted in the previous researches (Baik and Kim, 2002; Chan et al., 2002; Di Sabatino et al., 2007). However, predicting accurate vertical velocity is far more difficult. For instance, Koutsourakis et al. (2012) tested several turbulence models and found that none of them predicted very accurate vertical velocity profiles on two vertical lines (see Figure 2.17 below). This is probably because on these two lines, vertical velocities were an order of

magnitude larger than horizontal velocities. Thus, the predicted vertical velocities had larger errors compared to the predicted horizontal velocities.

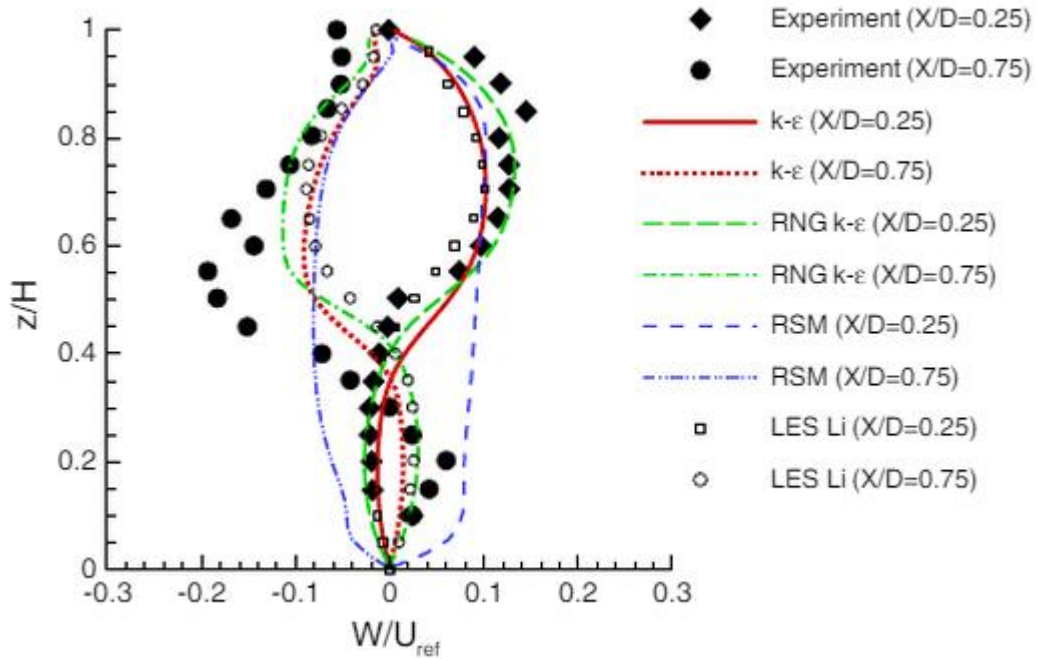


Figure 2.17: Vertical velocity profiles evaluation against wind tunnel data, on the leeward and windward quarter lines. Solid symbols: wind tunnel data, hollow symbols: LES, and line plots: RANS models. Adapted from Koutsourakis et al. (2012).

Under-predicting turbulent kinetic energy (TKE) in street canyon has been agreed as one of the critical limitations of using the k - ϵ type of turbulence model (Cheng and Liu, 2011; Guillas et al., 2014). For example, Solazzo et al. (2009) reported that the standard k - ϵ model predicted much lower TKE than the experimental measurements, even though they had made attempt to modify the model constants to improve the prediction. It is thought that the under-prediction of TKE has two effects on flow and concentration, which are pointed out as follows:

First, the governing equations for velocity components, TKE and dissipation are coupled. This means inaccurate TKE would affect the predictions of other flow properties. However, the significance of this effect is unclear.

Second, it is realised that the under-prediction of TKE has a huge effect on predicting pollutant dispersion. In the pollutant transport equation, the turbulent diffusion term (see Equation 3.6 in 3.2.1 and Equation 3.17 in Section 3.4) appears as a form in proportion to k^2 . It means that the under-prediction of TKE leads to much weaker turbulent diffusion effect than it should be (by square in terms of magnitude). Therefore,

concentration will be over-predicted if TKE is under-predicted. For this reason, many studies use turbulent Schmidt numbers ($Sc_t = \mu / \rho \Gamma_t$, also defined in Equation 3.17 in Section 3.4) much smaller than the values measured from experiments (e.g. reducing Sc_t from 0.9 to 0.3 in Riddle et al. (2004) and Di Sabatino et al. (2007)), as a remedy action for the pollutant dispersion model.

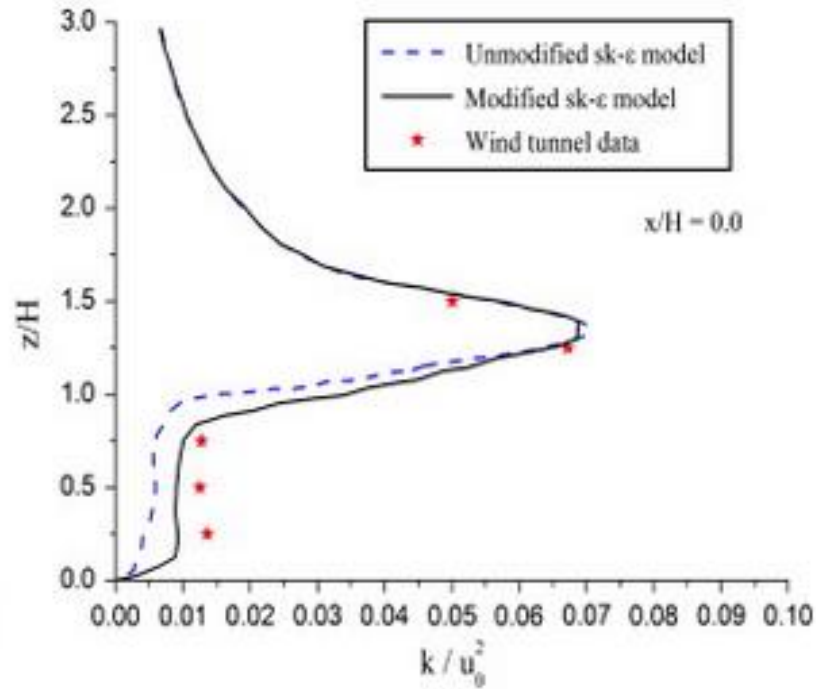


Figure 2.18: TKE profile evaluation against wind tunnel data, on the mid vertical line. Solid: the standard k- ϵ model, dash: the same model with modified model constants, star: the wind tunnel data in Kastner-Klein et al. (2004). Adapted from Solazzo et al. (2009).

Accurate predictions of pollutant concentration in street canyons have been reported in some studies (e.g., Chan et al. (2002) and Salim et al. (2011)). Nevertheless, the accuracy is thought to be over-stated more or less, since the validations in these studies were based on near-wall positions or positions on building surfaces. The CFD modelling results at these positions are considered to be less reliable than those in the far-wall region, because the results are affected by the wall function and the wall function is sensitive to the near-wall mesh resolution. For this reason, the predicted concentrations in these studies are thought to be not very confident.

3 Introduction of Computational Fluid Dynamics

Computational Fluid Dynamics (CFD) refers to using computational techniques to solve the governing equations for fluid flows (Versteeg and Malalasekera, 2007). It provides an alternative to theoretical and experimental fluid dynamics to study fluid flows. With the development of computer technology in recent years, CFD has been used as powerful research and design tools in many disciplines (Versteeg and Malalasekera, 2007). In particular, it has been successfully applied to model airflow in urban areas.

This thesis uses CFD modelling as research methodology, considering the advantages of CFD discussed in Section 2.6.1. Thus, the primary goal of this chapter is to introduce the fundamental of CFD. Section 3.1 introduces the Navier-Stokes equations as the governing equations for fluid flows. Section 3.2 introduces the concept of turbulence model, since the direct solving of Navier-Stokes equations are not feasible for high Reynolds number turbulent flow at present. Two widely-used turbulence models, namely the standard k - ϵ model and the RNG k - ϵ model, are introduced and discussed in detail, as they will be tested and used in this thesis. Section 3.3 introduces two types of techniques to treat fluid flows in the near-wall region. Section 3.4 explains how pollutant dispersion was modelled through an economical way in the literature. This modelling method is also used in this thesis.

3.1 Navier-Stokes equations

The fundamental of numerical simulations of fluid flows (including CFD modelling) is the Navier-Stokes equations. They are a set of non-linear partial differential equations that describe the motion of viscous fluid through expressing the conservation of mass, momentum and energy in any control volume (Patankar, 1980). The Navier-Stokes equations for incompressible isothermal flows are given as Equations 3.1 and 3.2.

The continuity equation is

$$\frac{\partial U_i}{\partial x_i} = S_m \quad (3.1)$$

where U_i is the i component of velocity and x_i is the Cartesian coordinate of i component, and S_m is the additional source term of mass.

The momentum equations (three equations for three velocity components) are

$$\frac{\partial U_i}{\partial t} + U_j \frac{\partial U_i}{\partial x_j} = -\frac{1}{\rho} \frac{\partial p}{\partial x_i} + \frac{\partial}{\partial x_j} \left(\nu \frac{\partial U_i}{\partial x_j} \right) + F_i \quad (3.2)$$

where t is the time, ρ is the density, p is the static pressure, ν is the kinematic viscosity, and F_i is the i component of additional source term of momentum due to the gravitational force and other external body forces. The five terms from left to right denote the time change rate of velocity, convection, diffusion due to viscosity, internal source due to pressure and external source.

The Navier-Stokes equations are possible to be solved directly. Such approach is termed Direct Numerical Simulation (DNS), in which all the scales of motion are resolved. Pope (2000, pp.356–357) states the uppermost advantage of DNS that “where it can be applied, DNS provides a level of description and accuracy that cannot be equalled with other approach”. However, the use of DNS has been limited to basic flows with low or medium Reynolds numbers, due to extremely high computational cost. For example, Le et al. (1997) used DNS to model the flow over a backward-facing step with $Re=5,100$. The simulation took 1,300h on a domain with a total number of nodes 8.3×10^6 and a total number of time steps 2.1×10^5 . Performing DNS for flows with high Reynolds numbers is impractical at present, since the computational cost for DNS increases steeply at a rate of Re_L^3 , where the turbulent Reynolds number Re_L is defined as $Re_L = k^2/(\epsilon \nu)$ (Pope, 2000).

3.2 Turbulence model

As mentioned before, the extremely high computational cost prohibits the use of DNS to resolve all the scales of fluid motions. To overcome this limitation, turbulence approximation is made to model small-scale motions, through making either time average or space average of the Navier-Stokes equations (Tu et al., 2008). These two approaches derive two general categories of turbulence models—Reynolds-Averaged Navier–Stokes (RANS) model and Large Eddy Simulation (LES).

After making either average, the continuity equation has the same form as before. However, the momentum equations contain additional terms (i.e. Reynolds stress terms for RANS model and subgrid-scale stress terms for LES) to take account of the effects of small-scale motions. These additional terms are modelled by different approximation methods and by different additional model equations, which are known as various turbulence models under each general category (Wilcox, 2006).

Here, two specific RANS models, the standard k- ϵ model and the RNG k- ϵ model, are introduced and discussed, as they have been frequently used in modelling street canyon flow. They will be tested in the Chapter 5, and one of them will be used after in the following chapters.

3.2.1 The standard k- ϵ model

The standard k- ϵ model is a widely-used and validated turbulence model in many fields, for its robustness, economy and reasonable accuracy (Versteeg and Malalasekera, 2007). After reviewing relevant literature, it is found that the standard k- ϵ model is the most frequently used turbulence model for modelling street canyon flow.

The continuity and momentum equations for the standard k- ϵ model are derived by making time average of the Navier-Stokes equations. The time-averaged velocity is denoted by a bar above U_i , and the fluctuation velocity is denoted by the lowercase u_i . The continuity equation for the model has the same form to the Navier-Stokes equations (compare Equation 3.1 in Section 3.1 and Equation 3.3 in this section), but the momentum equations for the model differ from the Navier-Stokes equations (Equation 3.2 in Section 3.1) by an extra term—the Reynolds stress term (the last term in Equation 3.4). This term is modelled by the turbulent viscosity assumption (Equation 3.5), which links the deviatoric Reynolds stresses $(-\overline{u_i u_j} + \frac{2}{3} k \delta_{ij})$ to the mean rate of strain velocity $(\frac{\partial \overline{U_i}}{\partial x_j} + \frac{\partial \overline{U_j}}{\partial x_i})$ by a positive scalar coefficient ν_t (Pope, 2000). This coefficient is

named as turbulent viscosity or eddy viscosity, since it has the same unit as kinematic viscosity. It is specified by Equation 3.6 in which ν_t is proportional to k^2/ε , where k is the turbulent kinetic energy, ε is the turbulent dissipation (here simply called dissipation) and C_μ is one of the model constants for the standard k- ε model (Launder and Spalding, 1974).

The turbulent viscosity assumption has introduced two additional unknown quantities — k and ε . To close the model equations, the transport equations for k and ε are added (Equations 3.7 and 3.8), which explains that the standard k- ε model is a two-equation model (Tu et al., 2008). These equations are not mathematically derived from the Navier-Stokes equations, but they are derived according to phenomenological considerations and empiricism (Launder and Spalding, 1974). In Equation 3.7 from left to right, TKE k is balanced between the advection of TKE, the diffusion of TKE, the production of TKE due to mean velocity gradients, the dissipation of TKE, and additional source of TKE (Versteeg and Malalasekera, 2007). In Equation 3.8 from left to right, dissipation ε is balanced by the advection of dissipation, the diffusion of dissipation, the production of dissipation due to mean velocity gradients, the destruction of dissipation, and additional source of dissipation (Versteeg and Malalasekera, 2007). The last two terms in Equation 3.8 are assumed to be proportional to the last two terms in Equation 3.7 respectively (Versteeg and Malalasekera, 2007).

Continuity equation

$$\frac{\partial \bar{U}_i}{\partial x_i} = S_m \quad (3.3)$$

Momentum equations

$$\frac{\partial \bar{U}_i}{\partial t} + \bar{U}_j \frac{\partial \bar{U}_i}{\partial x_j} = -\frac{1}{\rho} \frac{\partial \bar{P}}{\partial x_i} + \frac{\partial}{\partial x_j} \left[(\nu + \nu_t) \frac{\partial \bar{U}_i}{\partial x_j} \right] - \frac{\partial}{\partial x_j} (\overline{u_i u_j}) + F_i \quad (3.4)$$

Turbulent viscosity assumption

$$-\overline{u_i u_j} + \frac{2}{3} k \delta_{ij} = \nu_t \left(\frac{\partial \bar{U}_i}{\partial x_j} + \frac{\partial \bar{U}_j}{\partial x_i} \right) \quad (3.5)$$

$$\nu_t = C_\mu \frac{k^2}{\varepsilon} \quad (3.6)$$

Turbulent kinetic energy equation

$$\frac{\partial k}{\partial t} + \bar{U}_j \frac{\partial k}{\partial x_j} = \frac{\partial}{\partial x_j} \left[\left(\nu + \frac{\nu_t}{\sigma_k} \right) \frac{\partial k}{\partial x_j} \right] + \overline{u_i u_j} \frac{\partial \bar{U}_j}{\partial x_i} - \varepsilon + S_k \quad (3.7)$$

Dissipation equation

$$\frac{\partial \varepsilon}{\partial t} + \bar{U}_j \frac{\partial \varepsilon}{\partial x_j} = \frac{\partial}{\partial x_j} \left[\left(\nu + \frac{\nu_t}{\sigma_\varepsilon} \right) \frac{\partial \varepsilon}{\partial x_j} \right] + C_{1\varepsilon} \frac{\varepsilon}{k} \bar{u}_i \bar{u}_j \frac{\partial \bar{U}_j}{\partial x_i} - C_{2\varepsilon} \frac{\varepsilon^2}{k} + S_\varepsilon \quad (3.8)$$

There are five model constants in the standard k- ε model— C_μ , $C_{1\varepsilon}$, $C_{2\varepsilon}$, σ_k , and σ_ε . The default values for these constants used in FLUENT are proposed by Launder and Sharma (1974). These values, which are given in Table 3.1 below, are suitable for a wide range of flows.

Model constant	C_μ	$C_{1\varepsilon}$	$C_{2\varepsilon}$	σ_k	σ_ε
Value	0.09	1.44	1.92	1.0	1.3

Table 3.1: The model constants for the standard k- ε model, proposed by Launder and Sharma (1974).

The standard k- ε model has an obvious defect in terms of model accuracy. It performs poorly for complex flows which involve severe pressure gradient, separation and strong streamline curvature. Pope (2000) attributes the poor performance to the turbulent viscosity assumption and the dissipation (ε) equation. Violating the turbulent viscosity assumption and introducing new modelling approach, such as what have been done in Reynolds Stress Model (RSM), are rather complicated and are not economical. On the other hand, modifying the ε equation is a more economical solution. The RNG k- ε model, which will be discussed in the following section, is a good example that improves model accuracy by modifying the existing terms and introducing a new term in the ε equation.

3.2.2 The RNG k- ε model

The RNG k- ε model is proposed using a statistical technique “Re-Normalization (RNG) method” by Yakhot and Orszag (1986). In contrast, the model equations of the standard k- ε model are not derived from the Navier-Stokes equations in any systematic fashion (Yakhot and Orszag, 1986).

The RNG k- ε model has similar model equations to the standard k- ε model, except for different model constants given in Table 3.2 below and a new dissipation (ε) equation given as Equation 3.9. These model constants are derived by statistical approaches, compared to the model constants empirically determined in the standard k- ε model. The dissipation equation contains an additional term (the highlighted term in Equation 3.9) that accounts for the effects of small-scale motions (Yakhot and Orszag, 1986). This

term is specified by mean rate of strain S , TKE k and dissipation ε , and η_0 and β are two model constants for the RNG k- ε mode.

$$U_j \frac{\partial \varepsilon}{\partial x_j} = \frac{\partial}{\partial x_j} \left[\left(\nu + \frac{\nu_t}{\sigma_\varepsilon} \right) \frac{\partial \varepsilon}{\partial x_j} \right] + C_{1\varepsilon} \frac{\varepsilon}{k} \overline{u_i u_j} \frac{\partial U_j}{\partial x_i} - C_{2\varepsilon} \frac{\varepsilon^2}{k} - \frac{C_\mu \eta^3 (1 - \eta/\eta_0) \varepsilon^2}{1 + \beta \eta^3} \frac{\varepsilon^2}{k}$$

$$\text{where } \eta \equiv S \frac{k}{\varepsilon}, S \equiv \sqrt{\frac{1}{2} \left(\frac{\partial U_i}{\partial x_j} + \frac{\partial U_j}{\partial x_i} \right) \left(\frac{\partial U_i}{\partial x_j} + \frac{\partial U_j}{\partial x_i} \right)}, \eta_0 = 4.38, \text{ and } \beta = 0.012$$

(3.9)

Model constant	C_μ	$C_{1\varepsilon}$	$C_{2\varepsilon}$	σ_k	σ_ε
Value	0.0845	1.42	1.68	0.7194	0.7194

Table 3.2: The model constants of the RNG k- ε model, proposed by Yakhot et al. (1992).

Owing to the abovementioned changes, the effect of swirling turbulence is included in the RNG k- ε model, which improves the accuracy for flows with rapid strain and streamline curvature (e.g. separation flows and cavity flows) (ANSYS Inc., 2009a). ANSYS Inc. (2009a) recommends the RNG k- ε model as a more accurate and reliable model for a wider class of flows than the standard k- ε model. Similar recommendations have also been found in many text books, such as Tao (2001), Versteeg and Malalasekera (2007), and Tu et al. (2008).

3.3 Wall treatments

Modelling the near-wall flow is a challenge, because the viscous effect is not negligible in the near-wall region, which leads to steep gradients of velocity and turbulence statistics across the near-wall boundary layer (Craft, 2011). In order to resolve the steep gradients by turbulence models, very fine grids are required in the near-wall region to provide adequate numerical resolutions. Moreover, the model equations need to be modified to include the viscous effect, which is usually done by adding ‘near-wall damping’ terms and other source terms (Craft, 2011). Such modelling strategy is known as low-Reynolds-number modelling (Jones and Launder, 1973; Launder and Sharma, 1974).

Alternatively, an approach is designed to model the flow in the near-wall region rather than resolve it. Thus, the computational cost can be greatly reduced. This approach is known as wall function simulation. Compared to low-Reynolds-number modelling, the computational cost for near-wall flow can be greatly reduced by using wall function simulation. For this reason, it is not surprising that the wall function is used to model the near-wall flow in most cases.

In the wall function, implicit relations are established between velocity, turbulence statistics and the wall distance (i.e., the distances between a wall and the first grids away from the wall) (Launder and Spalding, 1974). Based on these relations, the effective wall boundary conditions are imposed on the first grids away from the wall (Launder and Spalding, 1974).

There are several types of wall functions available in FLUENT. Two of them are thought to be suitable for modelling street canyon flow. The basic one is the scalable wall function, and the more advanced one is the enhanced wall function. The scalable wall function is discussed in detail here, whereas the enhanced wall function is introduced briefly.

In the scalable wall function, two fundamental assumptions are made: (1) the mean velocity in the near-wall region satisfies a logarithmic law and (2) the production of turbulent kinetic energy in the near-wall region is balanced by the dissipation, which is known as the equilibrium assumption (Pope, 2000). To ensure the validity of these assumptions, most of the first grids away from the wall should have y^+ values (a type of dimensionless distance from the wall, defined by $y^+ = yU_\tau/\nu$, where y is the wall distance, U_τ is the friction velocity, and ν is the kinematic viscosity) above about 30 up to 500–

1000 (Blocken et al., 2007). The y^+ issue about the first nodes for street canyon flow will be discussed later in Section 4.3.

The implicit relations between the velocity, turbulence statistics and wall distance for the scalable wall function are given as follows.

The logarithmic law for mean velocity yields

$$U^* = \frac{1}{\kappa} \ln(Ey^*) \quad (3.10)$$

where E is an empirical constant which has a value of 9.793, and the dimensionless velocity U^* and the dimensionless distance from the wall y^* are defined as follows.

$$U^* \equiv \frac{U_p C_\mu^{1/4} k_p^{1/2}}{\tau_w / \rho} \quad (3.11)$$

$$y^* \equiv \frac{\rho C_\mu^{1/4} k_p^{1/2} y_p}{\mu} \quad (3.12)$$

In the equations above, U_p , k_p and y_p are the velocity, the TKE and the wall distance at point p respectively. C_μ is the model constant of the turbulence model, ρ is the density, and μ is the dynamic viscosity, and τ_w is the wall shear stress.

It should be mentioned that U^* and y^* are different from the conventional dimensionless quantities— U^+ and y^+ —used to define the logarithmic law. The use of U^* and y^* is aimed to avoid singularity when the first grids are very close to the wall. When the first grids are all in the logarithmic law region, U^* and U^+ are approximately equal, so are y^* and y^+ (ANSYS Inc., 2009b).

In the scalable wall function, the y^* is forced to have a lower limit of 11.225. The purpose of this treatment is to force the first grids in the logarithmic layer. As a result, any inaccuracy and stability issues due to the nodes in the viscous layer can be avoided. The U^* is forced to have the same value to y^* when y^* is below the limit.

$$U^* = y^* \text{ for } y^* \leq 11.225 \quad (3.13)$$

The TKE k has a zero gradient along the normal direction of the wall

$$\frac{\partial k}{\partial n} = 0 \quad (3.14)$$

where n is the local coordinate normal to the wall.

The production of TKE is computed as below.

$$G_k \approx \tau_w \frac{\partial U}{\partial y} = \tau_w \frac{\tau_w}{\kappa \rho k_p^{1/2} y_p} \quad (3.15)$$

The dissipation ε at point p is calculated from an analytical equation as below.

$$\varepsilon_p = \frac{C_\mu^{3/4} k_p^{3/2}}{\kappa y_p} \quad (3.16)$$

The second type of wall function is the enhanced wall function. The equations for this wall function are not provided here due to its complexity. Only its concept is briefly introduced below.

The enhanced wall function is a two-layer model with special near-wall treatment (ANSYS Inc., 2009a). It is more advanced than the scalable wall function. In this wall function, the near-wall domain is subdivided into two regions: the viscous-affected region and the fully-turbulent outer region. The standard k- ε model or Reynolds Stress Model is employed in the fully-turbulent region, and the one-equation model of Wolfstein is employed in the viscous-affected region (ANSYS Inc., 2009a). A special treatment makes a smooth blend of the wall treatments at the two regions as a single wall law. Thus, the enhanced wall function is capable to handle both coarse near-wall mesh (the first grids in the fully-turbulent region) and fine near-wall mesh (the first grids in the viscous-affected region) (Kader, 1981).

3.4 Modelling pollutant dispersion

An economical method to model pollutant dispersion, which has been used in most previous studies, is to treat the pollutant as a passive scalar. It requires that the pollutant is non-reactive and has a low mass fraction so that it does not interfere with fluid motion (Warhaft, 2000). By using this method, flow field and pollutant concentration are coupled in one way (i.e. concentration is solved after completing the calculation for the flow), which greatly reduces the computational time compared to two-way coupling.

The transport of a passive scalar is usually described by an advection-diffusion equation, which is given as Equation 3.17 with ϕ representing the pollutant concentration. This equation has two terms on the left hand side which describe the dispersion due to mean flow and turbulence respectively. The turbulent dispersion is assumed to have a diffusive form, which is analogue to the turbulent viscosity assumption (discussed in Section 3.2.1). The term on the right hand side S_ϕ is the additional source term, which is zero at most positions except at the emission source.

The effective diffusion coefficient Γ_{eff} is made up of a laminar part and a turbulent part. The laminar part is defined by the molecular diffusion coefficient (Γ), and the turbulent part is specified by the turbulent viscosity (ν_t) divided by the turbulent Schmidt number (Sc_t). Many experimental results show that the turbulent Schmidt number is a constant and has an order of 1. It has typical values ranging from 0.7 to 0.9, and these values are also used in many CFD modelling works (Tominaga and Stathopoulos, 2007). The appropriate value of the turbulent Schmidt number will be discussed in depth in the benchmarking chapter (see Sections 5.3.3 and 5.6.4).

$$\bar{U}_j \frac{\partial \bar{\phi}}{\partial x_j} - \frac{\partial}{\partial x_j} \left(\Gamma_{eff} \frac{\partial \bar{\phi}}{\partial x_j} \right) = S_\phi, \text{ where } \Gamma_{eff} = \Gamma + \Gamma_t \text{ and } \Gamma_t = \frac{\nu_t}{Sc_t} \quad (3.17)$$

4 Methodology

This chapter discusses how to use CFD as methodology for modelling street canyon flow. Several important CFD settings are highlighted. Those settings agreed in different literature will be used in this thesis, while the other argued settings will be tested in the next chapter. The structure of this chapter is given as below.

Section 4.1 briefly introduces the general processes for conducting CFD modelling. Section 4.2 reviews the turbulence models used in the literature and chooses two of them to be tested in the next chapter. Section 4.3 chooses the wall functions which will be tested in the next chapter, and discusses the issue of near-wall mesh resolution for applying the wall function. Section 4.4 discusses appropriate boundary conditions, including boundary types, boundary positions and relevant parameters. Section 4.5 provides suitable CFD solver settings.

4.1 General processes for CFD modelling

Running a CFD model always involves five stages no matter what software is used:

- Creating geometry
- Meshing
- Pre-process
- Solving-process
- Post-process

The ANSYS CFD package v12.0 is used for the modelling work in this thesis. It is a reputable commercial CFD software package that contains at least one type of software for each of the five stages. ANSYS ICEM is used for the first two stages, as it is advantageous in generating high quality mesh and controlling cell number, compared to the other meshing software in the package. ANSYS FLUENT is used for the third and fourth stages, owing to its capability of modelling almost any types of flow, its high efficiency in iteration and calculation, and its wide application for multi-physics (ANSYS Inc., 2016). ANSYS CFD-Post is used for the last stage, because this software is easy to use and provide many types of high quality image. MATLAB (not in the package) is also used for the last stage in the case that ANSYS CFD-Post does not fully meet the requirement for presenting model results. A summary of the software used in each stage is given in Table 4.1 below.

Stage	Software used
Creating geometry	ANSYS ICEM
Meshing	ANSYS ICEM
Pre-process	ANSYS FLUENT
Solving-process	ANSYS FLUENT
Post-process	ANSYS CFD-Post and MATLAB

Table 4.1: The CFD software used in the thesis.

4.2 Selecting turbulence model

Choosing appropriate turbulence model is crucial for any CFD modelling work, as different turbulence models would give more or less different results and some of them might fail in some cases. Appropriate turbulence model should provide reasonably accurate results in the first place. This is usually judged by comparing CFD modelling results with experimental measurements. Apart from accuracy, computational cost and the ease of applying the turbulence model also need to be considered.

Table 4.2 summarizes the turbulence models used in the literature for modelling street canyon flow. The representative work for each turbulence model is also given in the table. As mentioned in Section 3.2, the standard k- ϵ model and the RNG k- ϵ model are the most widely-used turbulence models found in the literature, so they will be tested in the benchmarking chapter. The other turbulence models are not used in this thesis, and the reasons are stated in Table 4.2.


	Turbulence model	One of the previous studies using the turbulence model	Reason(s) for not using the turbulence model in this thesis
Increase of computational cost 	Spalart-Allmaras model	Scungio et al. (2013)	Intended for aerodynamic application, not calibrated for general flow
	Standard k- ϵ model	Takano and Moonen (2013)	–
	RNG k- ϵ model	Cheng et al. (2009)	–
	Realisable k- ϵ model	Gromke and Blocken (2015)	Not widely used for modelling airflow in urban areas
	Low-Reynolds-number k- ϵ model	Allegrini et al. (2012)	High computational cost, providing better predictions near the wall but is not important for modelling large-scale flow
	SST k- ω model	Borsani et al. (2008)	Predicting wrong flow pattern (see Figure 4.1 below)
	Reynolds Stress Model (RSM)	Panagiotou et al. (2013)	High computational cost, low robustness, and less accurate than the k- ϵ type of turbulence model in many cases
	Large Eddy Simulation (LES)	Moonen et al. (2013)	Extremely high computational cost

Table 4.2: A summary of the turbulence models used in the literature for modelling street canyon flow.

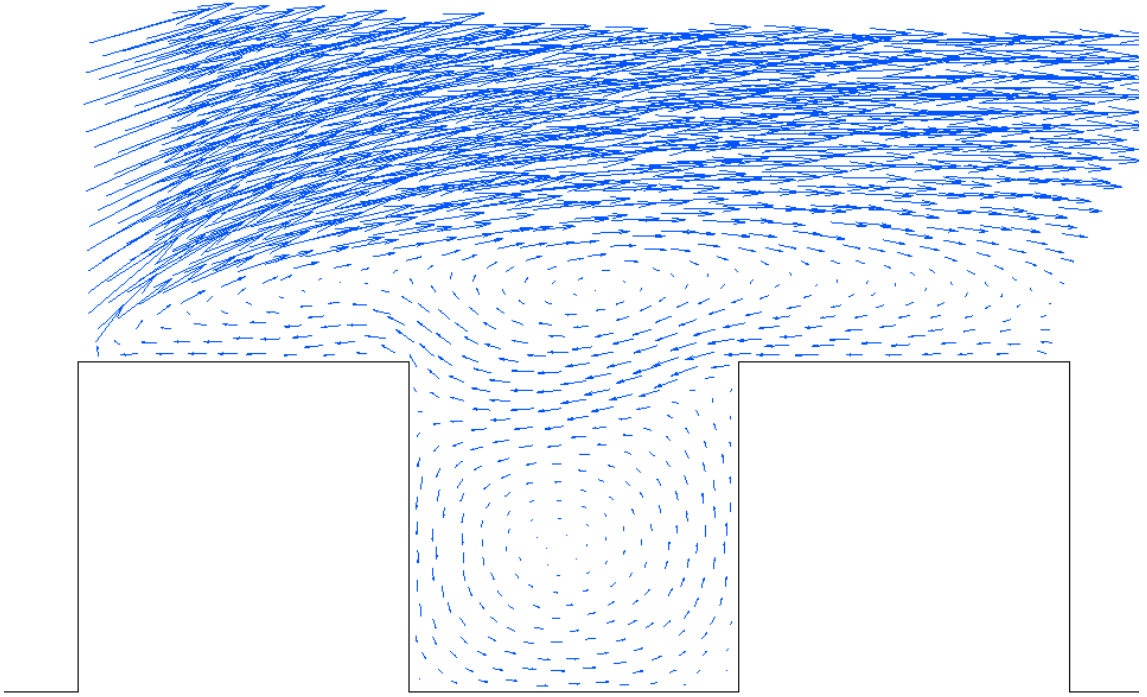


Figure 4.1: The wrong flow pattern predicted by the SST $k-\omega$ turbulence model.

4.3 Selecting the wall function

Both the scalable wall function and the enhanced wall function are considered to be possible appropriate wall function. Both of them result in similar computational time. Thus, a test of them will be made in the benchmarking chapter.

It should be pointed out that large y^+ (defined by $y^+ = yU_o/\nu$) values in full-scale street canyon models do not affect the model accuracy in the main flow region, although the y^+ values are supposed to be controlled below 500–1000. As discussed by van Hooff et al. (2011), for CFD modelling of atmospheric flow, the first grids are usually positioned at a distance on the order of 0.1m or 1m away from the wall, aimed to avoid overly high computational cost. Sometimes, the first grids are forced to be positioned at a distance on the order of 1m away, to model the roughness on the ground (e.g., shrubs and hurdles). Such distance leads to typical y^+ values between 15,000 and 20,000, which significantly exceed the upper limit of 500–1000. Nevertheless, van Hooff et al. (2011) bore out that such large values do not affect model performance in the far-wall region.

4.4 Specifying boundary condition

Boundary conditions for CFD are a set of additional constraints for the Navier-Stokes equations or the governing equations of turbulence model. For CFD models that use the same turbulence model, the governing equations are the same, so the different boundary conditions are the reason for the different solutions. Thus, setting appropriate boundary conditions is a key point for CFD modelling. A boundary condition is specified by its type, its position and some parameters on it, which are discussed separately in Sections 0, 4.4.2 and 4.4.3. In these sections, the boundary conditions used in the literature are reviewed to determine the boundary conditions to be used in this thesis.

4.4.1 Boundary type

A typical street canyon model is created by a rectangular domain which encloses all geometries. Boundary conditions are defined on six surfaces of the rectangular domain, on building surfaces and on emission sources. After reviewing the boundary types used in the literature, the boundary types for this thesis are determined and given in Table 4.3 below. It should be mentioned that an emission source is usually specified as a velocity inlet with extremely small velocity (set as 0.001m/s in this thesis) and zero turbulence, for the purpose of not intruding the original flow in the street canyon. Pollutant concentration is defined as zero flux on all the boundaries except on the emission source that concentration is defined to have a fixed value (set as 0.04 in this thesis). The detailed value will not affect the normalized concentration in the computational domain, due to the similarity law.

Name	Boundary type and essential parameters
Inlet boundary	Velocity inlet with appropriate velocity, TKE and dissipation profiles
Outlet boundary	Outflow or pressure outlet with 0Pa (i.e. equal to the reference pressure defined in CFD model)
Bottom boundary	No-slip wall with no roughness or no-slip wall with appropriate roughness parameters
Top boundary	Symmetry boundary (for full-scale real street canyons) or no-slip wall (for scaled-down experimental models)
Side boundaries	Symmetry boundary (for full-scale real street canyons) or no-slip wall (for scaled-down experimental models)
Building surface	No-slip wall with no roughness
Emission source	Velocity inlet with a very small normal velocity and 0% turbulence intensity

Table 4.3: Typical boundary conditions for a CFD model that simulates flow around street canyon.

4.4.2 Boundary position

To perform CFD modelling of street canyon flow, sufficient distances should be placed between street canyon geometries and the boundaries of the computational domain, in order to generate sensible flow fields around the street canyons. The COST best practice guideline (Franke et al., 2007) and the AIJ guidelines (Tominaga et al., 2008) have recommended the minimum distance for each boundary measured by characteristic building height (H), as summarized in Table 4.4 below. These requirements are observed in most CFD modelling.

It should be noted that providing longer distances after and alongside street canyon geometries does not affect the flow in the streets. However, pointed out that providing a too long distance between inlet boundary and the first building could cause less accurate approaching flow. The reason was that the atmospheric boundary layer could not be sustained without setting an appropriate shear stress at top boundary, but estimating accurate shear stress was difficult. Therefore, the distance between inlet boundary and the first building should be specified neither too long nor too short, just around $5H$.

Boundary	Minimum distance
Inlet boundary	$5H$ before the first building
Outlet boundary	$15H$ after the last building
Side boundaries	$5H$ from the flank of the buildings
Top boundary	$10H$ above the ground

Table 4.4: Minimum distances between the boundaries and the buildings for modelling street canyon flow. Recommended by the COST best practice guideline (Franke et al., 2007) and the AIJ guidelines (Tominaga et al., 2008).

4.4.3 Inlet boundary profile

Amongst all the boundaries of a CFD model, inlet boundary has the uppermost importance on the flow in computational domain. In one aspect, it is the only type of boundary on which additional parameters need to be defined, contrasting to outflow, symmetry and wall boundaries on which only boundary type need to be specified. In another aspect, it is apparent that the approaching flow condition will affect the downstream flow.

For k - ϵ type of turbulence models, mean velocity, TKE and dissipation need to be defined on the inlet boundary. They are usually specified in the forms of empirical profiles. These specifications are more precise than specifying velocity, TKE and

dissipation as constants, and are more robust and convenient than importing measured data. Discussions of these empirical profiles are made below.

In modelling street canyon flow, the **velocity** of inlet boundary is usually defined by either a logarithmic law profile or a power law profile. The logarithmic law profile (Equation 4.1), which accounts for surface roughness and atmospheric stability, describe the wind velocity profile of the atmospheric boundary layer (ABL) more accurately. It is a preferred choice in modelling experimental flow, since the roughness can be accurately estimated from high-resolution experimental measurements and the stability can be controlled. On the other hand, when the roughness and stability information is not available, the wind velocity profile of the ABL is more reliably approximated by the power law profile (Equation 4.2). It is a preferred choice in modelling full-scale real cases, since friction velocity and roughness height are usually unable to be accurately estimated due to limited measurements at different heights.

The logarithmic law is usually specified by

$$U = \frac{U_\tau}{\kappa} \ln \frac{z + z_0}{z_0} \text{ or } U = \frac{U_\tau}{\kappa} \ln \frac{z}{z_0} \quad (4.1)$$

where U_τ is the friction velocity, κ is the von Karman constant and has a value of 0.41, and z_0 is the roughness height.

The power law is usually specified by

$$U = U_{ref} \left(\frac{z}{z_{ref}} \right)^\alpha \quad (4.2)$$

where z_{ref} is the reference height, U_{ref} is the velocity at the reference height, and α is the power law index.

The **TKE and dissipation profiles** of inlet boundary are specified by several forms in the literature. Three typical forms are provided below. Depending on the available information for the ABL, each of them might be a suitable choice to describe the turbulence information on the inlet boundary.

Richards and Hoxey (1993) proposed mathematically consistent turbulent kinetic energy and dissipation profiles for two-dimensional flows (Equations 4.3 and 4.4). These profiles are based on two assumptions that the ABL has a logarithm velocity profile and shear stress is constant in the ABL. The second assumption implies that TKE (k) remains constant in the ABL, dissipation (ϵ) decreases inversely with height.

These profiles have been applied in many CFD models which study atmospheric flow or street canyon flow (Blocken et al., 2007; Hargreaves and Wright, 2007; Xie et al., 2005a). These profiles are also recommended by the COST best practice guideline (Franke et al., 2007) and the AIJ guidelines (Tominaga et al., 2008) as preferred inlet boundary settings for street canyon models.

$$k = \frac{U_\tau^2}{\sqrt{C_\mu}} \quad (4.3)$$

$$\varepsilon = \frac{U_\tau^3}{\kappa(z + z_0)} \text{ or } \varepsilon = \frac{C_\mu^{3/4} k^{3/2}}{\kappa(z + z_0)} \quad (4.4)$$

The profiles proposed by Richards and Hoxey (1993), however, are not suitable to describe modelled ABL in scaled-down experiment. This is because in experimental models, shear stress and TKE are not constant but decreases with height. Solazzo et al. (2009) suggested that a suitable modification was to multiply both TKE and dissipation profiles by a factor of $(1 - z/\delta)$ (Equations 4.5 and 4.6), while Castro and Apsley (1997) suggested a different multiplier— $(1 - z/\delta)^2$ —only for TKE profile. Both modified profiles result in negative k and ε above the boundary layer height δ . Castro and Apsley (1997) provided a solution to this issue, by specifying constant k and ε above 0.9δ .

$$k = \frac{U_\tau^2}{\sqrt{C_\mu}} \left(1 - \frac{z}{\delta}\right) \quad (4.5)$$

$$\varepsilon = \frac{U_\tau^3}{\kappa(z + z_0)} \left(1 - \frac{z}{\delta}\right) \quad (4.6)$$

The AIJ guidelines (Tominaga et al., 2008) recommended TKE and dissipation profiles which was dependent on the model constant C_μ , the power-law index α and the boundary layer height δ (Equations 4.7 and 4.8). These profiles are used together with power law velocity profile, as power law index and boundary layer height are available in power law profile, while friction velocity and roughness height are not available or difficult to be estimated accurately.

$$k = 0.1U \left(\frac{z}{\delta}\right)^{-0.05-\alpha} \quad (4.7)$$

$$\varepsilon = C_\mu^{\frac{1}{2}} k \frac{U_{ref}}{z_{ref}} \alpha \left(\frac{z}{z_{ref}}\right)^{\alpha-1} \quad (4.8)$$

4.5 CFD solver settings

The CFD solver settings are briefly stated in this section. These settings are chosen according to previous experience, aimed at improving iteration efficiency without sacrificing model accuracy.

Semi-Implicit Method for Pressure Linked Equations Consistent (SIMPLEC) algorithm is used for the velocity-pressure coupling. This algorithm is found to be more efficient than the traditional SIMPLE algorithm.

Second-order upwind scheme is used to discretise the convection terms in the momentum, TKE and dissipation equations. It is an essential means to control the discretization error, compared to other low-order schemes such as first-order upwind scheme and power law scheme

The default under-relaxation factors (given in Table 4.5 below) are used to solve the model equations iteratively. These factors are found to be the optimum for iteration efficiency.

The residual criteria for the mass, momentum, TKE and dissipation equations are set as 10^{-6} , in order to guarantee the true convergence; the residual criterion for the pollutant transport equation is set as 10^{-8} , in order to guarantee not only the true convergence but also the mass flux balance (about pollutant) between the emission source and the outlet. In the case that not all of the criteria are met, velocity and TKE are monitored at a few positions to judge whether the solutions are truly converged.

Term	Value
Pressure	0.3
Density	1.0
Body force	1.0
Momentum	0.7
Turbulent kinetic energy	0.8
Turbulent dissipation rate	0.8
Turbulent viscosity	1.0
User scalar 0 (the passive scalar)	1.0

Table 4.5: The default values for the under-relaxation factors in FLUENT

5 Benchmark—validation of CFD models

A benchmark study is reported in this chapter, in order to assess the accuracy of CFD modelling. Three CFD models, which correspond to a 2D isolated street canyon, 2D consecutive street canyons and a 3D isolated street canyon, are validated against Kastner-Klein's experimental measurements. Moreover, this chapter tests several CFD modelling settings that are not agreed in the literature. The structure of this chapter is given as follows.

Section 5.1 states the objectives of the benchmark study. Section 5.2 introduces three experiments that are used for benchmarking three CFD models. Section 5.3 describes detail CFD modelling settings and discusses how to conduct mesh sensitivity tests in this study. The results of the three benchmark cases are presented and analysed in Sections 5.4, 5.5 and 5.6 respectively. Each of these sections covers discussing mesh sensitivity test results, comparing flow patterns between the model and the experiment, comparing flow properties, and analysing error statistics for the model. Finally, Section 5.7 summarizes the assessment of the three CFD models and the most appropriate CFD settings.

5.1 Objectives

The primary objective of this chapter is to benchmark three CFD models that are performed based on the same geometry and wind condition to the experiments carried out by Kastner-Klein and Plate (1999) at the University of Karlsruhe in Germany. The model accuracy is evaluated by comparing the errors between the model results and the experimental measurements.

The second objective is to test the CFD modelling settings that are not agreed in the literature, including mesh resolution, turbulence model, the wall function and turbulent Schmidt number. After the tests, the most appropriate settings will be used in the following chapters. In addition, these settings can be used in future work if the CFD model has comparable geometry and shares similar flow regimes to the current models.

Apart from the two objectives above, it is aimed to find and analyse the limitations of the current CFD models. It is supposed that these limitations are mostly related to the intrinsic weakness of CFD modelling (e.g., the inaccuracy stems from turbulence approximation) and are unable to be overcome by CFD users. Nevertheless, understanding these limitations is helpful to avoid them or reduce their impacts.

5.2 Experiments used for benchmarking

The experiments carried out by Kastner-Klein and Plate (1999) are chosen for validation, considering high quality measurements and relatively complete data in these experiments. Specifically, both velocity and concentration were measured by high-precision apparatus (i.e., Laser Doppler Anemometry (LDA) and SF_6 sensor) at a few positions. These experiments have also been used in many studies for validation purposes (e.g., Glover (2015) and Solazzo et al. (2009)).

5.2.1 Descriptions of experimental setup

The full experiment report can be found in Kastner-Klein (1999). The main experimental setup is introduced here together with a schematic diagram as shown in Figure 5.1 below. The test section of the wind tunnel was 1m high and 2m wide. Two buildings were placed in the wind tunnel, constructing an ideal street canyon with an aspect ratio of one. This street canyon was treated as test street canyon (the last street canyon in Figure 5.1). One or two additional buildings (the first two buildings in Figure 5.1) were placed before the upwind building of the test street canyon in some of the experiments, in order to investigate the influence of additional upstream building(s) (Kastner-Klein, 1999). All the buildings had a $0.12\text{m} \times 0.12\text{m}$ square-shape cross-section. The street width (or the distance between adjacent buildings) was fixed at 0.12m ($1H$). The street length (or the building length) was purposely set as 0.6m ($5H$), 1.2m ($10H$) or 1.8m ($15H$), in order to study the impact of street length on airflow (Kastner-Klein, 1999).

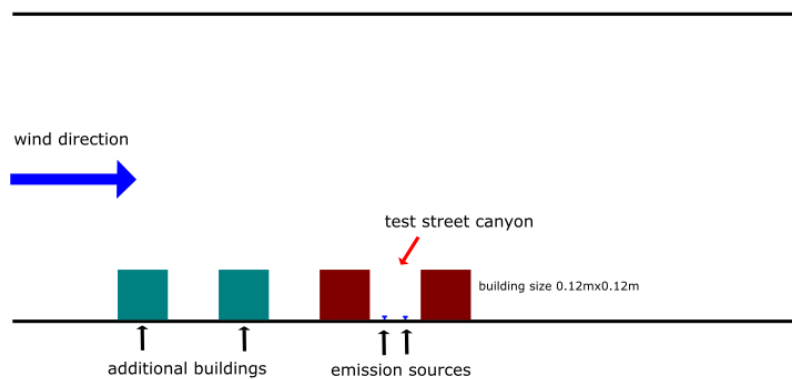


Figure 5.1: A sketch of Kastner-Klein's experimental setup. Replotted following Kastner-Klein (1999).

5.2.2 Wind condition for approaching flow

The laboratory work corresponded to a scaled-down model of 1:150. According to this scale, the building height of 0.12m in the experiment represented a characteristic building height of 18m in the real world. The approaching velocity profile was also appropriately scaled from a full-scale atmospheric boundary layer (Kastner-Klein, 1999). The scaled-down model had a Reynolds number of 63,000.

The approaching flow was directed perpendicular to the axis of the street. Its velocity profile could be described by either a power law profile or a logarithm law profile. The power law profile (Equation 5.1) could describe the mean velocity profile of the boundary layer in the wind tunnel, whereas the logarithmic law profile (Equation 5.2) was more accurate in the lower part of the boundary layer ($20\text{mm} \leq z \leq 100\text{mm}$) (Kastner-Klein, 1999).

$$\frac{U}{U_{ref}} = \left(\frac{z-d_0}{z_{ref}-d_0} \right)^\alpha \quad (5.1)$$

with reference height $z_{ref}=480\text{mm}$ which is approximate to the boundary layer height (δ), the velocity at the reference height $U_{ref}=7.7\text{m/s}$, displacement height $d_0=2\text{mm}$, and power law index $\alpha=0.23$.

$$\frac{U}{U_\tau} = \frac{1}{\kappa} \ln \left(\frac{z}{z_0} \right) \quad (5.2)$$

with friction velocity $U_\tau=0.385\text{m/s}$, von Karman constant $\kappa=0.41$, and roughness height $z_0=0.8\text{mm}$.

Turbulence information of the approaching flow was available as the root mean square (R.M.S.) of each velocity component. It is illustrated in Figure 5.2 below. With this information, turbulent intensity (TI) and turbulent kinetic energy (TKE) can be calculated from Equation 5.3 and Equation 5.4 respectively. The calculated TKE profile is used for defining turbulence information on the inlet boundary, which is discussed later in Section 5.3.1.

$$I = \frac{\sqrt{[(u)^2+(v)^2+(w)^2]/3}}{U} \quad (5.3)$$

$$k = \frac{1}{2} [(u)^2 + (v)^2 + (w)^2] \quad (5.4)$$

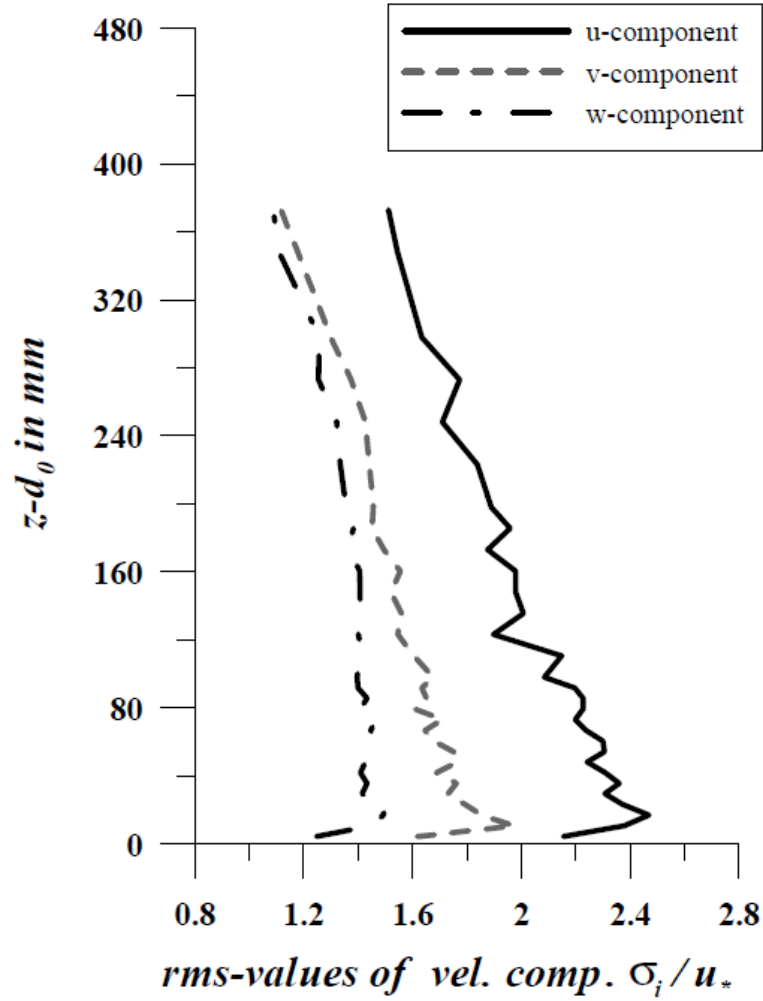


Figure 5.2: Measured R.M.S. of each velocity component. Adapted from Kastner-Klein (1999).

5.2.3 Traffic emission information

Sulphur hexafluoride (SF_6) was used as trace gas in the experiment, to model traffic emission. The use of SF_6 is thought to be owing to four reasons: (1) it is not reactive with the composition of air and the building surface, (2) its concentration can be measured with a satisfactory accuracy at very low concentrations, (3) its concentration in the atmosphere is negligible (Hogan, 2011), and (4) it has low settling velocity in the air.

A mixture of air and SF_6 was released from a line source which was positioned on the bottom of the test street canyon, either 35mm away from the leeward wall or 35mm away from the windward wall (Kastner-Klein, 1999). Thus, two different emission scenarios were established. For simplicity, they are called Emission Case A and Emission Case B here. The source intensity varied between different experiments, in

order to make the concentrations at all the measuring points lying in the sensor's measuring range. Nevertheless, the measured concentration was presented in the normalized form defined by Equation 5.5, so the result is independent of source intensity.

$$c^* = \frac{cU_0H}{Q/L_q} \quad (5.5)$$

with free-stream velocity $U_0=7\text{m/s}$, building height $H=0.12\text{m}$, source length $L_q=1.42\text{m}$ which has an additional length of 0.11m out of each street end, and the emission rate of SF_6 (Q) varies between different experiments.

Note: the free-stream velocity (U_0) is the velocity at a height of 0.12m before the buildings, which is different from the reference velocity (U_{ref}) at the boundary layer height ($\delta \approx 0.48\text{m}$).

5.3 CFD models

Taking on the work of Kastner-Klein and Plate (1999), three experiments are modelled in CFD. Their geometries in the CFD models are summarized in Table 5.1 below. In the CFD modelling, Cases 1 and 2 are modelled by 2D geometries to save computational cost. This modelling method is valid because the length of each building ($L=15H$) was sufficiently long to produce two-dimensional flow and dispersion characteristics in the centre of the street (Kastner-Klein, 1999). On the other hand, the flow pattern for the case with $L=10H$ was not fully two-dimensional, which has been discussed in the literature review in Section 2.4.1. To capture the different flow patterns induced by building length, Case 3 must be modelled by 3D geometries.



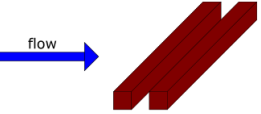
Case number	Number of building row & building length	Model dimension	Building and street geometries
1	2 building rows, $L=15H$	2D	
2	4 building rows, $L=15H$	2D	
3	2 building rows, $L=10H$	3D	

Table 5.1: Summary of three benchmark cases.

The boundary conditions used in the current CFD models are displayed in Figure 5.3 below. The specification of boundary types and positions generally follows the best practice guidelines in the methodology chapter (Section 4.4). In detail, distances of $6H$ and $15H$ are given before the first building and after the last building respectively. The domain height for all the cases and the domain width for benchmark case 3 are kept the same as the experimental setup (i.e., 1m high and 2m wide). Among all the boundaries, inlet boundary would have the strongest influence on the flow in the computational domain. For this reason, the inlet boundary for the current study is discussed in detail in Section 5.3.1 below.

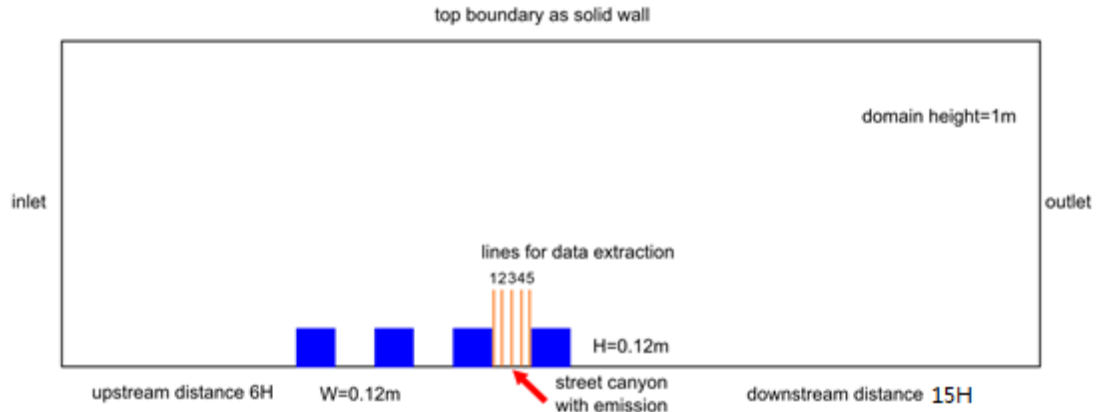


Figure 5.3: A sketch of the modelling domain of benchmark case 2 and the boundary conditions.

In all the three CFD models, each emission source is defined having a width of 0.008m ($1/12H$). Such narrow width is reasonable to model the line source in the experiment. It has been further tested that the variation of source width in the range of $0.01H$ to $0.1H$ has a very weak impact on pollutant concentration at most positions. The specification of the emission sources follows the best practice guidelines given in Section 4.4.1. Modelled concentration is also presented in the normalized form defined in Section 5.2.3, which matches the presentation used in the experiments.

Two turbulence models and two wall functions are tested in this study. The testing approaches and criteria are provided in Section 5.3.2 below. Section 5.3.3 discusses appropriate turbulent Schmidt numbers. Section 5.3.4 introduces mesh sensitivity test as an essential means to reduce discretisation error of CFD model and explains how the test is carried out in this study. Section 5.3.5 points out what types of data are compared between the models and the experiments and where the comparisons are made.

5.3.1 Inlet boundary condition

The power law profile (Equation 5.1) is used to define velocity information on the inlet boundary. The specification of any profile, including the velocity profile on the inlet boundary, is conducted by using User Defined Function in FLUENT. As shown in Figure 5.4 below, the power law profile is in good consistency with the measurements from the ground to the boundary layer height ($\delta \approx 480\text{mm}$). The logarithmic law profile (Equation 5.2) is not used here, because it gives relatively large errors above the height of 100mm (not shown here).

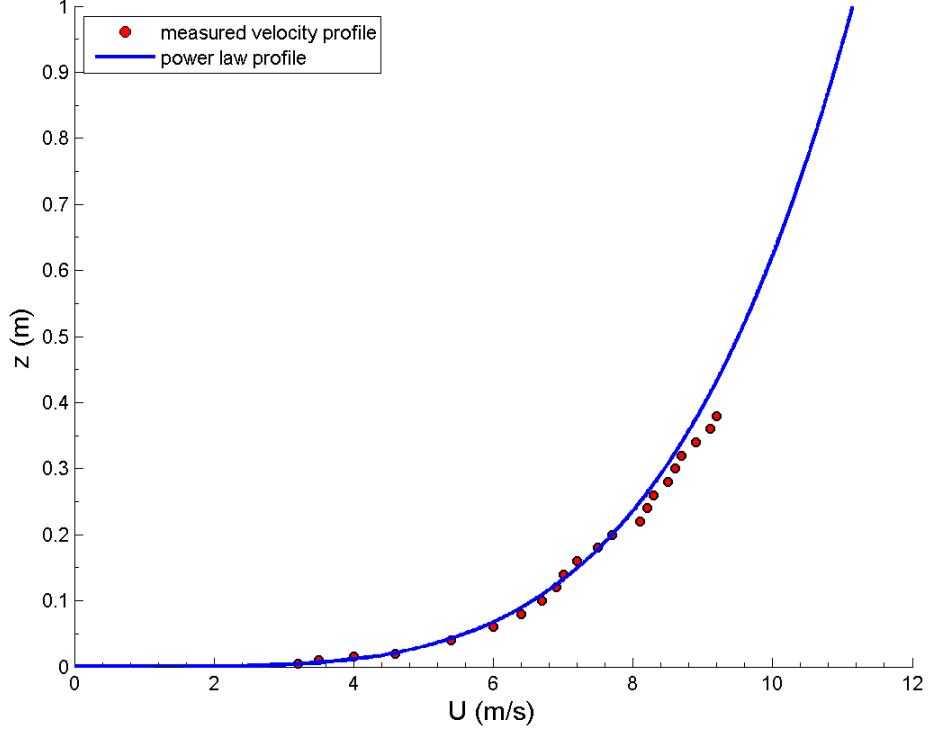


Figure 5.4: The velocity profile at the inlet boundary: red circle—experimental measurements, blue solid line—specified by a power law and used in CFD models. Replotted following Kastner-Klein (1999).

The TKE on the inlet boundary is specified by fitting the experimental measurements and assuming constant TKE above certain height. The measured TKE up to the height of $z=0.37\text{m}$ is calculated from the R.M.S. of three velocity components (see Figure 5.2 in Section 5.2.2). It reveals a linear relation between TKE and height up to the topmost measuring point, except for the place near to the ground (see red circles in Figure 5.5 below). Therefore, it is reasonable to define a linear TKE profile below 90% of the boundary height ($0.9\delta \approx 0.43\text{m}$) and constant TKE above this height, which follows the specification of TKE in Castro and Apsley (1997) and Salim et al. (2011) (see the discussion in Section 4.4.3). After fitting the measured TKE, the TKE profile for the inlet boundary is obtained as Equation 5.6 and is displayed by blue solid line in Figure 5.5.

$$k = \begin{cases} -2.71z + 1.73, & \text{when } y < 0.9\delta \\ 0.56, & \text{when } y \geq 0.9\delta \end{cases} \quad (5.6)$$

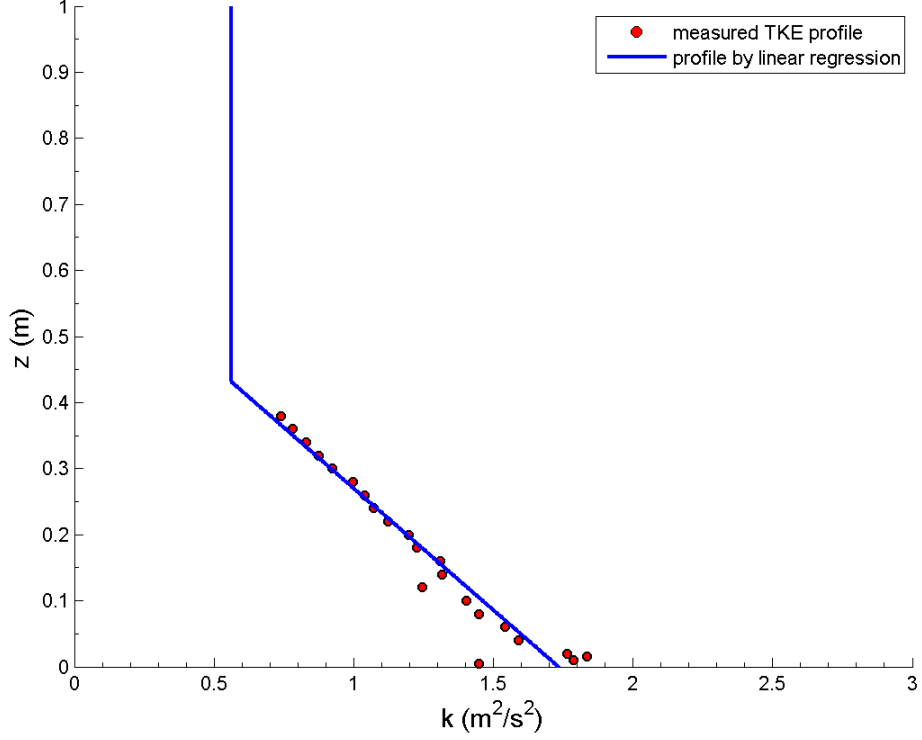


Figure 5.5: TKE for approaching flow. Red circle: experimental measurements from Kastner-Klein, and blue solid line: the TKE profile obtained by fitting the measurements and used for the inlet boundary.

Turbulent dissipation information is not available in the experiment, so the dissipation on the inlet boundary is defined by an empirical profile. Equation 5.7 is preferred among the empirical dissipation profiles given in Section 4.4.3. It is because in this relation, the dissipation only relies on the TKE, which is reliably measured from the experiment; in contrast, the other profiles further require the estimation of friction velocity U_τ , which introduces more uncertainty into the dissipation profile.

$$\varepsilon = \frac{C_\mu^{\frac{3}{4}} k^{\frac{3}{2}}}{\kappa(z+z_0)} \quad (5.7)$$

5.3.2 Turbulence model and the wall function

The flow properties and concentration modelled by the standard k- ε model and the RNG k- ε model are compared with the experimental measurements to judge which model is better. The closeness of modelled velocities and measured velocities is regarded as a primary judging criterion. If both turbulence models predict similar velocities, the closeness of modelled concentrations and measured concentrations is regarded as a secondary criterion.

The application of different wall functions should only affect the model results near the building walls and the ground. Thus, the modelled near-wall concentrations and the measured near-wall concentrations are compared to judge which wall function is better, as the flow information in the near-wall region is not available in the experiment.

5.3.3 Turbulent Schmidt number

A range of turbulent Schmidt number (i.e. $Sc_t=0.3, 0.5, 0.7, 0.9$ and 1.1) has been tested before the benchmarking study, as different values of this number would strongly affect the turbulent diffusion of pollutant and therefore affect overall concentration in street canyon.. It is found that the values 0.7 and 0.9 provide the closet prediction of concentration to the measurements for benchmark cases 1 and 2 which are modelled by 2D geometries. This finding is consistent with many experimental results (not the experiments for this study) that the turbulent Schmidt number is typically in the range of $0.7-0.9$ for various types of flow. Therefore, it has been determined to use $Sc_t=0.9$ for benchmark cases 1 and 2 before making other tests, and all the modelled concentrations for these two cases are based on $Sc_t=0.9$.

However, the value 0.9 is found to cause large over-predictions of concentration in benchmark case 3 which is modelled by 3D geometries. This issue is also found in the literature. Riddle et al. (2004) and Di Sabatino et al. (2007) suggested that a small Sc_t , such as a value of 0.3 might be more suitable for predicting dispersion around plumes in open country and around a single building, regardless the inconsistency between this value and the typical values derived from experiments (i.e., in the range of $0.7-0.9$). Thus, different turbulent Schmidt numbers are tested for benchmark case 3, and the test results is discussed in Section 5.6.4.

5.3.4 Mesh sensitivity test

Since a CFD model is solved by numerical methods, the solution at each node is only approximated and contains errors. Many theoretical studies have shown that the discretisation schemes used in CFD models are the main source for these errors (Celik et al., 2008; Franke and Frank, 2008). It is possible to reduce this type of error by increasing mesh resolution, until the mesh is fine enough to get converged results. Thus, one important task during CFD modelling is to seek an optimum mesh resolution that minimizes the discretisation errors to an acceptable level but does not make too heavy burden for computing. The optimum mesh is usually achieved by making systematic

refinements of mesh along each direction, and comparing the model results obtained under different meshes is called “mesh sensitivity test”.

A mesh sensitivity test is usually with respect to either primary quantities solved from the governing equations (e.g., velocity components, pressure and TKE) or interested secondary quantities derived from the primary quantities (e.g., drag coefficient and heat transfer coefficient). In the current benchmarking study, primary quantities including horizontal velocity, vertical velocity, TKE and concentration are tested because these quantities will be compared between the models and the experiments.

To have an impression of the optimum mesh resolution for modelling street canyon flow, the mesh resolutions used in the literature are examined. However, it is found that they are not in good agreement with each other. In general, there are three mesh resolutions used in the literature, which is described by the cell number along building height or the cell number between buildings. (1) The COST best practice guideline (Franke et al., 2007) suggested that at least 10 cells should be placed between building separation to simulate flow pattern. (2) Most CFD modelling work used mesh resolutions finer than this basic requirement (Gromke and Blocken, 2015; Gromke et al., 2008; Solazzo et al., 2009). In these studies, the minimum cell size was typically ranged from $0.025H$ to $0.05H$. In other words, around 20 to 40 cells were allocated along the building height if the cells are uniformly spaced. (3) Only a few studies, such as Koutsourakis et al. (2012), set more than 40 cells along the building height. The discrepancy about the different mesh resolutions used in the literature is believed to be owing to the diverse criteria used for judging mesh independence, which even stresses the necessity of mesh sensitivity test as a part of the benchmark study.

The mesh information for each benchmark case is summarized in Table 5.2 below. Four mesh resolutions are tested in Cases 1 and 3, and they are named as ‘coarse mesh’, ‘normal mesh’, ‘fine mesh’ and ‘ultra-fine mesh’. For the coarse mesh, there are 12 cells along the building height and the street width, which satisfy the basic requirement proposed in the COST best practice guideline (Franke et al., 2007). The normal mesh, the fine mesh and the ultra-fine mesh are refined from the coarse mesh by factors of 2, 3 and 4 along each direction of the Cartesian coordinate. The refinement is made across the whole computational domain in Case 1. However, the full refinement would make too many cells in Case 3, so that a nested mesh strategy (or called as non-conformal mesh in FLUENT) is utilized to reduce total cell number without sacrificing model

accuracy in key regions. A good illustration of the nested mesh is given in Figure 5.6 below. Refinement is applied in the region $1H$ before the first building, $3H$ after the last building and $1H$ above all the buildings. The initial mesh in this region is refined by a factor of two in each direction.

Total cell number				
Case	Coarse	Normal	Fine	Ultrafine
1	3,375	13,500	30,375	54,000
2	-	-	81,900	-
3	423,416	1,084,664	2,879,480	6,374,648
Cell number along the building height				
Case	Coarse	Normal	Fine	Ultrafine
1	12	24	36	48
2	-	-	42	-
3	12	24	36	48

Table 5.2: Mesh information for each benchmark case.

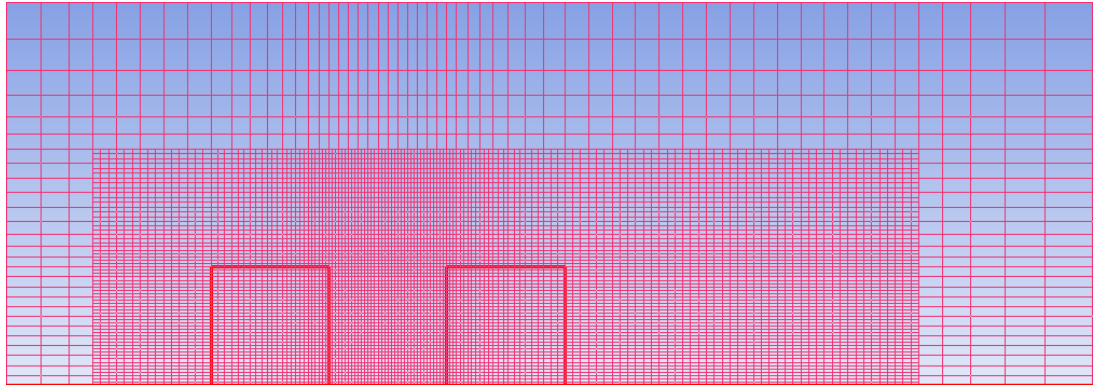


Figure 5.6: The nested mesh for benchmark case 3.

It should be pointed out that all of the mesh sensitivity studies in this chapter are on the basis of using the standard k - ϵ model, the scalable wall function and a turbulent Schmidt number of 0.9.

5.3.5 Data used for comparison

The comparisons between the CFD modelling results and the experimental measurements are made on five vertical lines in the test street. The positions of these lines are shown in Figure 5.7 below. They are denominated as leeward side line (magenta), leeward quarter line (red), middle line (blue), windward quarter line (green) and windward side line (cyan). In the oncoming results sections, both the experimental measurements and the CFD results on these lines are plotted in accordance with the five designated colours.

In the experiment, the measured concentrations are available on the two side lines, and the measured velocities are available on the other three lines. In the CFD modelling, flow properties and concentration are available on all the five lines.

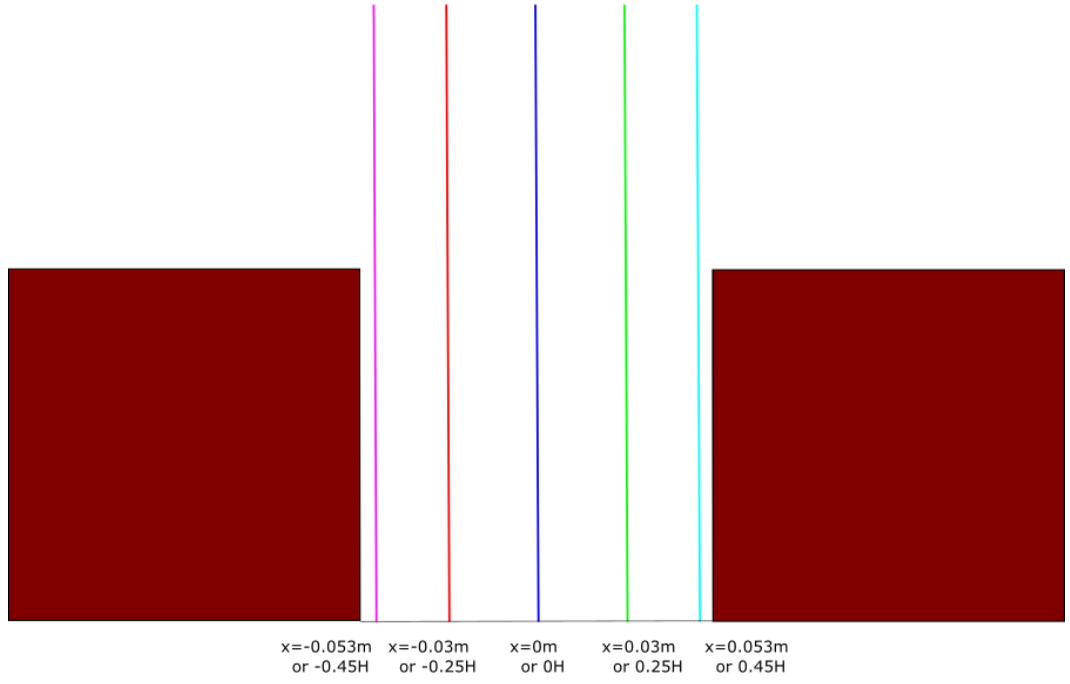


Figure 5.7: The positions for data comparison, magenta $x=-0.053\text{m}$ (or $-0.45H$), red $x=-0.03\text{m}$ (or $-0.25H$), blue $x=0\text{m}$, green $x=0.03\text{m}$ (or $0.25H$) and cyan $x=0.053\text{m}$ (or $0.45H$).

5.4 Results and analyses—benchmark case 1

The results for benchmark case 1 are presented and analysed in five sub-sections. In the first and the second sub-sections, two mesh sensitivity tests are carried out on the middle line and on two side lines. In the third sub-section, flow pattern on the mid vertical plane is compared between the model and the experiment. In the fourth sub-section, flow properties and concentration are compared between the model and the experiment. The last sub-section introduces the hit-rate (Q_{hit}) as a means to assess model accuracy and discusses the calculated hit-rates for benchmark case 1.

5.4.1 Mesh sensitivity test on middle line

Mesh sensitivity is first tested on the middle line of the street canyon, as the converged solutions in the main-stream area are a good indicator of small discretisation errors. This is also the typical approach used in the literature (e.g., Koutsourakis et al. (2012), Takano and Moonen (2013) and Guillas et al. (2014)) to seek for mesh independent results. The horizontal velocity U , vertical velocity W , turbulent kinetic energy k , and concentration c solved under four different meshes are plotted in Figure 5.8 below. All of these quantities are presented in normalized forms.

As shown in Figure 5.8(a) below, the horizontal velocity (U) on the middle line is well converged. Even the U profile obtained under the coarse mesh has little difference from the U profiles obtained under the other three meshes. The only visible error appears at the first node away from the ground (at $z=0.08H$), because different near-wall mesh resolutions results in different degrees of uncertainty in the application of the wall function. Nevertheless, this error is not large and disappears under the other three meshes. Thus, mesh independence for horizontal velocity is considered to be achieved from the normal mesh.

As shown in Figure 5.8(b) below, the vertical velocity (W) profiles obtained under the fine and ultra-fine meshes are very similar, while the W profiles obtained under the coarse and normal meshes show large difference between each other. According to this finding, mesh independence for vertical velocity is considered to be achieved from the fine mesh. Comparing to horizontal velocity, it requires finer mesh to achieve mesh independent vertical velocity. This is because vertical velocity is an order of magnitude lower than horizontal velocity on the middle line.

After comparing Figure 5.8(c) below with Figure 5.8(a) below, it is noted that the convergence performance for TKE (k) is similar to that for horizontal velocity. Accordingly, mesh independence for TKE is considered to be achieved from the normal mesh.

The convergence performance for concentration (c) hinges on emission case. For Emission case A, the errors caused by different meshes are uniform along the middle line (see Figure 5.8(d) below). The c profiles obtained under the fine and ultra-fine meshes are similar. Thus, mesh independence for concentration is considered to be achieved from the fine mesh in Emission case A.

For Emission case B, the middle line is downstream to the emission source. As a result, the concentration on the middle line is higher in Emission case B than in Emission case A. In addition, the c profile has a large value on the ground and has a sharp gradient between the ground and the first node away from the wall (at height $z=0.08H$) (see Figure 5.8(e) below). Since near-wall mesh resolution affects the application of wall function, it is not surprising to see that different meshes lead to large errors in the region with sharp-gradient. Nevertheless, the errors between the fine mesh and the ultra-fine mesh are not so large (e.g., the normalized c on the ground is 92 and 97 for the fine and ultra-fine meshes respectively). Thus, mesh independence for concentration is considered to be achieved from the fine mesh in Emission case B.

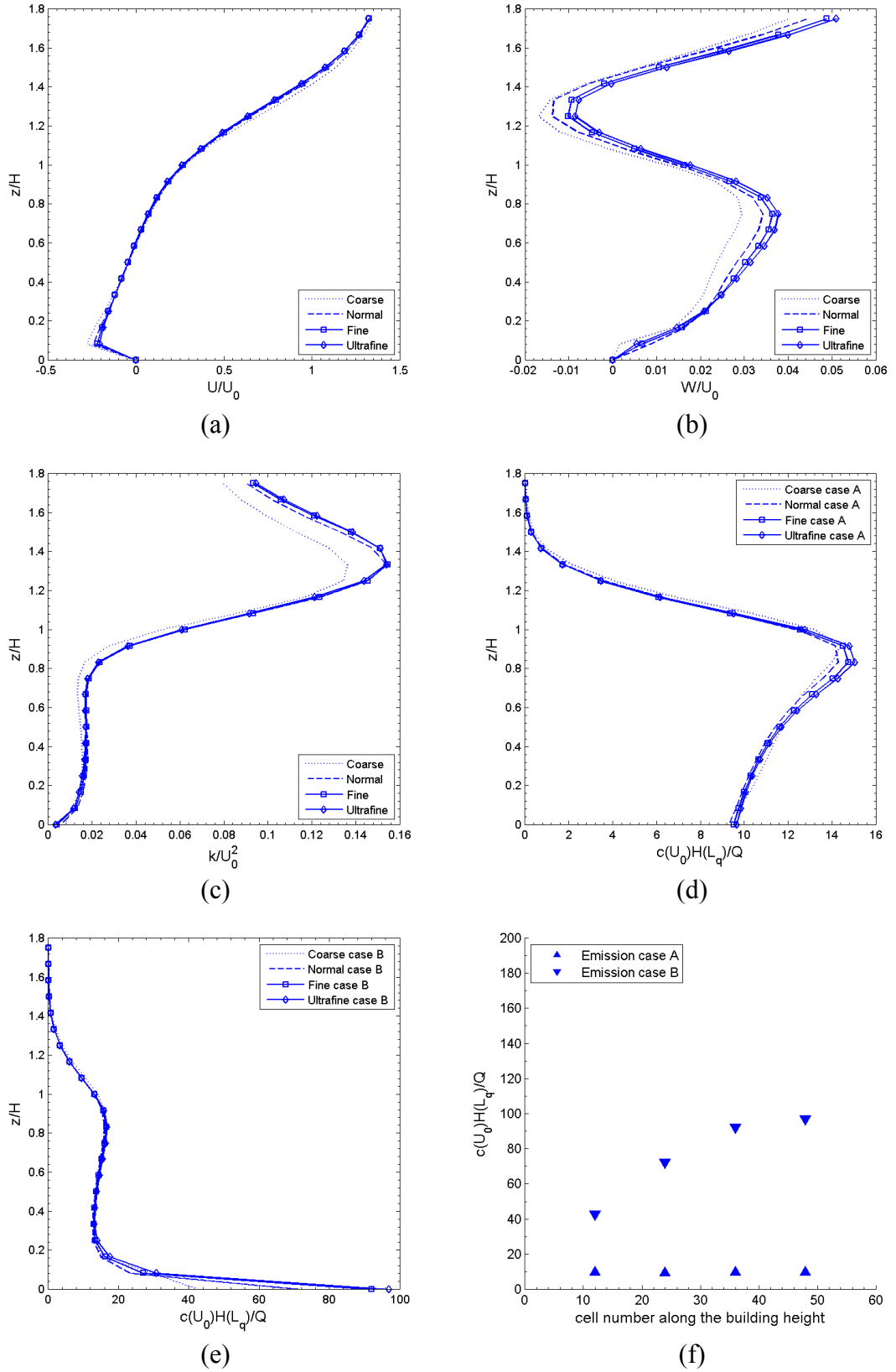


Figure 5.8: Mesh independence tests on the middle line ($x=0$): (a) U , (b) W , (c) k , (d) c for Emission case A, (e) c for Emission case B, and (f) c on the lowest point (ground) of the middle line for both emission cases vs mesh resolution.

5.4.2 Mesh sensitivity test on two side lines

It has been mentioned before that the experimental measurements of concentration were only available at a few near-wall positions which are 7mm away from the building walls. To make reliable comparisons between the measurements and the modelled concentrations, the model errors at these positions must be reduced to an acceptable level.

The mesh sensitivity test in the last section cannot guarantee that the errors at the near-wall positions are as small as those on the middle line. For this reason, a separate mesh sensitivity test is carried out in this section, on two side lines which are 7mm away from the building walls. The test results are plotted in Figure 5.9 below. It should be pointed out that both discretisation error and the uncertainty about the wall function are possible sources of error in the near-wall region, in contrast to the error on the middle line that discretisation error is the only source.

After comparing Figure 5.9 with Figure 5.8, it is realised that convergence is more difficult to be achieved on the two side lines than on the middle line. In detail, the coarse and normal meshes produce large errors in the W profiles (see Figure 5.9(b)) and in the k profiles (see Figure 5.9(c)) on both side lines; the coarse mesh causes very large errors in c profile on the leeward side line (see Figure 5.9(d) and (e)). According to these findings, the fine mesh is the "minimum requirement" to achieve mesh independence for any flow properties or concentration on the two side lines; in contrast, the normal mesh is fine enough to obtain mesh independent horizontal velocity and TKE on the middle line.

The near-wall mesh resolution for the fine mesh is found to be in accordance with the recommendation proposed by VDI (The Association of German Engineers). VDI (2005) recommended putting at least two nodes between the wall and the position of interest, when making a dispersion study. In the current study, the coarse, normal, fine and ultra-fine meshes give 0, 1, 2 and 2 nodes between the wall and the side line. It is found that the model errors on the side lines are acceptable when the fine mesh is used. Thus, the recommendation given by VDI is verified once again by the mesh sensitivity test results.

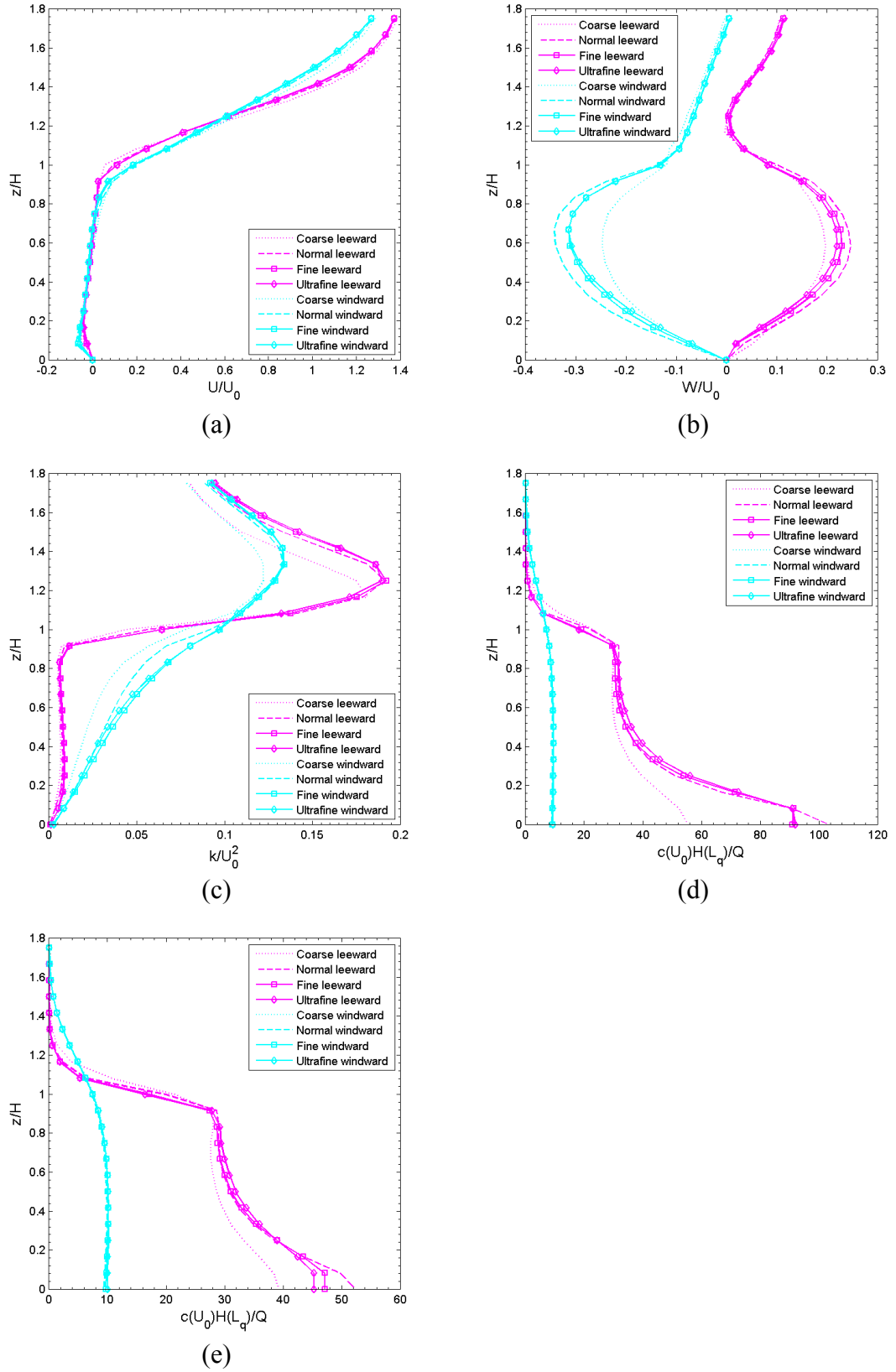


Figure 5.9: Mesh independence tests on the leeward and windward side lines ($x=-0.45H$, magenta; $x=0.45H$, cyan): (a) U , (b) W , (c) k , (d) c for Emission case A, and (e) c for Emission case B.

5.4.3 Comparison of flow pattern

Previous section confirms that the fine mesh ensures mesh independent results for benchmark case 1. This section and the next section make comparisons between the model results and the experimental measurements. The flow pattern on the mid vertical plane is examined in this section.

The flow pattern obtained from the experiment is shown in Figure 5.10 below. It is presented in form of velocity vectors whose length is proportional to the magnitude of the velocity. The origin of each vector indicates each measuring position in the experiment. It should be mentioned that the actual flow observed in the experiment is not stable, and the flow pattern shown here is based on the time-average velocity.

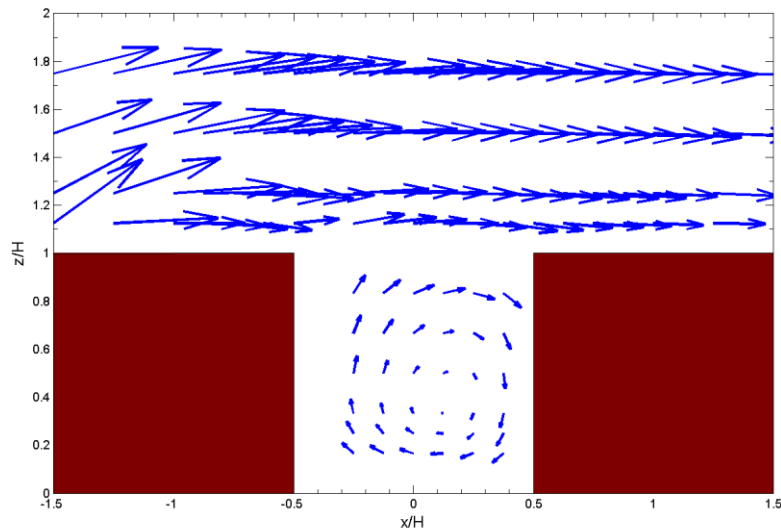
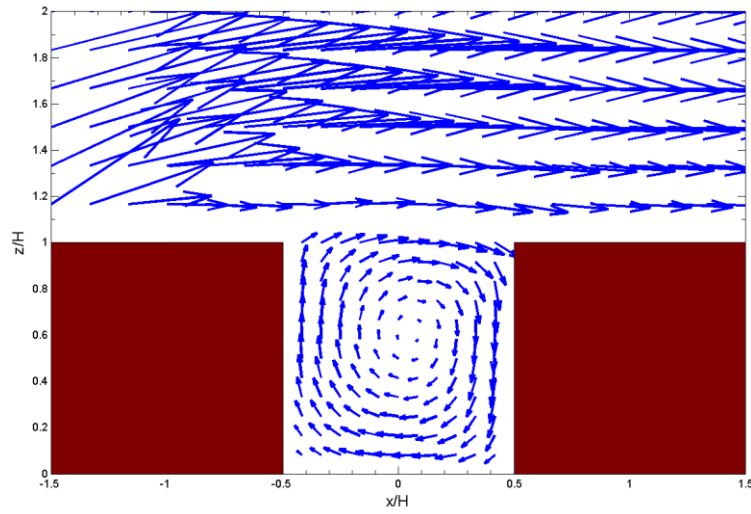


Figure 5.10: Velocity vectors on the mid vertical plane of an isolated street canyon with $L=15H$, experimental results. Replotted following Kastner-Klein et al. (2004).

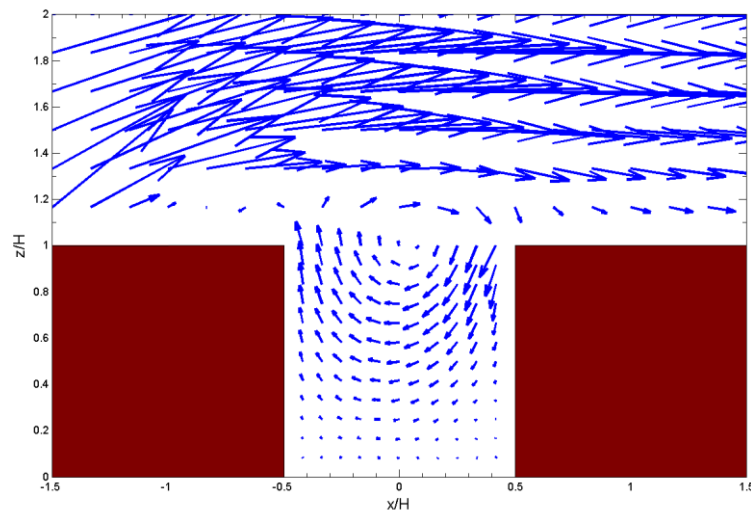
Two principal flow characteristics are observed from Figure 5.10—(1) the flow separation at the upwind edge of the first building and (2) the vortex flow in the street canyon. Owing to the flow separation, the flow above the first building and the flow above the street are not parallel to the ground, which are a unique flow feature for isolated street canyon. Meanwhile, the vortex centre does not locate at the geometric centre. It is relatively close to the windward wall and the ground.

In terms of CFD modelling, both the standard $k-\epsilon$ model and the RNG $k-\epsilon$ model are used to model the street canyon flow. The flow patterns obtained under these two

turbulence models are shown in Figure 5.11(a) and (b) below respectively. The vectors used in these figures have the same scale with the vectors in Figure 5.10.



(a)



(b)

Figure 5.11: Velocity vectors on the mid vertical plane of an isolated street canyon with $L=15H$, modelled by (a) the standard $k-\epsilon$ model, and (b) the RNG $k-\epsilon$ model.

After comparing the modelled flow pattern in Figure 5.11(a) with the measured flow pattern in Figure 5.10, it is confirmed that the standard $k-\epsilon$ model is able to reproduce a reasonable flow pattern around the street canyon. Two principal flow characteristics

observed in the experiment (i.e., the flow separation above the first building and the vortex flow in the street) are successfully captured by the standard k- ϵ model. The modelled flow at the roof level is not parallel to the ground, which is also consistent with the observation from the measured flow pattern.

On the other hand, the flow pattern predicted by the standard k- ϵ model is not perfectly accurate. Compared with the measured flow pattern, the predicted vortex has a slightly different shape, and the vortex centre is higher than its actual position. They are due to the limitation of the steady-state model, as the model is based on the steady-state assumption and therefore is unable to accurately model time-averaged flow pattern of transient flow.

Comparing Figure 5.11(b) with Figure 5.10, it is noted that the RNG k- ϵ model fails to predict correct flow pattern in the street. In Figure 5.11(b), the vortex centre is displaced upwards to the roof top. This flow pattern is completely different from the measured flow pattern shown in Figure 5.10. The failure is likely owing to the significant over-prediction of the flow separation by the RNG k- ϵ model, indicated by a much larger recirculation zone above the first building in Figure 5.11(b). Thus, the flow above the street is greatly uplifted, causing the upwards displacement of the vortex.

According to the comparisons, it is determined that the standard k- ϵ model is suitable to model the flow in an isolated street canyon, but the RNG model should be avoided for modelling this type of flow. Thus, the quantitative comparisons in the next section are based on the results modelled by the standard k- ϵ model.

5.4.4 Comparisons of flow properties and concentration

After reviewing the flow pattern, efforts are focused on comparing flow properties and concentration on five vertical lines within the street canyon. The positions of these lines have already been given in Figure 5.7 in Section 5.3.5. Here, their horizontal coordinates are restated— $x=-0.45H$, $-0.25H$, 0 , $0.25H$ and $0.45H$ —from the leeward side to the windward side. The experimental measurements are plotted by circles in Figure 5.12 to Figure 5.15 below, and the model results are plotted by solid lines in the same figures.

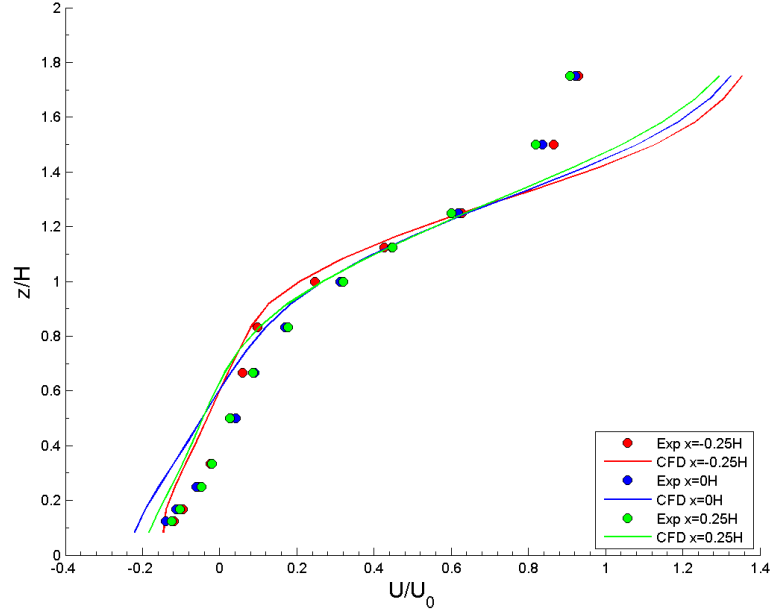


Figure 5.12: Horizontal velocity U on the middle line and on the leeward and windward quarter lines. Solid line: CFD model results for benchmark case 1, and circle: Kastner-Klein's experimental measurements.

As can be seen in Figure 5.12 above, the horizontal velocity U profiles are reasonably predicted by the CFD model. The experimental measurements show similar profiles along the three vertical lines, and the CFD model can reproduce this feature successfully. In addition, the model gives accurate predictions between $z=0.7H$ and $z=1.3H$ on all of these lines.

However, the predictions out of this region are not very accurate. The model over-predicts the flow strength above $z=1.3H$. This is because the flow above this height is strongly affected by the flow separation above the first building, and the flow separation in the CFD model is only qualitatively consistent with the experimental results but not quantitatively accurate. Thus, the flow strength above the street is accurately predicted, appearing as the over-prediction of U . The over-prediction also leads to stronger flow strength in the street. Thus, it is observed that the predicted U below $z=0.7H$ has smaller magnitudes than the experimental measurements. The errors below $z=0.7H$ are an interpretation of the slightly inconsistent flow patterns between the model and the experiment, which have been pointed out before in Section 5.4.3.

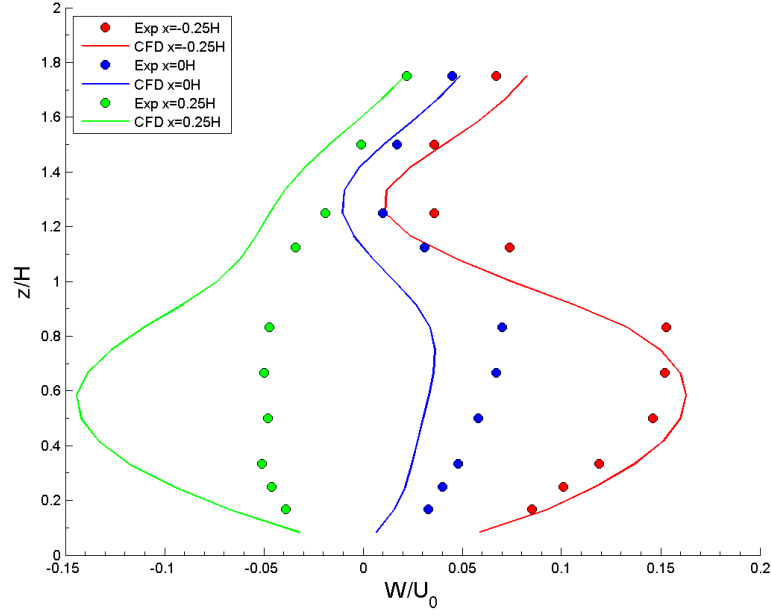


Figure 5.13: Vertical velocity W on the middle line and on the leeward and windward quarter lines. Solid line: CFD model results for benchmark case 1, and circle: Kastner-Klein's experimental measurements.

The predicting accuracy for the vertical velocity W hinges on position. As can be seen in Figure 5.13 above, the predicted W profile on the leeward quarter line (red) is very close to the profile measured in the experiment, but the predicted W profiles on the middle line (blue) and the windward quarter line (green) have large differences from the measurements.

The inaccurate W on the middle line and the windward quarter line can be explained as follows. The CFD model predicts a vortex flow pattern whose centre locates close to the middle. Therefore, the predicted W profiles on the two quarter lines (red solid and green solid) almost have mirror shapes. In contrast, the vortex centre in the experiment locates at a position on the half way between the middle line and the windward quarter line. Therefore, the measured W profile on the leeward quarter line (red circle) has larger magnitudes than on the windward quarter line (green circle). Thereby, the largest errors for W occur on the windward quarter line.

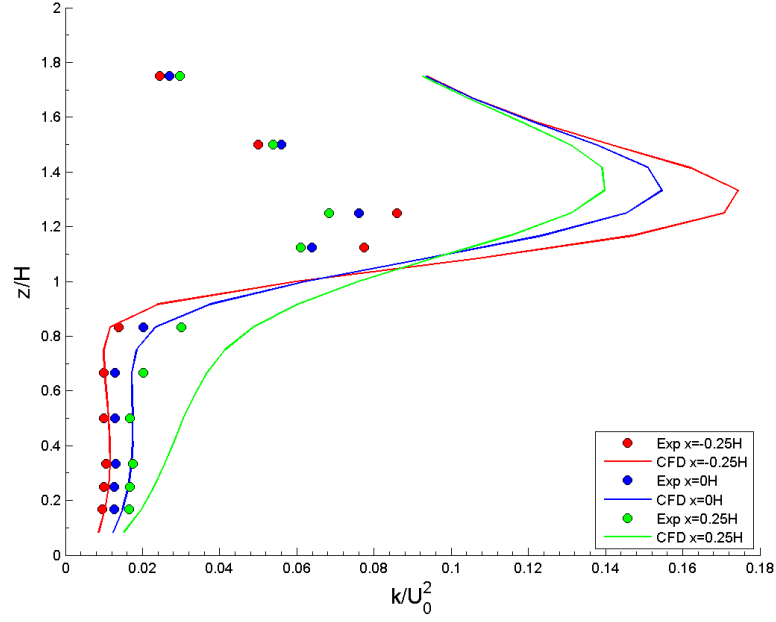
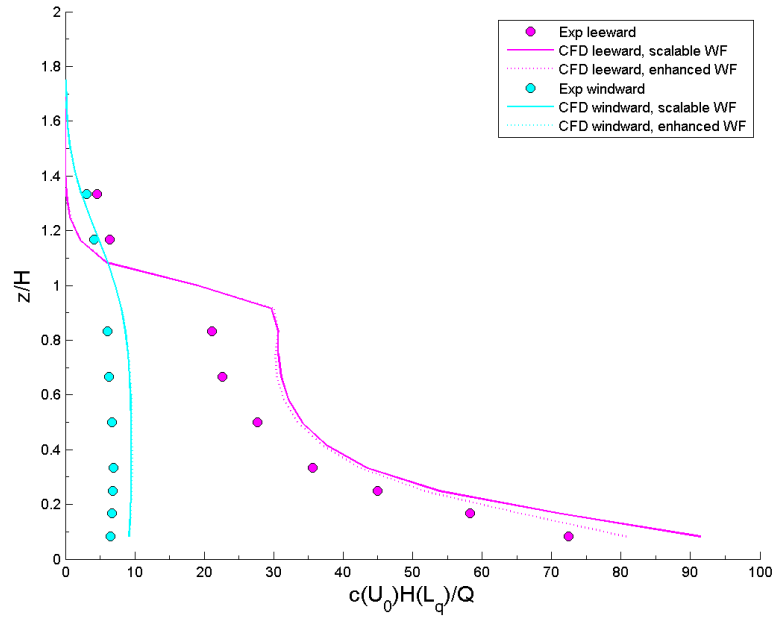


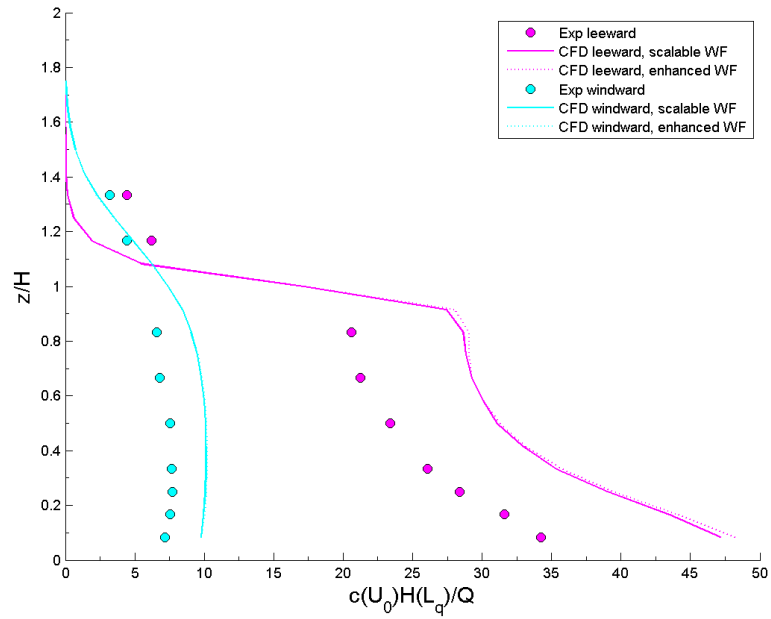
Figure 5.14: Turbulent kinetic energy k on the middle line and on the leeward and windward quarter lines. Solid line: CFD model results for benchmark case 1, and circle: Kastner-Klein's experimental measurements.

The issue of under-predicting TKE in street canyon, which has been found in many CFD studies (mentioned in Section 2.6.2), does not happen in this benchmark case. Instead, as indicated by Figure 5.14 above, TKE is greatly over-predicted (more than twice) above the roof level as well as at some positions in the street canyon. The root cause of these over-predictions is that the flow separation above the first building is unable to be quantitatively accurately predicted by using 2D geometry and the standard k - ϵ model, which will be discussed later in Section 5.6.4.

The excessive TKE above the street is transported into the street canyon, so the TKE in the street is also over-predicted. However, as can be noticed from Figure 5.14, the TKE in the street decays rapidly from the windward side to the leeward side, so that the predicted TKE on the leeward quarter line (red solid) are almost the same as the measurements (red circle). According to this observation, a hypothesis is proposed: the production of TKE in the canyon is under-predicted by the standard k - ϵ model, but in this case, the excessive TKE transported from the outside outweighs the under-prediction and causes an over-prediction of TKE in the street. This hypothesis is validated later in Section 5.6.4, by analysing the TKE profiles for benchmark case 3.



(a)



(b)

Figure 5.15: Concentration c on the leeward and windward side lines, (a) Emission case A and (b) Emission case B. Solid line: CFD model results for benchmark case 1, and circle: Kastner-Klein's experimental measurements.

The modelled and measured concentrations on the two side lines are plotted in Figure 5.15(a) and (b) above. It is first noticed from the figures that using different wall functions has a limited impact on the results. Thus, the scalable wall function is

considered to be a better choice here, as it is easier to apply and is cheaper in computing compared to the enhanced wall function.

The pollutant distributions on the side lines are successfully captured by the CFD model (i.e., similar profile shapes). However, concentration is uniformly over-predicted along each of the lines. For both emission cases, the over-prediction is around 3 units of normalized concentration on the windward side line (cyan) and is around 10–20 units of normalized concentration on the leeward side line (magenta).

By analysing the concentration profiles between the model and the experiment, it is discovered a limitation of CFD modelling specific for benchmark case 1. As mentioned before, the CFD model over-predicts horizontal velocity, vertical velocity and TKE in most places, which means both advection and turbulent diffusion effect are stronger in the model than they should be. In theory, this should give under-predictions of concentration in the street. However, over-predictions of concentration is observed in this case.

The above discrepancy can only be explained by the limitation of the steady-state model. As pointed out by Meroney et al. (1996), the flow in an isolated street canyon is characterized by an intermittent eddy circulation, which makes pollutant regularly vented upwards to the main flow above the street. However, the steady model is unable to realise this transient mechanism, leading to much less efficient ventilation and pollutant removal. Thus, concentration is over-predicted in benchmark case 1, even though flow properties are over-predicted in this case.

5.4.5 Assessment of model accuracy

The last section has shown the profiles of flow properties and concentration on five vertical lines. The errors between the model and the experiment on these lines can be directly observed by comparing the corresponding profiles. However, it is not easy to judge whether the predictions in the current case are more accurate than the predictions in the literature. For this consideration, it is required a clear standard to assess CFD model accuracy.

The hit-rate (Q_{hit}) proposed by Schlunzen et al. (2004) is a good choice of the standard specific for modelling airflow in urban areas. This statistical quantity has been used in a few studies, such as Solazzo et al. (2009) and Buccolieri et al. (2010). Its concept and its definition are introduced below.

A point is marked as ‘on-hit’ if the difference between prediction and measurement on at a position is lower than either a defined upper limit of relative error or a defined upper limit of absolute error. Schlunzen et al. (2004) defined a fixed value 25% for the former limit, but stated that the value for the latter limit should depend on flow property type. They suggested a value of 0.05 for each normalized velocity component and a value of 0.017 for normalized turbulent kinetic energy. These values are also adopted in the current study. The number of the “on-hit” points divided by the total sample points gives the hit-rate (Q_{hit}). A group of predictions with Q_{hit} greater than 66% is regarded as accurate predictions (Schlunzen et al., 2004).

As for concentration, the upper limit of absolute error is not defined in any previous studies. Thus, it is defined as a value of 10, referring the definition of the upper limit for horizontal velocity. It is calculated that the upper limit for horizontal velocity (i.e., 0.05) corresponds to around 43% of average horizontal velocity magnitude on the middle line in benchmark case 1. The definition of the upper limit for concentration (i.e., 10) will correspond to around 26% and 33% of average concentration (for all the 14 measuring points) in Emission cases A and B respectively. Thus, the defined upper limit for concentration is a stricter criterion compared to the upper limit for horizontal velocity, which means that the value of 10 is an appropriate upper limit of absolute error for concentration.

The hit-rate (Q_{hit}) for each profile for benchmark case 1 is given in Table 5.3 below, and the hit-rates lower than 66% are marked by red. These hit-rates are calculated on the basis of the fine mesh, the standard k- ϵ model, the scalable wall function and $Sc_t=0.9$.

It is noted that the hit-rates for U on three lines are all below 66%, indicating the predictions are not very accurate. Referring to the U profiles in Figure 5.12 in the last section, this is because the predicted U out of the region between $z=0.7H$ and $z=1.3H$ have relatively large difference from the measurements.

Although it has been observed from Figure 5.13 and Figure 5.14 in the last section that the predicted W and k have large relative errors, the hit-rates for them are above 66% except for W on the leeward quarter line. This is because the absolute errors for W and k are below their defined upper limits, so most predictions are “on-hit”. The low hit-rate for W on the leeward quarter line is consistent with the previous finding that the predicted W on this line has the largest errors amongst the three vertical lines.

The hit-rates for c are generally above 66%. One exception is c on the leeward side line in Emission case B, which is indicated in Figure 5.15 in the last section.

Quantity, position and figure number	Mean absolute error	Max absolute error	Mean relative error	Max relative error	Hit rate Q_{hit}
U , leeward quarter line (Figure 5.12)	0.043	0.064	93%	267%	63%
U , middle line (Figure 5.12)	0.073	0.099	136%	495%	25%
U , windward quarter line (Figure 5.12)	0.065	0.078	128%	362%	25%
W , leeward quarter line (Figure 5.13)	0.014	0.020	11%	16%	100%
W , middle line (Figure 5.13)	0.026	0.036	49%	52%	100%
W , windward quarter line (Figure 5.13)	0.065	0.094	136%	196%	33%
k , leeward quarter line (Figure 5.14)	0.001	0.002	10%	16%	100%
k , middle line (Figure 5.14)	0.004	0.005	28%	37%	100%
k , windward quarter line (Figure 5.14)	0.011	0.019	55%	82%	83%
c , leeward side line, Emission Case A (Figure 5.15(a))	10.5	19.0	28%	46%	86%
c , windward side line, Emission Case A (Figure 5.15(a))	2.7	3.0	41%	47%	100%
c , leeward side line, Emission Case B (Figure 5.15(b))	9.8	12.9	37%	39%	57%
c , windward side line, Emission Case B (Figure 5.15(b))	2.6	3.0	36%	44%	100%

Table 5.3: Model error statistics for benchmark case 1. $Q_{hit} < 66\%$ marked by red.

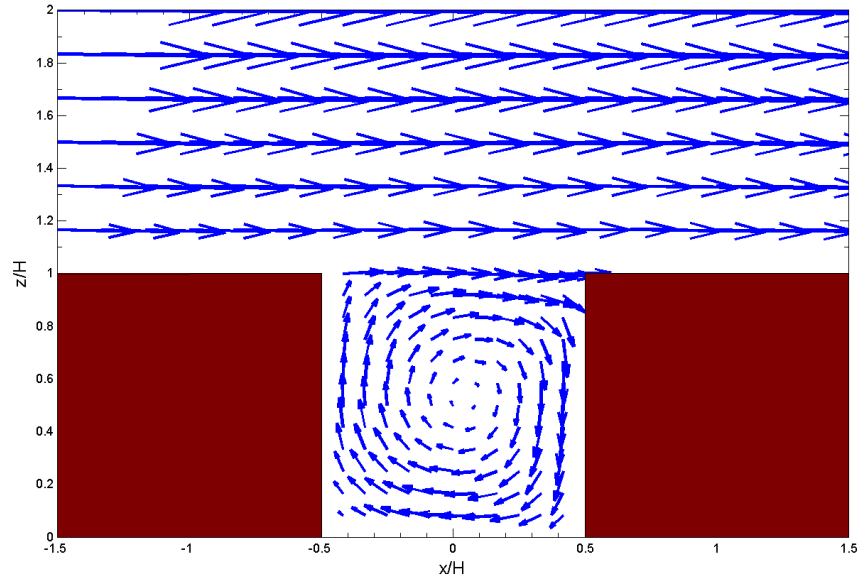
5.5 Results and analyses—benchmark case 2

Benchmark case 2 is different from benchmark case 1 by the numbers of street and building, whereas the dimension of each building and the space between adjacent buildings are the same between these two cases. For this reason, the previous conclusion for the mesh sensitivity test should still be valid in this case, and mesh independence is not tested in this case. This section is made up of the comparison of flow pattern, the comparisons of flow properties and concentration and the discussion about the calculated hit-rates, following the same structure for the last section.

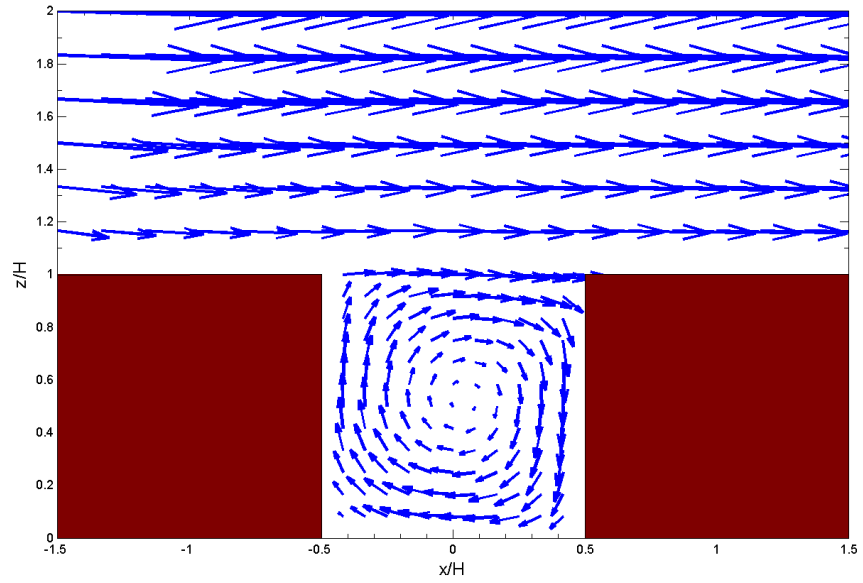
5.5.1 Comparison of flow pattern

For benchmark case 2, velocity information is not available in the experiment. Comparison is only made between the flow pattern obtained by the standard k- ϵ model and the flow pattern obtained by the RNG k- ϵ model. The modelled flow patterns are shown in Figure 5.16(a) and (b) below, and the vectors in these figures have the same scale as before.

A very consistent vortex flow pattern is observed between Figure 5.16(a) and Figure 5.16(b). The predicted vortex centre is almost at the geometric centre of the street, which is different from the prediction for benchmark case 1. The consistency between the two turbulence models is because the test street canyon (i.e., the third street) is free from the influence of the flow separation above the first building.



(a)



(b)

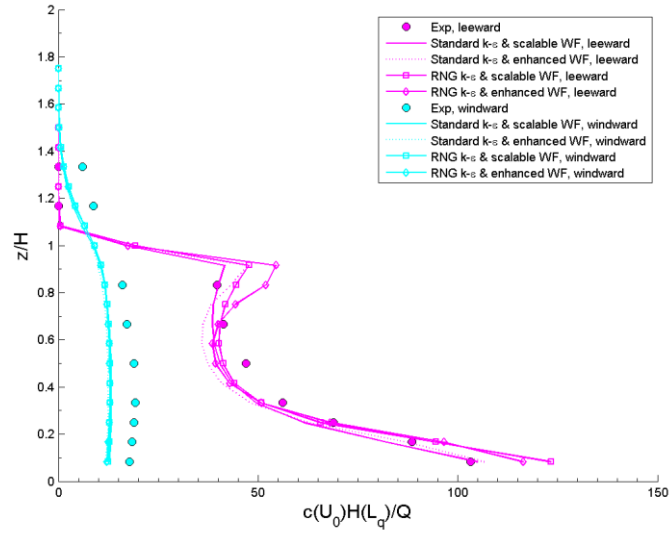
Figure 5.16: Velocity vectors on the mid vertical plane of an isolated street canyon with $L=10H$, modelled by (a) the standard $k-\epsilon$ model, and (b) the RNG $k-\epsilon$ model.

5.5.2 Comparison of concentration

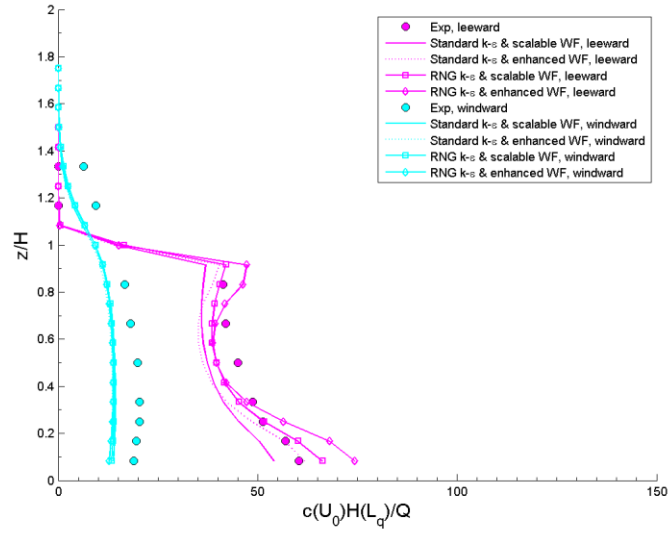
Figure 5.17(a) and (b) below show the measured and modelled concentrations on two side lines. As can be noticed from the figures, the concentrations on the windward side line (cyan) are independent of the turbulence models and wall functions. However, it is not the case on the leeward side line (magenta). The different sensitivities to turbulence model and the wall function are relevant to viscous effect. It is found that the average y^+ value on the leeward side line ($y^+=14$) is smaller than that on the windward side line ($y^+=27$), which indicates a stronger viscous effect on the leeward side line. As various turbulence model and wall function do not predict the same viscous effect, especially when this effect is strong, the concentrations on the leeward side line are therefore sensitive to the used turbulence models and wall functions.

As can be seen Figure 5.17(a) and (b), the standard k- ϵ model and the RNG k- ϵ model make moderately different predictions of concentration on the leeward side line (magenta). For Emission case A, the standard k- ϵ model gives better prediction at the positions close to the roof and at the positions near the ground. For Emission case B, the RNG k- ϵ model gives slightly better predictions below the height $z=0.8H$. Thus, both the standard k- ϵ model and the RNG k- ϵ model are acceptable for benchmark case 2, and the former is preferred due to better robustness and slightly lower computational cost.

Comparing the modelled concentration profiles with the experimental measurements, it is found that both the scalable wall function and the enhanced wall function result in reasonable predictions. Nevertheless, the concentration profiles predicted by the scalable wall function have more consistent shapes to the measurements. Thus, the scalable wall function is better choice for benchmark case 2.



(a)



(b)

Figure 5.17: Concentration c on the leeward and windward side lines, (a) Emission case A and (b) Emission case B. Solid line: CFD model results for benchmark case 2, and circle: Kastner-Klein's experimental measurements.

Comparing the measured concentrations in benchmark case 2 (Figure 5.17 above) with the measured concentrations in benchmark 1 (Figure 5.15 in Section 5.4.4), it is realised that concentration is higher in a non-isolated street canyon than in an isolated street canyon. This is due to weaker turbulent transfer efficiency for non-isolated street canyon than isolated street canyon, which has been discussed in the literature review in Section 2.2.

The current model (for benchmark case 2) successfully captures the trend that the concentrations at all the measuring points are higher compared to benchmark case 1. In addition, the current model predicts even more accurate concentrations than the previous model for benchmark case 1. As can be seen from Figure 5.17(a) and (b) above, the concentrations on the leeward side line (magenta) are in good agreement with the measurements for both emission cases, which are much better compared to benchmark case 1. On the windward side line (cyan), the concentrations are over-predicted by around 5 units of normalized concentration, which are similar to the situation for benchmark case 1. The better modelling performance in benchmark case 2 is because the flow in this case is truly steady, whereas the flow in benchmark case 1 is transient.

5.5.3 Assessment of model accuracy

The hit-rate (Q_{hit}) for each concentration profile for benchmark case 2 is given in Table 5.4 below. These hit-rates are calculated on the basis of the fine mesh, the standard k- ϵ model, the scalable wall function and $Sc_T=0.9$.

As can be found in the table, all the concentration profiles have a perfect hit-rate, indicating accurate predictions in benchmark case 2. This is because the absolute errors for c are all below their defined upper limits. The perfect hit rates also reflect that the predictions are much more reliable in benchmark case 2 than in benchmark case 1.

Quantity, position and figure number	Mean absolute error	Max absolute error	Mean relative error	Max relative error	Hit rate Q_{hit}
c , leeward side line, Emission Case A (Figure 5.17 (a))	4.5	7.4	7%	14%	100%
c , windward side line, Emission Case A (Figure 5.17 (a))	5.3	6.0	29%	31%	100%
c , leeward side line, Emission Case B (Figure 5.17 (b))	6.4	7.6	13%	17%	100%
c , windward side line, Emission Case B (Figure 5.17 (b))	5.3	6.1	28%	30%	100%

Table 5.4: Model error statistics for benchmark case 2. $Q_{hit}<66\%$ marked by red.

5.6 Results and analyses—benchmark case 3

Benchmark case 3 is different from benchmark case 1 by building length. As mentioned before, benchmark case 3 is modelled by 3D geometries, whereas benchmark case 1 is modelled by 2D geometries. Therefore, it is essential to test mesh sensitivity for this case by following the same procedures for benchmark case 1. After the test, comparisons between the model and the experiment are made, and model accuracy is assessed. In general, this section follows the same structure for benchmark case 1. There are two pieces of additional discussions: (1) the flow pattern on a horizontal plane in Section 5.6.3 and (2) the impact of turbulent Schmidt number in Section 5.6.4.

5.6.1 Mesh sensitivity test on middle line

Similar to the first sub-section for benchmark case 1, mesh sensitivity is first tested on the middle line of the street canyon. The horizontal velocity U , vertical velocity W , turbulent kinetic energy k , and concentration c solved under four different meshes are plotted in Figure 5.18 below.

In general, convergence performance is found similar between the current case and benchmark case 1. After reviewing the profiles in Figure 5.18, it is noted that the normal mesh is fine enough to achieve mesh independence for horizontal velocity (U) and TKE (k); the fine mesh is essential to achieve mesh independence for vertical velocity (W) and concentration (c).

However, the current case is different from benchmark case 1 in one aspect. As can be seen in Figure 5.18, using the coarse mesh leads to extremely large errors for vertical velocity W and concentration c for Emission case A; in contrast, these errors are not so large in benchmark case 1. According to this find, any mesh with a resolution comparable to the coarse mesh (i.e., 12 cells along building height) should not be used for modelling street canyon flow with 3D geometries.

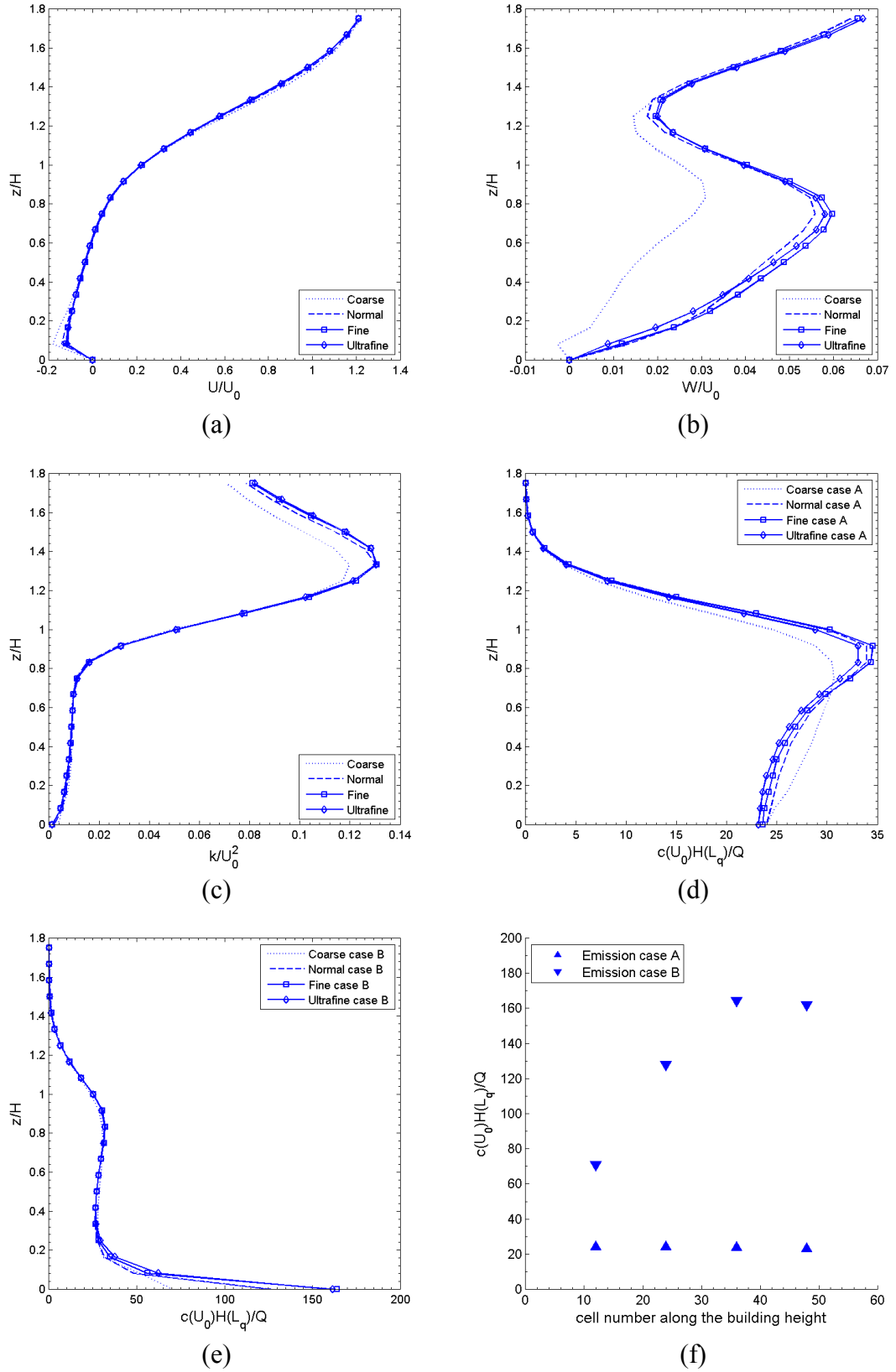


Figure 5.18: Mesh independence tests on the middle line ($x=0m$): (a) U , (b) W , (c) k , (d) c for Emission case A, (e) c for Emission case B, and (f) c on the lowest point (ground) of the middle line for both emission cases vs mesh resolution.

5.6.2 Mesh sensitivity test on two side lines

For the same reason given in the first paragraph of Section 5.4.2, mesh sensitivity is also tested on two side lines. The results are plotted in Figure 5.19 below.

After reviewing the profiles in Figure 5.19 and comparing them with the results for benchmark case 1, three main findings are summarised. First, the errors caused by different meshes are larger on the two side lines than on the middle line. This trend is also found in benchmark case 1. Second, using the coarse mesh leads to extremely large errors on the side lines for all the quantities except horizontal velocity (see Figure 5.19(b), (c), (d) and (e)). This is even worse than the situation on the middle line. Third, the normal mesh is not fine enough to reduce the errors on the side lines to an acceptable level, and the fine mesh must be used if any quantity on the side lines is interested.

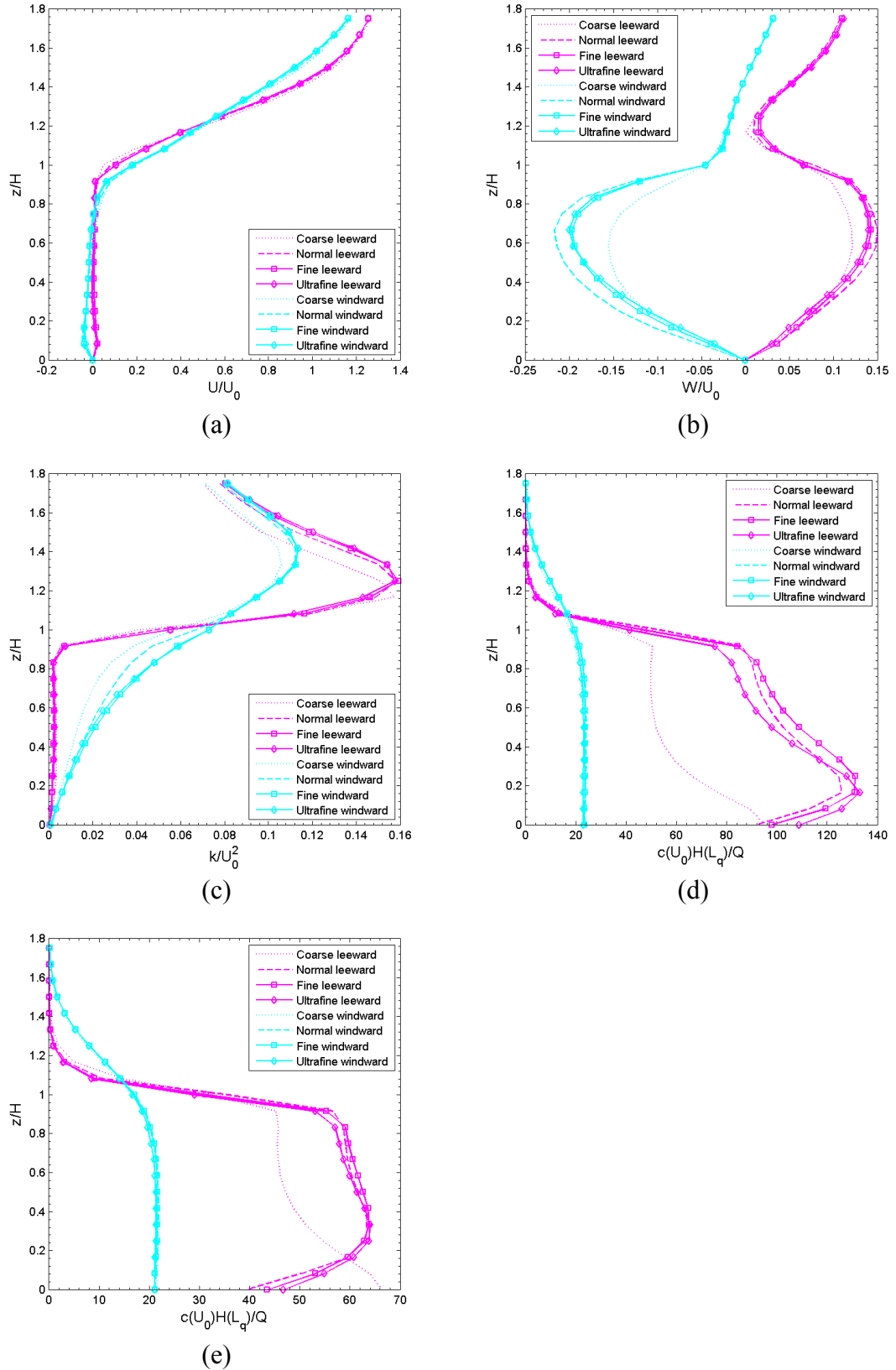


Figure 5.19: Mesh independence tests on the leeward and windward side lines ($x=-0.45H$, magenta; $x=0.45H$, cyan): (a) U , (b) W , (c) k , (d) c for Emission case A, and (e) c for Emission case B.

5.6.3 Comparison of flow pattern

For benchmark case 3, the RNG k- ϵ model fails to obtain strictly converged solutions. The residuals of the governing equations do not drop below 10^{-6} , as shown in Figure 5.20 below. Flow pattern is checked after 3000 iterations that all the residuals cannot drop further. Compared to the measured flow pattern, the modelled flow pattern is wrong (not shown here). Thus, the standard k- ϵ model is the only suitable turbulence model for benchmark case 3.

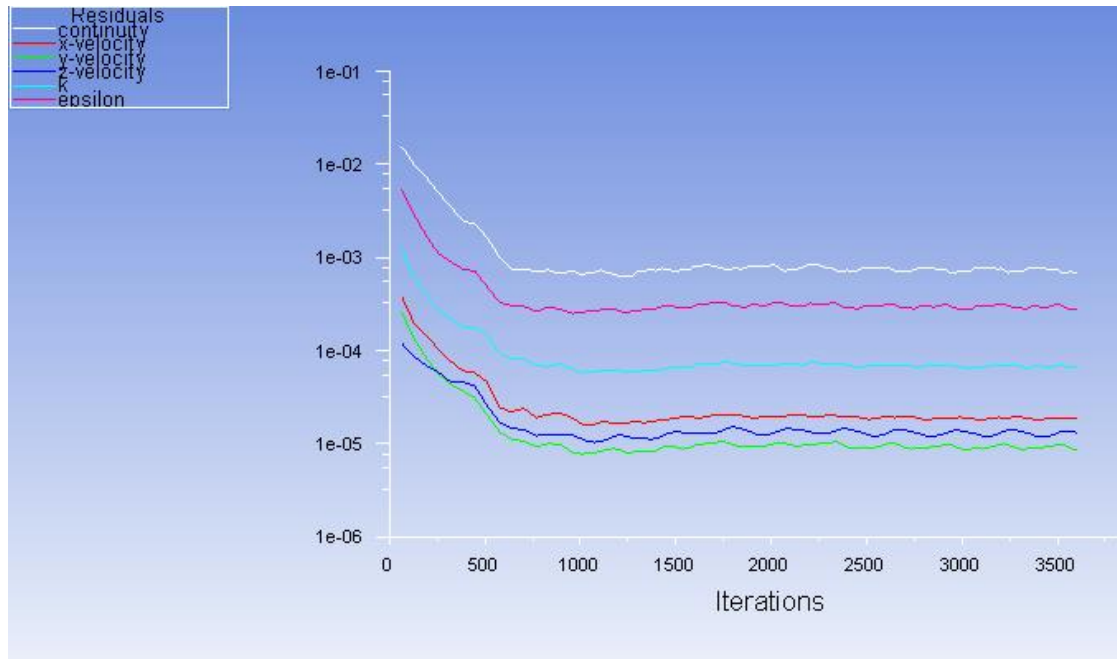


Figure 5.20: The iteration history for benchmark case 3, modelled by the RNG k- ϵ model.

The measured flow pattern on the mid vertical plane is shown in Figure 5.21 below, and the modelled flow pattern on the mid vertical plane is shown in Figure 5.22 below. According to these two figures, the CFD model successfully predicts the vortex flow pattern for benchmark case 3. The position of vortex centre is consistent between the model and the experiment—both centres are slightly above and on the right of the geometric centre. In contrast, the position of vortex centre is not accurately predicted in benchmark case 1. In addition, the CFD model predicts a similar recirculation zone above the first building, which supports that the vortex flow pattern is accurately predicted in this case. The good model performance is believed owing to the use of 3D model. In this circumstance, three-dimensional flow features, such as lateral flow from two street ends, are possible to be correctly modelled. Thus, the three model leads to more accurate predictions in the centre part of the street.

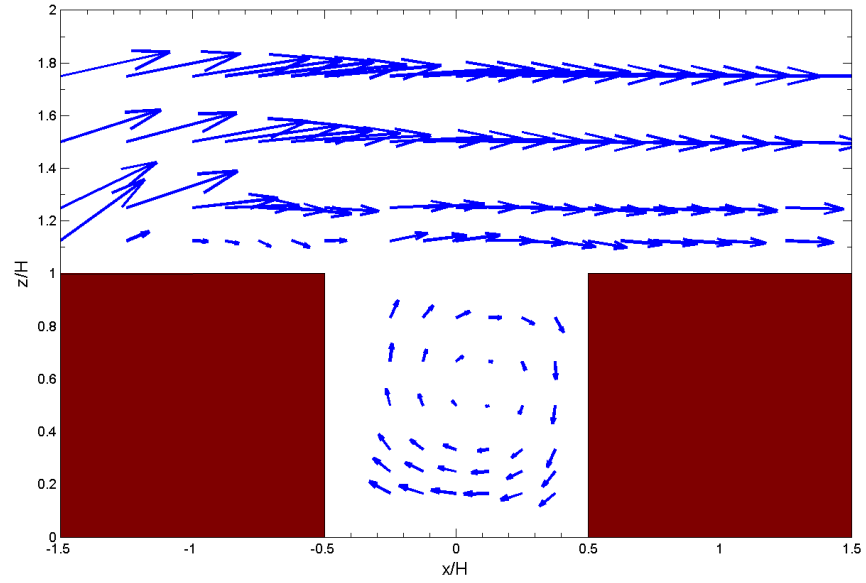


Figure 5.21: Velocity vectors on the mid vertical plane of an isolated street canyon with $L=10H$, experimental results. Replotted following Kastner-Klein et al. (2004).

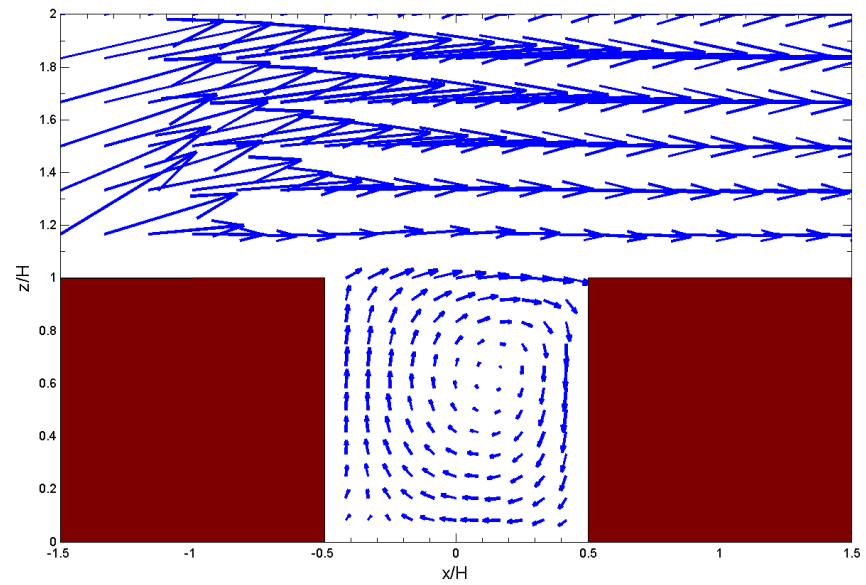


Figure 5.22: Velocity vectors on the mid vertical plane of an isolated street canyon with $L=10H$, modelled by the standard $k-\epsilon$ model.

However, after comparing the flow patterns in Figure 5.21 and Figure 5.22 above, it is observed that the predicted flow near the leeward bottom corner is not accurate enough.

The CFD model predicts a weak stream from the leeward bottom corner towards the main vortex flow. This stream occupies a $0.3H \times 0.3H$ area next to the corner. In contrast, the velocity vector at the most bottom-left position in Figure 5.21 suggests that the predicted stream does not exist in the experiment. The inconsistency is found to be relevant to the prediction of the lateral flow along the street, which is discussed as follows in association with flow pattern on a horizontal plane.

The measured flow pattern on the horizontal plane at $z=0.25H$ is shown in Figure 5.23 below, and the modelled flow pattern on the same plane is shown in Figure 5.24 below. The velocity vectors in these two figures provide good illustrations of the lateral flow from two street ends in the experiment and in the model. The combination of the flow patterns on this horizontal plane and on the mid vertical plane provides an outline of the three-dimensional flow in the street canyon.

The measured flow pattern in Figure 5.23 indicates that a horizontal semi-vortex forms at each street end. The semi-vortex attaches to the leeward building after reaching a depth of $0.8H$ from the street end. The attached flow keeps on travelling along the leeward wall with a decay of strength, until it reaches a distance of $3.5H$ from the street end. In the region of $y=-1.5H$ to $y=1.5H$ (here y means along-street direction), airflow is almost two-dimensional since the across-street velocity component is close to zero.

Comparing Figure 5.24 with Figure 5.23, it is noted that the CFD model over-predicts the strength of the lateral flow from each street end. The over-predicted lateral flow also attaches to the leeward building after reaching a depth of $0.8H$ from the street end, but it travels much longer distance along the building (up to the mid vertical plane) and has larger along-street velocity component than the actual lateral flow in the experiment. As a result, the over-predicted lateral flow drives a stream from the leeward bottom corner towards the main vortex flow on the mid vertical plane, which has been observed in Figure 5.22 above.

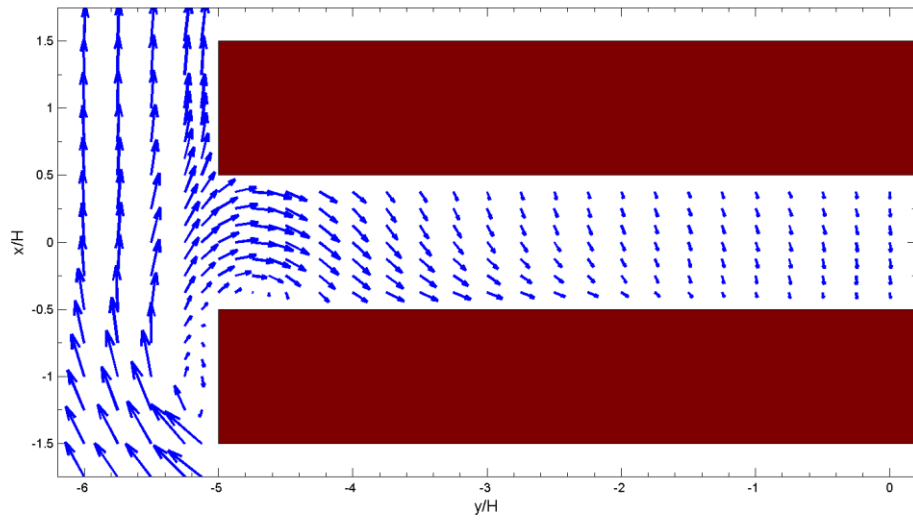


Figure 5.23: Velocity vectors on the horizontal plane at $z=0.25H$, experimental results. Replotted following Kastner-Klein et al. (2004).

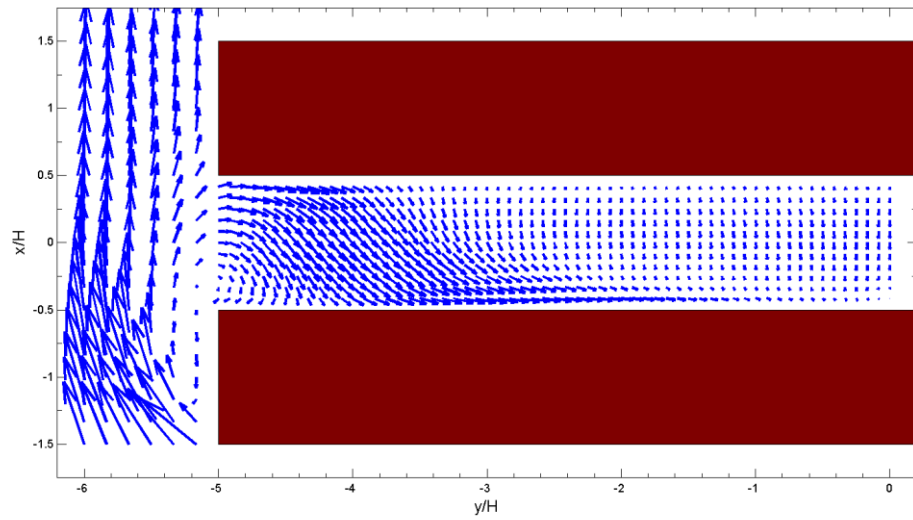


Figure 5.24: Velocity vectors on the horizontal plane at $z=0.25H$, modelled by the standard $k-\epsilon$ model.

5.6.4 Comparisons of flow quantities and concentration

The experimental measurements of flow properties and concentration are plotted by circles in Figure 5.25 to Figure 5.28, and the model results are plotted by solid lines in the same figures.

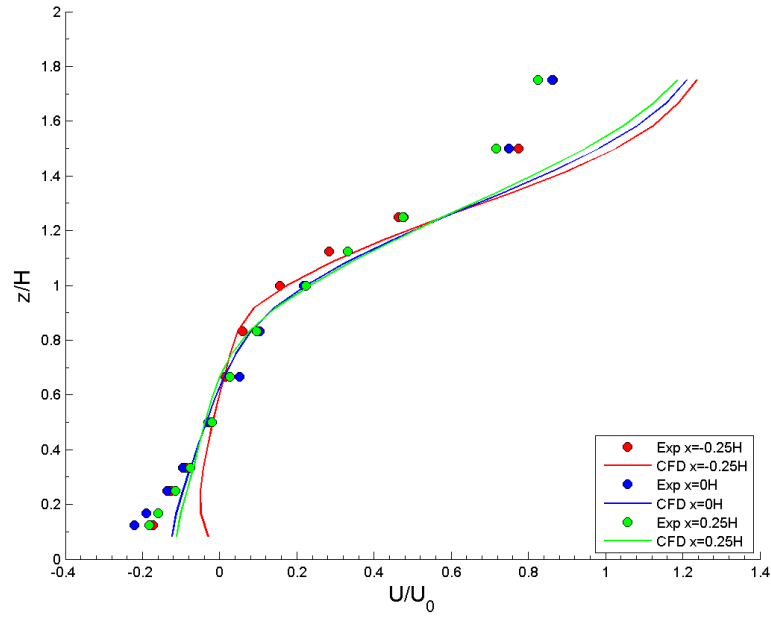


Figure 5.25: Horizontal velocity U on the middle line and on the leeward and windward quarter lines. Solid line: CFD model results for benchmark case 3, and circle: Kastner-Klein's experimental measurements.

As can be seen in Figure 5.12 above, the CFD model predicts very accurate horizontal velocity (U) between $z=0.3H$ and $z=1.3H$. In contrast, the predicted U in benchmark case 1 is only accurate between $z=0.7H$ and $z=1.3H$. Above the height $1.3H$, U is over-predicted due to the difficulty in predicting accurate flow separation above the first building. Below the height $0.3H$, U is under-predicted, which is associated with the inaccurate prediction of the flow pattern (mentioned in the last sub-section) that a stream travels from the leeward bottom corner towards the main vortex flow on the mid vertical plane.

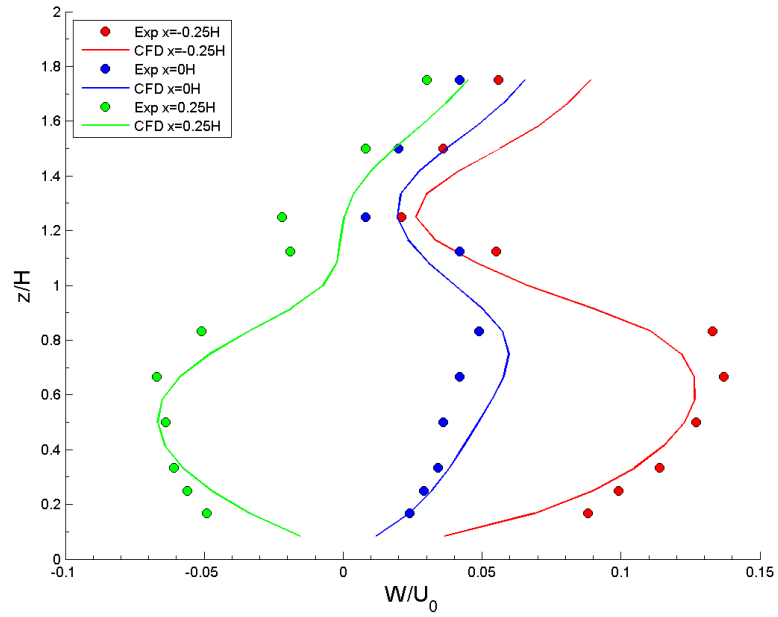


Figure 5.26: Vertical velocity W on the middle line and on the leeward and windward quarter lines. Solid line: CFD model results for benchmark case 3, and circle: Kastner-Klein's experimental measurements.

As shown in Figure 5.26 above, vertical velocity (W) is accurately predicted on all the three lines. This is due to the accurate prediction of the vortex flow pattern, which has been mentioned in the last sub-section. In contrast, W is poorly predicted in benchmark case 1, since the measured and predicted flow patterns for that case are not very consistent.

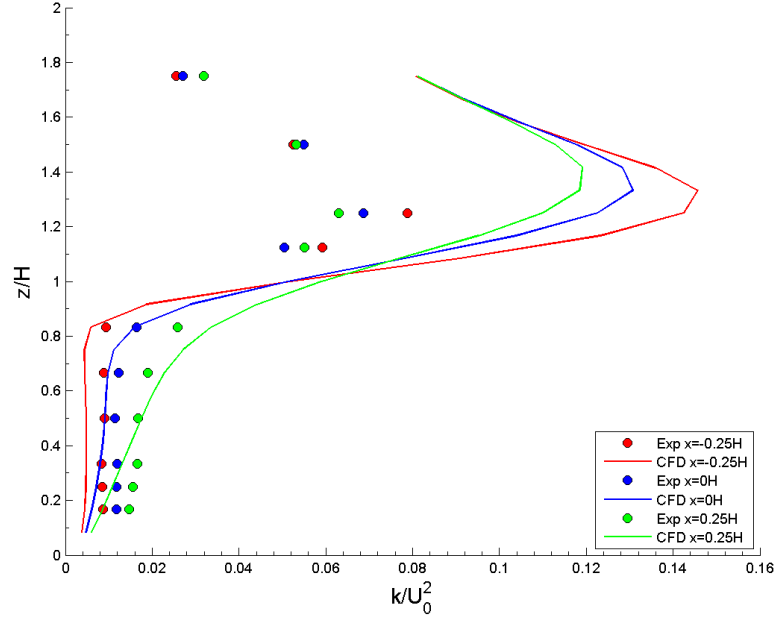
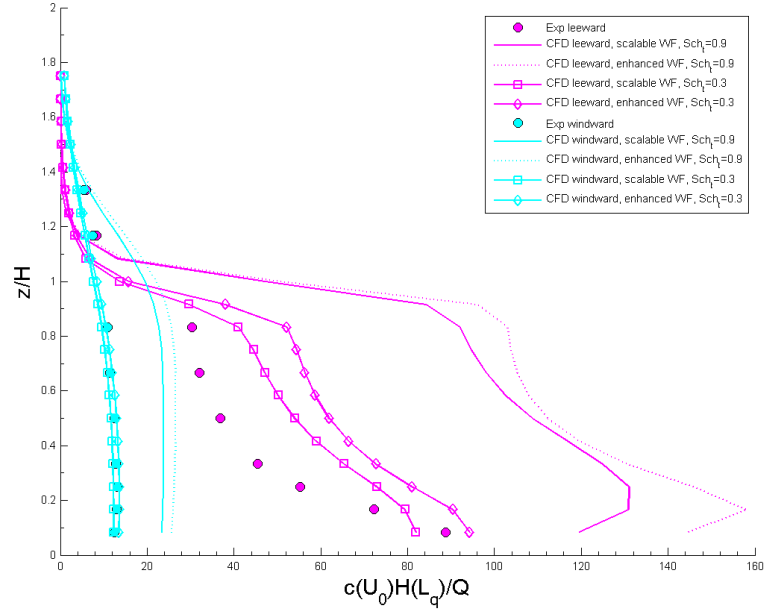
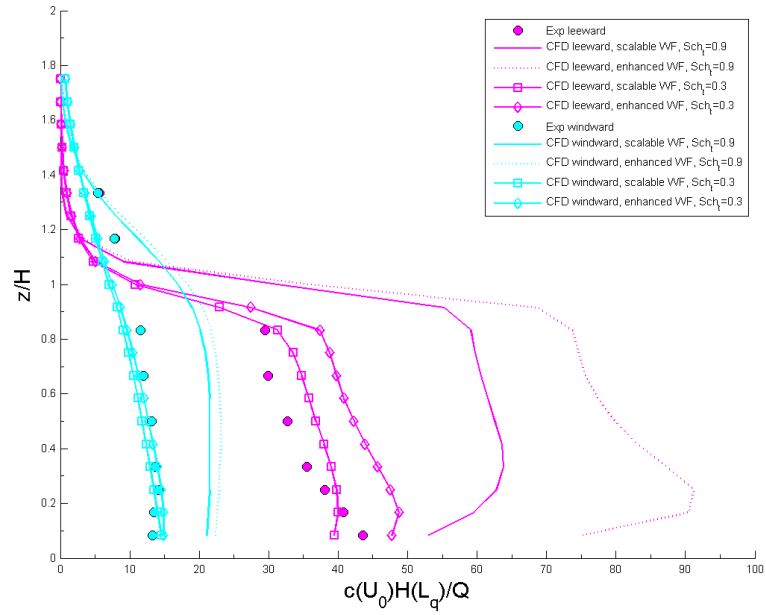


Figure 5.27: Turbulent kinetic energy k on the middle line and on the leeward and windward quarter lines. Solid line: CFD model results for benchmark case 1, and circle: Kastner-Klein's experimental measurements.

Figure 5.27 above shows that the CFD model over-predicts TKE above the roof level, but the over-prediction in this case is less significant than in benchmark case 1 (see Figure 5.14 in Section 5.4.4). The over-predication is also associated with the difficulty in predicting accurate flow separation above the first building. However, it is found from Figure 5.27 that TKE is under-predicted at most positions, which is opposite to the situation for benchmark case 1. Since TKE is over-predicted above the roof level in this case, the under-prediction of TKE in the street must be due to the previous hypothesis (mentioned in Section 5.4.4) that the standard k - ϵ model under-predicts the production of TKE in street canyon. In detail, less excessive TKE from outside is transported into the street in the current case, and the under-predicted production of TKE outweighs the excessive TKE, resulting in the under-prediction of TKE in the street.



(a)



(b)

Figure 5.28: Concentration c on the leeward and windward side lines, (a) Emission case A and (b) Emission case B. Solid line: CFD model results for benchmark case 3, and circle: Kastner-Klein's experimental measurements.

As shown in Figure 5.28 above, concentration is unduly over-predicted on all the positions when using the same turbulent Schmidt number to benchmark case 1 ($Sc_t=0.9$). As the predicted velocity components U and V are even closer to the experimental

measurements in the current case than in benchmark case 1, the only possible reason is about the under-prediction of TKE in the street. The under-prediction of TKE leads to much smaller turbulent diffusion term in the pollutant transport equation. In this circumstance, defining a smaller turbulent Schmidt number is a suitable remedial action to solve the issue. After reducing turbulent Schmidt number from 0.9 to 0.3, which is equivalent to amplify the TKE at every position by a factor of 1.7, it is found the predictions of concentration are greatly improved and are quite close to the measurements (see Figure 5.28). Thus, the turbulent Schmidt number $Sc_t=0.3$ is suitable for modelling pollutant dispersion in benchmark case 3. All the discussion below is based on this value.

According to the concentration profiles in Figure 5.28, the wall function has a significant impact on the predicted concentration on two side lines. The scalable wall function always gives closer predictions to the measurements than the enhanced wall function. This trend is even more conspicuous on the leeward side line (magenta). Thus, the scalable wall function is a better choice for benchmark case 3.

It is observed from Figure 5.28 that the concentrations on the windward side line (cyan) are accurately predicted. On the leeward side line (cyan), concentration is slightly over-predicted above the height $0.2H$ by less than 5 normalized units and slightly under-predicted below the height $0.2H$ by less than 5 normalized units. All these errors are much smaller than those in benchmark case 1.

The only minor problem in this case is that the CFD model predicts a positive concentration gradient below the height $0.2H$ on the leeward side line, but the actual gradient below this height on the same line is negative according to the measurements. This problem is once again because the CFD model predicts an unrealistic stream from the leeward bottom corner towards the main vortex flow on the mid vertical plane.

5.6.5 Assessment of model accuracy

The hit-rate (Q_{hit}) for each profile for benchmark case 3 is given in Table 5.5 below, and the hit-rates lower than 66% are marked by red. These hit-rates are calculated on the basis of the fine mesh, the standard k- ϵ model, the scalable wall function and $Sc_t=0.3$.

As can be noted from Table 5.5, almost all the profiles have a hit-rate above 66%, which indicates that flow properties and concentration are generally accurately predicted in benchmark case 3. Comparing to benchmark case 1 that have 5 out of 13

profiles that have a hit-rate below 66%, the model accuracy for the current case is much better.

In the current case, only the U profile on the leeward quarter line and the c profile on the leeward side line in Emission case A have a hit-rate below 66%. The former low hit-rate is because the predicted U out of the region between $z=0.3H$ and $z=1.3H$ have relatively large differences from the measurements, which can be observed in Figure 5.25 in the last sub-section. The latter low hit-rate is because the predicted c in the region between $z=0.3H$ and $z=0.9H$ have relatively large differences from the measurements, which can be observed in Figure 5.28(a) in the last sub-section.

Quantity, position and figure number	Mean absolute error	Max absolute error	Mean relative error	Max relative error	Hit rate Q_{hit}
U , leeward quarter line (Figure 5.25)	0.051	0.131	44%	76%	63%
U , middle line (Figure 5.25)	0.040	0.103	33%	76%	75%
U , windward quarter line (Figure 5.25)	0.031	0.076	41%	96%	75%
W , leeward quarter line (Figure 5.26)	0.012	0.022	11%	22%	100%
W , middle line (Figure 5.26)	0.007	0.016	19%	38%	100%
W , windward quarter line (Figure 5.26)	0.009	0.017	17%	34%	100%
k , leeward quarter line (Figure 5.27)	0.004	0.004	44%	50%	100%
k , middle line (Figure 5.27)	0.003	0.006	27%	48%	100%
k , windward quarter line (Figure 5.27)	0.004	0.008	25%	42%	100%
c , leeward side line, Emission Case A (Figure 5.28(a))	13.5	20.0	32%	47%	29%
c , windward side line, Emission Case A (Figure 5.28 (a))	0.7	1.4	6%	13%	100%
c , leeward side line, Emission Case B (Figure 5.28 (b))	3.0	4.8	9%	16%	100%
c , windward side line, Emission Case B (Figure 5.28 (b))	1.2	2.5	10%	21%	100%

Table 5.5: Model error statistics for benchmark case 3. $Q_{hit}<66\%$ marked by red.

5.7 Concluding remarks

The main findings of the benchmarking study are summarized below.

The normal mesh, which has 24 cells along the building, is fine enough to obtain mesh independent horizontal velocity and TKE on the middle. This mesh resolution is economic for qualitative study of airflow in street canyon. The fine mesh, which has 36 cells along the building, is necessary to ensure mesh independent vertical velocity and concentration on the middle line. In addition, if any near-wall quantity is of interest, the fine mesh must be used to reduce discretisation error and the uncertainty about the wall function. Thus, the fine mesh is considered to have appropriate mesh resolution for the three benchmark cases.

The standard k- ϵ model predicts reasonable flow patterns and generally accurate flow properties and concentrations for all the three benchmark cases. However, the RNG k- ϵ model predicts wrong flow patterns in the cases with an isolated street canyon (i.e., benchmark cases 1 and 3). Thus, the standard k- ϵ model is considered to be the suitable turbulence model.

Using different wall functions has limited impact on the prediction of concentration in benchmark case 1. However, for benchmark cases 2 and 3, the scalable wall function provides more accurate predictions of concentration in the near-wall positions than the enhanced wall function. Thus, the scalable wall function is considered to be the suitable wall function.

The turbulent Schmidt number $Sc_t=0.9$ is found to correctly model pollutant dispersion in benchmark cases 1 and 2 with 2D geometries. However, the number must be reduced from 0.9 to 0.3 in benchmark cases 3 with 3D geometries, to guarantee reliable predictions of concentration. This modification acts as a remedial action to solve the issue about the under-prediction of TKE in that case.

In benchmark case 1, the CFD model predicts a reasonable vortex flow pattern in the street. However, the position of the predicted vortex centre does not match the actual position observed from the measurements, due to the difficulty in predicting flow separation above the first building. As a result, the predicted velocity profiles, TKE profiles and concentration profiles are reasonable compared to the measurements but are not perfectly accurate. According to the calculated hit-rates, 8 out of 13 profiles are accurately predicted.

In benchmark case 2, the CFD model predicts accurate concentration at all the measuring positions. This statement is supported by the closeness between the measured and the modelled concentration profiles as well as the perfect hit-rates. The excellent accuracy in this case is because the test street is free from the influence of flow separation above the first building.

Compared to the experiment measurements, CFD model predicts more consistent flow pattern and more reliable velocities in benchmark case 3 than in benchmark case 1. This is because benchmark case 3 is modelled by 3D geometries. However, TKE in street canyon is significantly under-predicted in benchmark case 3, due to the difficulty in predicting flow separation above the first building. As a result, the turbulent Schmidt number needs to be reduced, since the modelled TKE gives weaker turbulent diffusion of pollutant than it should be. After reducing the turbulent Schmidt number from 0.9 to 0.3, concentration is accurately predicted at most measuring position. In general, the model accuracy for benchmark case 3 is much better than for benchmark 1, which is reflected by the hit-rate data that 11 out of 13 profiles are accurately predicted.

6 A Parametric Study of Two-dimensional Street Canyons with Pitched Roofs

In the history of studying street canyon flow, most research work assumed that buildings have flat roofs. However, this assumption does not represent real roof structures in many cases, as roofs are usually designed to have slopes for the purpose of draining the rain water.

The effects of roof structure on the surrounding airflow have been attended by some researchers since the 90s. A summary of the relevant literature is made in Section 2.4.4. In the literature, two types of pitched roofs, which have rise-to-run ratios of 8:12 and 12:12, are frequently studied; unique flow patterns are found compared to the corresponding cases with flat roofs. However, the pitched roofs with such sharp slopes are not commonly seen on the buildings adjacent to real street canyons. To extend the understanding of the effects of pitched roofs, this chapter carries out a parametric study of pitched roofs, based on realistic roof structures and systematically varied parameters.

6.1 Model geometry

This chapter models airflow and pollutant dispersion in an idealized urban structure which consists of six rows of building and five consecutive street canyons. The roof structures on these buildings are studied through a parametric approach. In order to avoid any uncertainty from model scale, all the models are built upon full-scale geometries. A sketch of one of the model geometries is shown in Figure 6.1 below. All the buildings are 12m wide and 12m tall up to the eave. Street width is defined as one of the parameters in the current study, but the street widths in the same model are kept as the same.

Two identical line sources are placed on the grounds of the third and the fourth street canyons. Each source is set 1m away from the street centre. The positions of the sources are chosen based on the assumption of two-way traffic and the fact that the pipe-tails of the UK cars are on the right side of their rears. Each source is defined to be 0.3m ($0.025H$) wide, which is sufficiently narrow to model line sources.

The third street canyon is chosen as the test canyon. The flow properties and concentration in this street will be presented and analysed. Apart from the test street, the concentration in the fourth street will also be concerned, in order to understand the combined effect of local emission and non-zero background concentration due to the emission from the upstream test street canyon.

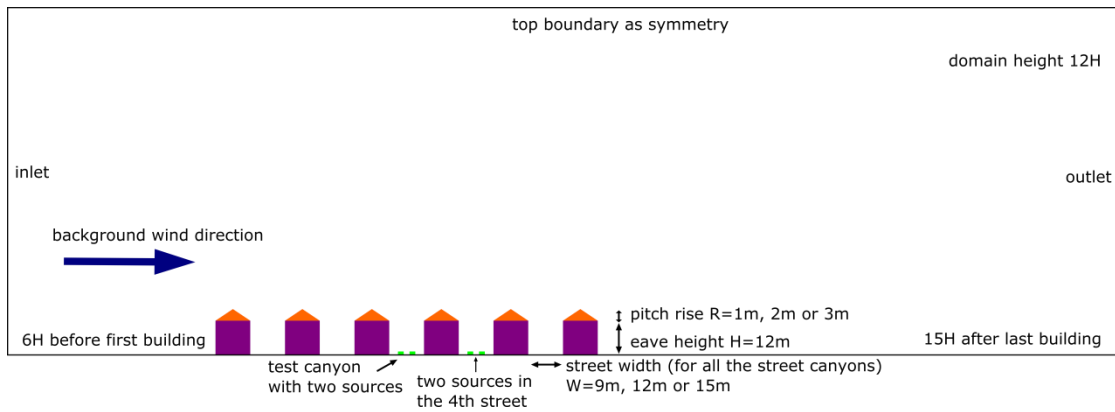


Figure 6.1: A sketch of the computational domain and street canyons for a typical case.

6.2 Parameters and nomination rule

Three parameters are defined in this study.

Parameter 1—**aspect ratio**: The street width is defined to be 9m, 12m, and 15m, whereas the building height is fixed as 12m. Thus, the aspect ratio of building height to street width has three values: AR=0.8, 1.0 and 1.33. It is mentioned again that in any studied case, the five consecutive street canyons have the same aspect ratio.

Parameter 2—**pitch rise**: The pitch rise is defined to be 1m, 2m and 3m, whereas the building width is fixed as 12m. They give three rise-to-run ratios: 2:12, 4:12, and 6:12, which correspond to non-perfect flat roof, low-slope roof and conventional roof respectively (see the classifications in Section 2.4.4). These three pitch rises are named as low rise, medium rise, and high rise. It is mentioned that in any studied case, all the pitched roofs have the same pitch rise. Pitch rise is denoted by the symbol 'R'.

Parameter 3—**roof arrangement**: The roofs on the buildings adjacent to the third street (test street) are defined to be either flat or pitched, whereas all the other roofs are pitched. They give four different roof arrangements.

Pitch rise and roof arrangement are collectively referred to **roof structure** in this study.

Reference cases: Under each aspect ratio, a case with flat roofs on all the buildings is modelled. It is regarded as the reference case, and the results of this case are used for comparison purpose. Since three aspect ratios are studied, there are three reference cases.

Figure 6.2 below illustrates the geometries for a complete group of cases with AR=1.0. These cases are named Cases A to M. In the figure, the four different roof arrangements are distinguished by four different colours. These colours are retained in the data presentation in the following sections.

The naming protocol is also denoted in Figure 6.2. The name of each case is made up of two parts, and they are separated by an underscore. The characters before the underscore indicate roof arrangement; the characters after the underscore indicate pitch rise. For example, for case I: 3P1F2P_R2, 3P1F2P stands for the roof arrangement that has pitched roofs on the first, second and third buildings, a flat roof on the fourth building, pitched roofs on the fifth and sixth buildings; R2 stands for 2m high pitch rise.

A full list of the model cases is given in Table 6.1 below. The table also provides the information about the roofs structures on the buildings adjacent to the third street.

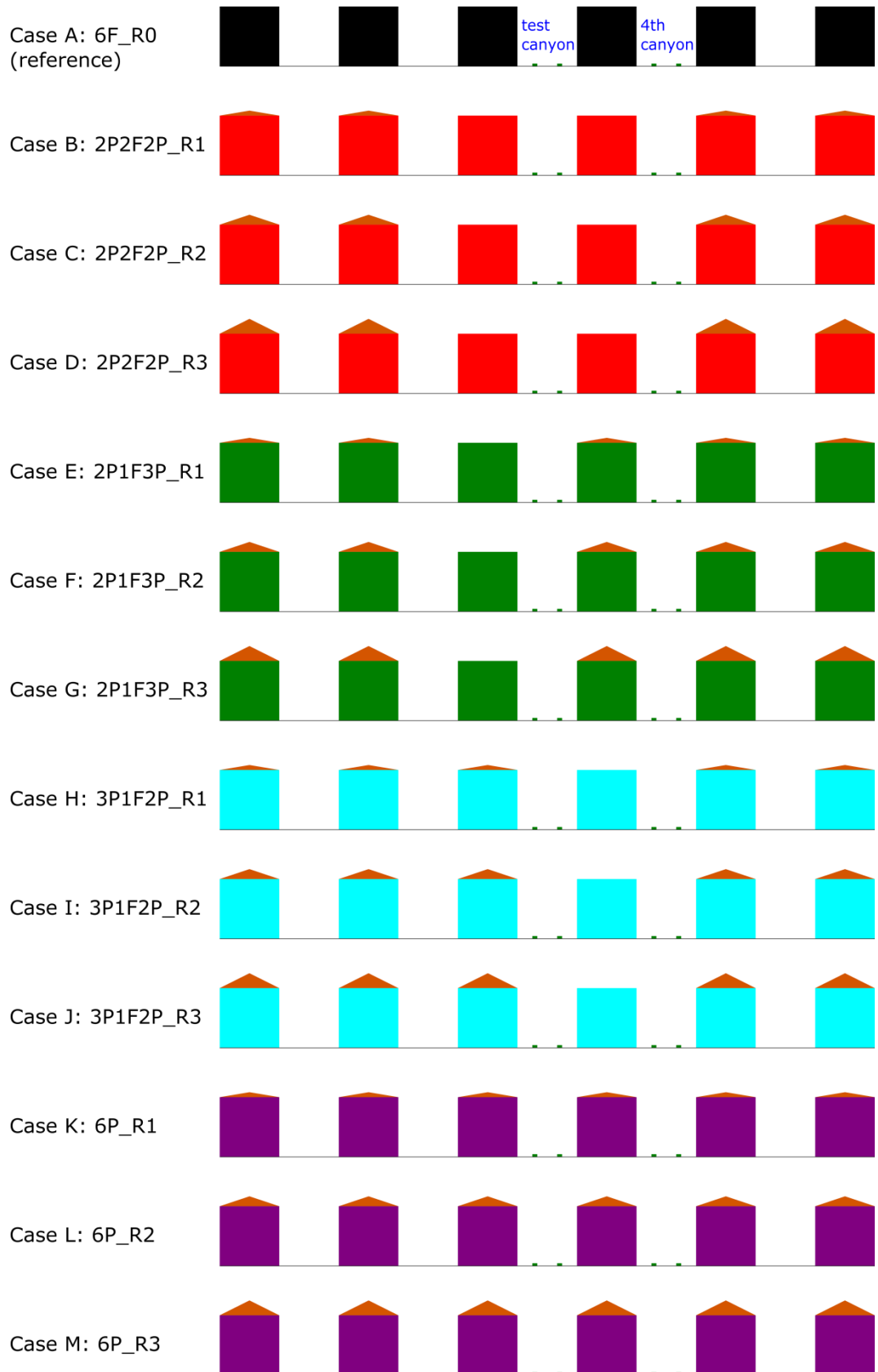


Figure 6.2: A sketch of the geometries of thirteen studied cases, AR=1.0.

Aspect ratio	Roof on the leeward building of the third street	Roof on the windward building of the third street	Case name
0.80	flat for all buildings (reference case)		AR080_6F_R0
	flat	flat	AR080_2P2F2P_R1
	flat	flat	AR080_2P2F2P_R2
	flat	flat	AR080_2P2F2P_R3
	flat	pitched, $R=1\text{m}$	AR080_2P1F3P_R1
	flat	pitched, $R=2\text{m}$	AR080_2P1F3P_R2
	flat	pitched, $R=3\text{m}$	AR080_2P1F3P_R3
	pitched, $R=1\text{m}$	flat	AR080_3P1F2P_R1
	pitched, $R=2\text{m}$	flat	AR080_3P1F2P_R2
	pitched, $R=3\text{m}$	flat	AR080_3P1F2P_R3
	pitched, $R=1\text{m}$	pitched, $R=1\text{m}$	AR080_6P_R1
	pitched, $R=2\text{m}$	pitched, $R=2\text{m}$	AR080_6P_R2
	pitched, $R=3\text{m}$	pitched, $R=3\text{m}$	AR080_6P_R3
1.00	flat for all buildings (reference case)		AR100_6F_R0 (Case A)
	flat	flat	AR100_2P2F2P_R1 (Case B)
	flat	flat	AR100_2P2F2P_R2 (Case C)
	flat	flat	AR100_2P2F2P_R3 (Case D)
	flat	pitched, $R=1\text{m}$	AR100_2P1F3P_R1 (Case E)
	flat	pitched, $R=2\text{m}$	AR100_2P1F3P_R2 (Case F)
	flat	pitched, $R=3\text{m}$	AR100_2P1F3P_R3 (Case G)
	pitched, $R=1\text{m}$	flat	AR100_3P1F2P_R1 (Case H)
	pitched, $R=2\text{m}$	flat	AR100_3P1F2P_R2 (Case I)
	pitched, $R=3\text{m}$	flat	AR100_3P1F2P_R3 (Case J)
	pitched, $R=1\text{m}$	pitched, $R=1\text{m}$	AR100_6P_R1 (Case K)
	pitched, $R=2\text{m}$	pitched, $R=2\text{m}$	AR100_6P_R2 (Case L)
	pitched, $R=3\text{m}$	pitched, $R=3\text{m}$	AR100_6P_R3 (Case M)
1.33	flat for all buildings (reference case)		AR133_6F_R0
	flat	flat	AR133_2P2F2P_R1
	flat	flat	AR133_2P2F2P_R2
	flat	flat	AR133_2P2F2P_R3
	flat	pitched, $R=1\text{m}$	AR133_2P1F3P_R1
	flat	pitched, $R=2\text{m}$	AR133_2P1F3P_R2
	flat	pitched, $R=3\text{m}$	AR133_2P1F3P_R3
	pitched, $R=1\text{m}$	flat	AR133_3P1F2P_R1
	pitched, $R=2\text{m}$	flat	AR133_3P1F2P_R2
	pitched, $R=3\text{m}$	flat	AR133_3P1F2P_R3
	pitched, $R=1\text{m}$	pitched, $R=1\text{m}$	AR133_6P_R1
	pitched, $R=2\text{m}$	pitched, $R=2\text{m}$	AR133_6P_R2
	pitched, $R=3\text{m}$	pitched, $R=3\text{m}$	AR133_6P_R3

Table 6.1: Full list of the model cases and the roof structures on the buildings adjacent to the third street.

6.3 CFD modelling settings

All the CFD models in this chapter are modelled by 2D geometries. Following the appropriate settings found in the last section, more than 36 cells are set along the building; the standard k- ϵ model is used for modelling turbulence; the scalable is used for modelling near-wall flow; the turbulent Schmidt number $Sc_t=0.9$ is used for modelling pollutant dispersion.

The specification of boundary condition follows the COST best practice guideline (Franke et al., 2007) and the AIJ guidelines (Tominaga et al., 2008) mentioned in Section 4.4. The boundary types and boundary positions are shown in Figure 6.1 at the beginning this chapter.

The specification of velocity information on inlet boundary is according to the prototype of the wind profile in Kastner-Klein's experiment. The full-scale prototype is described by a power-law profile. It has the reference velocity $U_{ref}=7.7\text{m/s}$ at the reference height $z_{ref}=72\text{m}$ and the power-law index $\alpha=0.18$ (Kastner-Klein, 1999). The displacement height is ignored, giving the profile as Equation 6.1. It should be mentioned that scaling the profile by a factor of 1/150 and modifying the power-law index from 0.18 to 0.23 give the velocity profile for the inlet boundary used in the benchmark study.

The TKE and dissipation information in the prototype is not given by Kastner-Klein. Thus, their profiles on the inlet boundary are defined as Equations 6.2 and 6.3, which are suitable for describing turbulence information in the atmospheric boundary layer (discussed before in Section 4.4.3).

$$U = U_{ref} \left(\frac{z}{z_{ref}} \right)^\alpha \quad (6.1)$$

$$k = \left[0.1 U \left(\frac{z}{z_{ref}} \right)^{-\alpha-0.05} \right]^2 \quad (6.2)$$

$$\epsilon = C_\mu^{1/2} k \frac{U_{ref}}{z_{ref}} \alpha \left(\frac{z}{z_{ref}} \right)^{\alpha-1} \quad (6.3)$$

6.4 Results and Analyses

This section discusses and analyses the model results. Section 6.4.1 presents the flow patterns around the test street for six typical cases and analyses how the three parameters affect the flow patterns. Section 6.4.2 presents velocity and TKE profiles on three vertical lines and investigates the impacts of the three parameters on these flow properties. Section 6.4.3 presents concentration data in several ways and compares the data between the cases with pitched roofs and the reference case. Sections 6.4.4 and 6.4.5 propose several bulk parameters to assess ventilation efficiency and pollutant removal performance respectively. Amongst the five sub-sections, Section 6.4.2 and 6.4.3 are based on the results for a group of cases with $AR=1.0$, and the other sub-sections are based on the results for all the cases.

All the results in this section are shown in normalized forms. Velocity components and TKE are normalized by the free-stream velocity $U_0=7\text{m/s}$. The normalisation of concentration follows the same approach used in the benchmark chapter, which is given in Equation 6.4. However, the values of the quantities used for normalisation are different from before.

$$c^* = \frac{cU_0H}{Q/L_q} \quad (6.4)$$

with free-stream velocity $U_0=7\text{m/s}$, building height $H=12\text{m}$, and emission rate divided by source length $Q/L_q=2.4\times 10^5\text{g/m}\cdot\text{s}$.

6.4.1 The effect of aspect ratio and roof structure on flow pattern

The flow patterns for six typical cases are illustrated by combined velocity vectors and velocity magnitude contour in Figure 6.3 below. These cases are chosen to show the most different flow patterns amongst all the cases.

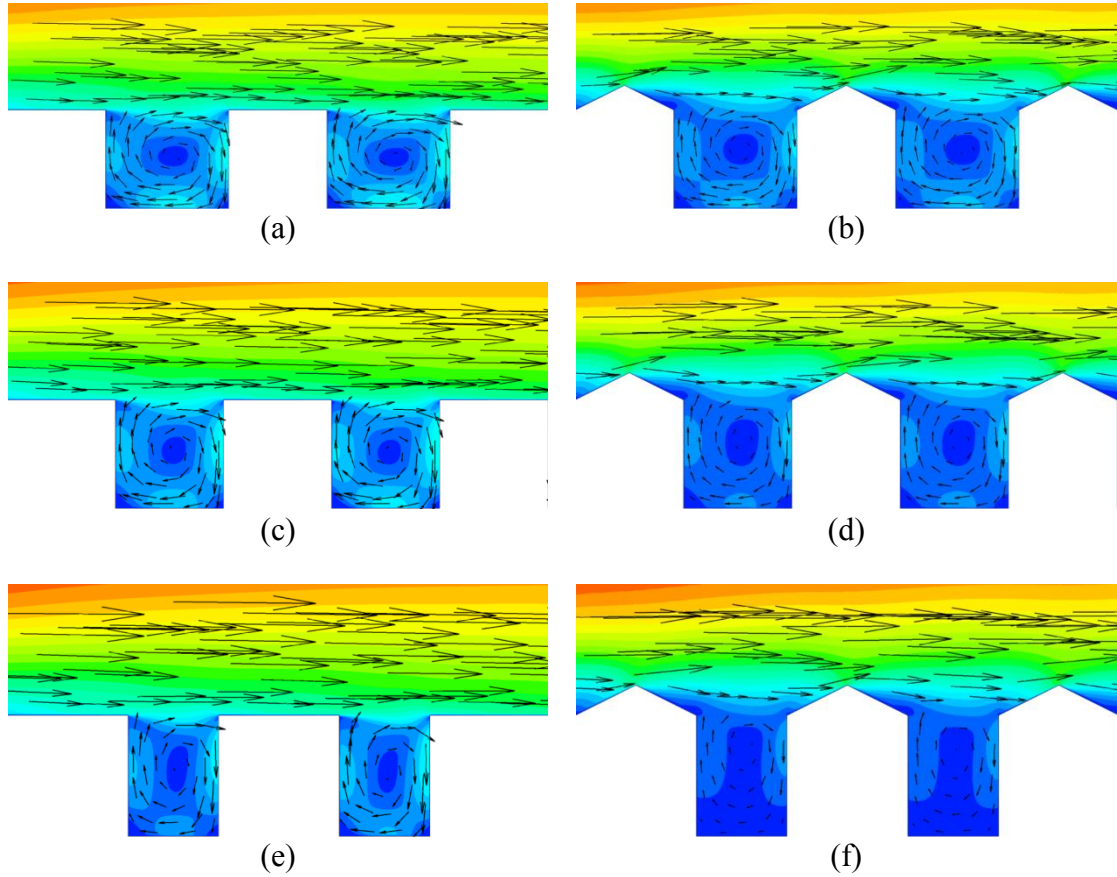


Figure 6.3: The flow patterns in the third (test) and the fourth street canyons: (a) AR080_6F_R0, (b) AR080_6P_R3, (c) AR100_6F_R0 (case A), (d) AR100_6P_R3 (case M), (e) AR133_6F_R0, and (f) AR133_6P_R3.

As can be seen in Figure 6.3, vortex flow forms in each street canyon in all the six cases. These flow patterns are very different from the patterns given in the literature that double-vortex flow forms when rise-to-run ratio is 12:12 and vortex flow disappears when rise-to-run ratio is 8:12 (mentioned in Section 2.4.4). The lower rise-to-run ratios (up to 6:12) in the current study are the main reason for the differences. In the current study, vortex shape is mainly determined by aspect ratio. The increase of aspect ratio leads to the compression of vortex shape in the horizontal direction. Moreover, the increase of aspect ratio is responsible for the decrease of wind speed in the street, which is reflect by the bigger dark blue area (standing for velocity magnitude below 0.7m/s) in the deeper street in Figure 6.3.

According to Figure 6.3, roof structure has secondary effects on the vortex flow. The pitched roofs with a rise of 3m ($R=3m$) disturbs airflow above the roof level, whereas in the cases with flat roofs, the flow above the roof level is almost parallel to the ground. Moreover, the pitched roofs make the vortex flow slightly extend above the street, as typically observed in a slightly deeper street canyon with flat-roof buildings. Thus, the presence of pitched roofs is regarded as equivalent to increase aspect ratio. Compared to flat roofs, the pitched roofs also decrease wind speed in the street. The decrement is noticeable around the vortex centre and near the ground, and the decrement is more significant for the deeper street as indicated in Figure 6.3(f).

6.4.2 The effect of roof structure on flow properties

This section focuses on comparing flow properties between the cases with $AR=1.0$, in order to quantify the impacts of different roof structures. Horizontal velocity (U), vertical velocity (W) and TKE (k) are extracted from three vertical lines, whose positions are shown in Figure 6.4 below. The profiles of these flow properties are plotted in Figure 6.5, Figure 6.6, Figure 6.7, Figure 6.8 and Figure 6.9 below.

In the five figures, the cases with the same pitch rise are assigned to the same line style; the cases with the same roof arrangement are assigned to the same colour. In detail, the solid lines denote the cases with a high pitch rise; the dot lines denote the cases with a medium pitch rise; the dash lines denote the cases with a low pitch rise. The four roof arrangements—2P2F2P, 2P1F3P, 3P1F2P and 6P—are denoted by red, green, cyan and purple respectively, which follows the colour scheme in Figure 6.2 in Section 6.3. The reference profiles in these figures are marked by black solid dots.

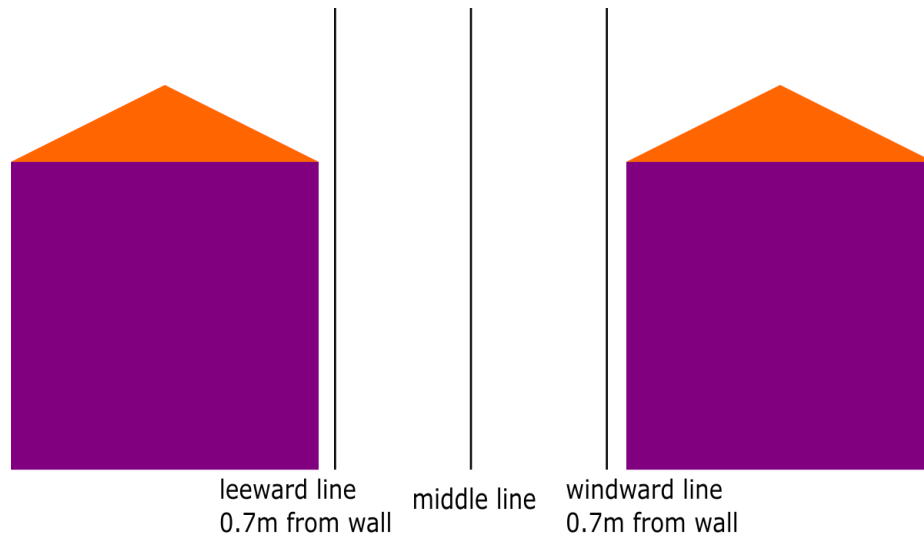


Figure 6.4: Three vertical lines in the test canyon for plotting flow properties.

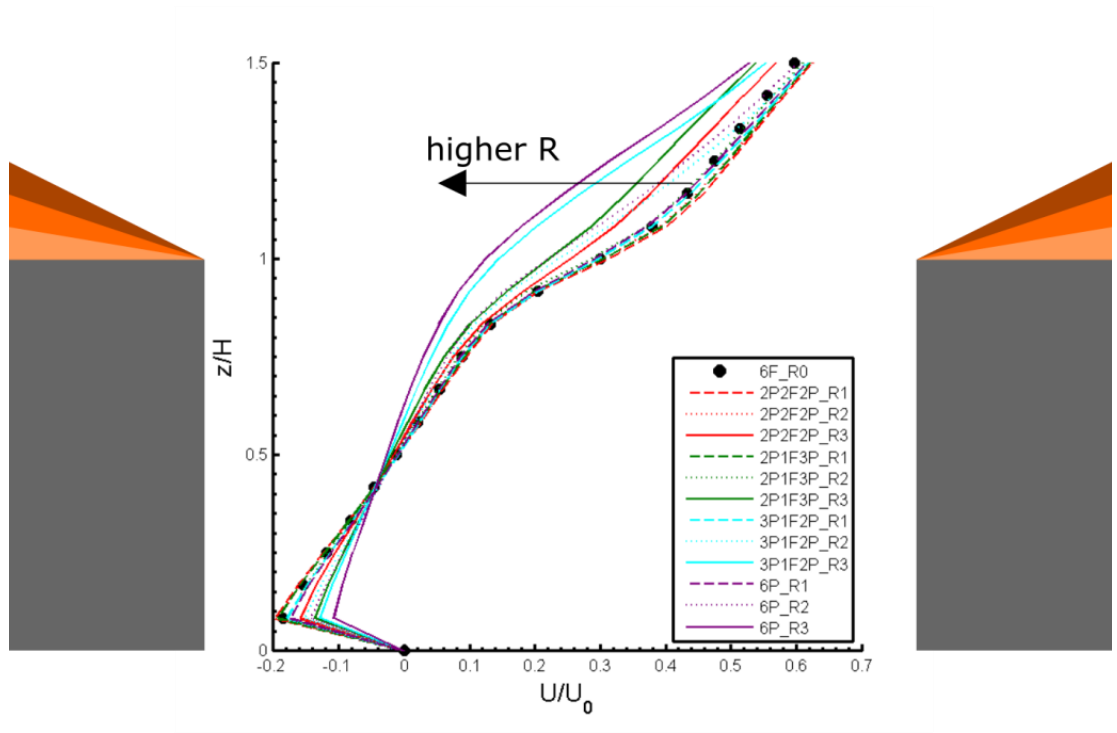


Figure 6.5: Horizontal velocity U on the middle line for Cases A to M.

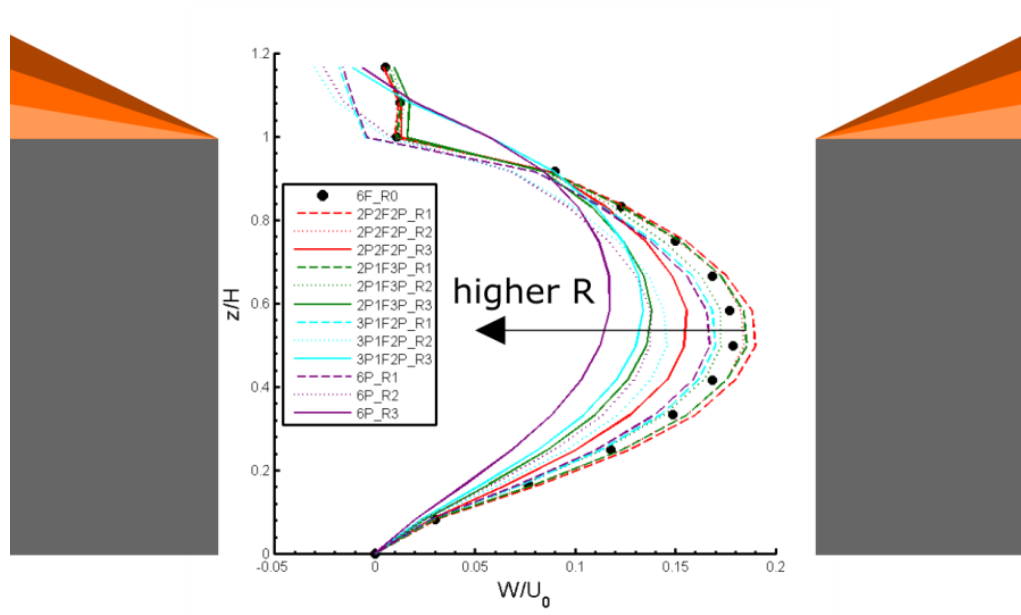


Figure 6.6: Vertical velocity W on the leeward side line for Cases A to M.

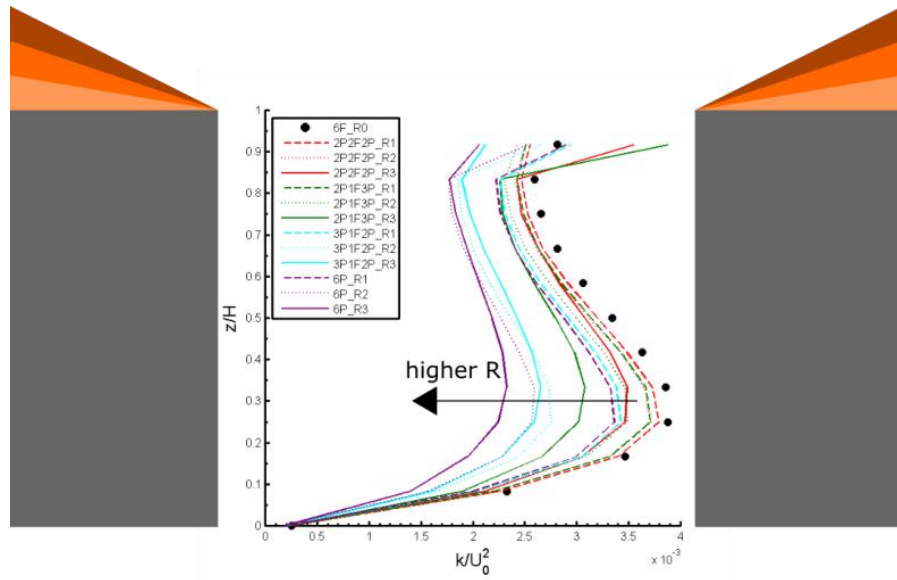


Figure 6.7: Turbulent kinetic energy k on the leeward side line for Cases A to M.

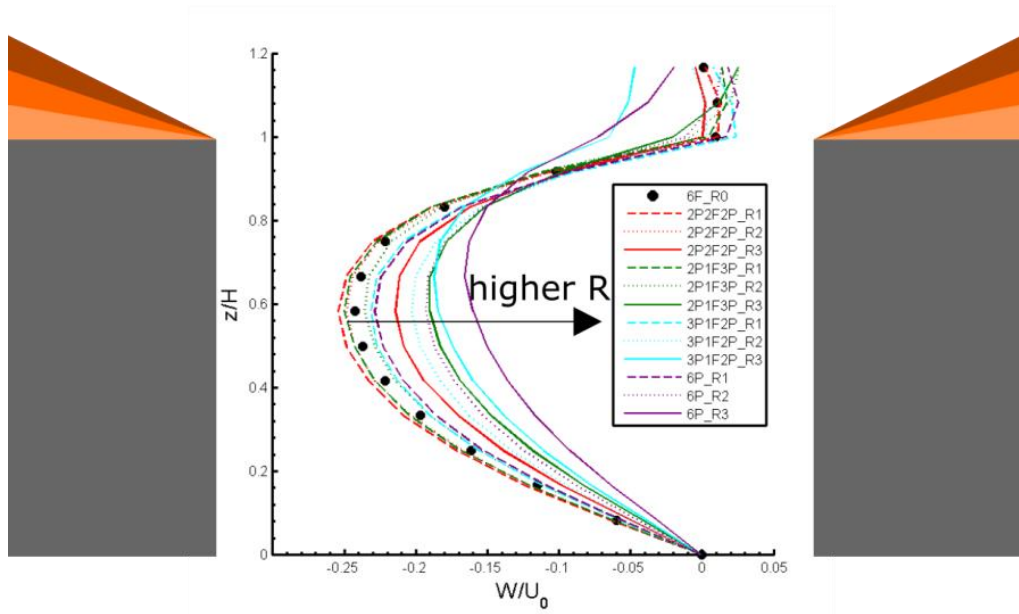


Figure 6.8: Vertical velocity W on the windward side line for Cases A to M.

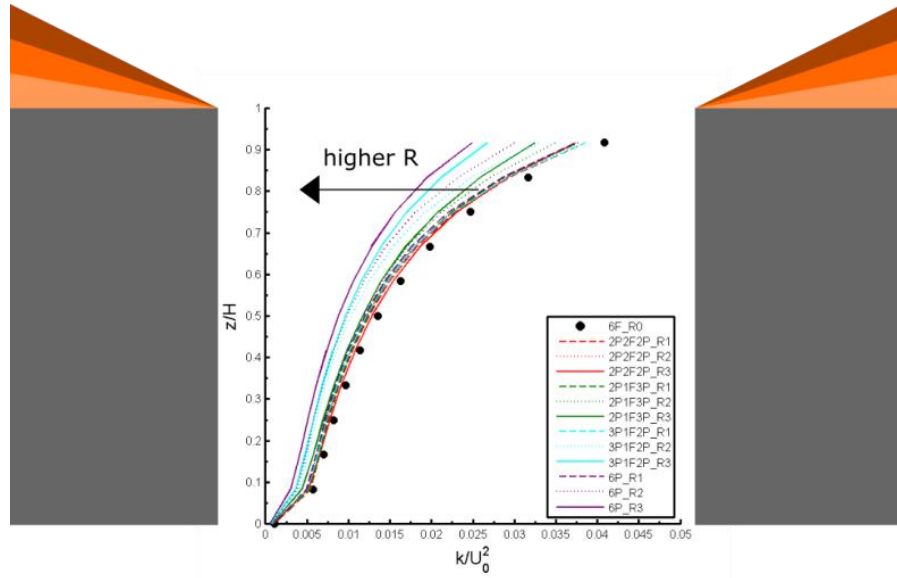


Figure 6.9: Turbulent kinetic energy k on the windward side line for Cases A to M.

6.4.2.1 Pitch rise

As can be seen in Figure 6.5 above, the cases with high pitch rise ($R=3\text{m}$, solid lines) have much smaller horizontal velocities above the street than the reference case, regardless of the detailed roof arrangements. On the other hand, the cases with low pitch rise ($R=1\text{m}$, dash lines) have similar profiles above the street to the reference case.

The impact of pitch rise on the mean flow in the street is analysed by comparing the horizontal velocity (U) profiles in Figure 6.5 above and the vertical velocity (W) profiles in Figure 6.6 and Figure 6.8 above. As can be observed in these figures, most cases have a smaller U profile and smaller W profiles than the reference case. According to this finding, it is claimed that pitched roofs weaken mean flow strength in street canyon whatever detailed roof structure is.

For a given roof arrangement, the four cases with high pitch rise have the smallest magnitudes of U and W in the street. In terms of U , the difference between these cases and the reference case is up to 45%, which happens near the ground and near the roof level. In terms of V , the difference between these cases and the reference case is up to 40%, which happens at the height $z=0.5H$.

After reviewing the TKE (k) profiles in Figure 6.7 and Figure 6.9 above, it is noted that the presence of pitched roofs always contributes to a reduction of k on both leeward and windward sides from the reference, which happens at the height $z=0.3H$ for the leeward side and near the roof level for the windward side. In addition, for a fixed roof

arrangement, it is found that higher pitch rise always leads even lower k in the street canyon.

6.4.2.2 Roof arrangement

Apart from the effect of pitch rise, roof arrangement also has significant impacts on the flow properties. As can be observed from the profiles in Figure 6.5 to Figure 6.9, for a fixed pitch rise, the magnitudes of U , V , and k all become larger with this order of roof arrangement '6P→3P1F2P→2P1F3P→2P2F2P→6F', which is schematically shown in Figure 6.10 below. In addition, this trend is even more apparent in the four cases with high pitch rise ($R=3\text{m}$).

After reviewing the order in Figure 6.10, it is believed that both the pitched roof on the leeward building and the pitched roof on the windward building have an effect in weakening airflow and turbulence in the street. This explains why the roof arrangement 6P is at the bottom of the order. Moreover, the pitched roof on the leeward building make a more significant effect than the pitched roof on the windward building. This explains why the roof arrangement 3P1F2P is below the roof arrangement 2P1F3P in the order.

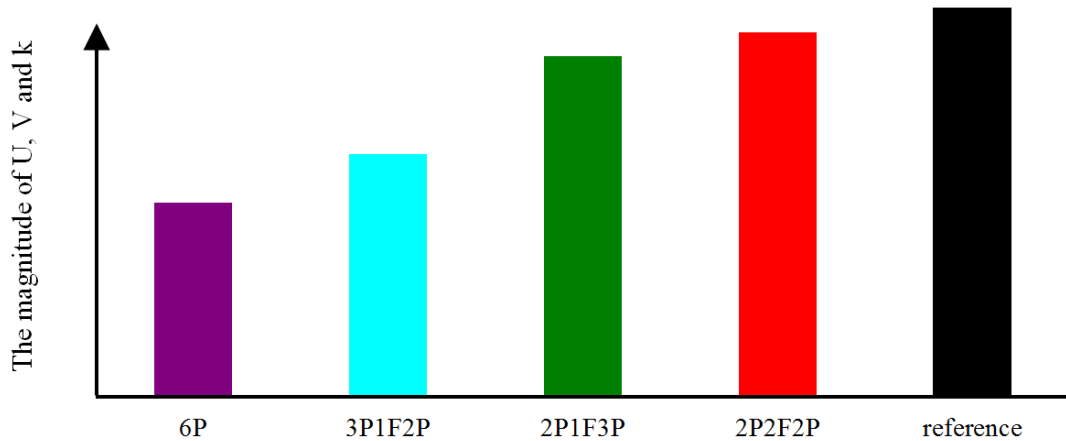


Figure 6.10: Schematic diagram of the relationship between flow properties and roof arrangement

6.4.2.3 Special cases

Cases J and M are two special cases, as they have a 3m pitched roof on the leeward building. They not only have the lowest velocities and TKE throughout the street canyon, but also have different velocity profiles from the others. For example, as can be seen in Figure 6.6 and Figure 6.8 above, all the other cases show sudden changes of

vertical velocity profiles at the roof level, indicating a demarcation of the vortex flow in the street and the horizontal flow above the roof level; however, Cases J and M have smooth vertical velocity profiles from the ground to the height $z=1.2H$. This difference suggests that the vortex flow in Cases J and M extends above the roof level, whereas the vortex flow in the other cases is below the roof level. They have already been revealed in Figure 6.3 in Section 6.4.1.

6.4.3 The effect of roof structure on concentration

This section compares pollutant concentration between the reference case (i.e., Case A) and the other twelve cases (i.e., Cases B–M). Contour plot is used to show concentration distribution across the street. In order to illustrate the deviation from the reference case, the contour is plotted as the ratio of the concentration in that case to the concentration in the reference case. The concentration contours for the third street canyon are shown in Figure 6.11 below, and the concentration contours for the fourth street canyon are shown in Figure 6.12 below. The deviation range in each contour is clipped between 0.5 and 1.5. Values out of this clipped range are given the same colour for the upper limit or the lower limit.

6.4.3.1 The 3rd street canyon

The discussion in this section is focused on the concentration in the third street canyon and is based on the concentration contours in Figure 6.11 below.

The contours for Cases B–D are similar to those for Cases E–G respectively; the contours for Cases H–J are similar to those for Cases K–M respectively. The former two groups of cases are characterized by the roof arrangements 2P2F2P and 2P1F3P respectively, which all have a flat roof on the leeward building; the latter two groups of cases characterized by the roof arrangements 3P1F2P and 6P respectively, which all have a pitched roof on the leeward building. This finding indicates that roof shape on the leeward building has a major effect on pollutant dispersion in street canyon, while roof shape on the windward building only has a minor effect.

In the cases with low pitch rise ($R=1\text{m}$, Cases B, E, H and K), concentration is higher compared to the reference case at almost all the positions of the street. The deviation of concentration from the reference is typically around +10% and is slightly larger in the windward part than in the leeward part. The small deviation is because the low pitch rise produces comparable mean flow to the reference case but weaker turbulence, as pointed out in the last section.

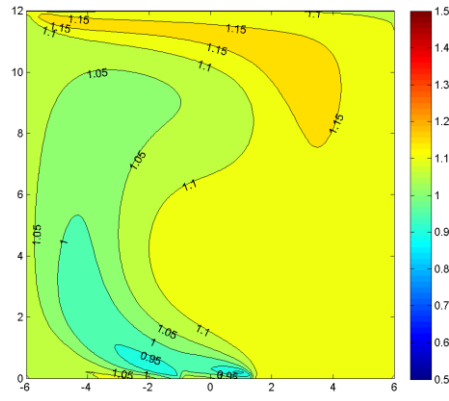
In the cases with medium pitch rise ($R=2\text{m}$, Cases C, F, I and L), concentration is also higher compared to the reference case at almost all the positions. This can be explained by the same reason for the small deviation in the last paragraph. However, the deviation of concentration from the reference is different between the cases. In Cases C and F which have a flat roof on the leeward building, the deviation is typically around +20% and is relatively uniform across the street. The relatively large deviation is because the

pitched roof with medium rise on the leeward building produces weaker mean and weaker turbulence than the reference case, which can be found in Figure 6.5 to Figure 6.9 in the last section.

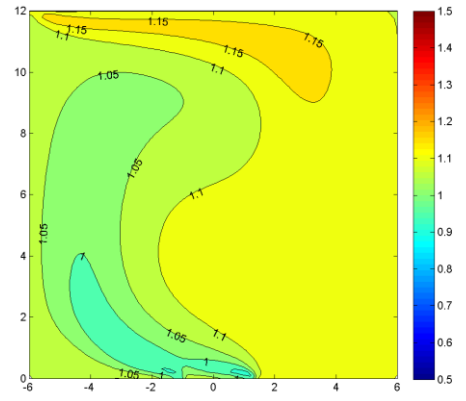
When pitch rise is high ($R=3m$, Cases D, G, J and M), severe aggravation of concentration is found near the two emission sources as well as in the lower half of the leeward part. In these regions, the deviation of concentration for Cases D, G, J and M (from the reference) is up to +20%, +35%, +45% and +70% respectively. The root cause of this aggravation is that the high pitch rise leads to much lower horizontal velocity near the ground (see Figure 6.5 in Section 6.4.2), much lower vertical velocity near the leeward building (see Figure 6.6 in Section 6.4.2) and lower TKE in the street, compared to the reference case and the cases with low or medium pitch rise.

The severe aggravation of concentration means that more pollutants accumulate in the leeward part and at the ground, and fewer pollutants are brought to the roof level. As a consequence, fewer pollutants are entrained into the street from the windward roof corner, and the concentration in the windward part is decreased by around -10% in the four cases with high pitch rise. Nevertheless, the amelioration in the windward does not counterbalance the aggravation in the leeward part.

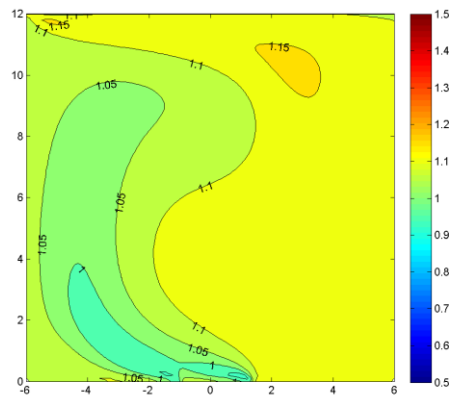
As can be seen in Figure 6.11(j) and (m), severe aggravation of concentration at the roof level only happens in Cases J and M, which are the two special cases mentioned before in Section 6.4.2.3. This is because the vortex flow in these two cases extends above the roof level, which does not happen in the other cases. In detail, the extended vortex brings more pollutants to the roof level and makes concentration comparable between at the roof level and in the street.



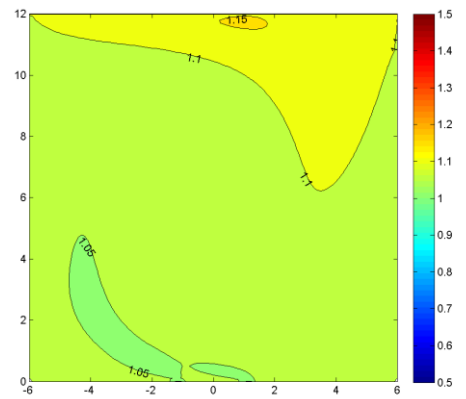
(b)Case B: AR100_2P2F2P_R1, the 3rd street canyon



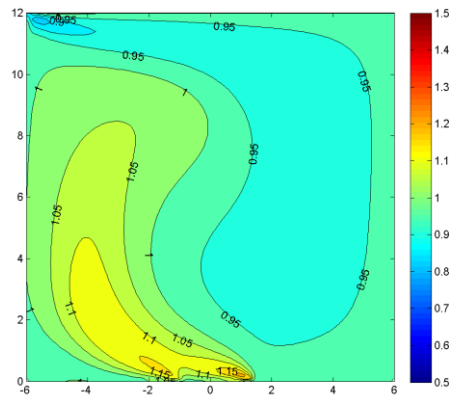
(e)Case E: AR100_2P1F3P_R1, the 3rd street canyon



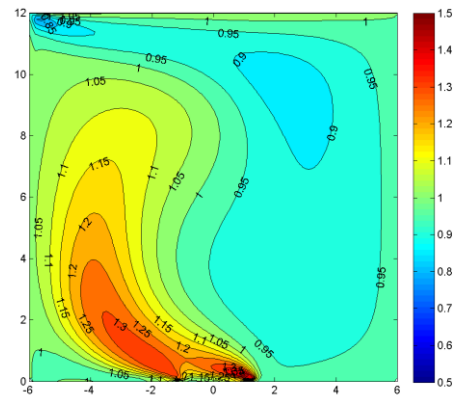
(c)Case C: AR100_2P2F2P_R2, the 3rd street canyon



(f)Case F: AR100_2P1F3P_R2, the 3rd street canyon

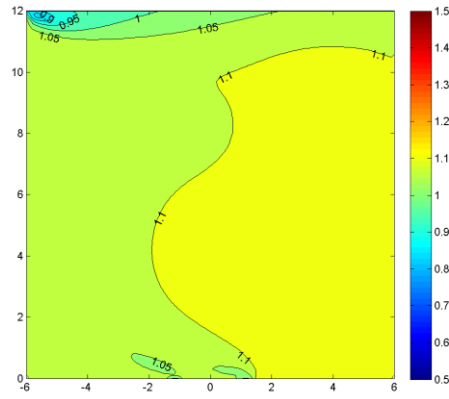


(d)Case D: AR100_2P2F2P_R3, the 3rd street canyon

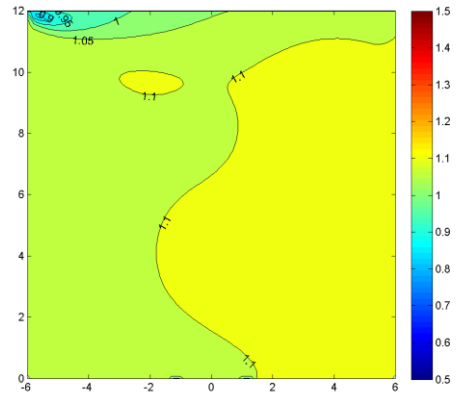


(g)Case G: AR100_2P1F3P_R3, the 3rd street canyon

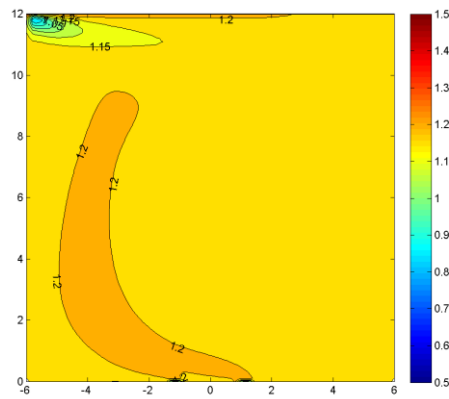
Figure 6.11 (b)–(g): The deviation of concentration from the reference case, cases B–G, the third street canyon.



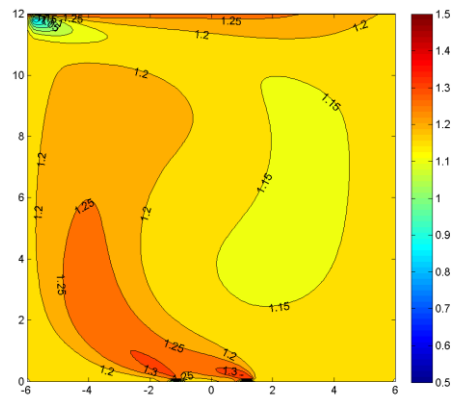
(h)Case H: AR100_3P1F2P_R1, the 3rd street canyon



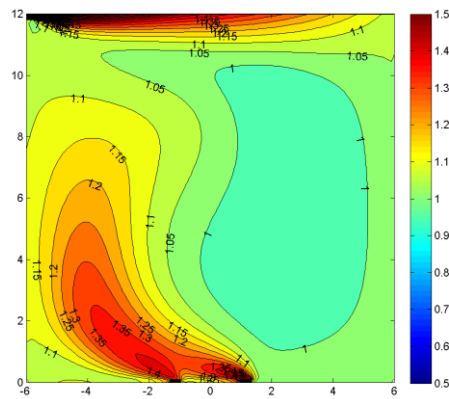
(k)Case K: AR100_6P_R1, the 3rd street canyon



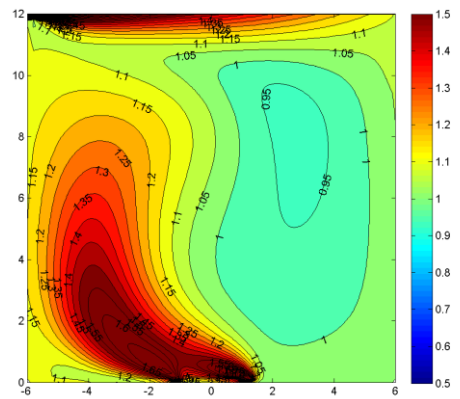
(i)Case I: AR100_3P1F2P_R2, the 3rd street canyon



(l)Case L: AR100_6P_R2, the 3rd street canyon



(j)Case J: AR100_3P1F2P_R3, the 3rd street canyon



(m)Case M: AR100_6P_R3, the 3rd street canyon

Figure 6.11 (h)–(m): The deviation of concentration from the reference case, cases H–M, the third street canyon.

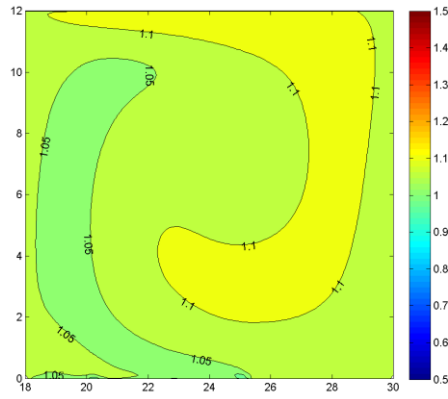
6.4.3.2 The 4th street canyon

The discussion in this section is focused on the concentration in the fourth street canyon and is based on the concentration contours in Figure 6.12 below.

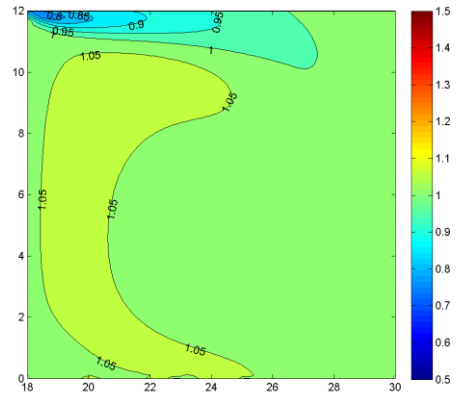
The contours for Cases B–D are similar to those for Cases H–J respectively; the contours for Cases E–G are similar to those for Cases K–M respectively. These similarities for the fourth street seem not the same as the similarities for the third street found in the last sub-section. However, comparing local geometries between the third street and the fourth street, the two categories of similarities are fundamentally same. Cases B–D and Cases H–J all have a flat roof on the leeward building for the fourth street, and Cases E–G and Cases K–M have the same pitched roof on the leeward building for the fourth street. They are also explained by the previous finding that roof shape on the leeward building has a major effect on pollutant dispersion in street canyon, and the leeward building is with respect to the fourth street canyon in this sub-section but the third street canyon in the last sub-section.

In the cases with low pitch rise (Cases B, E, H and K) and two of the cases with medium pitch rise (Cases C and I), the concentrations are higher compared to the reference case at almost all the positions, which is similar to the situation for the third street. However, the deviation of concentration from the reference is typically around +5%, which is less than the typical deviation for the third street (+10%).

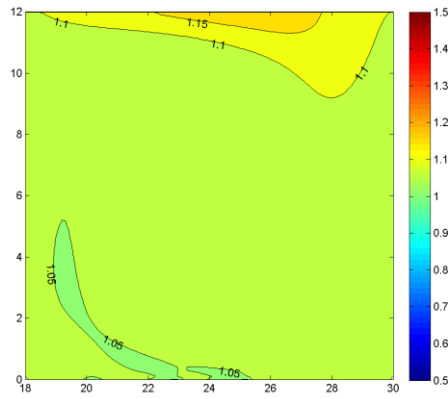
In the cases with high pitch rise (Cases D, G, J and M) and two of the cases with medium pitch rise (Cases F and L), severe aggravation of concentration is also found near the two emission sources and in the lower half of the leeward part. However, for the fourth street canyon, the amelioration in the windward part is more significant than for the third street, which is up -30% (i.e., 30% less concentration compared to the reference). Owing to the great amelioration, it is possible to have lower overall concentration in the six cases than in the reference case, which will be checked later in Section 6.4.5.



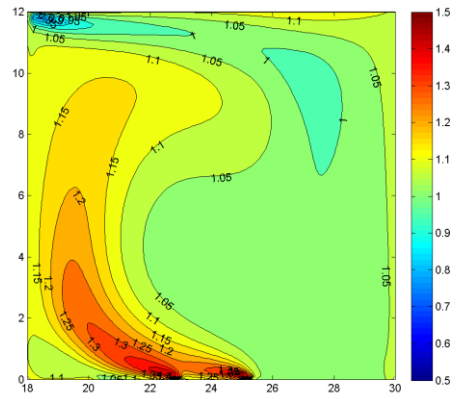
(b)Case B: AR100_2P2F2P_R1, the 4th street canyon



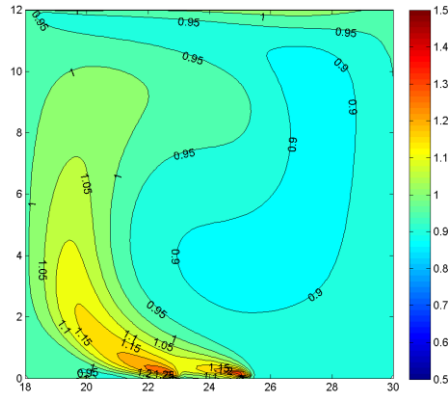
(e)Case E: AR100_2P1F3P_R1, the 4th street canyon



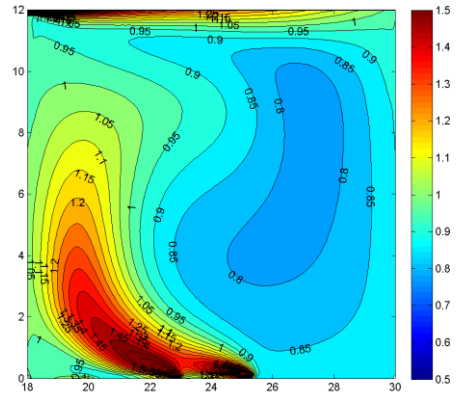
(c)Case C: AR100_2P2F2P_R2, the 4th street canyon



(f)Case F: AR100_2P1F3P_R2, the 4th street canyon

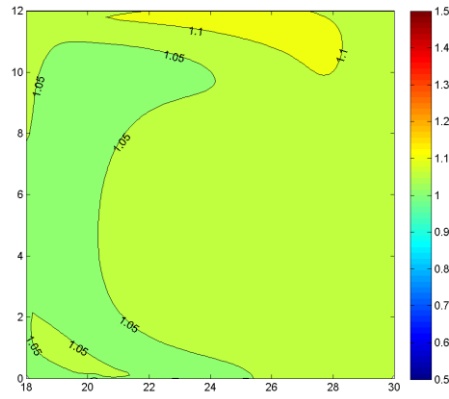


(d)Case D: AR100_2P2F2P_R3, the 4th street canyon

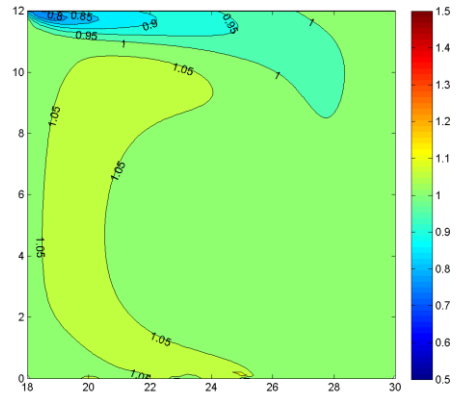


(g)Case G: AR100_2P1F3P_R3, the 4th street canyon

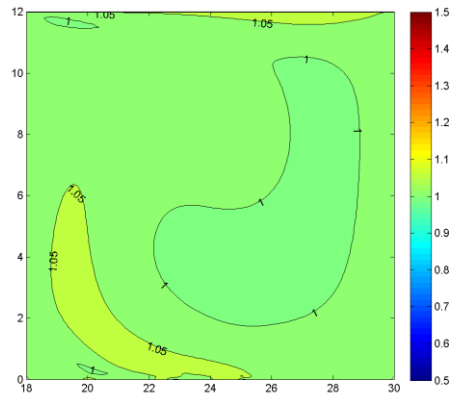
Figure 6.12 (b)–(g): The deviation of concentration from the reference case, cases B–G, the fourth street canyon.



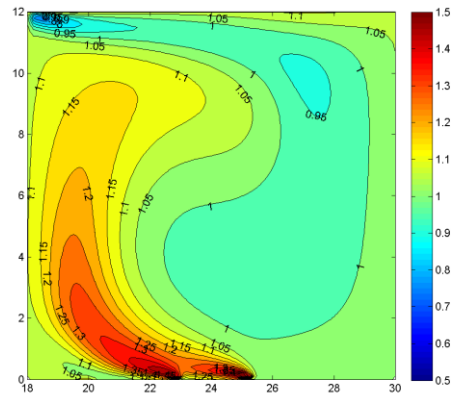
(h)Case H: AR100_3P1F2P_R1, the 4th street canyon



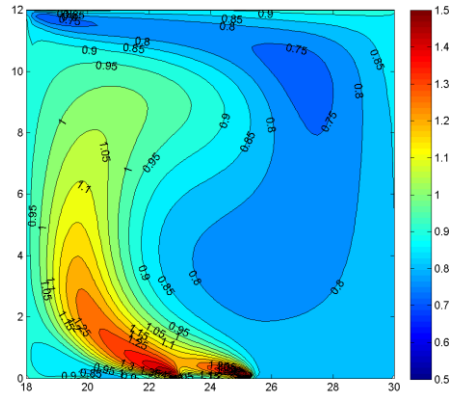
(k)Case K: AR100_6P_R1, the 4th street canyon



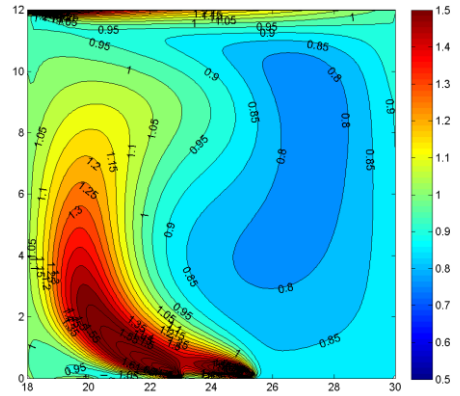
(i)Case I: AR100_3P1F2P_R2, the 4th street canyon



(l)Case L: AR100_6P_R2, the 4th street canyon



(j)Case J: AR100_3P1F2P_R3, the 4th street canyon



(m)Case M: AR100_6P_R3, the 4th street canyon

Figure 6.12 (h)–(m): The deviation of concentration from the reference case, cases H–M, the fourth street canyon.

6.4.4 Assessment of ventilation

Considering that all the cases have vortex flow pattern, two bulk parameters are proposed to assess ventilation efficiency from two aspects. They are mixing velocity U_{mix} that represents air mixing or vortex strength in the street canyon and exchange velocity U_{ex} that represents air exchange across the street opening. The exchange velocity has been used in the literature to assess city breathability, such as Buccolieri et al. (2010) and Panagiotou et al. (2013). On the other hand, the mixing velocity has not been used before. It is believed that mixing air across the street and mixing air between the bottom and the top are an important respect of ventilation that is unable to be reflected by the magnitude of exchange velocity. For this reason, the mixing velocity plays an important role in assessing ventilation efficiency.

The mixing velocity is simply defined as the average absolute horizontal velocity along the mid vertical line in a street canyon (Equation 6.5). The exchange velocity is defined as the total momentum flux across an exchange plane divided by the difference between the mass flux above and below that plane (Equation 6.6), according to the theory proposed by Hamlyn and Britter (2005). In Equation 6.6, U_{can} is the in-canopy velocity, which is defined as the characteristic velocity below a canopy (Hamlyn and Britter, 2005). It has been estimated by empirical relations based on friction velocity in the literature (Panagiotou et al., 2013; Zajic et al., 2011). However, in this thesis, it is defined as spatial-averaged velocity magnitude below the roof level (Equation 6.7), which can be directly obtained from FLUENT.

$$U_{mix} = \frac{\int_{L_{mid}} |U| dl}{L_{mid}} \quad (6.5)$$

$$U_{ex} = \left| \frac{\iint_{A_{ex}} (\rho U W + \rho \bar{u} \bar{w}) dS}{\rho A_{ex} (U_{ref} - U_{can})} \right| \quad (6.6)$$

$$U_{can} = \frac{\iiint_{V_{can}} (U^2 + W^2)^{1/2} dV}{V_{can}} \quad (6.7)$$

The complete data for exchange velocity and mixing velocity are provided in Appendix 11.2. Figure 6.13 below shows the normalized exchange velocities and mixing velocities by a scatter plot. In the figure, aspect ratio is distinguished by symbol type, pitch rise is distinguished by symbol size, and roof arrangement is distinguished by symbol colour.

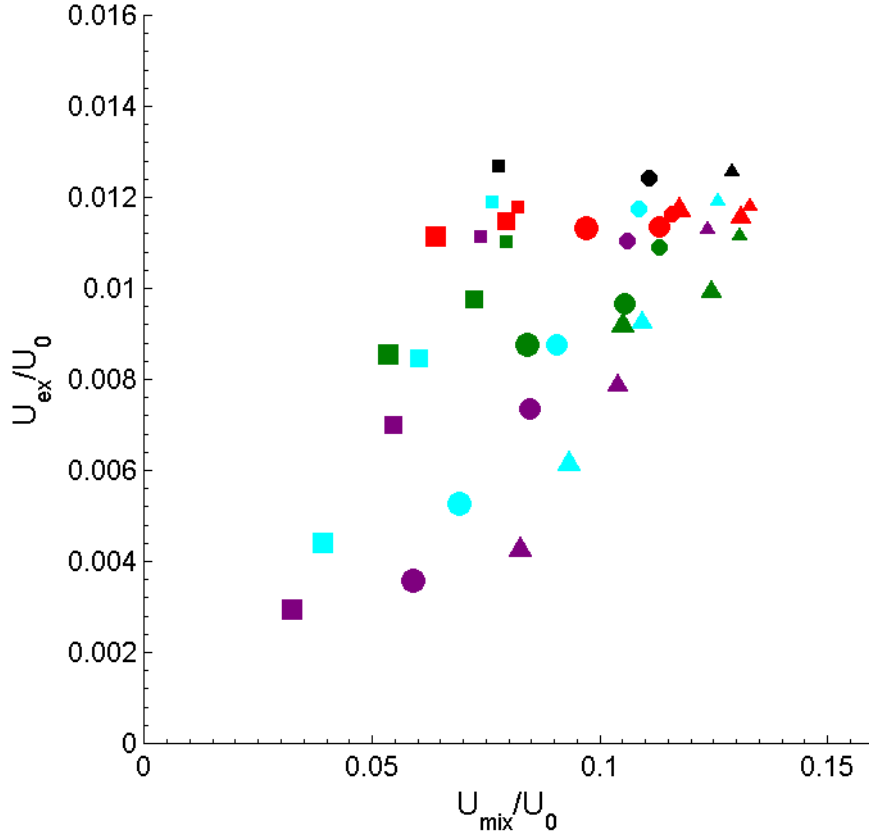


Figure 6.13: The scatter plot of normalized U_{mix} vs normalized U_{ex} , the third (test) street canyon. Triangle: AR=0.8, circle: AR=1.0 and square: AR=1.33. Large symbol represents high pitch rise, and the same colour scheme in Figure 6.2 is used to distinguish different roof arrangements.

As can be found in Figure 6.13, the mixing velocities (U_{mix}) are an order of magnitude larger than the exchange velocities (U_{ex}), but are an order of magnitude smaller than the free-stream velocity (U_0). The data points in the figure lie in a right-skewed parallelogram region, which indicates a general positive correlation between U_{mix} and U_{ex} .

For fixed pitch rise and roof arrangement, the increase of aspect ratio from 0.8 to 1.33 makes a rapid decrease of U_{mix} . On the other hand, aspect ratio has limited impact on U_{ex} , unless for the cases with a medium- or high-rise pitched roof on the leeward building (purple and cyan symbols with medium and large sizes). In those cases, the increase of aspect ratio results in a moderate decrease of U_{ex} .

For fixed aspect ratio and roof arrangement, the increase of pitch rise always leads to a moderate decrease of U_{mix} and a large decrease of U_{ex} . Both trends are more significant

for the cases with a pitched roof on the leeward building (purple and cyan) than for the cases with a flat roof on the leeward building (black, red and green).

When pitch rise is low, roof arrangement has limited impact on both U_{mix} and U_{ex} . However, when pitch rise is high, the cases with a pitched roof on the leeward building (purple and cyan symbols with large size) have much lower U_{mix} and much lower U_{ex} than the other cases.

6.4.5 Assessment of pollutant removal

Two bulk parameters are proposed here to assess pollutant removal effect. Canyon concentration c_{can} , which is defined as the volume-average concentration below the roof level, reflects the performance that removes pollutants out of street through the opening of the street canyon. Pedestrian concentration c_{ped} , which is defined as the volume-average concentration below the pedestrian level (defined as 2m in this thesis), reflects the performance that removes pollutants from the bottom of the street to the upper part. Pedestrian concentration is of interest in this study because it has a direct impact on pedestrian health. The mathematical definitions of these two bulk quantities are given in Equations 6.8 and 6.9.

$$c_{can} = \frac{\iiint_{V_{can}} c \, dV}{V_{can}} \quad (6.8)$$

$$c_{ped} = \frac{\iiint_{V_{ped}} c \, dV}{V_{ped}} \quad (6.9)$$

where V_{ped} is defined as the volume below 2m.

The complete data for canyon concentration and pedestrian concentration are provided in Appendix 11.2. Both concentrations are normalized by Equation 6.4 in Section 6.3. Figure 6.14 below shows the normalized canyon concentrations and pedestrian concentrations by a scatter plot. The symbols used in the figure are identical to those used in Figure 6.13 before.

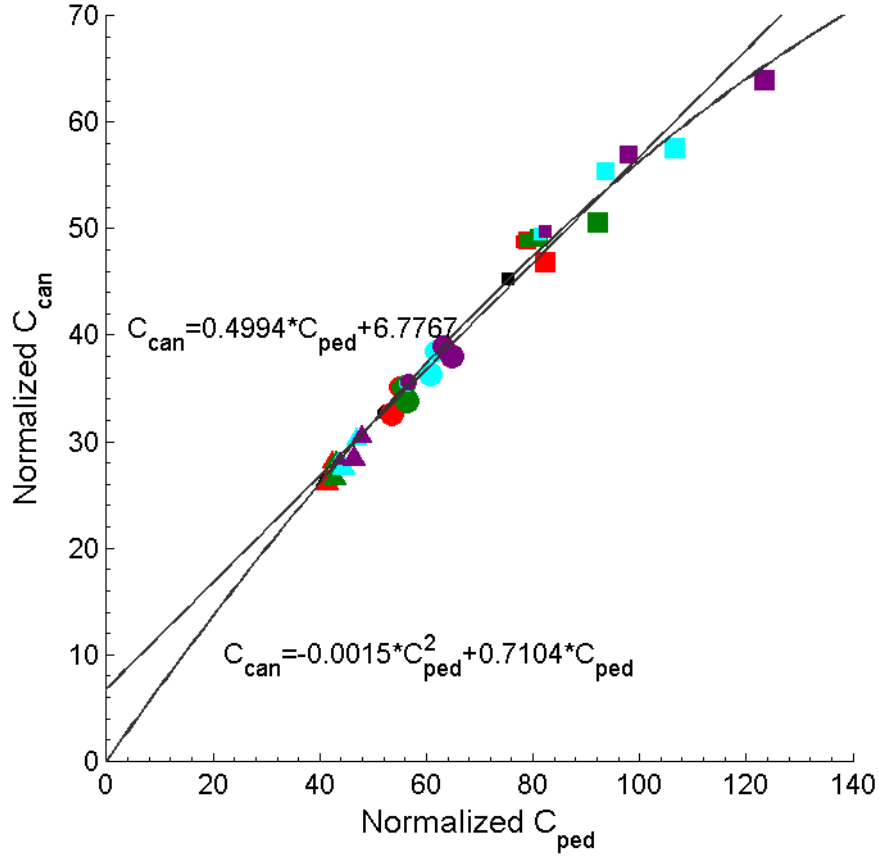


Figure 6.14: The scatter plot of normalized c_{ped} vs normalized c_{can} , the third (test) street canyon. Triangle: AR=0.8, circle: AR=1.0 and square: AR=1.33. Large symbol represents high pitch rise, and the same colour scheme in Figure 6.2 is used to distinguish different roof arrangements.

As can be seen in Figure 6.14 above, there are three clusters of data points which correspond to three groups of cases of different aspect ratios. Comparing any case in the group with a larger aspect ratio with any case in the group with a smaller aspect ratio, both canyon concentration (c_{can}) and pedestrian concentration (c_{ped}) are higher in the former case. Roof structure affects both c_{can} and c_{ped} but not as significant as aspect ratio. In addition, the variations c_{can} and c_{ped} due to different pitch rises and different roof arrangements are more significant in a group of cases with a larger aspect ratio.

The data points in Figure 6.14 reveal a clear positive linear correlation. According to this finding, it is thought that c_{can} and c_{ped} provide the same type of information in this parametric study, and any one of them can be replaced by the other. The positive linear correlation further suggests that although the three parameters (i.e., aspect ratio, pitch

rise and roof arrangement) have different weights in affecting c_{can} and c_{ped} , the proportion between the weight for c_{can} and the weight for c_{ped} is the same.

The data points in Figure 6.14 assemble in three clusters, which is not advantageous for studying the impacts of pitch rise and roof arrangement. For this reason, the canyon concentrations (c_{can}) in the figure are displayed in Table 6.2 below, and their percentage changes from the corresponding reference case are calculated and displayed in the table as well. Furthermore, the c_{can} in the fourth street is calculated for all the cases, and the results are displayed in Table 6.2.

According to the data in Table 6.2, the canyon concentrations (c_{can}) in the fourth street canyon are up to 30% higher than in the third street canyon. This is because the pollutants ventilated out from the third street cause non-zero background concentration for the fourth street, and some of them are entrained into the fourth street.

The data in Table 6.2 suggest that for the third street canyon, pitched roofs make generally higher c_{can} than flat roofs. Amongst 36 cases that have pitched roofs, only 2 cases have slightly lower c_{can} than the corresponding reference case, whereas the other 34 cases have higher c_{can} . Amongst the 34 cases with higher c_{can} , the percentage change of c_{can} exceeds +10% in 11 cases. All the 11 cases have either a medium pitch rise or a high pitch rise, and 10 out of the 11 cases have a pitched roof on the leeward building. According to these findings, it is confirmed that the presence of a pitched roof with medium or high rise on the leeward building is the worst roof structure for the third street in terms of pollutant removal.

The case AR133_6P_R3 has the highest c_{can} amongst all the cases. The percentage change of c_{can} for this case is +41%, which is much higher than the changes for the other cases. To find the reason for the high percentage change, the deviation of concentration plot for AR133_6P_R3 is provided as Figure 6.15 below. As can be seen in the figure, the high-rise pitched roofs on the two buildings make significantly higher (up to +200%) concentrations in the whole leeward part and around the emission sources than the reference, which are not found in any of the plots in Figure 6.11 in Section 6.4.3.1.

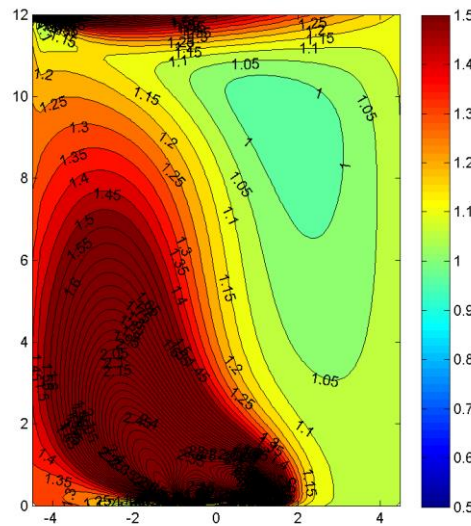
For the fourth street canyon, the presence of various pitched roof structures does not lead to such high percentage changes of c_{can} for the third street canyon. In addition, amongst 36 cases that have pitched roofs, 9 cases have up to 10% lower c_{can} than the corresponding reference case. The 9 cases all have high pitch rise but have different

roof arrangements. Referring to the previous contour plots for these cases (see Figure 6.12 in Section 6.4.3.2), the lower c_{can} is because the high-rise pitched roofs make critical reductions of concentration in the windward part and in the upper leeward part from the reference case, which outweighs the increments of concentration in the lower leeward part and around the emission sources.

It is further found that whatever aspect ratio is, the lowest c_{can} in the fourth street always happens in the case with the roof structure 3P1F2P_R3. In the three cases with this roof structure, the c_{can} in the fourth street is comparable to (when AR=0.8 and 1.0) or even lower than (when AR=1.33) the c_{can} in the three street, which never happens for the other roof structures. The outstanding pollutant removal performance for this roof structure is owing to two reasons, which are discussed as follows:

First, the roof structure 3P1F2P_R3, which has a high-rise pitched roof on the leeward building and a flat roof on the windward building of the third street, makes more pollutants accumulate in the third street, compared to the reference. Thus, the background concentration for the fourth street is relatively low under this roof structure than under the roof arrangements 6F (reference case), 2P2F2P and 2P1F3P.

Second, the roof structure 3P1F2P_R3, which has a flat roof on the leeward building and a high-rise pitched roof on the windward building of the fourth street, is a design that have similar pollutant removal performance to flat roofs on all the buildings.



Aspect ratio	Roof arrangement	the 3 rd street canyon		the 4 th street canyon	
		Normalized concentration	Percentage change from the reference	Normalized concentration	Percentage change the reference
AR=0.8	6F (ref)	26.2 (ref)	–	33.6 (ref)	–
	2P2F2P_R1	27.9	6.4%	35.7	6.1%
	2P2F2P_R2	28.0	6.9%	36.1	7.2%
	2P2F2P_R3	26.1	-0.4%	33.0	-2.0%
	2P1F3P_R1	27.9	6.5%	34.9	3.7%
	2P1F3P_R2	28.0	7.1%	36.4	8.2%
	2P1F3P_R3	26.6	1.7%	32.0	-5.0%
	3P1F2P_R1	28.2	7.8%	35.4	5.1%
	3P1F2P_R2	30.2	15.3%	34.3	2.1%
	3P1F2P_R3	27.5	5.2%	31.1	-7.6%
	6P_R1	28.3	8.1%	34.7	3.1%
	6P_R2	30.5	16.5%	36.1	7.2%
	6P_R3	28.4	8.6%	32.6	-3.0%
AR=1.0	6F (ref)	32.7 (ref)	–	42.0 (ref)	–
	2P2F2P_R1	35.1	7.3%	44.8	6.7%
	2P2F2P_R2	35.2	7.5%	44.8	6.7%
	2P2F2P_R3	32.6	-0.2%	41.0	-2.5%
	2P1F3P_R1	35.1	7.5%	43.4	3.3%
	2P1F3P_R2	35.3	7.9%	45.9	9.2%
	2P1F3P_R3	33.8	3.4%	41.7	-0.8%
	3P1F2P_R1	35.5	8.6%	44.5	5.8%
	3P1F2P_R2	38.4	17.6%	42.7	1.7%
	3P1F2P_R3	36.3	11.0%	38.5	-8.3%
	6P_R1	35.6	8.9%	43.1	2.5%
	6P_R2	39.0	19.4%	45.2	7.5%
	6P_R3	38.1	16.4%	42.7	1.7%
AR=1.33	6F (ref)	45.3 (ref)	–	57.1 (ref)	–
	2P2F2P_R1	48.8	7.8%	62.0	8.6%
	2P2F2P_R2	48.9	7.9%	61.6	8.0%
	2P2F2P_R3	46.8	3.4%	55.3	-3.1%
	2P1F3P_R1	48.8	7.8%	59.2	3.7%
	2P1F3P_R2	49.1	8.4%	64.4	12.9%
	2P1F3P_R3	50.5	11.5%	65.1	14.1%
	3P1F2P_R1	49.4	9.2%	60.9	6.7%
	3P1F2P_R2	55.3	22.2%	58.5	2.5%
	3P1F2P_R3	57.5	27.1%	54.3	-4.9%
	6P_R1	49.7	9.8%	58.8	3.1%
	6P_R2	56.9	25.7%	63.7	11.7%
	6P_R3	63.9	41.1%	67.9	19%

Table 6.2: Normalized volume-average concentrations in the 3rd and 4th street canyons, and deviations from reference case. Reference cases marked by coral, increase >10% marked by red, and decrease marked by green.

The above discussion about canyon concentration helps to understand the impacts of the three parameters (i.e., aspect ratio, pitch rise and roof arrangement) on pollutant removal performance. However, canyon concentration does not show any information about the deviation of concentration from the reference in a specific part of the street. To obtain this type of information, it must refer to concentration contours such as Figure 6.11 and Figure 6.12. Nevertheless, it is not easy to make comparisons between the concentration contours for several cases or even more cases. To overcome the abovementioned weaknesses for canyon concentration and concentration contour, a new presentation is used to provide intermediate information between the average concentration for a street canyon and the concentration for a specific position.

The new presentation is based on the volume-average concentrations of different parts of street canyon. In this study, the third and fourth streets are equally divided into eight rectangular parts, each of which is 3m tall and half street wide. The calculated volume-average concentrations for all the cases are plotted by coloured rectangles and assembled in one figure. Thus, comparison can be straightforwardly made in the figure. This presentation is named as 'heat-map' in this study. The 'heat-maps' for the third street and fourth street are shown in Figure 6.16 and Figure 6.17 below.

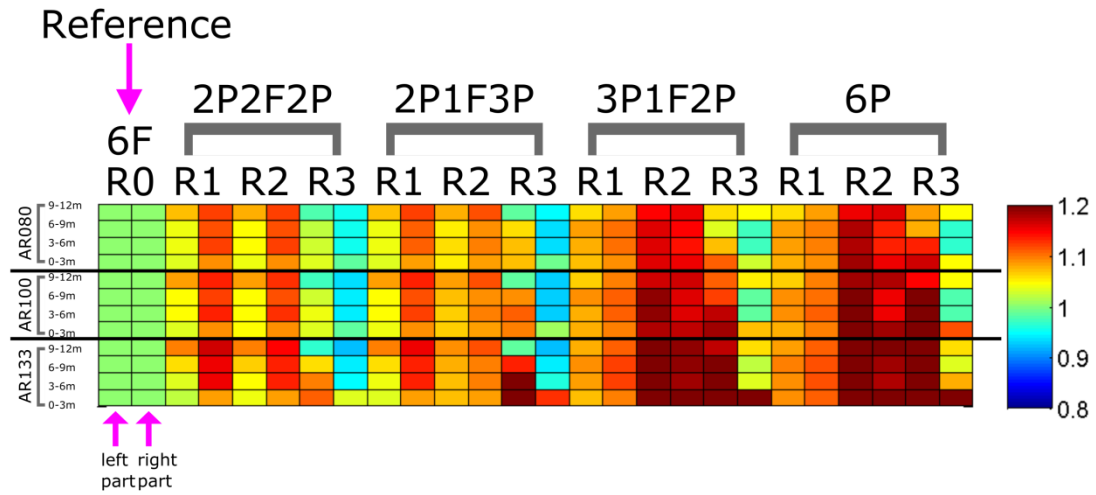


Figure 6.16: 'Heat-map' of volume-average concentration for eight parts of the third (test) street canyon.

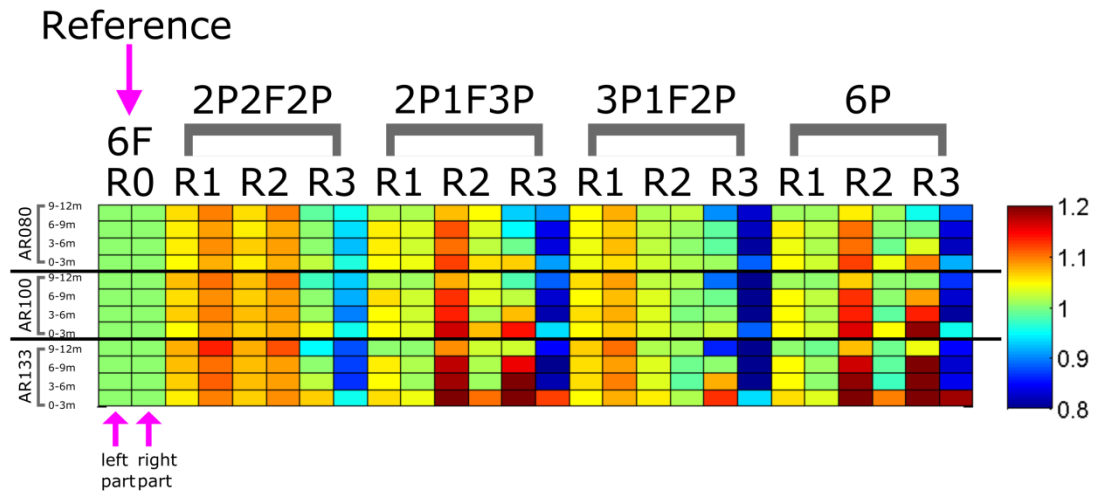


Figure 6.17: 'Heat-map' of volume-average concentration for eight parts of the fourth street canyon.

According to Figure 6.16 above, the presence of pitched roofs causes an increase of concentration from the reference in most parts of the third street. The increments are relatively large ($>20\%$) in the parts near the ground and first floors of the leeward building and in the parts near the ground, first and second floors of the windward building. On the other hand, the presence of pitched roofs leads a decrease of concentration in limited cases. The decrease is mainly in the part near the third floor of the leeward building and in the parts near the first, second and third floors of the windward building. The decrements are around 10%.

According to Figure 6.17 above, the presence of pitched roofs causes an increase of concentration from the reference in some parts of the fourth street, but the increments are much smaller than those for the third street. For the fourth street, there are many cases having decreased concentration in the part near the third floors of the windward building. Moreover, the cases with high-rise pitched roofs all have decreased concentration in the parts near all the floors of the windward building.

It has been observed from the previous concentration contours (i.e., Figure 6.11 and Figure 6.12) that (1) low pitch rise makes uniform and relatively low increases of concentration from the reference case, but high pitch rise makes high increases of concentration in the leeward part, and (2) for fixed pitch rise, the increase of concentration is more significant in the cases with a pitched roof on the leeward building than in the cases with a flat roof on the leeward building. These two important features can also be observed from the 'heat-maps' in Figure 6.16 and Figure 6.17, which indicates 'heat-map' as a useful presentation.

6.5 Summary of main findings

This chapter carries out a parametric study of pitched roofs. The aspect ratio of building height to street width, pitch rise and roof arrangement are defined as three parameters. A total of 39 cases are modelled, including three reference cases. The impacts of the three parameters are studied by comparing the results between the reference cases and the other cases with different pitched roofs. The main findings are summarized below.

A vortex flow pattern is found in each street canyon for all the cases. Vortex shape is mainly determined by aspect ratio, whereas pitch rise and roof arrangement have a secondary effect on vortex shape. In the cases with a high-rise pitched roof on the leeward building, the vortex flow slightly extends above the roof level; in all the other cases, the vortex flow is below the roof level.

It is found that the presence of pitched roofs weakens both mean airflow and turbulence in the street. For a fixed roof arrangement, higher pitch rise causes lower horizontal velocity, vertical velocity and turbulent kinetic energy in the street. For a fixed pitch rise, the presence of a pitched roof either on the leeward building or on the windward building contributes to lower horizontal velocity, vertical velocity and turbulent kinetic energy than the reference. The contribution made by the former is more significant than by the latter.

After comparing the concentration contours for the twelve cases with $AR=1.0$, it is found that roof the shape on the leeward building has a major effect on pollutant dispersion in street canyon, while the roof shape on the windward building only has a minor effect. Low pitch rise causes uniform small increases of concentration across the street from the reference, because it has limited impact on mean flow but weakens turbulence in the street. High pitch rise causes large increases of concentration in the lower leeward part and near the emission sources but small decreases of concentration in the windward part, because it significantly weakens mean airflow near the leeward building and the ground and weakens turbulence in the street.

Four bulk parameters—mixing velocity (U_{mix}), exchange velocity (U_{ex}), canyon concentration (c_{can}) and pedestrian concentration (c_{ped})—are proposed to assess ventilation efficiency and pollutant removal performance.

An increase of aspect ratio causes a decrease of U_{mix} but has limited impact on U_{ex} . An increase of pitch rise leads to a moderate decrease of U_{mix} and a significant decrease of

U_{ex} . The impacts of roof arrangement on U_{mix} and U_{ex} further hinge on pitch rise. When pitch rise is high, the pitched roof on the leeward building leads to significantly lower U_{mix} and U_{ex} than the other cases.

A clear positive linear correlation is found between canyon concentration and pedestrian concentration, which suggests that they give the same type of information in this study. It is found that canyon concentration is mainly determined by aspect ratio, as the c_{can} for any case in the group with relatively large aspect ratio is higher than the c_{can} for any case in the group with relatively small aspect ratio. For the third street canyon, the presence of pitched roofs makes 34 out of 36 cases have increased c_{can} compared to the corresponding reference case; for the fourth street canyon, the presence of pitched roofs makes 27 out of 36 cases have increased c_{can} compared to the corresponding reference case. In addition, the increments for the third street are generally larger than for the fourth street. A pitched roof with medium or high rise on the leeward building causes the largest increments of c_{can} for the third street, whereas high pitch rise is found to be responsible for decreases of c_{can} for the fourth street in 9 cases.

A new presentation, which is named as 'heat-map', is used to provide intermediate information between the average concentration for a street canyon and the concentration for a specific position.

According to the 'heat-map' for the third street, for most cases, the presence of pitched roofs causes a large (>20%) increase of concentration in the parts near the ground and first floors of the leeward building and in the parts near the ground, first and second floors of the windward building; however, for some cases, the presence of pitched roofs causes a slight decrease of concentration in the part near the third floor of the leeward building and in the parts near the first, second and third floors of the windward building.

According to the 'heat-map' for the fourth street, for some cases, the presence of pitched roofs causes an increase of concentration in the same parts as for the third street, but the increments are much smaller. Moreover, for many cases, the presence of pitched roofs causes a decrease of concentration in the parts near all or some of the floors of the windward building, and the decrements are more significant compared to those for the third street.

7 A Case Study of Airflow and Pollutant Dispersion in Gloucester Place and Its Surrounding Area

London has experienced poor air quality in the past. It is one of the three cities in the UK that exceeds the limits of EU's air quality standards (Vaughan, 2015). Poor air quality in London causes around 9,500 premature deaths every year, which occupies around 12% of the annual premature deaths related to air pollution in the UK (Vaughan, 2015).

Recent studies have shown that high levels of NO_2 and $\text{PM}_{2.5}$ are the main reason for large number of premature deaths in London (Walton et al., 2015). A majority of these two pollutants are produced by traffic, especially by diesel vehicles (Vaughan, 2015). Hence, reducing and removing traffic emission are crucial for improving the air quality in London.

The London area of Marylebone has been repeatedly reported as not achieving the Air Quality Strategy Objectives and has experienced relatively high pollutant concentration levels compared to the other areas in London (London Air Quality Network, 2015). For example, the hourly NO_2 concentrations, which are measured at two nearest monitoring sites to the Marylebone Road, have often exceeded EU's NO_2 limits (100ppb or $188\mu\text{g}/\text{m}^3$) in the past five years (930 exceedances out of 42,656 measurements at Marylebone Road station and 5,202 exceedances out of 21,655 measurements at Oxford Street station) (London Air Quality Network, 2015).

This chapter models airflow and pollutant dispersion in Gloucester Place and its surrounding area, in the London area of Marylebone. It is aimed to identify typical air flow and typical pollutant distribution in the modelled area and understand the impacts of the city blocks. The structure of this chapter is given as follows:

Section 7.1 introduces the background information of Gloucester Place and its surrounding area. Section 7.2 provides model geometries and CFD modelling settings. The airflow around the city blocks are visualized and discussed in Section 7.3. The flow patterns in different parts of the test street are discussed in detail in Section 7.4. Section 7.5 discusses pollutant distributions in and around the test street and explains how the specific flows mentioned in the last two sections cause these distributions. Section 7.6 concludes the key findings of this study.

7.1 Background information

Gloucester Place is a south-to-north one-way road in the London area of Marylebone. There is heavy traffic on the road. The average daily traffic volume for Gloucester Place was around 14,000 in the past five years (Department for Transport, 2015).

A part of Gloucester Place and the city blocks surrounding it, which are marked by yellow and blue frames respectively in Figure 7.1 below, are chosen as the research objective of this study for two reasons. First, this area is very likely to experience poor air quality in the past, due to heavy traffic, dense building blocks and high background concentration. Thus, performing CFD modelling is helpful to identify the air pollution issue in this area. Second, this area has several street canyons whose geometries are different but not very different from the homogeneous street canyons modelled in the parametric study in Chapter 6. By comparing the model results in this chapter to the previous chapter, it is possible to understand the different impacts made by ideal urban geometries and realistic urban geometries and identify what type of geometry contributes to the large difference in flow pattern and pollutant distribution

The street and building geometries of Gloucester Place are schematically shown in Figure 7.2 below. The road consists of two pavements (the red zones), three traffic lanes (the yellow zones) and one parking lane (the brown zones). A bus stop (the green zone) is around 30m away from the north street end and is next to the west building row. A T-junction exists between two east building rows and is around $\frac{1}{3}$ of the street length away from the south street end. The T-junction divides the test street into two parts: the north section and the south section. These two terms are frequently used in the following text.

Most of the buildings adjacent to Gloucester Place are hotels, clubs and offices. The buildings in the area around Gloucester Place are mostly shops, restaurants and private dwellings.

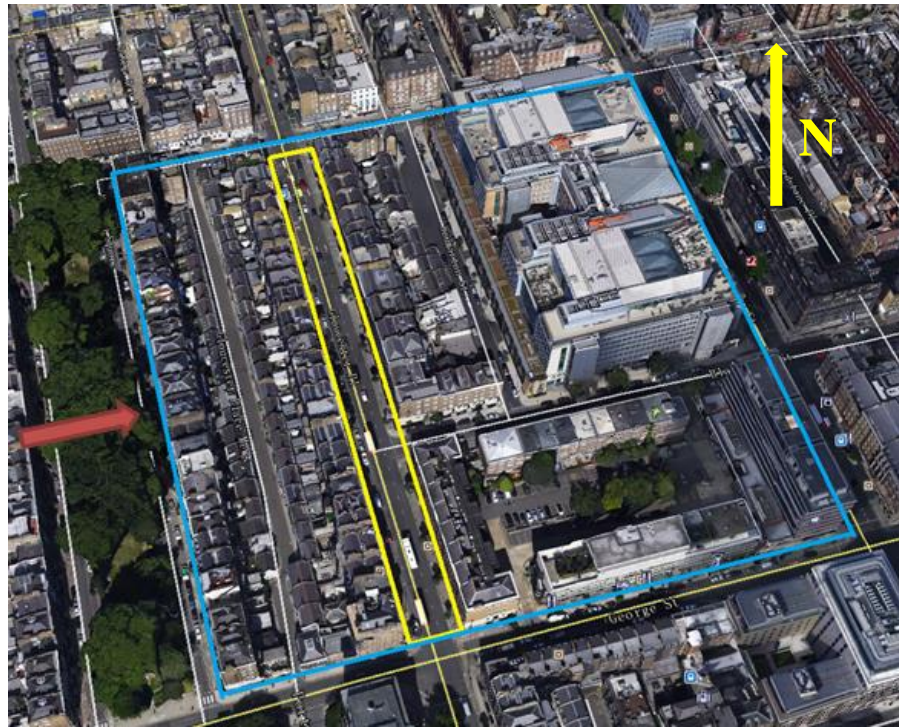


Figure 7.1: Gloucester Place in central London and the city blocks surrounding it. Map downloaded from Google Earth on 28th Nov, 2014. Red arrow—one of the prevailing wind directions, yellow frame—Gloucester Place, and blue frame—the model area.

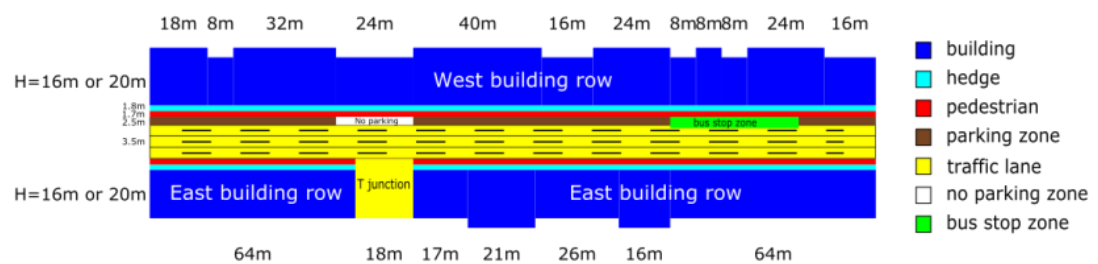


Figure 7.2: A schematic diagram of the geometry of Gloucester Place.

The wind rose for London Heathrow measured at 25m is used as the reference for the background wind. It contains both wind speed and wind direction information, as shown in Figure 7.3 below. According to this figure, the prevailing wind is mainly from the west and the south.

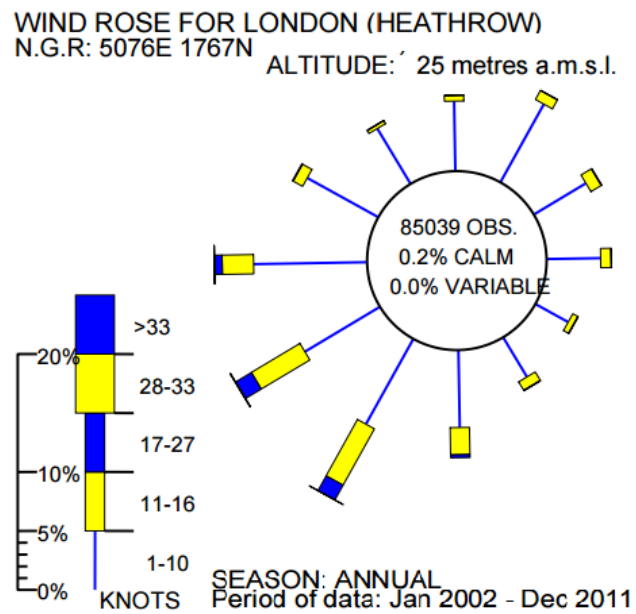


Figure 7.3: The wind rose for London Heathrow measured at 25 metres. Adapted from Met Office (2015). (Note: 1 knot=0.514m/s)

7.2 Model geometry and CFD modelling settings

The model geometry is sketched in Figure 7.4 below. It is made as simple and representative as possible, to reduce computational cost without sacrificing model accuracy. Gloucester Place, the third street canyon in the figure, is chosen as the test street. In Figure 7.4, the buildings adjacent to the test street are marked by blue. A tall building (green) and two relatively short parallel buildings (cyan) on the east side are included in the model, as they are tested to have great influence on the flow in the test street. A homogeneous building row to the west of the test street (magenta) is also included in the model. All of these buildings mentioned above are the real buildings in Gloucester Place and its surrounding area.

Additionally, three virtual building rows (yellow) are created in front of the first building and on the two sides of the real buildings. They are used to stabilise the approaching flow and , develop more realistic urban boundary layer above the buildings and make the flow in the test street free from the effect made by the flow separation above the first street.

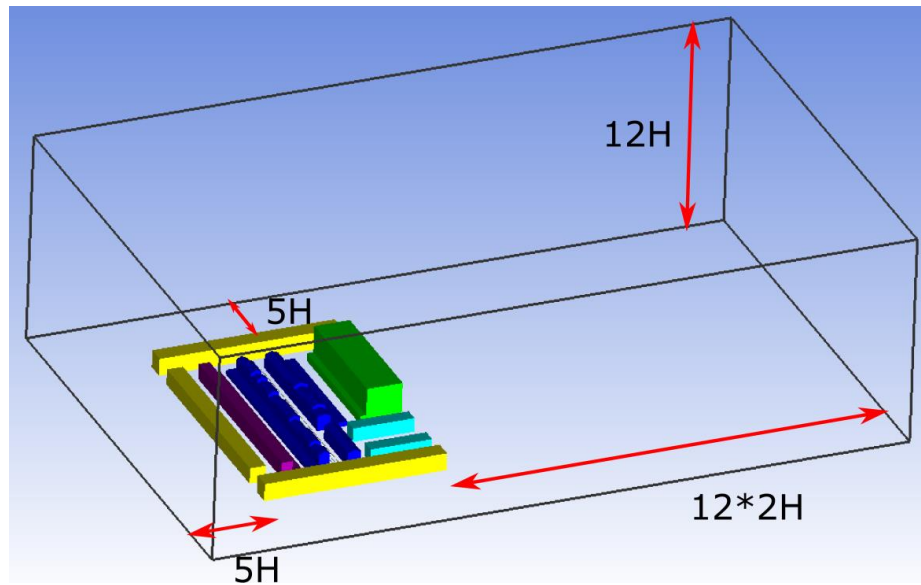


Figure 7.4: Sketches of computational domain and the building blocks in it.

The distances between the building blocks and the domain boundaries are annotated in Figure 7.4 above. They are defined on the basis of the characteristic building height $H=20\text{m}$. A distance $24H$ is provided behind the building blocks, longer than the distance $15H$ used in the benchmark study and the parametric study. Using a longer distance is aimed to ensure the full development of wake behind the tall building.

The dimensions of the buildings and the space between them are given in Figure 7.5 below. The test street is 20m wide. The buildings adjacent to the test street are either 16m or 20m tall. The height of the taller adjacent buildings (i.e., 20m) is defined as the characteristic building height (H). Only the buildings adjacent to the test street have pitched roofs with a fixed pitch rise $R=3m$, whereas the other buildings all have flat roofs. The heights of the other buildings are 16m, 18m or 20m, except that the tall building (green) is 40m tall.

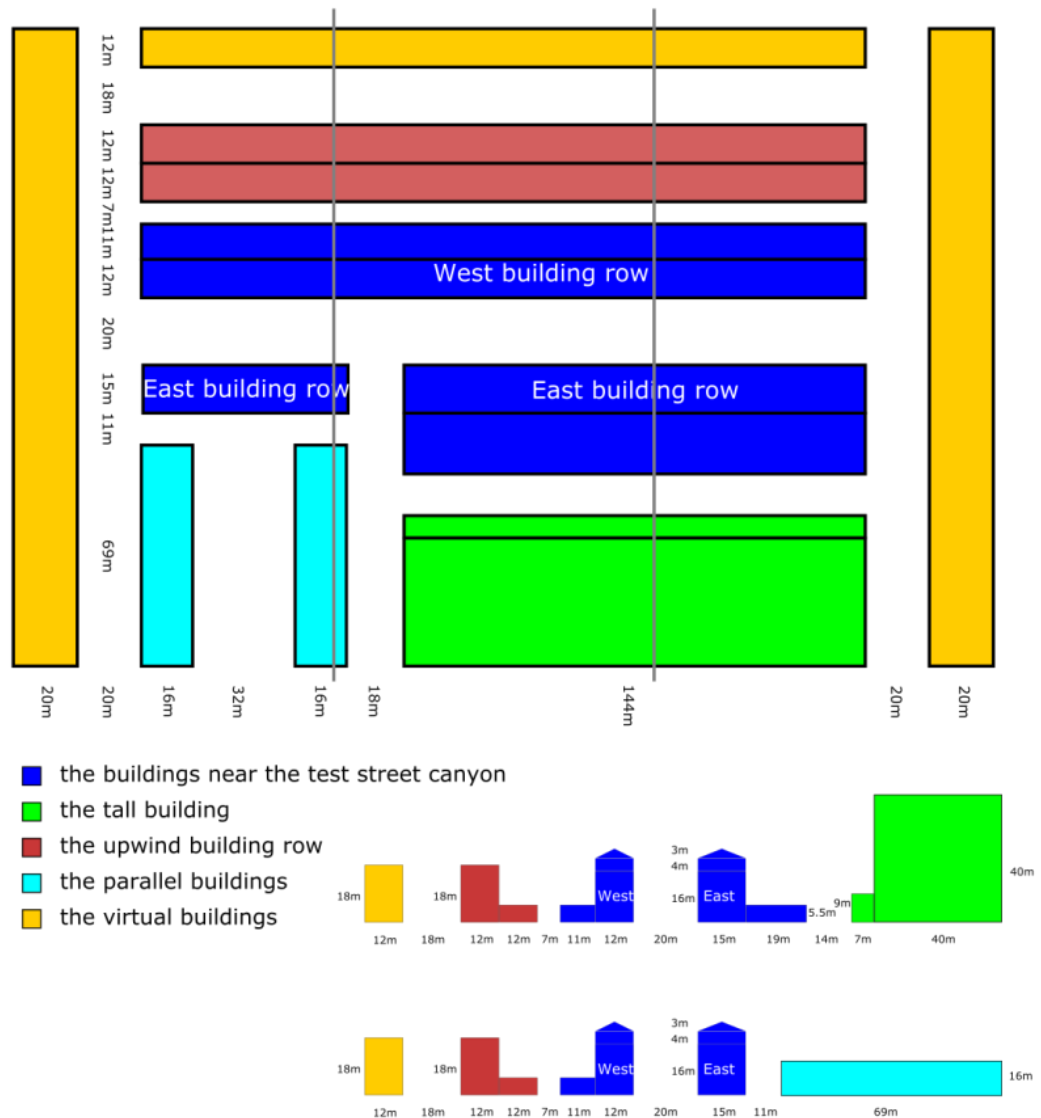


Figure 7.5: Sketches of a horizontal plane viewed from top (top) and two cross sections viewed from south (bottom).

As one of the prevailing wind directions (see Figure 7.3 above), the west-southwesterly wind is simulated in the CFD model. This wind direction is perpendicular to the axis of the test street, making the worst situation for ventilation. The profiles of the background

wind (i.e., velocity, TKE and dissipation profiles) are assumed to be the same as those used in the parametric study (see Equations 6.1, 6.2 and 6.3 in Section 6.3). The velocity profile gives a velocity of 5.8m/s (or 11.3knots) at $z=25\text{m}$, which is a typical wind speed according to Figure 7.3 above.

The specification of boundary condition follows the same approach used in the parametric study (see Section 6.3). In addition, the side boundaries are specified as symmetric boundaries. The dimensions of the emission sources are different from those in the parametric study. In this study, there are three identical emission sources on the ground of the test street. Each emission source is defined to be 0.6m (or $0.03H$) wide. The east source is 4.5m away from the east (windward) building rows, and the distance between each source is 3.5m, which follow the actual traffic arrangement shown in Figure 7.2 above. The intensity of each source is set the same as in the parametric study

The turbulent Schmidt number is still chosen as 0.9. Although a value of 0.3 was found to give more accurate prediction of concentration in benchmark case 3, using the value $Sc_t=0.9$ is aimed to make a fair comparison of pollutant concentration between the present study and the parametric study. Concentration is presented in a normalized form which has been defined as Equation 6.4 in Section 6.3. Here, it is re-stated as Equation 7.1. It should be pointed out that the characteristic height ($H=20\text{m}$) is used for normalization.

$$c^* = \frac{cU_0H}{Q/L_q} \quad (7.1)$$

A nested mesh is generated to avoid unaffordable computational cost. As shown in Figure 7.6 below, the nested region ranges from 20m (H) before the first building row to 120m ($6H$) after the tall building and extends 80m ($4H$) above the ground. The mesh in the nested region is made twice as fine as outside. There are 34 cells along the height of the leeward building of the test street, which follows the mesh resolution requirement proposed in the benchmark study. By using the nested mesh, total cell number is controlled below 4 million.

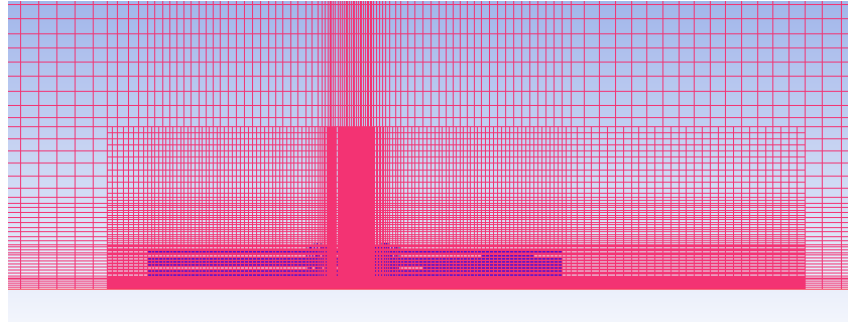


Figure 7.6: The nested mesh viewed from the south.

7.3 Airflow around the city blocks

The flow around the city blocks is shown by the streamlines in Figure 7.7 below. Four unique large-scale flow features are found from the figure, and they are marked by 'a', 'b', 'c', 'd' in the figure. The formation of these flow features is related to the uneven layout which contains the tall building and the two short parallel buildings. A detailed discussion about the four flow features is made in the following paragraphs.

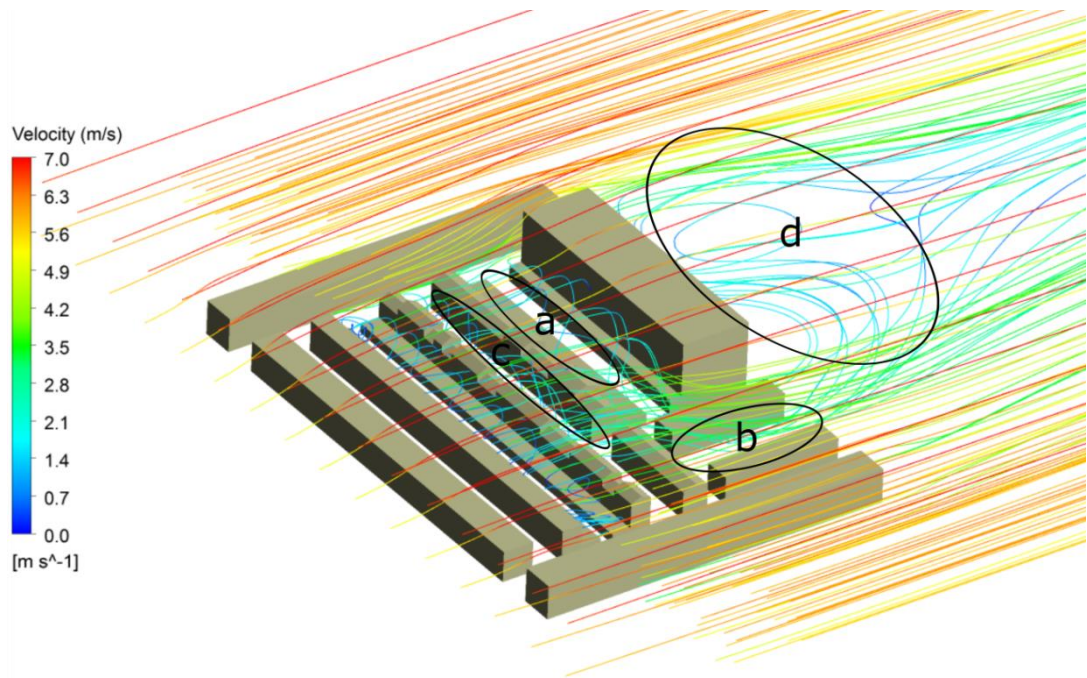


Figure 7.7: Streamlines around the building blocks.

Owing to the tall building whose width is four times as its height, the upstream flow ascends while travelling along the free-stream direction and then passes over it. This flow feature is apparent in the region just in front of the tall building, which is marked by “a” in Figure 7.7 above. It can also be noted from a velocity vector plot which is across the tall building, such as Figure 7.8 below. It causes the growth of boundary profile above the city blocks, as shown in Figure 7.10 below. This has an impact on the approaching flow for the test street, as the horizontal flow above the test street is not as strong as the horizontal flows above the first and the second streets.

Owing to the wide space between the two parallel buildings, the flow above the south section of the test street descends after passing over the windward buildings, which is marked by “b” in Figure 7.7 above. This flow feature can be noted from a velocity vector plot which is across the space, such as Figure 7.9 below. In this circumstance, the

south section acts as the last street canyon in the domain. The downstream flow has potential to influence the flow above the south section of the test street.

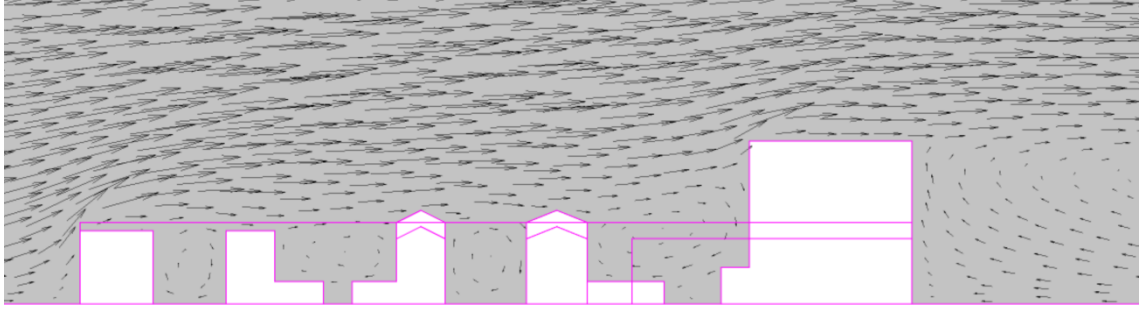


Figure 7.8: A vertical plane across the north section of the test street and the tall building (72m away from the north street end) and the velocity vectors on it.

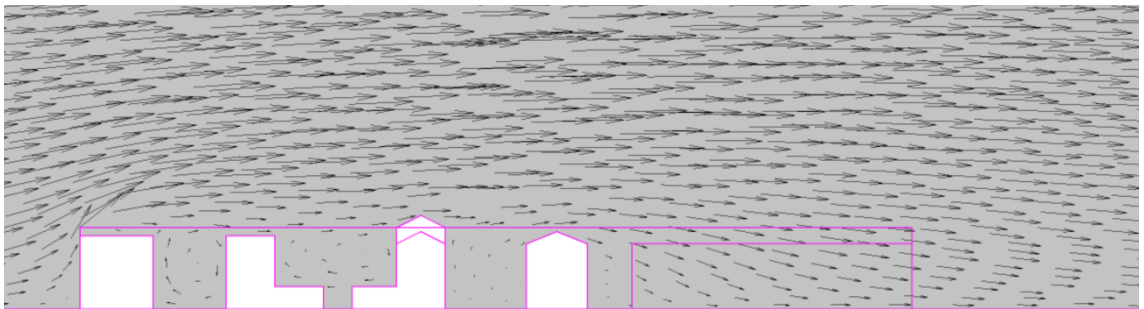


Figure 7.9: A vertical plane across the south section of the test street and the space between two short parallel buildings (32m away from the south street end) and the velocity vectors on it.

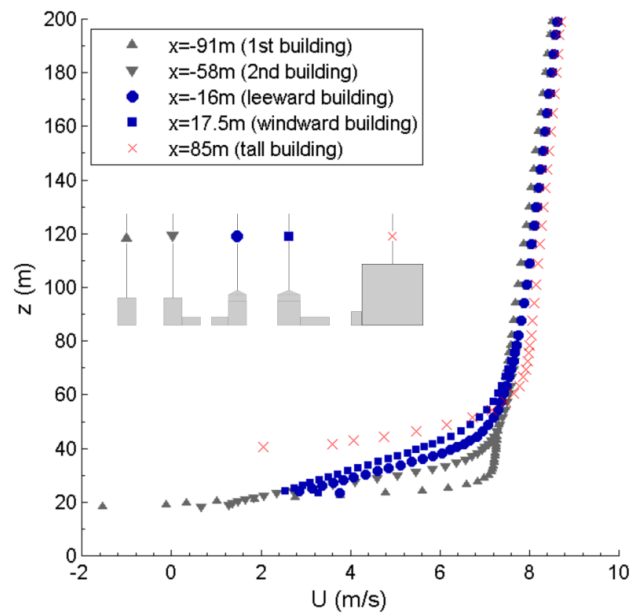


Figure 7.10: Horizontal velocity profiles above the five building rows (measured at 72m away from the north street end).

Owing to the tall building, the upstream flow also diverges while travelling along the free-stream direction and then passes around the tall building. This flow feature is marked by “c” in Figure 7.7 above. As can be perceived from Figure 7.11 below, the flow above the city blocks does not diverge until passing over the leeward buildings of the test street canyon. It is further observed from both Figure 7.7 and Figure 7.11 that the two branches of the diverged flow are asymmetrical; most of the flow above the test street deviates from the south to the north and then passes around the south side of the tall building or travels farther along the north-south direction. A reasonable explanation is that heterogeneous city blocks are generally favourable for maintaining span-wise flow compared to an open space without any building, and in the current case, there are more city blocks to the north-west of the tall building than to the south-west of the tall building.

The diverged flow further drives along-street flows in the test street and the street after it which can be seen in Figure 7.12 below. This statement is supported by the decay of the span-wise velocities V from the roof top of the test street to the ground of the test street, as shown in Figure 7.13 below. In addition, the vortex flow and the along-street flow are found to be able to coexist in the street canyon. As a good illustration, the coexistence of these two types of flow results in tilted vortex flow pattern in the north section, which is observed as the spiral streamlines in Figure 7.7 above. This specific flow pattern will be discussed in the next section.

The diverged flow (i.e., the first flow feature) and the along-street flow (i.e., the third flow feature) mentioned above are consistent with the model results in Gu et al. (2011). They modelled airflow around a non-uniform street canyon whose geometry is shown Figure 7.14 below. In their study, divergence of horizontal flow was observed in front of the tall building, and spiral recirculation was observed in the street canyon, as shown in Figure 7.14 below. Moreover, it was found that airflow approached the street from the end where the windward building is taller than the leeward building and then travelled along the street, which are the same in the current study.

Owing to the uneven layout made by the tall building and the two parallel buildings, the wake behind the tall building is asymmetrical, which is marked by “d” in Figure 7.7 above. As can be seen in the figure, two large horizontal vortices form behind the tall building, but they have different sizes. The horizontal vortex in the south side of the tall

building has relatively large size, because more flow passes around the south side of the tall building rather than the north side.

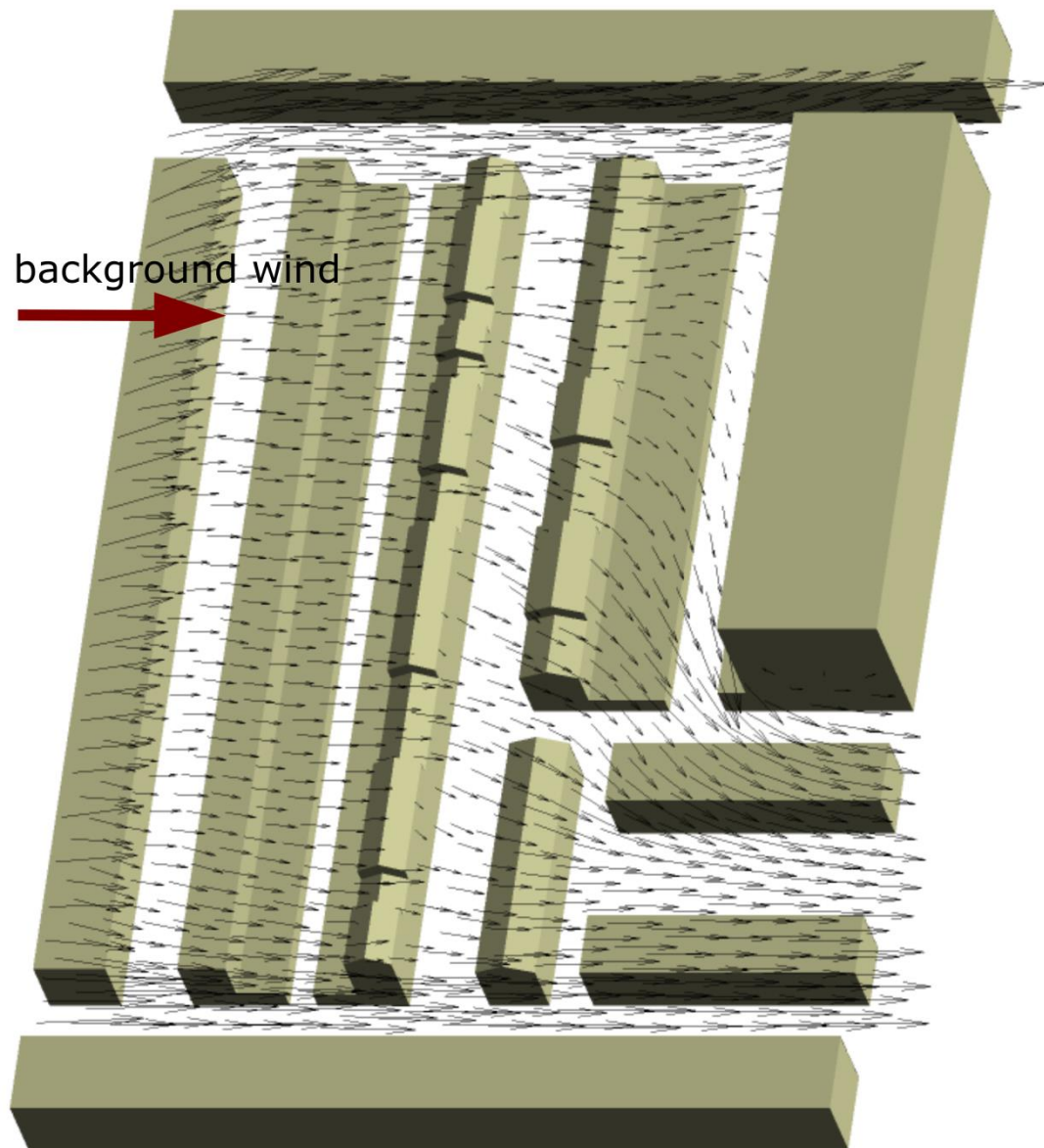


Figure 7.11: Velocity vectors on the horizontal plane at $z=21\text{m}$ (near roof level).

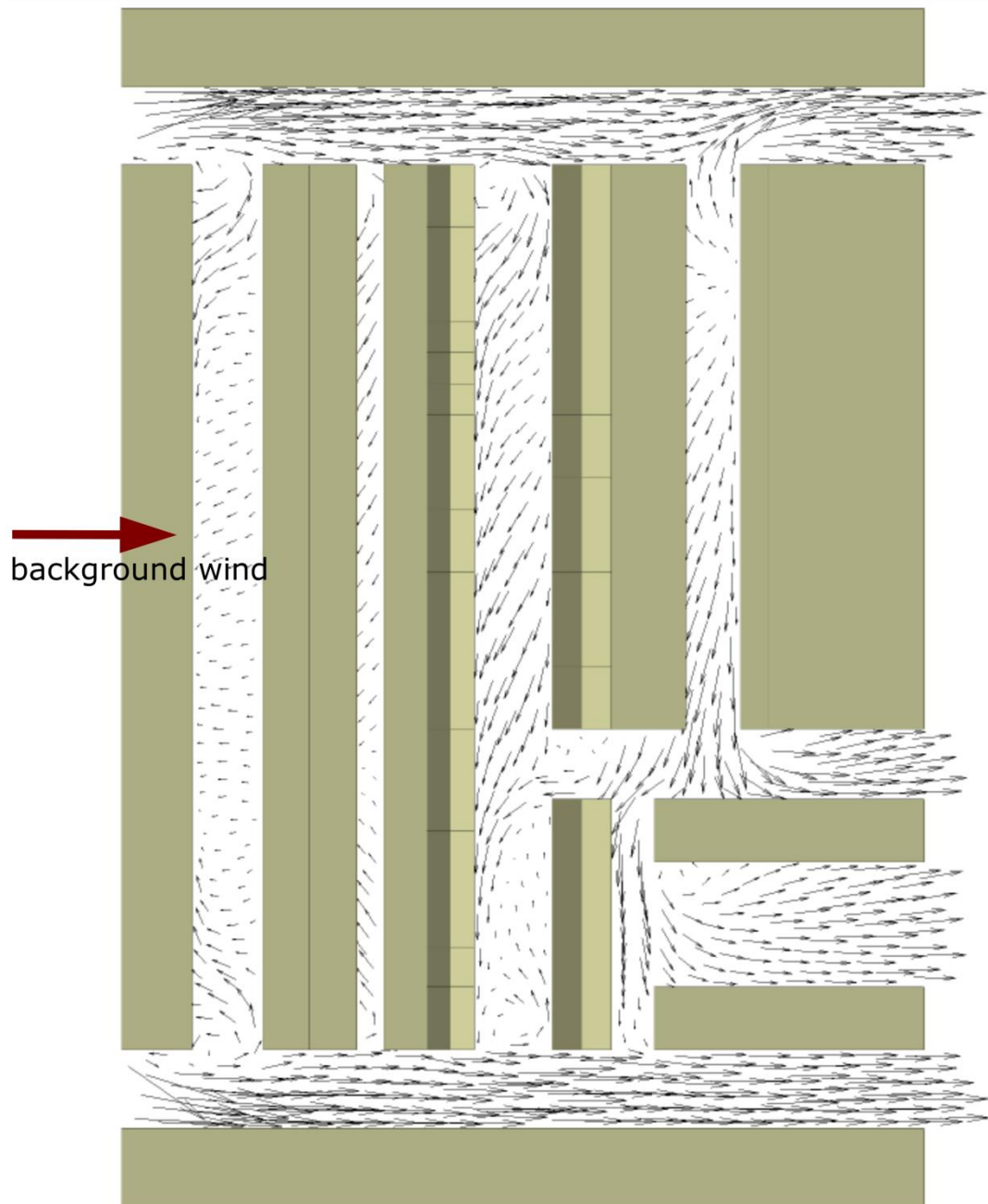


Figure 7.12: Velocity vectors on the horizontal plane at $z=5\text{m}$ ($0.25H$).

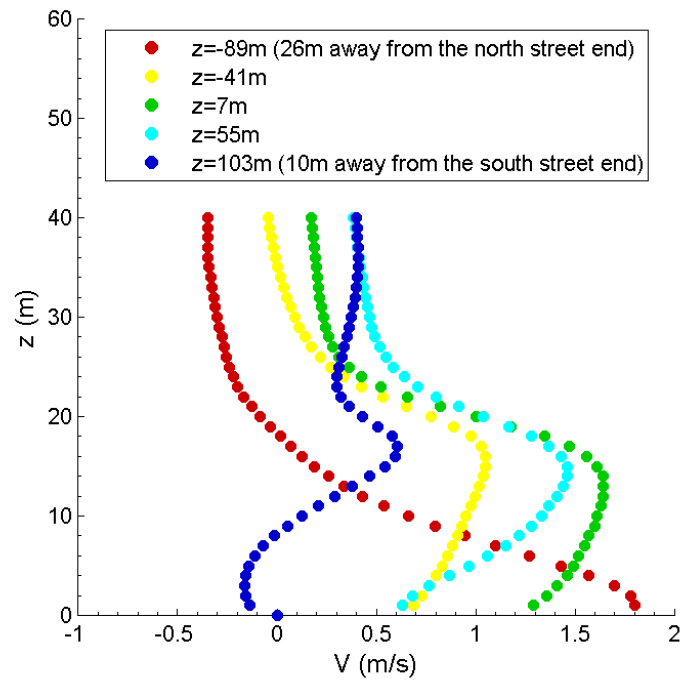


Figure 7.13: Velocity W on five equally spaced vertical lines in the test street (each line is 10m away from the leeward building and the windward building).

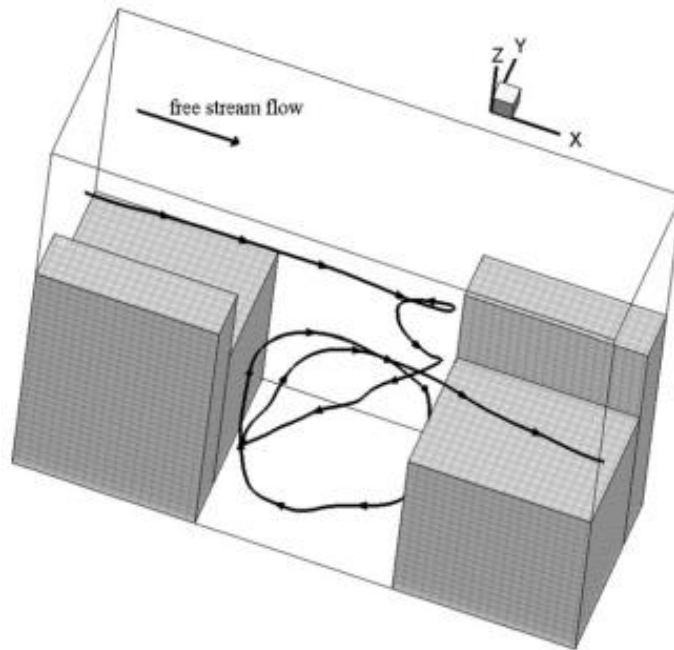


Figure 7.14: A typical streamline in the non-uniform stream canyon. Adapted from Gu et al. (2011).

7.4 Airflow in the test street canyon

This section presents and analyses airflow in the test street canyon. The general flow field is illustrated by the streamline plot in Figure 7.15 below. The streamlines in the figure start out from three locations of the test street: the coloured streamlines start out from the north street end, the black streamlines start out from the T-junction, and the magenta streamlines start out from the bottom of the south section.

Velocity vector plot, a traditional approach to visualise flow in experiment, is also used in this study. Thus, it is possible to make comparisons between the flow patterns on different across-street vertical planes, the flow patterns in the previous chapters and the typical flow patterns in the literature. Figure 7.16 below shows the velocity vector plots on nine vertical planes.

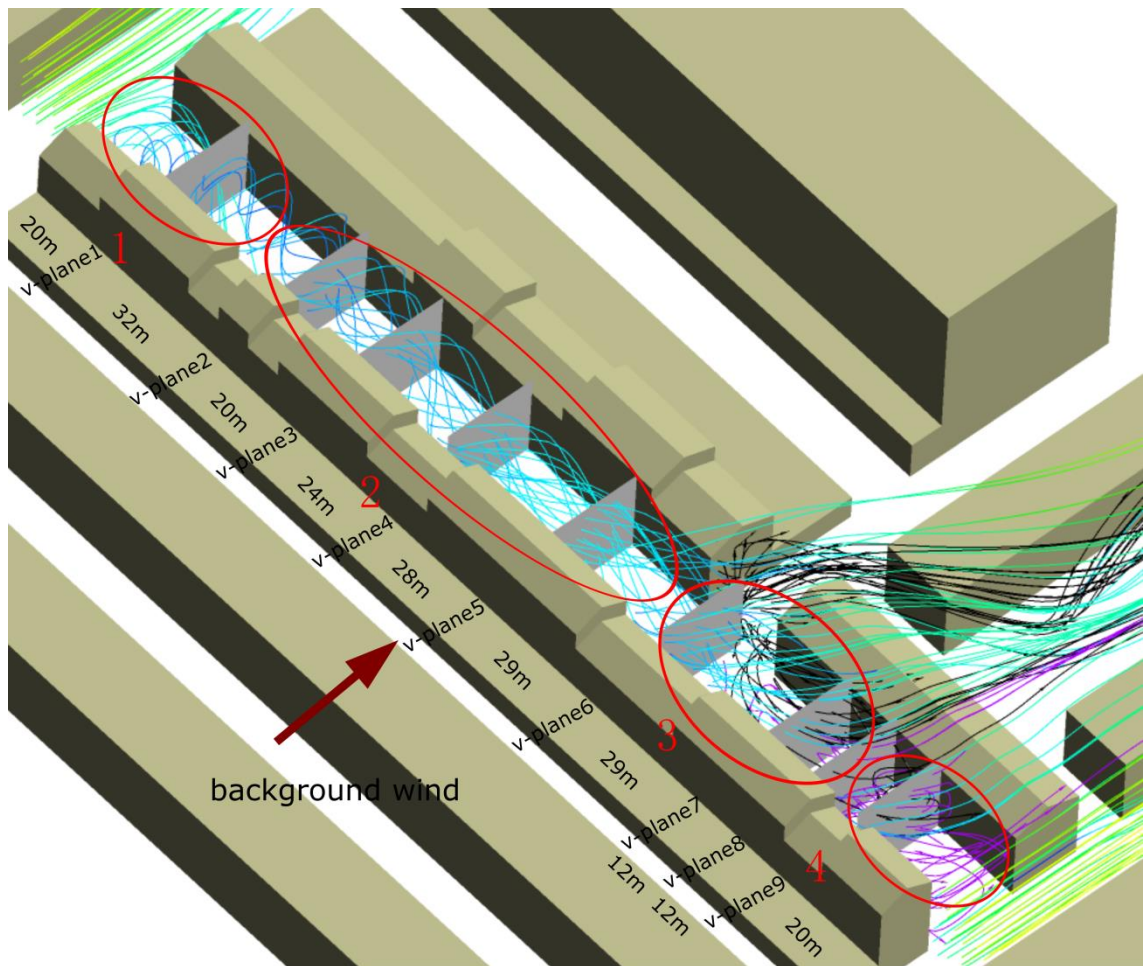
The positions and geometries of the nine vertical planes are given in Table 7.1 below. They are selected according to representativeness of different parts of the street and variety of the cross-section geometries. Four of them are either 20m (H) away from one of the street ends or 20m (H) away from the T-junction; one plane is across the T-junction; the other four planes are relatively far from the street ends.

In order to make a joint between the three-dimensional streamline plot and the planar velocity vector plots, the relative positions of the nine planes are precisely shown together with the streamlines in Figure 7.15(a) below.

According to the difference in flow structure, the test street is divided into four zones. The divisions of these four zones are schematically shown in Figure 7.15(a) below. Zone 1 starts from the north street end and extends around $2.5H$ in the along-street direction (from the north to the south). Most part of the north section of the test street is classified as Zone 2. The T-junction and most part of the south section are classified as Zone 3. Zone 4 starts from the south street end and extends around $1.5H$ in the along-street direction (from the south to the north). The flow structure in each zone is discussed in the following four sub-sections.

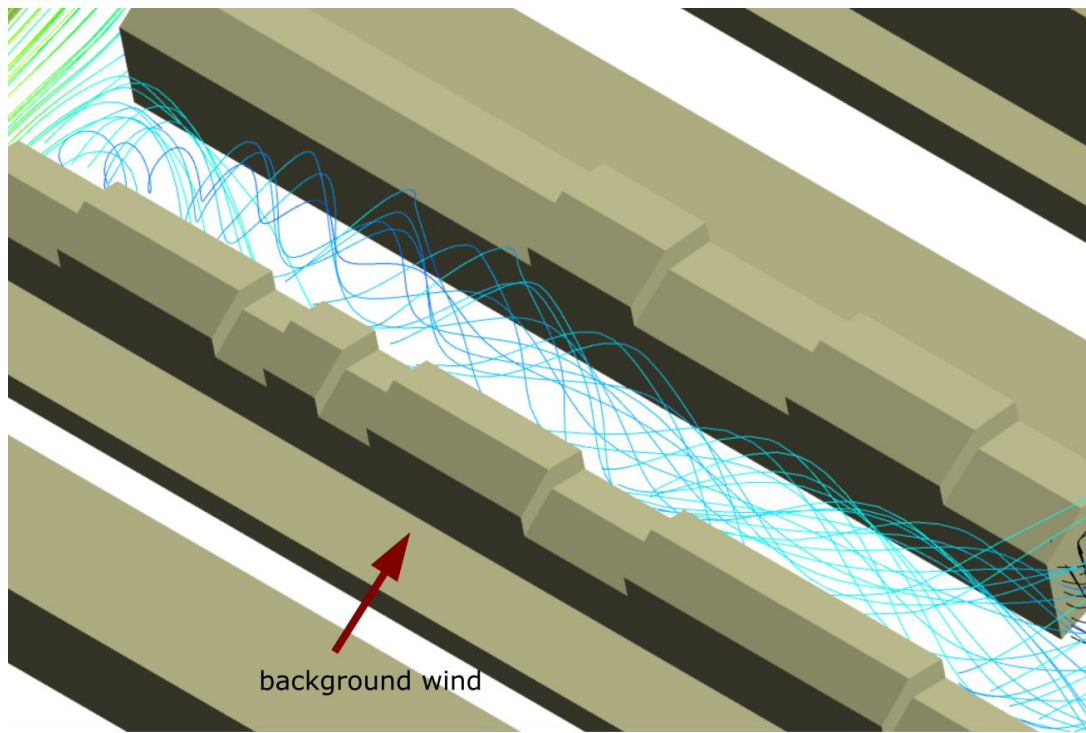
Plane name	Leeward building height (H_{lee})	Windward building height (H_{wind})	Description
v-plane1	20m	16m	Plane near the north street end
v-plane2	20m	16m	Plane in the north section
v-plane3	20m	20m	Plane in the north section
v-plane4	16m	16m	Plane in the north section
v-plane5	20m	20m	Plane in the north section, near the T-junction
v-plane6	16m	–	Plane across the T-junction
v-plane7	20m	16m	Plane in the south section, near the T-junction
v-plane8	20m	16m	Plane in the south section
v-plane9	16m	16m	Plane near the south street end

Table 7.1: Nine across-street vertical planes which are used to present velocity vectors and concentration contours.

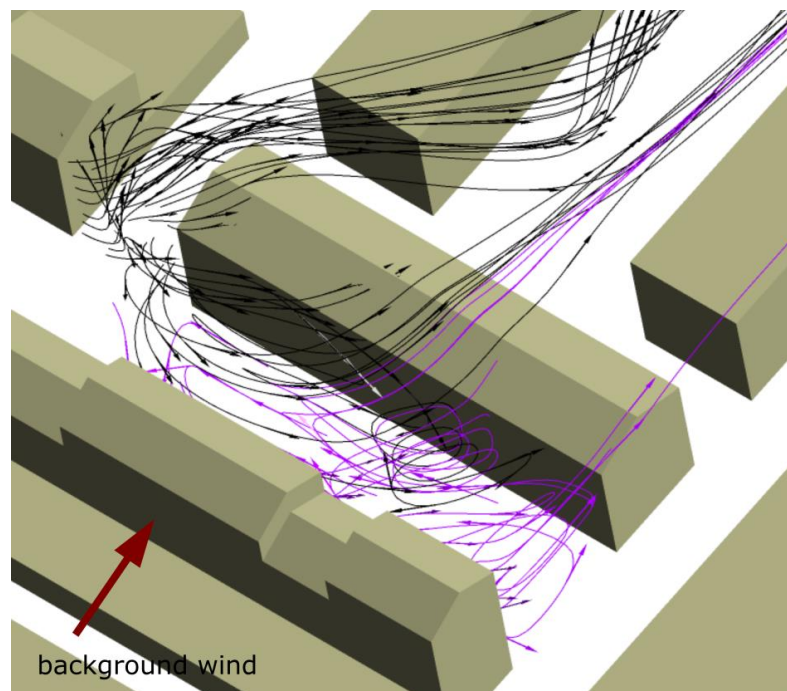


(a)

Figure 7.15(a)-(c): Streamlines in Gloucester Place, (a) overall view and relative positions of nine across-street vertical planes, (b) enlarged view for the north section, and (c) enlarged view for the south section.

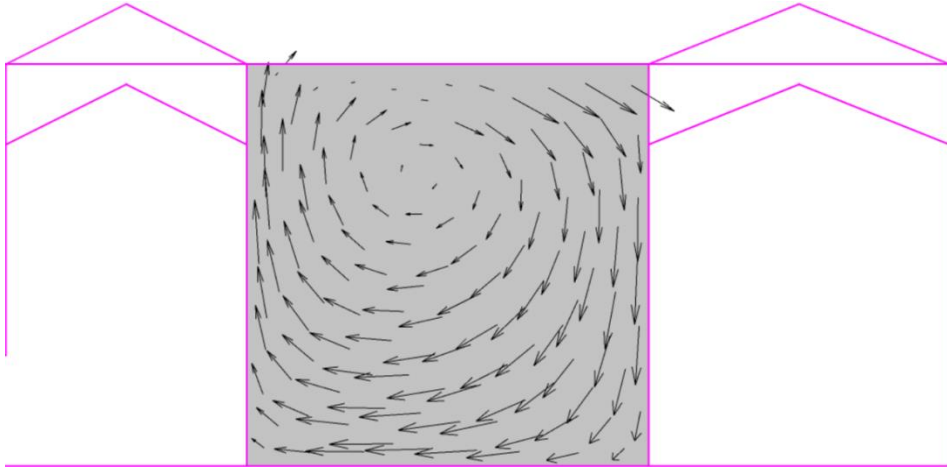


(b)

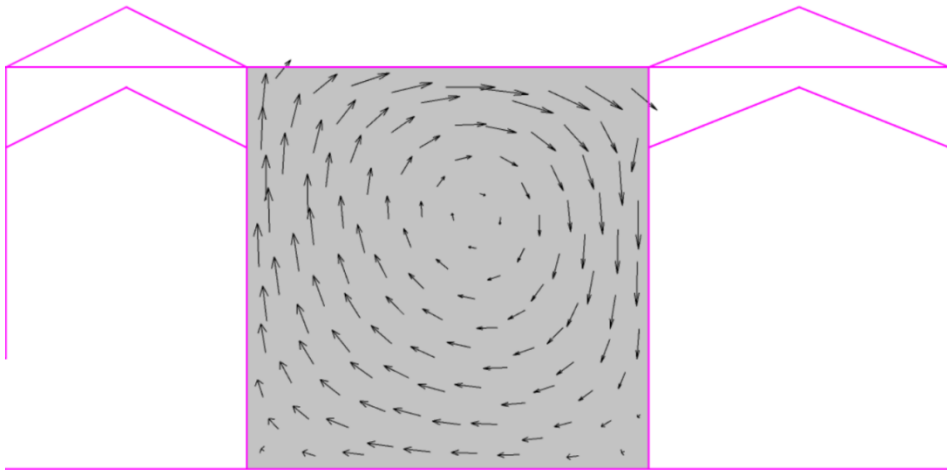


(c)

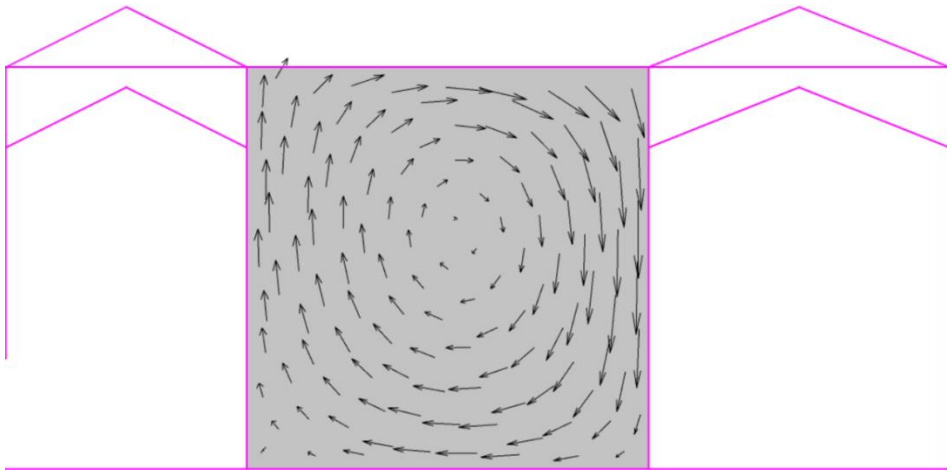
Figure 7.15(a)-(c) (continued): Streamlines in Gloucester Place, (a) overall view and relative positions of nine across-street vertical planes, (b) enlarged view for the north section, and (c) enlarged view for the south section.



(a)v-plane1, $H_{lee}=20\text{m}$ and $H_{wind}=16\text{m}$.

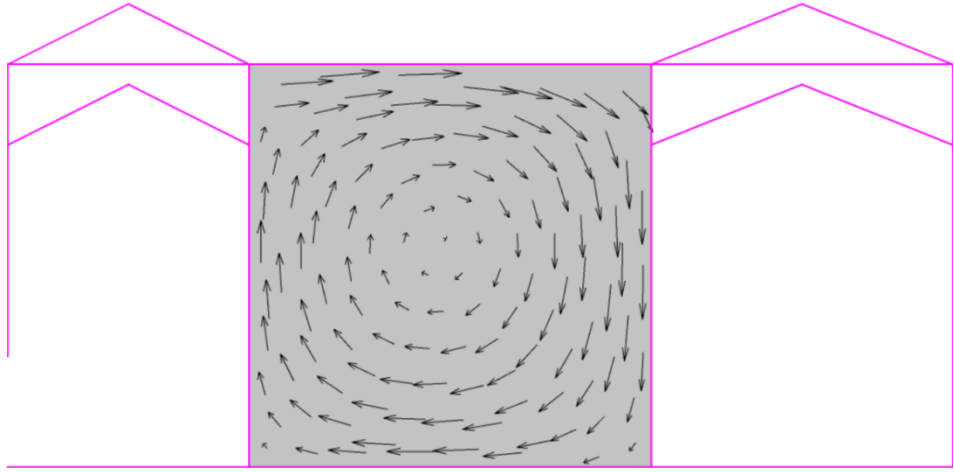


(b)v-plane2, $H_{lee}=20\text{m}$ and $H_{wind}=16\text{m}$.

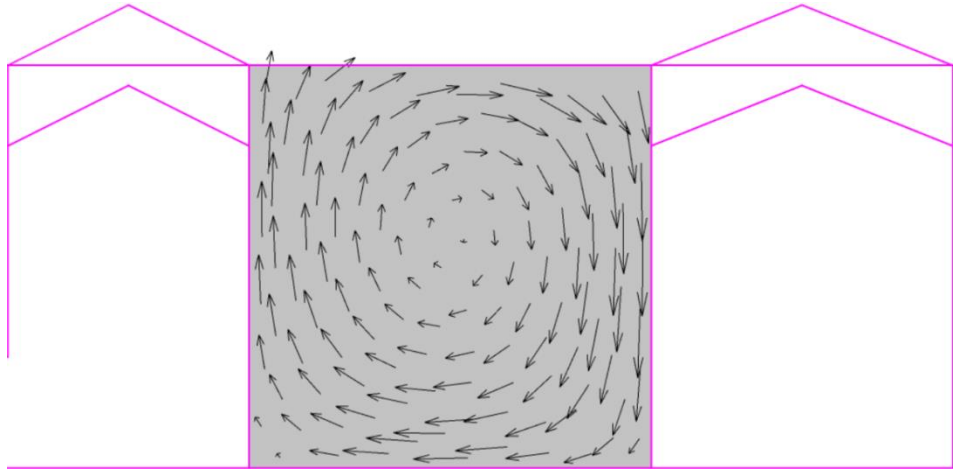


(c)v-plane3, $H_{lee}=20\text{m}$ and $H_{wind}=20\text{m}$.

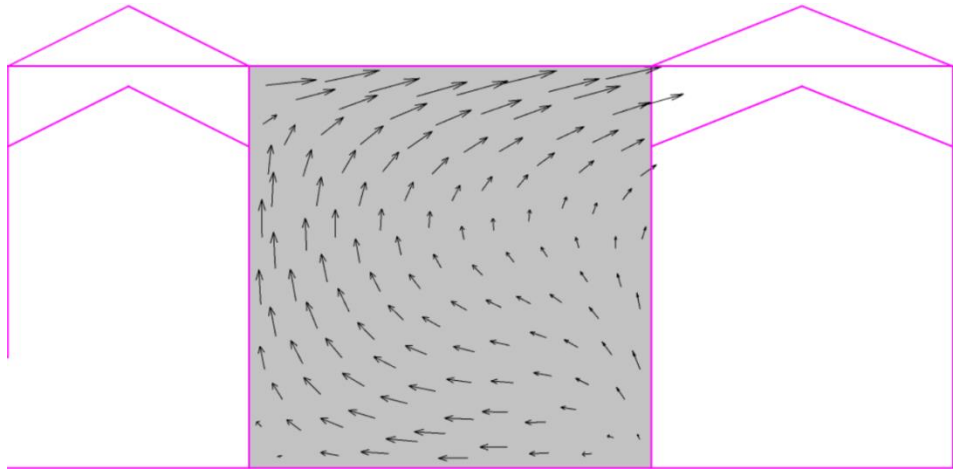
Figure 7.16: Velocity vectors on nine across-street vertical planes, (a)–(i): v-plane1 to v-plane 9.



(d)v-plane4, $H_{lee}=16\text{m}$ and $H_{wind}=16\text{m}$.

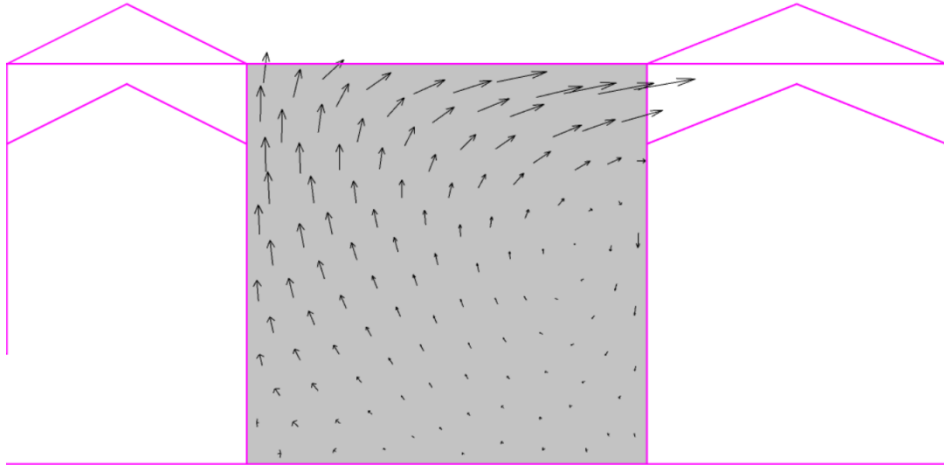


(e)v-plane5, $H_{lee}=20\text{m}$ and $H_{wind}=20\text{m}$.

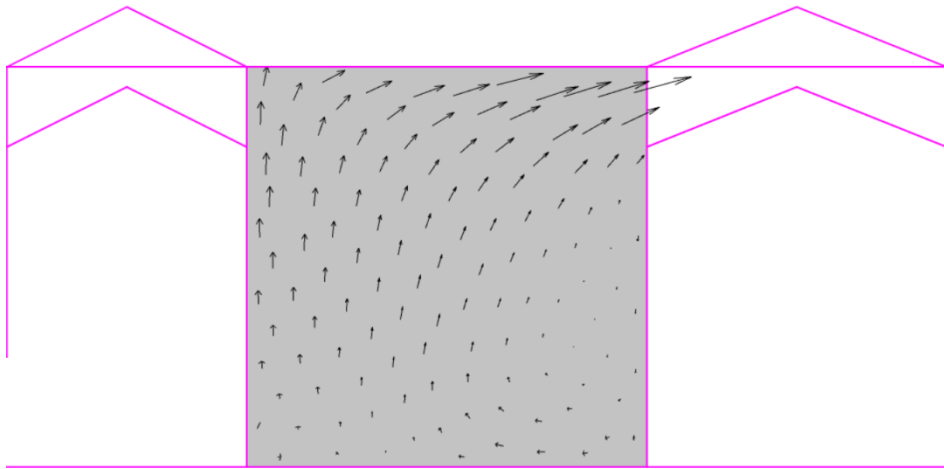


(f)v-plane6, $H_{lee}=16\text{m}$ (across the T-junction).

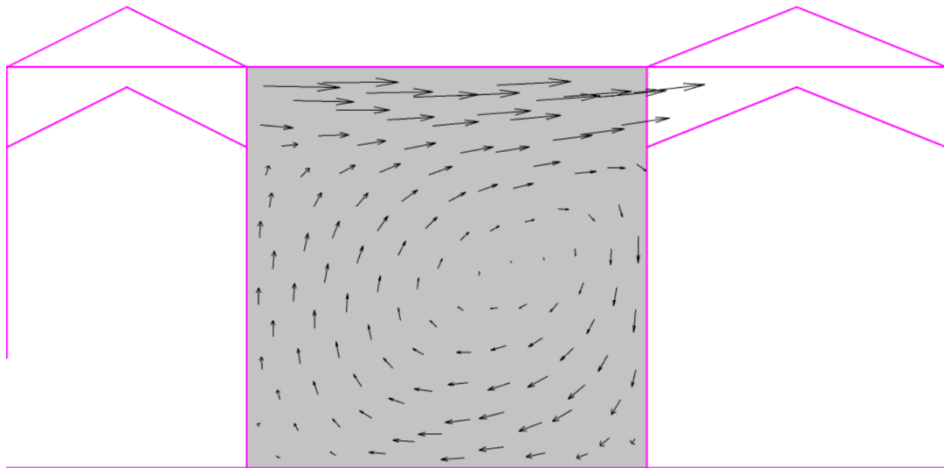
Figure 7.16 (continued): Velocity vectors on nine across-street vertical planes, (a)–(i): v-plane1 to v-plane 9.



(g)v-plane7, $H_{lee}=20\text{m}$ and $H_{wind}=16\text{m}$.



(h)v-plane8, $H_{lee}=20\text{m}$ and $H_{wind}=16\text{m}$.



(i)v-plane9, $H_{lee}=16\text{m}$ and $H_{wind}=16\text{m}$.

Figure 7.16 (continued): Velocity vectors on nine across-street vertical planes, (a)–(i): v-plane1 to v-plane 9.

7.4.1 Airflow in Zone 1

In Zone 1, flow approaches the test street not only from the top of the street but also from the north street end. As a result, a semi-vortex flow pattern forms in this zone, which is sketched in Figure 7.18 below. As shown in the figure, the semi-vortex is inclined with respect to the ground and the building walls. The top of the semi-vortex reaches to the windward building. The semi-vortex extends around $2.5H$ in the along-street direction (from north to south, judged according to Figure 7.12 above), which defines the size of Zone 1.

Projecting the semi-vortex on a horizontal plane also shows a semi-vortex pattern, which can be seen in Figure 7.12 above. A similar flow pattern is also found in Kastner-Klein's experiment (see Figure 5.23 in Section 5.6.3), on the horizontal plane that has the same relative height ($z=0.25H$) to the horizontal plane in Figure 7.12. However, the semi-vortex in the current study has stronger along-street momentum than in Kastner-Klein's experiment: in the experiment, the flow from the street end attaches to the leeward building after travelling $0.8H$ along the street; in the current study, the flow travels a longer distance (around $1.2H$) before attaching to the leeward building. This is because the diverged flow above the test street acts as an additional source to promote flow from the north to the south.

Additional vertical vortices are found forming above the semi-vortex, which are sketched in Figure 7.18 below. As suggested by the flow pattern on v-plane1 (see Figure 7.16(a) above), the centres of these vertical vortices are greatly above half of the characteristic building height ($0.5H$) and are relatively close to the leeward buildings. In addition, the tops of these vertical vortices are greatly above the roof level (H).

7.4.2 Airflow in Zone 2

In Zone 2, vortex flow and along-street flow coexists to produce tilted vortices, which are sketched in Figure 7.18 below. According to Figure 7.12 above, the along-street flow has relatively uniform velocity distribution on any vertical plane in Zone 2. On the other hand, the along-street flow accelerates until reaching the T-junction, which also can be seen in Figure 7.12.

V-plane2 to v-plane5 are in Zone 2. Vortex flow pattern is found on each of these planes (see Figure 7.16(b)–(e) above). The patterns are similar to each other and are also similar to the flow pattern for case AR100_6P_R3 in the parametric study (see Figure 6.3(d) in Section 6.4.1). These findings indicate that the along-street flow does

not severely interfere vortex flow in street canyon but acts as additional flow in the span-wise direction.

By scrutinizing the vortex flow patterns in Figure 7.16(b)–(e), it is noted that the vortex on v-plane4 is slightly smaller compared to the other three planes. It is also noted that the leeward and windward buildings for v-plane4 are 16m tall, whereas the leeward buildings for v-plane2, v-plane3 and v-plane5 are all 20m tall. Thus, it is thought that local aspect ratio still has an impact on the shape of vortex flow. However, this impact is not as significant as for 2D street canyon, since the difference between the vortices on v-plane4 and on any of other three planes is not as large as the difference between the vortex in a 2D street with $AR=0.8$ and the vortex in a 2D street with $AR=1.0$, such as the vortices shown in Figure 6.3(b) and (d) in Section 6.4.1.

7.4.3 Airflow in Zone 3

To understand the flow structure in Zone 3, it is necessary to understand the flow at the T-junction at first. Multiple flow directions are found across the T-junction plane, as shown in Figure 7.17 below. Affected by the main stream above the test street, flow leaves the street through the top of the T-junction plane. On the other hand, it is observed in Figure 7.17 that flow approaches the test street through the right part of the T-junction plane, and then merges into the flow coming from the north section. This flow direction is because along-street is even stronger in the street after the test street. In the rest parts of the T-junction plane, flow travels along the plane.

After the merge of the along-street flow and the flow approaching from the T-junction, span-wise velocity (W) decreases in the south section of the test street, as can be seen in Figure 7.12 above. The merged flow still travels from the north to the south in Zone 3 but loses its momentum gradually until meeting the flow from the south street end. These two opposite flows shear each other in Zone 3. As a result, the along-street flow ascends, deviates towards the windward buildings and finally passes over the windward buildings; the flow from the south street end descends, deviates to the leeward buildings and finally recirculates back to the south street end (see the sketches in Figure 7.18 below).

V-plane6 to v-plane8 are in Zone 3. Owing to the shear between the along-street flow and the flow from the south street end, vortex flow pattern does not appear on any of these planes (see Figure 7.16(f), (g) and (h) above). Since v-plane6 is across the T-junction, the flow pattern on this plane is a projection of the flow structure at the T-

junction. In detail, the flow out of the T-junction approaches the street from the lower part of the T-junction and then moves upward; the flow near the roof level travels from the leeward side to the windward side and then leaves the street from the upper part of the T-junction (see Figure 7.16(f) above). Unique flow patterns are found on v-plane7 and v-plane8 (see Figure 7.16(g) and (h) above). In the leeward part of each plane, flow moves from the bottom to the top; in the windward part and near the ground, both horizontal and vertical motions are very weak, which indicates relatively strong along-street motions at these positions.

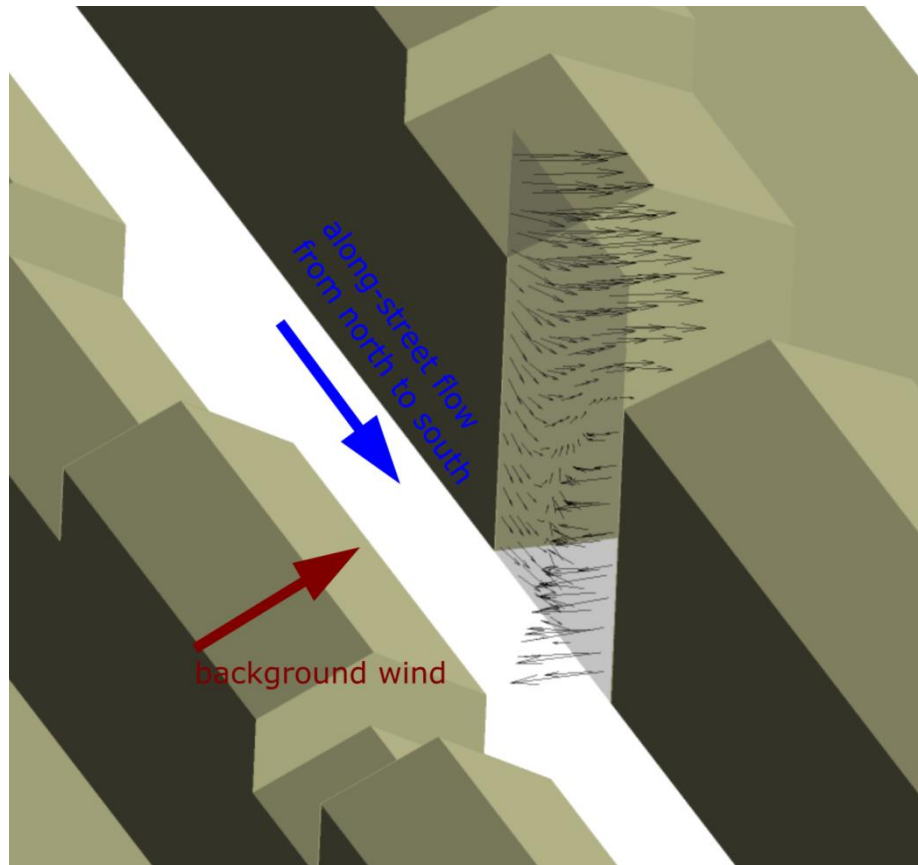


Figure 7.17: Velocity vectors across the T-junction plane.

7.4.4 Airflow in Zone 4

The flow in Zone 4 shares similar flow regime in Zone 1. A semi-vortex flow also forms in Zone 4, which is sketched in Figure 7.18 below. However, since the flow from the south street end has an opposite direction to the along-street flow in the south section of the test street, the semi-vortex is compressed towards the south street end. Consequently, compared to the semi-vortex in Zone 1, the semi-vortex in Zone 4 has a smaller tilt angle to the ground and extends a shorter distance in the along-street direction (around $1.5H$, judged according to Figure 7.12 above).

V-plane9 locates at the boundary between Zone 3 and Zone 4. As a result of the shear between the along-street flow and the flow from the south street end, an elliptical vortex flow pattern forms on this plane (see Figure 7.16(i) above). The top of the elliptical pattern is much below the roof level for the street ($H=20\text{m}$), because both the leeward and windward buildings for v-plane9 are only 16m tall.

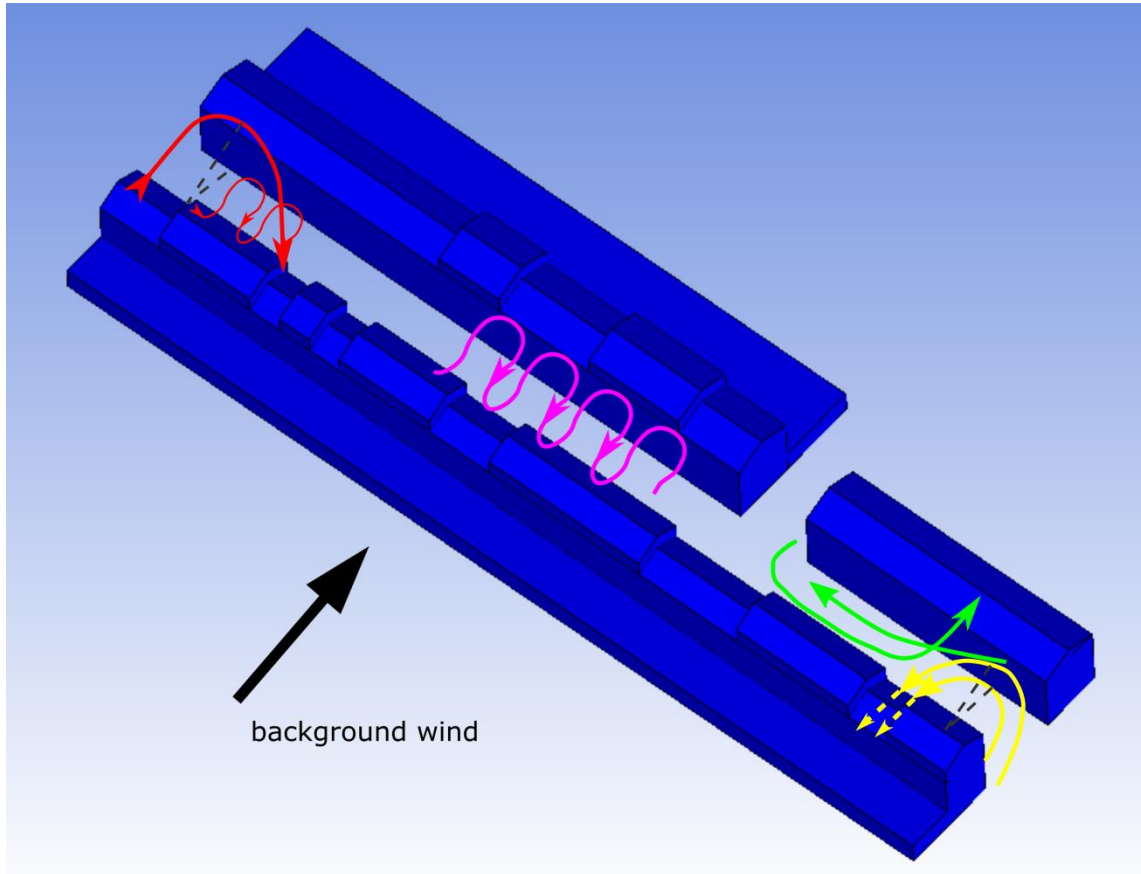


Figure 7.18: A sketch of flow structures in Zone 1(red), Zone 2 (pink), Zone 3 (green) and Zone 4 (yellow).

7.5 Pollutant concentration distribution

The pollutant distributions on the two horizontal planes (i.e., pedestrian level $z=2\text{m}$ and half of the characteristic building height $z=10\text{m}$) are shown in Figure 7.19 and Figure 7.20 below respectively. The pollutant distributions on the nine vertical across-street planes are shown in Figure 7.21 below. It should be mentioned that the legends used in the three figures are not the same, in order to offer the best vision for each contour.

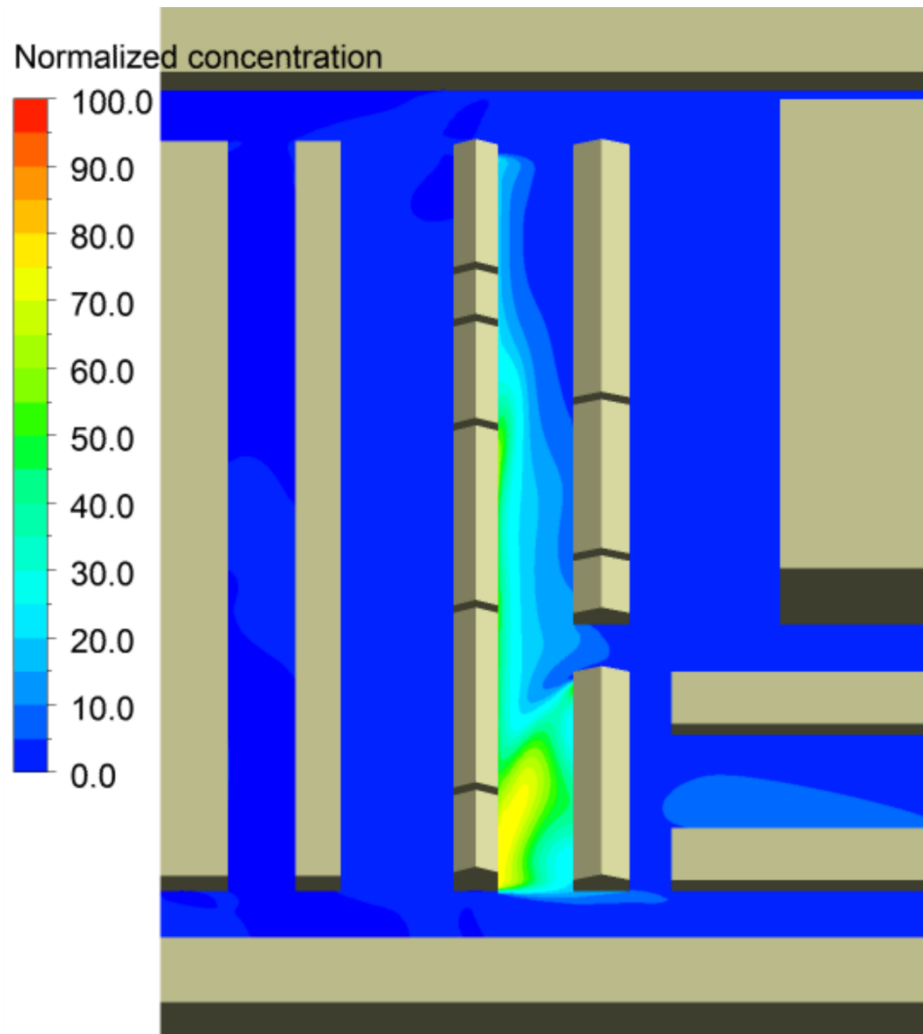


Figure 7.19: Pollutant concentration on the horizontal plane at height $z=10\text{m}$ ($0.5H$).

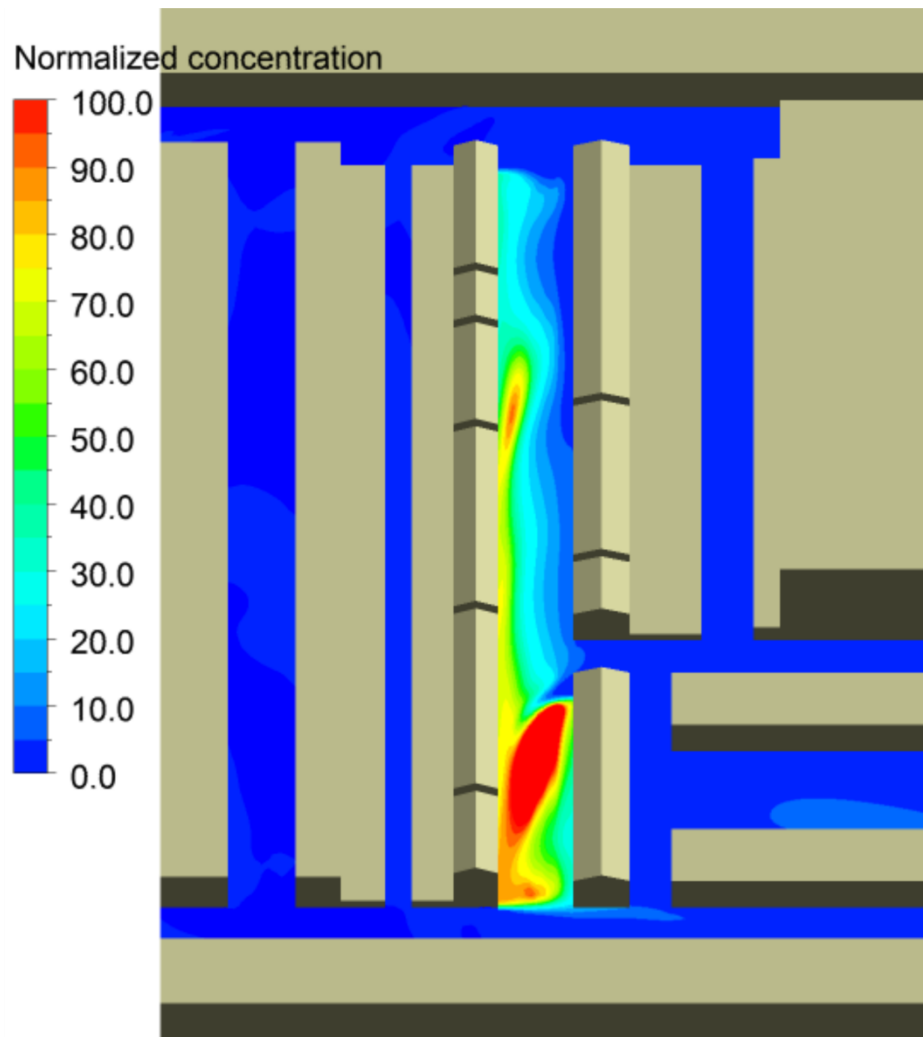


Figure 7.20: Pollutant concentration on the horizontal plane at height $z=2\text{m}$ ($0.1H$ and pedestrian level).

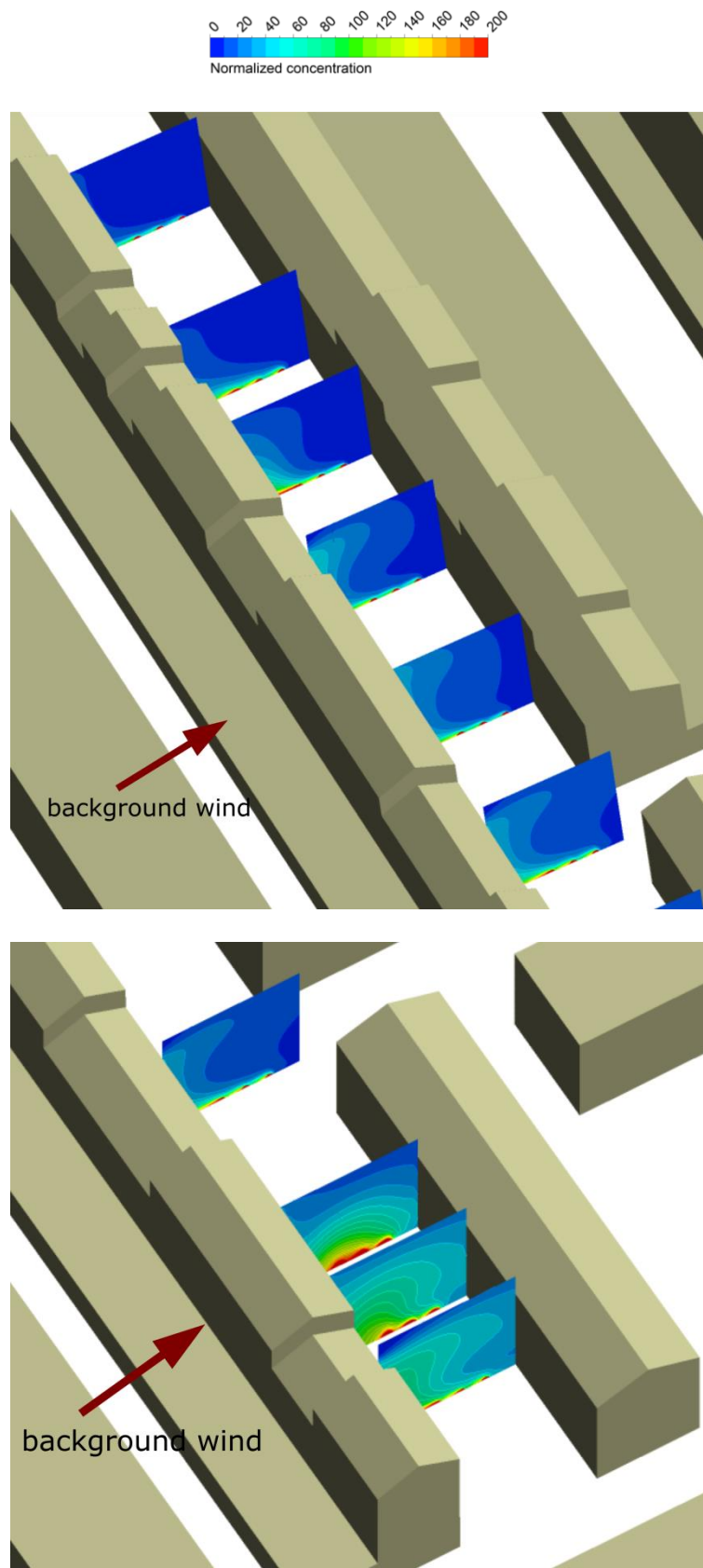


Figure 7.21: Pollutant concentration on nine across-street vertical planes: v-plane1 to v-plane 5 (top) and v-plane6 to v-plane9 (bottom).

All the concentration contours above show a clear difference between the north section and the south section of the test street. This is obviously related to the specific flow structures in these two sections.

In the north section of the test street, vortex flow and along-street flow coexist. Pollutants are removed away from the top of the street by the vortex flow. This type of flow causes relatively higher concentration in the leeward side than in the windward side (see Figure 7.21 above), which is consistent with the pollutant distribution in case AR100_6P_R3 in the parametric study. Moreover, the along-street flow in the north section flushes pollutants from the north to the south and generates an apparent gradient of concentration in the along-street direction (see Figure 7.19 and Figure 7.20 above). In contrast, the along-street flow does not exist in any 2D street canyon, such as the case AR100_6P_R3 in the parametric study. Consequently, the concentration on any vertical plane in the north section is significantly lower than the concentration in the case AR100_6P_R3 (mentioned by comparing their canyon concentrations later in Section 8.4.1.4).

Since vortex flow does not form in the south section of the test street, the overall concentration in the south section is several times higher than in the north side section and is even higher than in the case AR100_6P_R3. In addition, the weak horizontal air motions in the south section causes poor mixing performance across the street. Hence, the pollutants in the south section are evenly distribution between the leeward part and the windward part (see Figure 7.19, Figure 7.20 and Figure 7.21 above). Furthermore, since both horizontal and vertical velocities are extremely low near the ground of the south section, extremely high pollutant concentration is found around the three emission sources in Figure 7.21 above.

According to Figure 7.19 and Figure 7.20, it is further found that the concentrations inside the test street are much higher than outside the street. Thus, the traffic emission only affects local air quality and has limited impact on the surrounding area. However, there is one exception: the concentration behind the windward buildings of the south section is around 5–10 normalized units. This is because the flow above the test street, which brings the pollutants removed from the south section, descends after passing the windward buildings.

7.6 Summary of main findings

This chapter models airflow and pollutant dispersion in a real urban area—Gloucester Place and its surrounding city blocks. It is aimed to understand typical flow features in this area, what type of geometry cause them and how they impact on pollutant distribution. Gloucester Place is chosen as the test street. The prevailing wind coming from west-southwest is assumed, giving a perpendicular background wind condition for the test street.

The presence of a tall building at a downstream position in the model has a profound effect on the flow in the urban area. It causes the flow upstream to it ascend and diverge, and produces asymmetrical behind it. These flow features further affect the flow between the city blocks. As a good illustration, the diverged flow drives along-street flow in the two streets before the tall building, namely the test street and the street after the test street. This type of flow can transport pollutants along the street and reduce the concentration in the street.

The flow in the test street canyon are analysed in detail. Four flow features are found in the test street, which divide the street into four zones. The divisions are indicated in Figure 7.15, and the flow structure in each zone is sketched in Figure 7.18. (1) Semi-vortex flow forms near the north street end, and vertical vortices forms above it. The semi-vortex in this study has stronger along-street momentum than that in Kastner-Klein's experiment. (2) In the rest part of the north section of the street, vortex flow and along-street coexists, producing tilted vortices and flushing pollutants from the north to the south. They are responsible for much lower concentration in the north section than in the south section. In addition, the overall concentration in the north section is lower than the overall concentration in one of the cases in the parametric study that shares similar street and building geometries. (3) It is found that most flow near the T-junction approaches the street rather than leaves the street. The approaching flow merges into the flow from the north section. The merged flow further travels in the south section of the test street from the north to the south, until meeting the flow from south street end. These two opposite flows shear each other, causing the disappearance of vortex flow in the south section. As a result, the overall concentration in the south section is not only much higher than in the north section but also higher than in the case in the parametric study. In addition, owing to the weak horizontal velocity in the south section, pollutants are evenly distribution between the leeward part and the windward part. (4) The flow

near the south end shares similar regime to the north street end. However, as the flow from the south street end is opposite to the along-street flow in the south section, the semi-vortex flow is weaker near the south street end than near the north street end.

8 Analyses of the Effects of Three Urban Geometries

The last chapter has highlighted the formation of a few unique flow features due to the presence of a tall building at a downstream position. However, it has hidden the importance of other geometries in the model. For this consideration, this chapter aims to study three characteristic geometries in that model, namely heterogeneous buildings, pitched roofs and T-junction, which are commonly seen in the real world and are potential to have significant impacts on the airflow. The study is conducted by modifying one or some of these geometries to build up several additional models and then comparing the results for these models with the results for the original model.

The structure of this chapter is given as follows. Section 8.1 describes the model geometry of each case. Section 8.2 analyses the impacts of the three characteristic geometries on airflow by showing different flow patterns for the models with and without these geometries. Sections 8.3 and 8.4 use the bulk parameters proposed in the previous parametric study to assess ventilation efficiency and pollutant removal performance at different locations for each case. Section 8.5 summarizes the main findings of this chapter.

8.1 Model geometries

There are ten cases modelled in this study, and the geometries of them are sketched in Table 8.1 below. Case 10, a case identical to the model in the last chapter, is regarded as the reference for comparisons. Cases 3–9 modify one or some of the three characteristic geometries from Case 10, while all the CFD model settings are kept the same as before. By comparing various results for these cases, it is able to understand the roles of the three characteristic geometries in affecting local airflow.

Additionally, two of the models in the parametric study are included in the current study (i.e., Cases 1 and 2). They share similar aspect ratio and pitched roof geometry to some of the cases in Cases 3–10. By comparing the results for these two cases with the results for the above eight cases, it is possible to understand the different ventilation efficiency and pollutant removal performance for an ideal street canyon and for a real urban area and identify whether pitched roofs make consistent impacts under these two types of geometries.



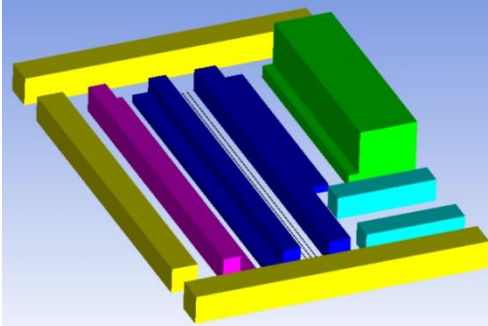
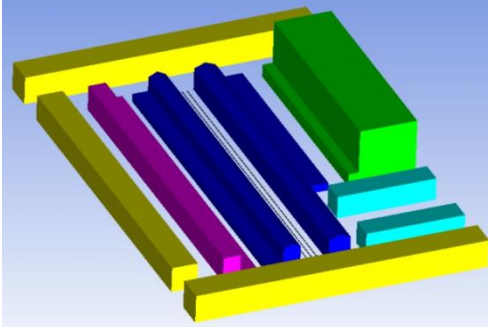
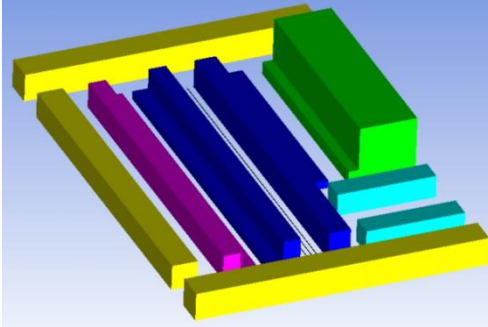
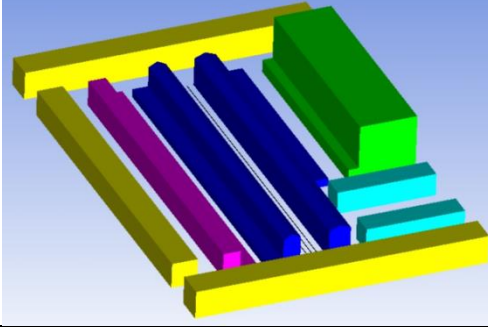
Case	Buildings adjacent to test street	Roof type	Junction	Sketch of geometry
1 (2D)	homogeneous ($H=12\text{m}$)	flat	no	
2 (2D)	homogeneous ($H=12\text{m}$)	pitched, $R=3\text{m}$	no	
3 (3D)	homogeneous ($H=16\text{m}$)	flat	no	
4 (3D)	homogeneous ($H=16\text{m}$)	pitched, $R=3\text{m}$	no	
5 (3D)	homogeneous ($H=20\text{m}$)	flat	no	
6 (3D)	homogeneous ($H=20\text{m}$)	pitched, $R=3\text{m}$	no	

Table 8.1: A summary of the characteristic urban geometries in ten studied cases.

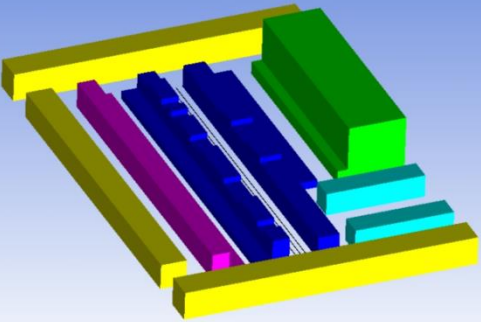
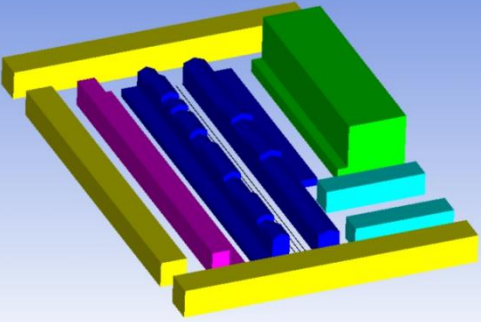
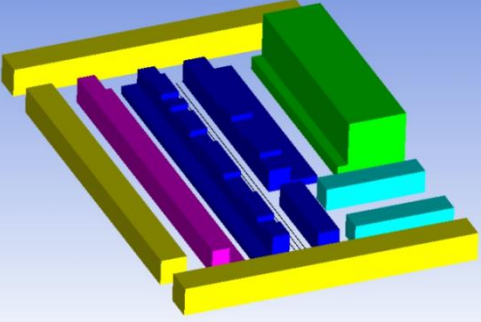
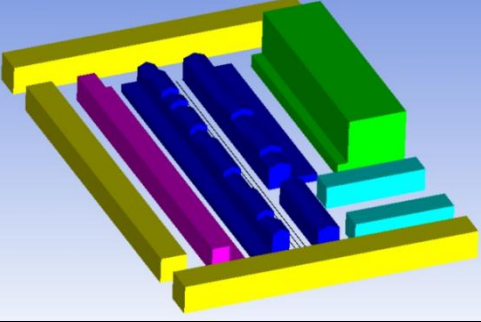
Case	Buildings adjacent to test street	Roof type	Junction	Sketch of geometry
7 (3D)	heterogeneous (either 16m or 20m tall)	flat	no	
8 (3D)	heterogeneous (either 16m or 20m tall)	pitched, $R=3\text{m}$	no	
9 (3D)	heterogeneous (either 16m or 20m tall)	flat	T-junction between windward buildings	
10 (3D)	heterogeneous (either 16m or 20m tall)	pitched, $R=3\text{m}$	T-junction between windward buildings	

Table 8.1 (continued): A summary of the characteristic urban geometries in ten studied cases.

8.2 Flow structures

This section analyses the impacts of heterogeneous buildings, pitched roofs and T-junction on the flow structures in Gloucester Place. The following three sub-sections show the most different flow structures between the cases with and without these geometries and discuss their significance.

8.2.1 Heterogeneous buildings

The heterogeneous buildings are found to have limited impact on the flow structures. Compared to the cases with either 16m tall homogeneous buildings or 20m tall homogeneous buildings on both sides of the test street, the heterogeneous buildings in Cases 7 and 8 still lead to vortex flow in the street. However, the vortex shape is slightly different. For example, Figure 8.1 below shows three vortex flow patterns on v-plane4 for Cases 4, 6 and 8. As can be observed from the figure, the vortex for Case 8 has a shape somewhere between the vortex shapes for the other two cases. In addition, the vortex shape for Case 8 is closer to the shape for Case 6 than for Case 4, even Case 8 has the same building heights on v-plane4 to Case 4 but not Case 6. This is because taller neighbouring buildings to v-plane4 produce a vortex whose top is above the height $z=16\text{m}$.

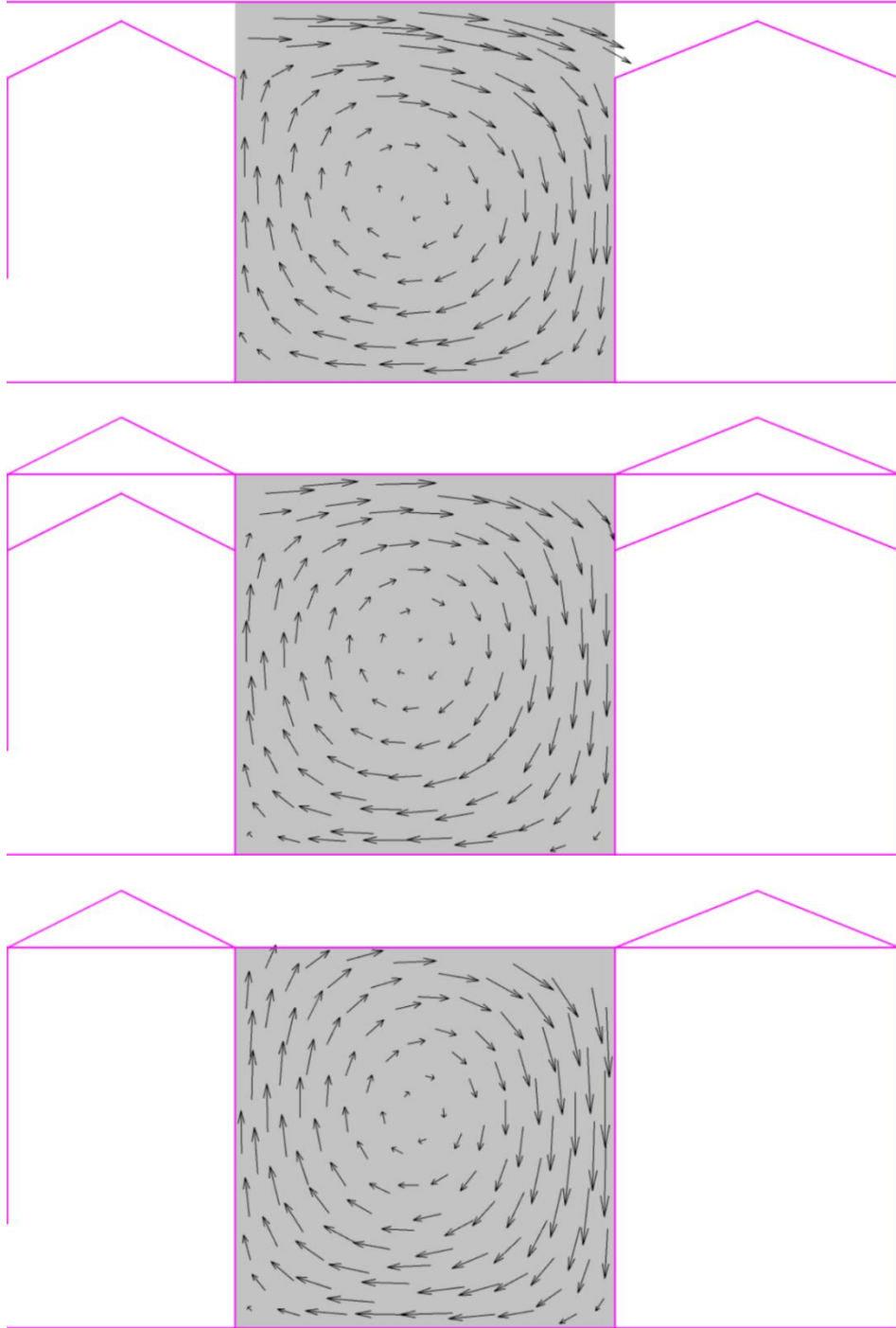


Figure 8.1: Velocity vectors on v-plane4. Top: Case 4, middle: Case 8 (heterogeneous buildings, $H_{lee}=H_{wind}=16\text{m}$ in that cross-section), and bottom: Case 6.

8.2.2 Pitched roofs

The pitched roofs are found to affect vortex shape in the north section of the test street. As a good illustration, Figure 8.2 below shows that vortex flow forms on v-plane3 in both Case 9 and Case 10. However, due to the presence of pitched roofs in Case 10, the vortex centre for Case 10 is slightly closer to the roof level than for Case 9, indicating a

larger vortex whose top is above the roof level. This is similar to the finding in the previous parametric study, which manifests that pitched roofs have consistent impacts on airflow between in the previous study and in the current study.

The pitched roofs have rather complicated effects on the flow in the south section of the test street.

First, the pitched roofs on the buildings in the north section lead to faster dissipation of vortex flow in the along-street direction, if the T-junction does not exist. As shown in Figure 8.3 below, a vortex forms on the third plane (counting from the north) in Case 7 (with pitched roofs), while vortex flow does not appear on the fourth plane. They suggest that the tilted vortices dissipate between these two planes in Case 7. On the other hand, vortex flow does not form from the third plane in Case 8 (with flat roofs). It suggests that the tilted vortices dissipate before the third plane in Case 8.

Second, the pitched roofs on the buildings in the south section promote flow coming from the south street end. As indicated by the different blue arrows between Figure 8.3 and Figure 8.4 below, the flow from the south street end occupies a larger volume over the ground in Case 8 than in Case 7 and travels a longer distance along the street in Case 8. Thus, the presence of pitched roofs should benefit ventilation and pollutant removal near the south street end.

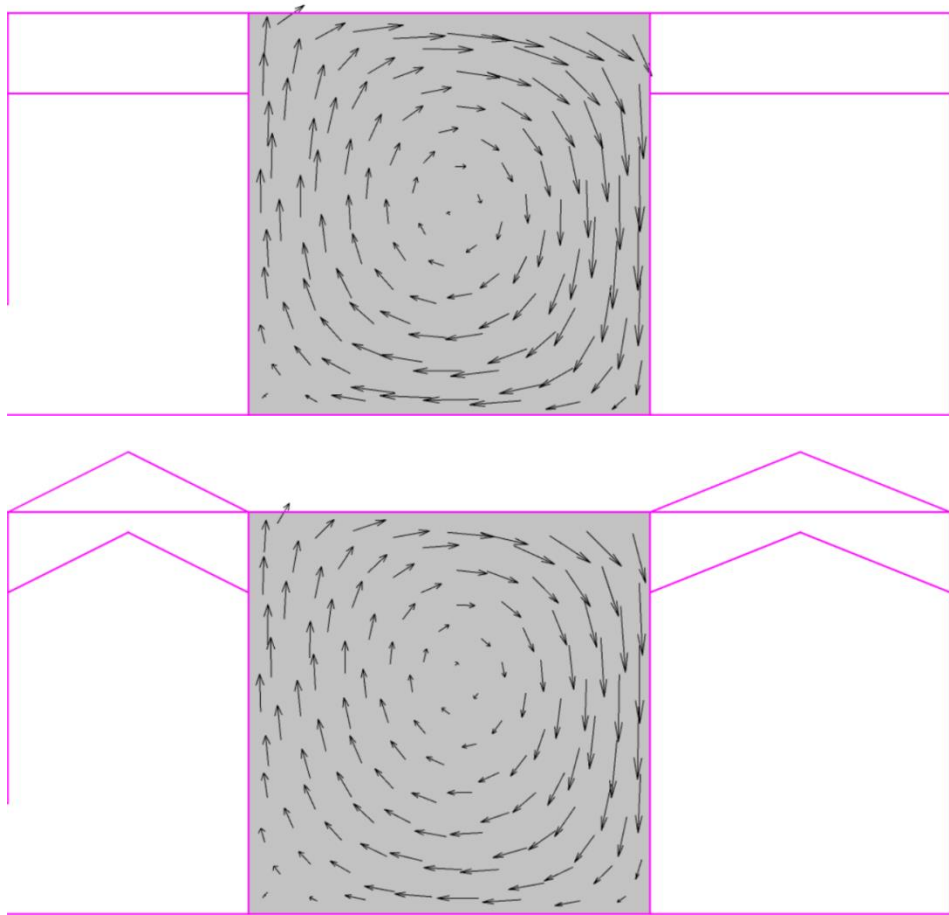


Figure 8.2: Velocity vectors on v-plane3, top: Case 9, and bottom: Case 10.

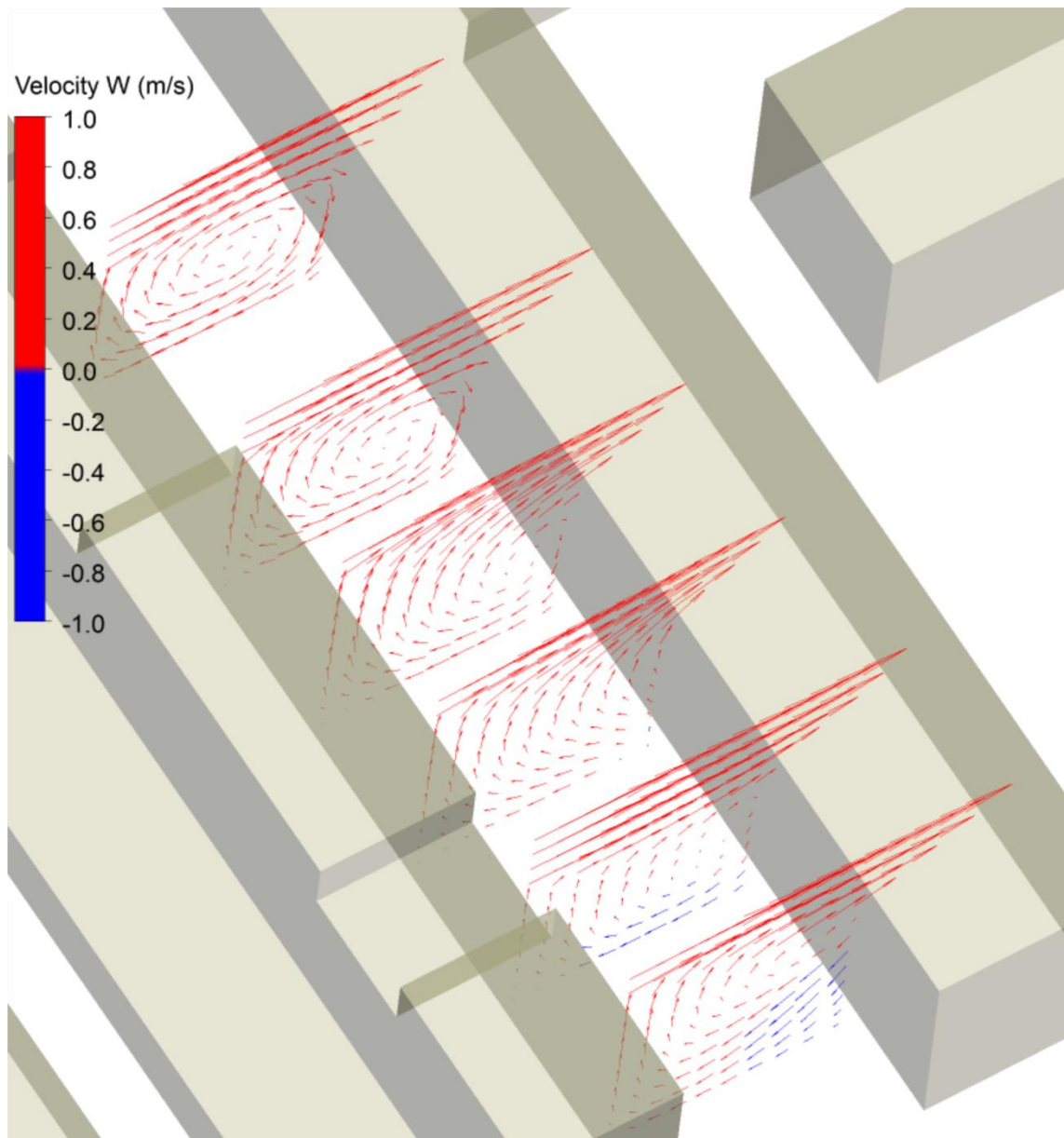


Figure 8.3: Tangential velocity vectors on six planes in the south section, Case 7.

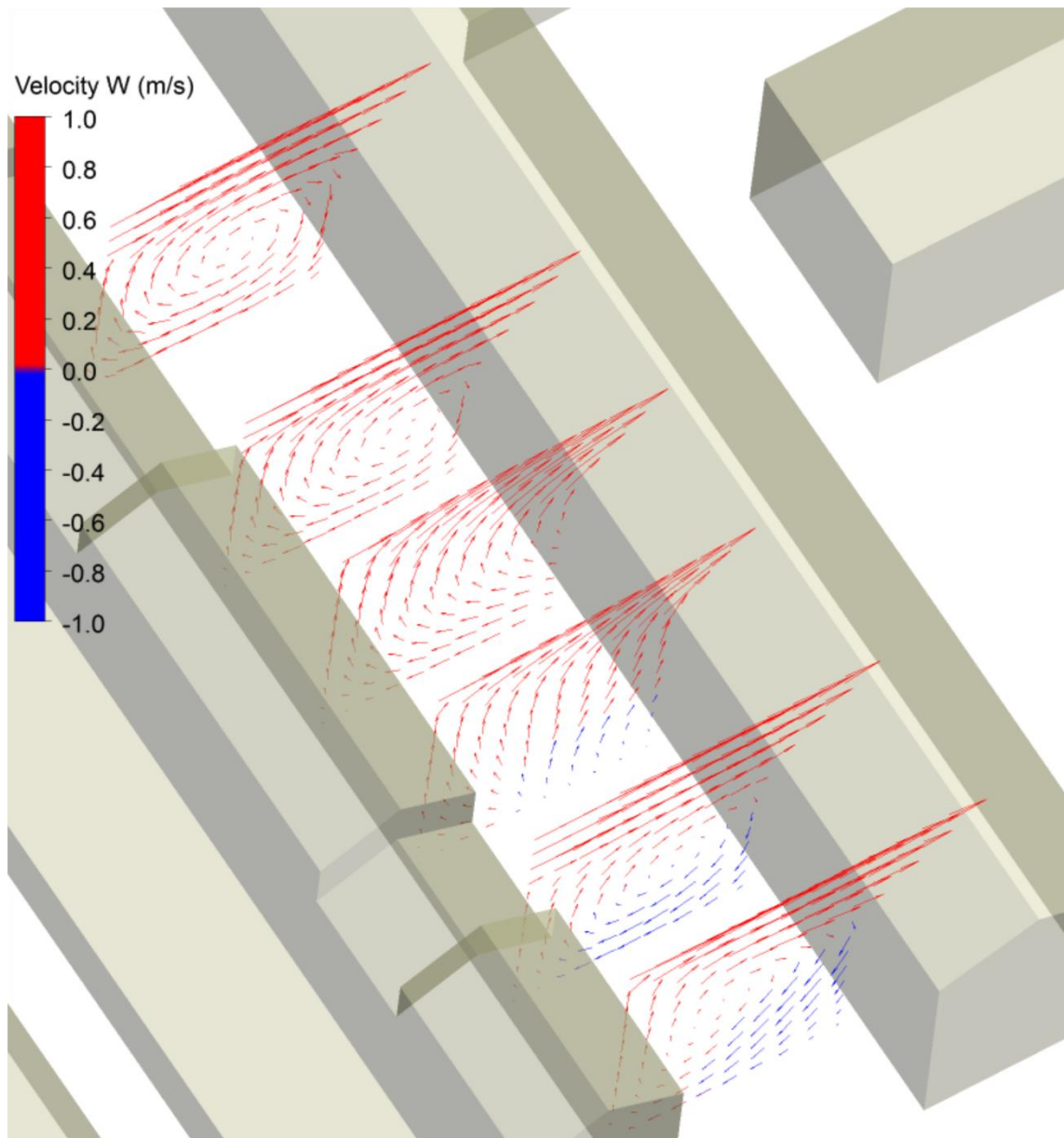


Figure 8.4: Tangential velocity vectors on six planes in the south section, Case 8.

8.2.3 T-junction

The T-junction between the windward buildings is found to have a profound effect on the flow around it and in the south section of the test street canyon. As can be seen in Figure 8.4 above, when T-junction does not exist, tilted vortices still form in some parts of the south section in Case 8. These vortices are gradually pushed towards the windward buildings after passing the T-junction and dissipate completely near v-plane7. However, in Case 10 which has a T-junction, airflow approaches the street through the T-junction, which can be seen in Figure 8.5 below and has been discussed in the last chapter. As a result, the titled vortices are terminated before the T-junction, as shown by the flow patterns on the first, second and third planes (counting from the north) in Figure 8.5.

Additionally, the flow from the T-junction merges into the flow from the north section, which weakens along-street flow in the south section. As a consequence, the flow from the south street end becomes stronger and penetrates deeper, as can be discovered after comparing the different blue arrows between Figure 8.4 above and Figure 8.5 below.

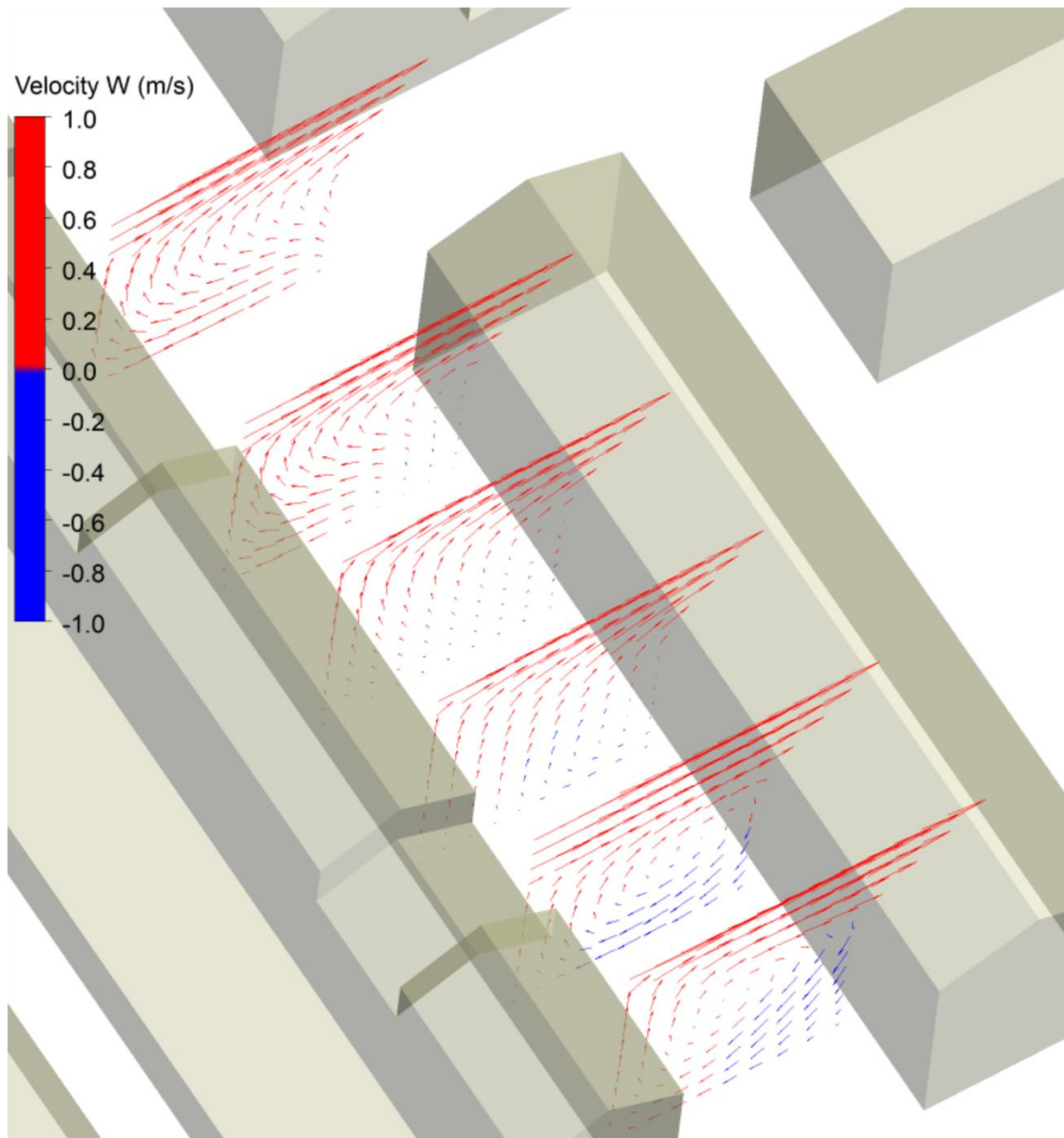


Figure 8.5: Tangential velocity vectors on six planes in the south section, Case 10.

8.3 Assessment of ventilation

This section uses two bulk parameters proposed in Section 6.4.4 to assess ventilation efficiency, namely mixing velocity U_{mix} and exchange velocity U_{ex} . The calculation of U_{mix} follows the same approach mentioned before, which is re-stated as Equation 8.1. However, as the flow in the span-wise direction exists in Cases 3–10, the calculation of U_{ex} should further include mean velocity V , mean momentum flux component v_w and turbulent momentum flux component $v'w'$. Thus, U_{ex} is calculated by Equations 8.2 and 8.3.

$$U_{mix} = \frac{\int_{L_{mid}} |U| dl}{L_{mid}} \quad (8.1)$$

$$U_{ex} = \frac{\iint_{A_{ex}} [(\rho UW + \rho \overline{u'w'})^2 + (\rho VW + \rho \overline{v'w'})^2]^{1/2} dS}{\rho A_{ex} (U_{ref} - U_{can})} \quad (8.2)$$

$$where U_{can} = \frac{\iiint_{V_{can}} (U^2 + V^2 + W^2)^{1/2} dV}{V_{can}} \quad (8.3)$$

Both mixing velocity U_{mix} and exchange velocity U_{ex} are calculated for the whole street and for nine across-street vertical planes whose positions are given before in Table 7.1 and shown in Figure 7.15(a) (see Section 7.4). Figure 8.6 and Figure 8.7 below display the calculated data for the whole street for each case, and Figure 8.8 and Figure 8.9 below display the calculated data for the nine across-street vertical planes for each case. All the data are normalized by the free-stream velocity $U_0=7\text{m/s}$.

8.3.1 Ventilation efficiency for whole test street

This section analyses the effects of heterogeneous buildings, pitched roofs and T-junction on ventilation efficiency for the whole test street. In addition, this section discusses different ventilation efficiencies between the 2D models and the 3D models.

8.3.1.1 The effect of heterogeneous buildings

The impact of heterogeneous buildings on ventilation is analysed by comparing the data between Cases 3, 4, 5, 6, 7 and 8.

As can be noted from Figure 8.6 below, for a fixed roof type, mixing velocity is higher in the case with 16m tall homogeneous buildings than in the case with 20m tall homogeneous buildings. Compared to these two cases, the case with heterogeneous buildings has an intermediate mixing velocity.

Amongst the cases with pitched roofs, the case with heterogeneous buildings (i.e., Case 8) has an intermediate exchange velocity compared to the two cases with 16m tall and 20m tall homogeneous buildings (see Figure 8.7 below). However, when the roofs are flat, the exchange velocity for the case with heterogeneous buildings (i.e., Case 7) is higher than the exchange velocities for the other two cases.

According to the above findings, the heterogeneous buildings give intermediate air mixing efficiency and air exchange efficiency, compared to the homogeneous buildings which have the same height to the tallest building in the heterogeneous buildings and the homogeneous buildings which have the same height to the lowest building in the heterogeneous buildings. However, the heterogeneous buildings enhance air exchange at the roof level when the buildings have pitched roofs.

8.3.1.2 The effect of pitched roofs

The impact of pitched roofs on ventilation is analysed by comparing the data between Cases 3, 4, 5, 6, 7, 8, 9 and 10.

As can be noted from Figure 8.6 below, the cases with pitched roofs always have around 20% lower mixing velocity compared to the cases with flat roofs. As can be seen from Figure 8.7 below, the presence of pitched roofs causes much lower exchange velocity in Cases 6, 8 and 10 than in Cases 5, 7 and 9. However, the pitched roofs in Case 4 makes higher exchange velocity than in Case 3.

According to the above findings, in general, the pitched roofs give worse air mixing and air exchange compared to the flat roofs.

8.3.1.3 The effect of T-junction

The impact of T-junction on ventilation is analysed by comparing the data between Cases 7, 8, 9 and 10.

Figure 8.6 below shows that mixing velocity is almost the same between Cases 7 and 9, and between Cases 8 and 10. After reviewing the bars in Figure 8.7 below, it is found that the cases with a T-junction (i.e., Cases 9 and 10) have around 10% lower exchange velocity compared the cases without a T-junction (i.e., Cases 7 and 8).

According to the above findings, the T-junction has limited impact on air mixing but slightly reduces air exchange efficiency.

8.3.1.4 The difference between the 2D models and 3D models

It is straightforwardly seen in Figure 8.6 below that when the roofs are flat, the 2D model (i.e., Case 1) has comparable mixing velocity to the four 3D models (i.e., Cases 3, 5, 7 and 9). The pitched roofs in Case 2 reduce mixing velocity by 50% from Case 1; however, the pitched roofs in the four 3D models (i.e., Cases 4, 6, 8 and 10) do not make such huge reductions. Thus, the 2D model with pitched roofs has up to 90% lower mixing velocity than the 3D models with pitched roofs.

As can be seen in Figure 8.7 below, when the roofs are flat, three out of four 3D cases (i.e., Cases 5, 7 and 9) have up to 40% higher exchange velocity than the 2D case (i.e., Case 1). The pitched roofs in Case 2 reduce exchange velocity by 70% from Case 1, which is even more significant than the reduction for mixing velocity. Thus, all the four 3D cases with pitched roofs, namely Cases 4, 6, 8, and 10, have an exchange velocity several times higher than the exchange velocity for Case 2.

According to the above findings, when the roofs are flat, the 3D models based on the real urban geometries have similar air mixing efficiency to the 2D model based on the ideal urban geometry, and have slightly more efficient air exchange than the 2D model. However, as the pitched roofs remarkably reduce the mixing velocity and exchange velocity in the 2D model, both air mixing and air exchange are much more efficient in the 3D models with pitched roofs than in the 2D model with pitched roofs.

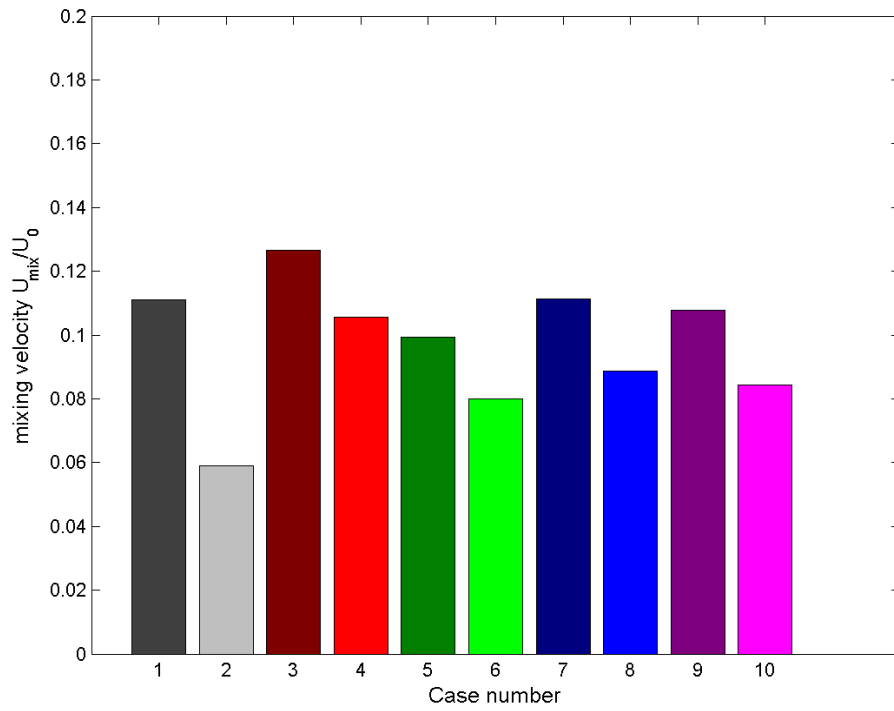


Figure 8.6: Mixing velocities for whole street canyon, Cases 1–10.

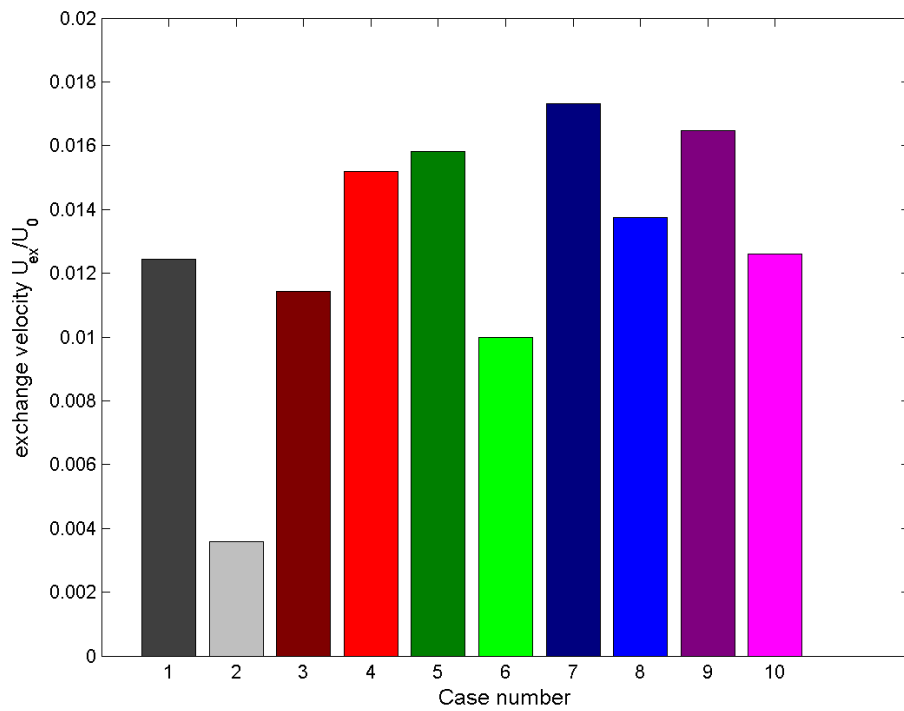


Figure 8.7: Exchange velocities for whole street canyon, Cases 1–10.

8.3.2 Ventilation efficiencies for different cross-sections

This section discusses the ventilation efficiencies for the nine across-street vertical planes. In addition, this section analyses how they are affected by the heterogeneous buildings, pitched roofs and T-junction.

It is apparent to see in Figure 8.8 and Figure 8.9 below that both mixing velocity and exchange velocity are generally lower in the south section of the test street than in the north section. This is because tilted vortices form in the north section, whereas vortex flow does not form in the south section, which have been discussed before in Section 7.4. In detail, the south section has very low across-street velocity components, so mixing velocity is low in this part of the street. Owing to the specific flow pattern in the south section, the mean momentum fluxes UW and the turbulent momentum fluxes $u'w'$ for the planes in the south section have comparable magnitudes but opposite signs, which are marked by yellow in Table 8.2 below. The counteraction between these two types of momentum leads to low exchange velocity in the south section.

In both the north section and the south section, the highest mixing velocity and the highest exchange velocity always happen on the plane nearest to the street end (i.e., v-plane1 and v-plane9). This finding indicates that airflow coming from street end benefits local ventilation.

Comparing the data for the 2D models with the data for the 3D models, it is found that for a fixed roof type, the mixing velocity and exchange velocity for the 2D case are lower than the velocities in the north section for the 3D cases, due to the presence of along-street flow that does not form in the 2D models. On the other hand, for a fixed roof type, the mixing velocity and exchange velocity for the 2D case are much higher than the velocities in the south section for the 3D cases, due to the disappearance of vortex flow in the south section.

The above findings show that the flow from street end and the along-street flow enhance air mixing and air exchange, while the disappearance of vortex flow denotes poor air mixing efficiency and air exchange efficiency.

Plane	UW	$u'w'$	VW	$v'w'$	$ UW+u'w' $	$ VW+v'w' $
v-plane1	-0.43	-0.59	-0.03	0.05	1.03	<0.01
v-plane2	-0.07	-0.35	0.06	0.14	0.18	0.04
v-plane3	-0.20	-0.36	-0.07	0.17	0.32	0.01
v-plane4	-0.29	-0.38	-0.15	0.17	0.45	<0.01
v-plane5	-0.09	-0.39	-0.02	0.16	0.23	0.02
v-plane6	0.24	-0.42	0.22	0.13	0.03	0.12
v-plane7	0.44	-0.53	0.25	0.08	0.01	0.10
v-plane8	0.43	-0.61	0.16	0.07	0.03	0.05
v-plane9	0.33	-0.64	0.09	0.07	0.09	0.03

Table 8.2: Momentum fluxes on the top of nine across-street vertical planes (Case 5), which are used for calculating exchange velocity.

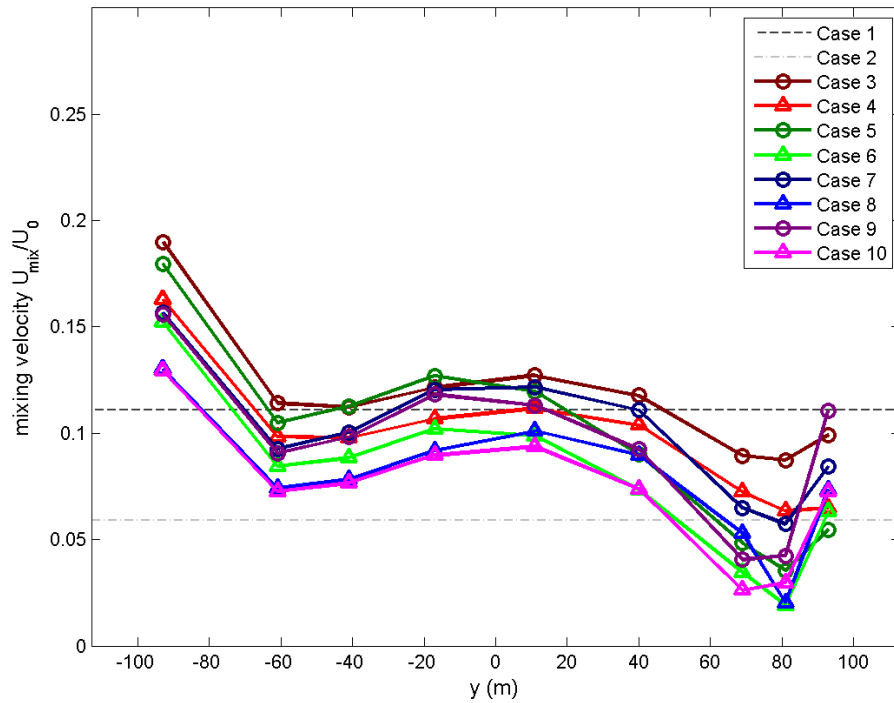


Figure 8.8: The mixing velocities for the nine across-street vertical planes in Cases 3–10, and the mixing velocities for Cases 1 and 2.

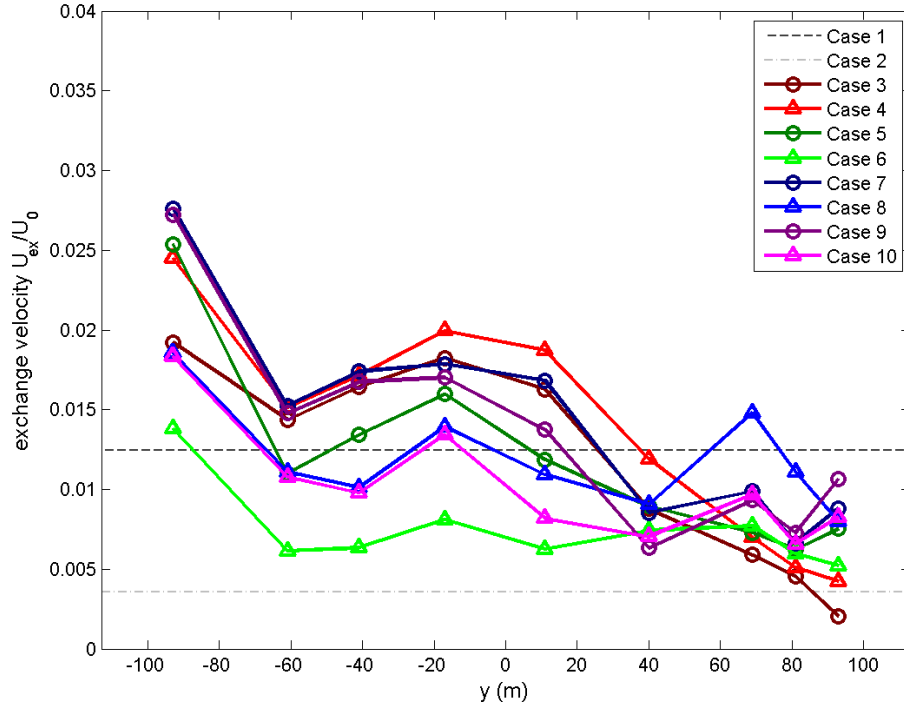


Figure 8.9: The exchange velocities for the nine across-street vertical planes in Cases 3–10, and the exchange velocities for Cases 1 and 2.

In order to quantify the effects of heterogeneous buildings, pitched roofs and T-junction, the percentage changes of mixing velocity and exchange velocity due to each of these geometries are calculated on each across-street vertical plane for each case. The calculation follows Equations 8.4, 8.5, 8.6 and 8.7. The results are shown in Figure 8.10 and Figure 8.11 below and are discussed in the following paragraphs.

$$\text{Percentage change due to heterogeneous buildings} = \sqrt{\frac{BP(\text{Case 7})}{BP(\text{Case 3})} \cdot \frac{BP(\text{Case 8})}{BP(\text{Case 4})}} - 1$$

(compared with 16m tall homogeneous buildings) (8.4)

$$\text{Percentage change due to heterogeneous buildings} = \sqrt{\frac{BP(\text{Case 7})}{BP(\text{Case 5})} \cdot \frac{BP(\text{Case 8})}{BP(\text{Case 6})}} - 1$$

(compared with 20m tall homogeneous buildings) (8.5)

Percentage change due to pitched roofs =

$$\sqrt[4]{\frac{BP(\text{Case 4})}{BP(\text{Case 3})} \cdot \frac{BP(\text{Case 6})}{BP(\text{Case 5})} \cdot \frac{BP(\text{Case 8})}{BP(\text{Case 7})} \cdot \frac{BP(\text{Case 10})}{BP(\text{Case 9})}} - 1$$

(8.6)

$$\text{Percentage change due to } T - \text{junction} = \sqrt{\frac{BP(\text{Case 9})}{BP(\text{Case 7})} \cdot \frac{BP(\text{Case 10})}{BP(\text{Case 8})}} - 1 \quad (8.7)$$

where *BP* stands for one of the four bulk parameters, namely mixing velocity, exchange velocity, canyon concentration and pedestrian concentration.

Compared to the 16m tall homogenous buildings and 20m tall homogenous buildings, the heterogeneous buildings lead to intermediate mixing velocity in the south section and intermediate exchange velocity in the north section.

However, the heterogeneous buildings slightly reduce mixing velocity in the north section. The reductions are up to 20%. In addition, the heterogeneous buildings significantly increase exchange velocity in the south section, especially on v-plane9 that the increment is around 190%.

The pitched roofs reduce mixing velocity on all the nine planes. The reductions are around 20–40%, and the largest reduction happens on v-plane8.

The pitched roofs reduce exchange velocity in the north section. The reductions are around 20–40%. However, the pitched roofs slightly increase exchange velocity in the south section. The increments are up to 20%.

The T-junction almost does not affect the mixing velocities and exchange velocities on v-plane1 to v-plane4, as these four planes are upstream to the T-junction with respect to the along-street flow.

However, the T-junction reduces both mixing velocity and exchange velocity on v-plane5 to v-plane7 which are around the T-junction. The reductions for the two velocities are up to 40% and 20% respectively. The reduced velocities on the three planes are because tilted vortices still form in this region if the T-junction does not exist, but the T-junctions in Case 9 and 10 terminate the vortices, which have been discussed before in Section 8.2.3.

The T-junction increases both mixing velocity and exchange velocity near the south street end. This is because the T-junction promotes flow approaching from the south street end, which has been discussed before in Section 8.2.3.

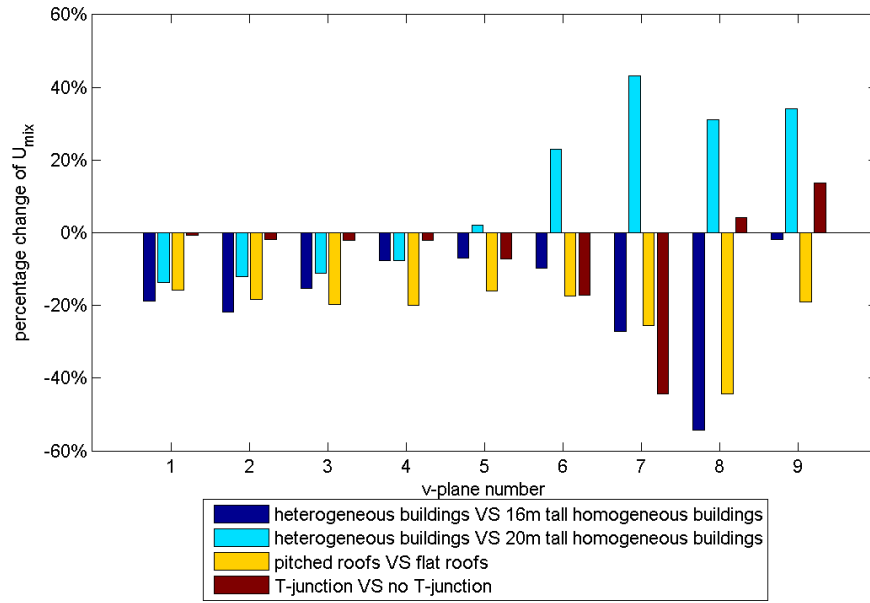


Figure 8.10: Percentage changes of the mixing velocities for nine across-street vertical planes in Cases 3–10.

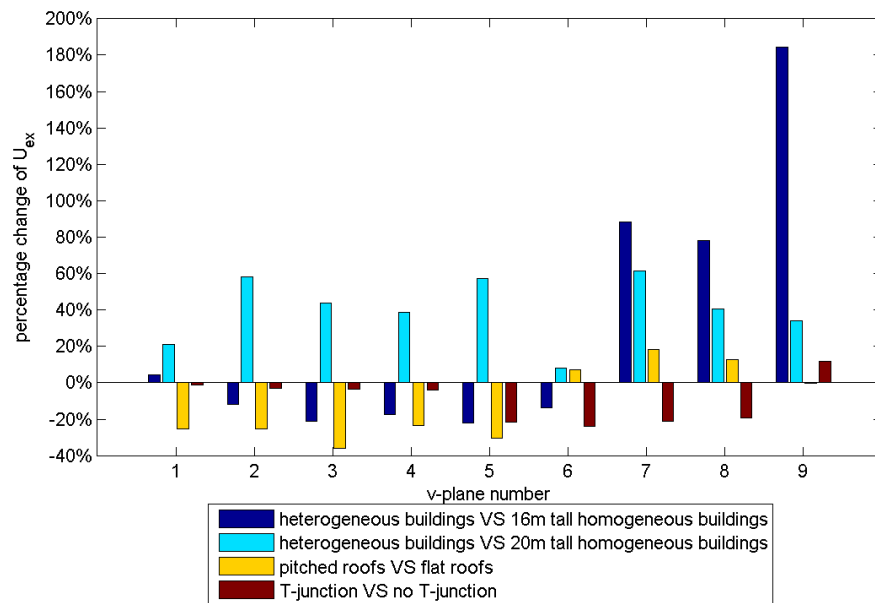


Figure 8.11: Percentage changes of the exchange velocities for nine across-street vertical planes in Cases 3–10.

8.4 Assessment of pollutant removal

This section uses two bulk parameters proposed in Section 6.4.5 to assess pollutant removal performance, namely canyon concentration c_{can} and pedestrian concentration c_{ped} . The calculation of these two bulk parameters follows the same approaches mentioned before, which are re-stated as Equations 8.8 and 8.9.

$$c_{can} = \frac{\iiint_{V_{can}} c \, dV}{V_{can}} \quad (8.8)$$

$$c_{ped} = \frac{\iiint_{V_{ped}} c \, dV}{V_{ped}} \quad (8.9)$$

where V_{ped} is defined as the volume below 2m.

Both canyon concentration c_{can} and pedestrian concentration c_{ped} are calculated for the whole street and for nine across-street vertical planes. Figure 8.12 and Figure 8.13 below display the calculated data for the whole street for each case, and Figure 8.14 and Figure 8.15 below display the calculated data for the nine across-street vertical planes for each case. All the data are presented in the normalized form which has been given as Equation 7.1 in Section 7.2.

8.4.1 Pollutant removal performance for whole test street

This section analyses the effects of heterogeneous buildings, pitched roofs and T-junction on pollutant removal performance for the whole test street. In addition, this section discusses different pollutant removal performance between the 2D models and the 3D models.

8.4.1.1 The effect of heterogeneous buildings

The impact of heterogeneous buildings on pollutant removal is analysed by comparing the data between Cases 3, 4, 5, 6, 7 and 8.

As can be noted from Figure 8.12 below, for a fixed roof type, the case with heterogeneous buildings has around 5 units of normalised canyon concentration lower than the case with 20m tall homogeneous buildings and has comparable canyon concentration to the case with 16m tall homogeneous buildings. On the other hand, for a fixed roof type, pedestrian concentration is similar between the cases with homogeneous buildings and the cases with heterogeneous buildings.

According to the above findings, the heterogeneous buildings give better pollutant removal performance than the homogeneous buildings which have the same height to the tallest building in the heterogeneous buildings, but give poorer pollutant removal performance than the homogeneous buildings which have the same height to the lowest building in the heterogeneous buildings.

8.4.1.2 The effect of pitched roofs

The impact of pitched roofs on pollutant removal is analysed by comparing the data between Cases 3, 4, 5, 6, 7, 8, 9 and 10.

As can be noted from Figure 8.12 below, the pitched roofs in Cases 6, 8 and 10 lead to around 2 units higher canyon concentration compared to Cases 5, 7 and 9 respectively. However, Case 4 with pitched roofs has lower canyon concentration than Case 3 with flat roofs. This can be explained by the previous finding that the exchange velocity for Case 4 is higher than the exchange velocity for Case 3.

Figure 8.13 below shows that the cases with pitched roofs have up to 5 units of normalised pedestrian concentration higher than the cases with flat roofs.

According to the above findings, the pitched roofs give worse pollutant removal performance than the flat roofs.

8.4.1.3 The effect of T-junction

The impact of T-junction on pollutant removal is analysed by comparing the data between Cases 7, 8, 9 and 10.

As can be seen in Figure 8.12 and Figure 8.13 below, the cases with a T-junction (i.e., Cases 9 and 10) have higher canyon concentration and higher pedestrian concentration than the cases without a T-junction (i.e., Cases 7 and 8). This trend is even more significant when the buildings have pitched roofs.

According to the above findings, the T-junction gives worse pollutant removal performance compared to the situation that T-junction does not exist.

8.4.1.4 The difference between the 2D models and 3D models

Figure 8.12 below shows that the canyon concentrations for the two 2D models are considerably higher than the canyon concentrations for the eight 3D models. This is because pollutants are removed by both the vortex flow and along-street flow in the 3D models, whereas pollutants are only removed by the vortex flow in the 2D models.

For the 2D models, the pitched roofs increase 5 units of normalised canyon concentration. In contrast, for the 3D models, the pitched roofs only increase around 2 units of normalised concentration. This is because the pitched roofs lead to much worse air mixing and air exchange in the 2D models than in the 3D models, which has been pointed out in Section 8.2.2.

As can be seen in Figure 8.13 below, pedestrian concentration is comparable between the 2D models and the 3D models. This indicates that the 2D models have higher concentration at the bottom of the street than the 3D models, as the buildings are 12m tall in the 2D models but either 16m or 20m tall in the 3D models, and pedestrian height is defined as 2m in all the models. In addition, similar to the situation for canyon concentration, the pitched roofs increase pedestrian concentration in both the 2D models and the 3D models, and the increment for the 2D models is larger than the increments for the 3D models.

According to the above findings, the 2D models give worse pollutant removal performance than the 3D models. In addition, the presence of pitched roofs causes even worse performance in the 2D models than in the 3D models.

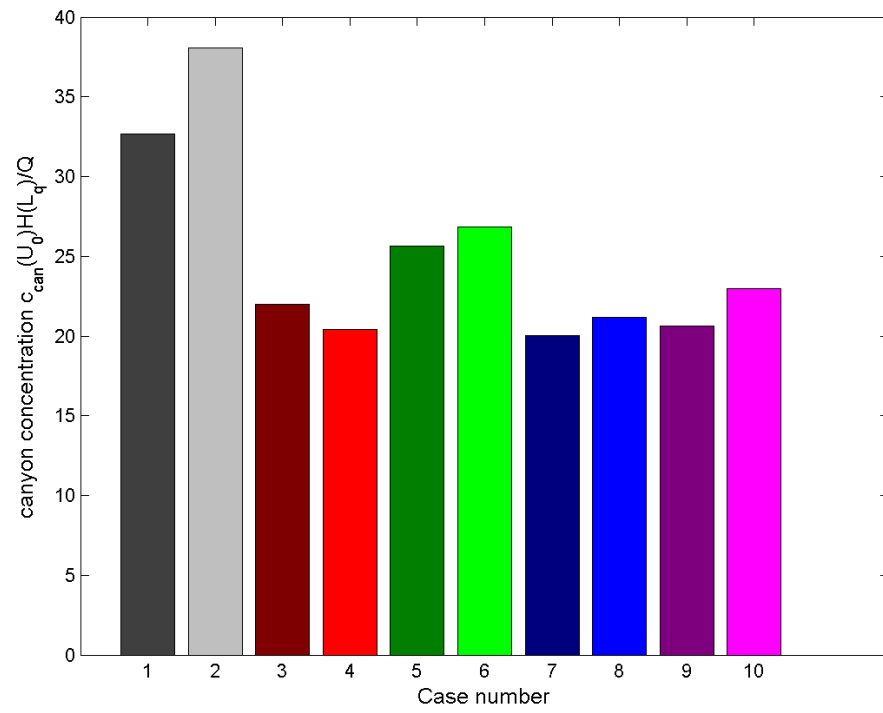


Figure 8.12: Overall canyon concentrations for Cases 1–10.

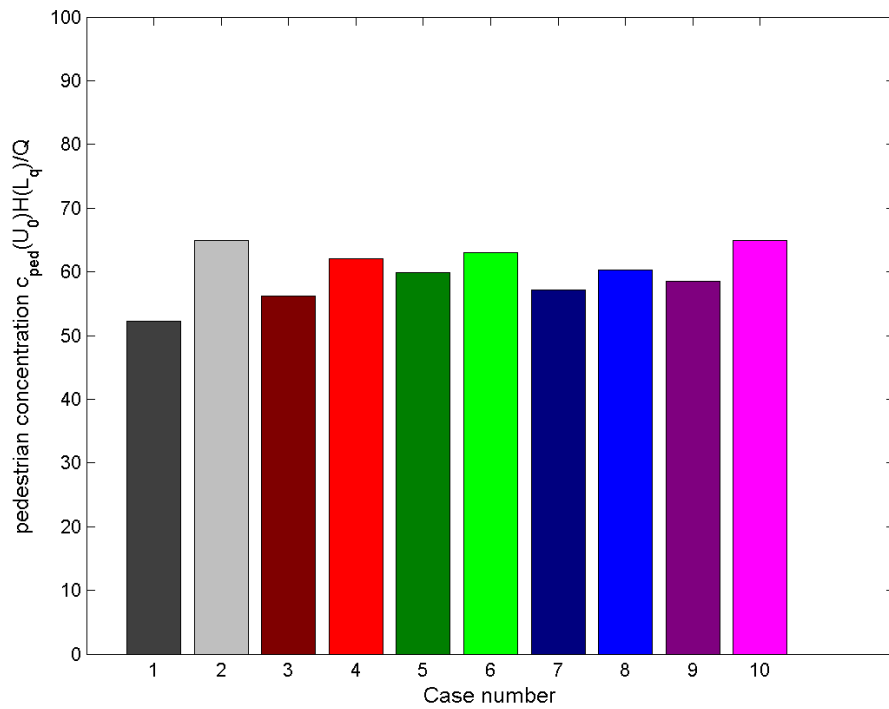


Figure 8.13: Overall pedestrian concentrations for Cases 1–10.

8.4.2 Pollutant removal performance for different cross-sections

This section discusses the pollutant removal performance for the nine across-street vertical planes. In addition, this section analyses how they are affected by the heterogeneous buildings, pitched roofs and T-junction.

According to Figure 8.8 and Figure 8.9 below, both canyon concentration and pedestrian concentration are much higher in the south section than in the north section. In addition, the lowest values of these two concentrations always happen on the plane nearest to the street end, namely v-plane1 in the north section and v-plane9 in the south section. Moreover, it is found that for a fixed roof type, the canyon concentration and pedestrian concentration for the 2D case are lower than those in the south section for the 3D cases, but higher than those in the north section for the 3D cases.

The above three findings about canyon concentration and pedestrian concentration can be perfectly explained by the previous three findings about mixing velocity and exchange velocity in Section 8.3.2. According to this relationship, the flow from street end and the along-street flow are also favourable for pollutant removal, while the disappearance of vortex flow is considered to be the main reason poor pollutant removal.

The percentage changes of canyon concentration and pedestrian concentration due to the heterogeneous buildings, pitched roofs or T-junction are calculated on each across-street vertical plane for each case. The calculation follows Equations 8.4, 8.5, 8.6 and 8.7, which are mentioned in Section 8.3.2. The results are shown in Figure 8.16 and Figure 8.17 below and discussed in the following paragraphs.

For most of the across-street planes, the heterogeneous buildings lead to higher canyon concentration compared to 16m tall homogeneous buildings, but lower canyon concentration compared to 20m tall homogeneous buildings. One exception is that heterogeneous buildings reduce canyon concentration on v-plane2.

The heterogeneous buildings increase pedestrian concentration by up to 20% on v-plane1, v-plane2 and v-plane3 which are relatively close to the north street end. However, the heterogeneous buildings decrease pedestrian concentration by up to 10% on v-plane4, v-plane 5 and v-plane6 which are relatively close the T-junction.

The pitched roofs increase canyon concentration by 10–20% on almost all the planes. The increment of canyon concentration is relatively large in the south section. The pitched roofs increase pedestrian concentration by up to 20% on all the planes. The

increment of pedestrian concentration is relatively large on v-plane 1, v-plane3 and v-plane7.

The T-junction sharply increases canyon concentration and pedestrian concentration on v-plane7, as this plane is the nearest downstream plane to the junction. The increments are around 60% and 50% respectively. The T-junction also increases both concentrations on v-plane5 (the nearest upstream plane to the T-junction) and on v-plane6 (the plane across the T-junction), but the increments are not as large as those on v-plane7.

The T-junction reduces canyon concentration and pedestrian concentration near the south street end, due to the improvement of air mixing and air exchange at this position. However, the decrements are smaller than the increments on v-plane7 and comparable to the increments on v-plane6.

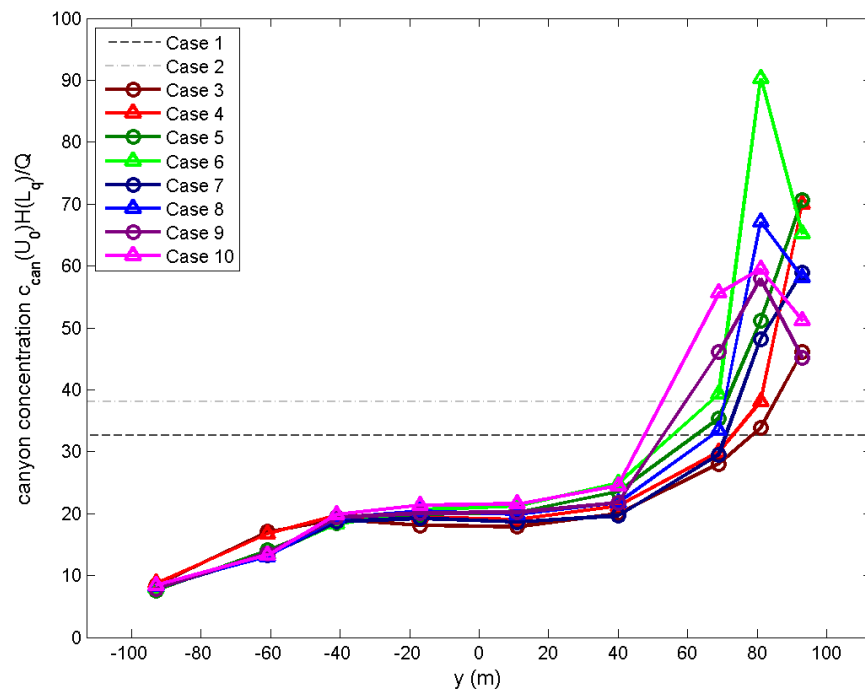


Figure 8.14: The canyon concentrations for the nine across-street vertical planes in Cases 3–10, and the canyon concentrations for Cases 1 and 2.

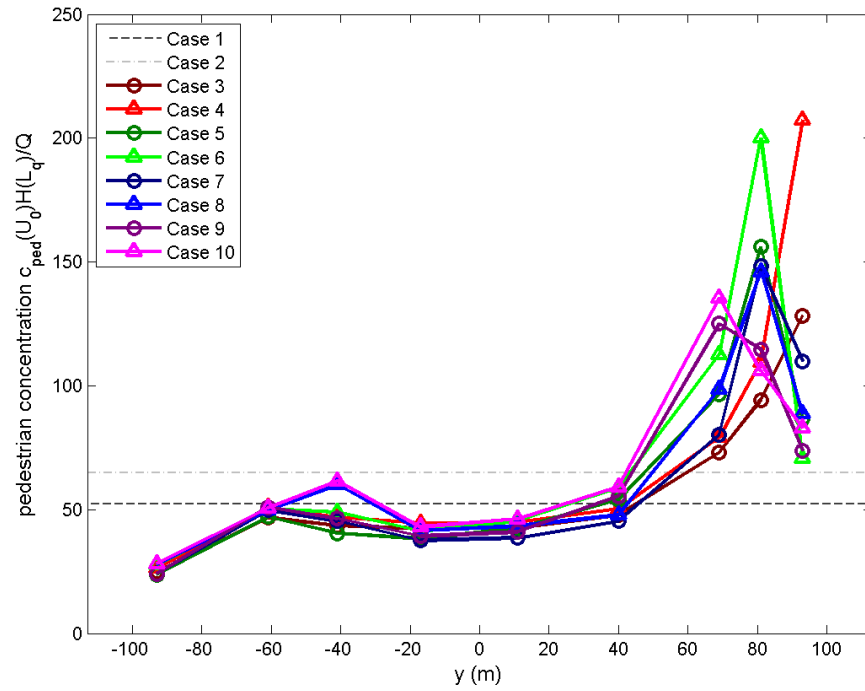


Figure 8.15: The pedestrian concentrations for the nine across-street vertical planes in Cases 3–10, and the pedestrian concentrations for Cases 1 and 2.

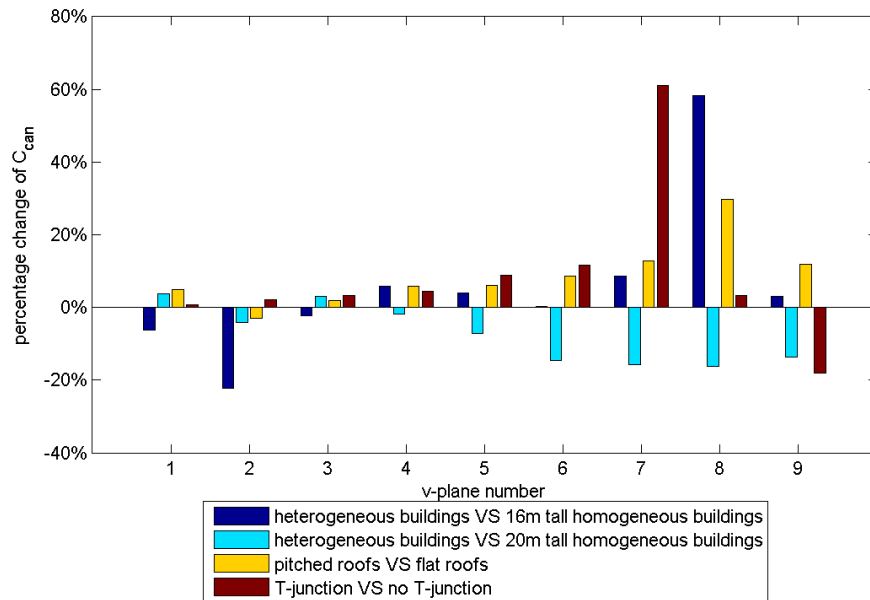


Figure 8.16: Percentage changes of the canyon concentrations for nine across-street vertical planes in Cases 3–10.

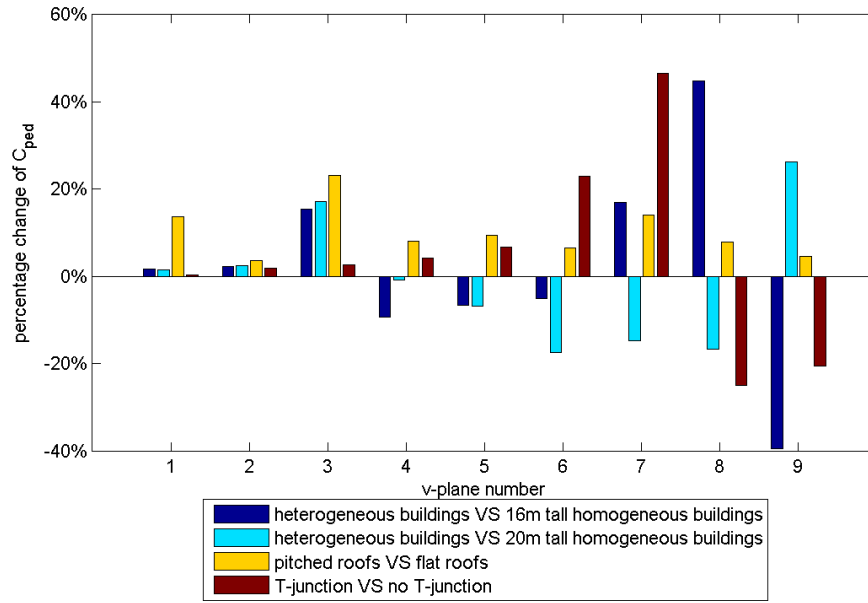


Figure 8.17: Percentage changes of the pedestrian concentrations for nine across-street vertical planes in Cases 3–10.

8.5 Summary of main findings

This chapter studies the impacts of three characteristic geometries, namely heterogeneous buildings, pitched roofs and T-junction. It is accomplished by creating ten models, each of which possesses one or some of the three geometries. The results of these ten cases are studied through both qualitative and quantitative approaches.

The impacts of the three geometries on flow structure are investigated at first. It is found that the heterogeneous buildings and the pitched roofs make slightly different vortex flow in the north section of the test street, in comparison to the homogenous buildings and the flat roofs. The T-junction has a huge impact on local flow. In detail, it breaks the vortex flow in front of it, which should form if the T-junction does not exist. It is further found that the pitched roofs and the T-junction promote flow coming from the south street end.

The impacts of the three geometries on ventilation are studied by evaluating two bulk parameters, mixing velocity and exchange velocity. For the whole street, it is found that the heterogeneous buildings increase exchange velocity when the buildings have pitched roofs; the pitched roofs reduce both mixing velocity and exchange velocity; the T-junction slightly reduces exchange velocity.

For different parts of the street, it is found that the heterogeneous buildings reduce mixing velocity in the north section of the test street, but significantly increase exchange velocity in the south section; the pitched roofs reduce mixing velocity on all the test planes, and reduce exchange velocity in the south section; the T-junction reduces both mixing velocity and exchange velocity on the three planes around the T-junction, but increases both mixing velocity and exchange velocity on the two planes closest to the south street end.

The impacts of the three geometries on pollutant removal are studied by evaluating two bulk parameters, canyon concentration and pedestrian concentration. For the whole street, it is found that the heterogeneous buildings slightly reduce canyon concentration; the pitched roofs increase both canyon concentration and pedestrian concentration; the T-junction increases both canyon concentration and pedestrian concentration.

For different parts of the street, it is found that the heterogeneous buildings increase pedestrian concentration by up to 20% on the three planes relatively close to the north street end, but decreases pedestrian concentration by up to 10% in the rest part of the

north section; the pitched roofs increase both canyon concentration and pedestrian concentration by up to 20% on almost all the test planes; the T-junction significantly increases both canyon concentration and pedestrian concentration on the three planes around the T-junction, but reduces both canyon concentration and pedestrian concentration near the south street end.

Amongst the ten cases, two 2D models are compared with eight 3D models. It is found that both mixing velocity and exchange velocity for the 2D cases are lower than those in the north section for the 3D cases, but higher than those in the south section for the 3D cases. Correspondingly, both canyon concentration and pedestrian concentration for the 2D cases are higher than those in the north section for the 3D cases, but lower than those in the south section for the 3D cases. These findings bear out that the coexistence of vortex flow and along-street flow in the north section benefits ventilation and pollutant removal, whereas the disappearance of vortex flow in the south section is very harmful to ventilation and pollutant removal.

9 Conclusion and Discussion

This thesis uses CFD modelling to study the impacts of pitched roof and other geometries on airflow and pollutant dispersion in street canyons. The research results and the miscellaneous findings during the research deepen the understanding of urban airflow and provide useful information for urban planning from environmental considerations. There are four main objectives proposed in the introduction. The following paragraphs conclude and discuss the main findings from the thesis in combination with these four objectives. After that, several limitations of the current research are pointed out.

Objective 1: to establish a reliable and economic method to model street canyon flow

This is accomplished by carrying out a benchmark study. The benchmark study validates three CFD models against Kastner-Klein's experiments. All the models give reasonable predictions of flow pattern, flow properties and pollutant concentration. It is found that the accuracy of CFD model is improved if the test street is free from the effect of flow separation above the first building and if the case is modelled by three-dimensional geometry.

During the benchmark study, it is found that 24 cells along the building height are the minimum requirement for mesh independent results in most part of a street canyon. It is recommended to set 36 cells or more cells along the building height, in order to control the discretisation errors for all the flow properties and concentration to an acceptable level and reduce uncertainty in the near-wall region. The standard k- ϵ model and the scalable wall function are found to be an economic and reliable option for modelling street canyon flow. The turbulent Schmidt number $Sc_t=0.9$ gives reliable predictions of concentration in the cases modelled by two-dimensional geometry. However, owing to the large over-prediction of turbulent kinetic energy (TKE) in the case modelled by three-dimensional geometry, the turbulent Schmidt number needs to be reduced, as a remedy action for compensating the over-prediction.

Objective 2: to study the impact of pitched roof on airflow and pollutant dispersion in street canyons

This is accomplished by conducting a parametric study. Three parameters are defined in that study, namely the aspect ratio of building height to street width, pitch rise and roof arrangement. It is found that the aspect ratio determines the shape of vortex flow in the street. On the other hand, pitch rise and roof arrangement have minor effects on the flow pattern, and various pitched roofs still result in single vortex in each street.

Compared to flat roofs, pitched roofs reduce horizontal velocity, vertical velocity and TKE in the test street canyon. The reductions are more significant when pitch rise is high and when there is a pitched roof on the leeward building rather than on the windward building. As a result, pitch roofs generally increase average concentration in the test street, and the increment is more significant in the cases with a high-rise pitched roof. It is further found that low pitch rise slightly raises concentration across the street; high pitch rise significantly raises concentration in the leeward part and around the emission sources.

Four bulk parameters are proposed to assess ventilation efficiency and pollutant removal performance. The mixing velocity (U_{mix}) indicates air mixing efficiency in street canyon; the exchange velocity (U_{ex}) indicates air exchange efficiency at street canyon opening; the canyon concentration (c_{can}) represents average concentration below roof level; the pedestrian concentration (c_{ped}) represents average concentration below pedestrian level. In general, for a fixed aspect ratio, the cases with pitched roofs have lower mixing velocity and exchange velocity and higher canyon concentration and pedestrian concentration than the reference case with flat roofs on all the buildings. These trends are the most significant when comparing the reference case with the cases with a high-rise pitched roof on the leeward building.

Objective 3: to make a case study of airflow and pollutant dispersion in a real urban area

This is accomplished by conducting a case study based on a real urban area—Gloucester Place and its surrounding city blocks, and creating several cases based on the modified geometries. Four typical geometries are studied, namely the tall building downstream to the test street, the heterogeneous buildings adjacent to the test street, the pitched roofs and the T-junction between the windward buildings. All of them are found to have some impacts on the flow and concentration in and around the test street.

The tall building is found to be responsible for excellent ventilation and pollutant removal in the north section of Gloucester Place. Compared to a non-isolated street canyon amongst several consecutive homogeneous street canyons, both mixing velocity and exchange velocity are much higher in that section, and canyon concentration and pedestrian concentration are around 1/3 lower in that section. These are because the tall building produces diverged horizontal flow in front of it; the diverged flow further drives along-street flow in the test street, and the along-street flow coexists with the vortex flow. On the other hand, the tall building leads to very low mixing velocity and exchange velocity and very high canyon concentration and pedestrian concentration in the south section of Gloucester Place, as it breaks vortex flow over there. The above findings indicate the great potential of isolated tall buildings to improve local air quality, but it hinges on appropriate planning.

The heterogeneous buildings are found to reduce mixing velocity in the north section of Gloucester Place but increase exchange velocity in the south section. However, they have limited impact on canyon concentration and pedestrian concentration, and almost do not affect the flow structures in the street.

Pitched roofs make consistent impacts between in this study and in the previous parametric study. In addition, in comparison with flat roofs, they cause lower mixing velocity and exchange velocity and higher canyon concentration and pedestrian concentration in almost all the parts of the street. However, the reductions of mixing velocity and exchange velocity are not as large as those in the parametric study, so are the increments of canyon concentration and pedestrian concentration. Furthermore, it is found that the pitched roofs enhance airflow from the south street end.

The T-junction is found to have profound effects on the flow and concentration around it. It breaks the vortex flow in front of it, which should form if it does not exist. On the other hand, the T-junction enhances airflow from the south street end. As a result, the T-junction reduces mixing velocity and exchange velocity around it, but increases mixing velocity and exchange velocity near the south street end; the T-junction significantly increase canyon concentration and pedestrian concentration around it, but reduces canyon concentration and pedestrian concentration near the south street end. Considering these findings, urban planners should be aware of the potential harmful effect of T-junctions on local air quality and should attempt to reduce their impacts on human health.

Objective 4: to present modelling results in concise and readable ways

This is accomplished by using several innovative figure presentations. (1) Plotting several profiles in the same figure is straightforward for comparison (e.g., Figure 6.5), but it requires a smart selection of symbol to stand for each profile. (2) The contour plot for the deviation of a certain quantity from the reference (e.g., Figure 6.11) is an effective presentation to show the difference across the street between two cases. It is especially useful when the normal contours for the two cases are difficult to be distinguished, but the difference between them needs to be quantified. (3) The ‘heat maps’ used in Section 6.4.5 (i.e., Figure 6.16 and Figure 6.17) give average concentration in different parts of the third street and the fourth street. This presentation is more concise compared to contour plot, but offers higher resolution than the canyon concentration as a bulk parameter.

Apart from the innovative figure presentations, the “hit-rate” Q_{hit} used in the benchmark study is a straightforward criterion to assess CFD model accuracy for modelling urban airflow. The four bulk parameters mentioned before are suitable for assessing ventilation efficiency and pollutant removal performance for street canyon; people can easily carry out the assessment by judging their magnitudes.

Research limitations:

However, this research has several limitations with respect to research methods and model assumptions. First, all the studies in this thesis are based on steady-state RANS models. Although RANS models are advantageous in computational cost, they are not as accurate as LES and are unable to predict turbulence structure. Second, only one type of background wind direction is modelled—perpendicular background wind condition, which is usually the worst condition for ventilation and pollutant removal. However, the impacts of pitched roofs and other geometries found under this condition might not be similar under other wind conditions. Third, background concentration is assumed to be zero in all the studies. It is obvious that non-zero background in the real world will cause even higher concentration in street canyons. However, it is unable to quantify the contribution of background pollutants to local concentration level. Fourth, thermal effect is not considered in this thesis. Thermal effects produced by solar radiation and other sources are universally existed in the real world and can have strong impacts on airflow and pollutant dispersion. Thus, ignoring thermal effect means reduced representativeness of the model. In the future, the primary goal will be breaking through

the above limitations, to achieve better accuracy and to model a variety of realistic situations.

10 References

- Allegrini, J., Dorer, V. & Carmeliet, J. 2013. Wind tunnel measurements of buoyant flows in street canyons. *Building and Environment*, 59, 315-326.
- Allegrini, J., Dorer, V. & Carmeliet, J. 2014. Buoyant flows in street canyons: Validation of CFD simulations with wind tunnel measurements. *Building and Environment*, 72, 63-74.
- Allegrini, J., Dorer, V., Defraeye, T. & Carmeliet, J. 2012. An adaptive temperature wall function for mixed convective flows at exterior surfaces of buildings in street canyons. *Building and Environment*, 49, 55-66.
- Amorim, J. H., Rodrigues, V., Tavares, R., Valente, J. & Borrego, C. 2013. CFD modelling of the aerodynamic effect of trees on urban air pollution dispersion. *Science of The Total Environment*, 461–462, 541-551.
- ANSYS Inc. 2009a. ANSYS FLUENT 12.0 Theory Guide. U.S.A.: ANSYS, Inc.
- ANSYS Inc. 2009b. ANSYS FLUENT 12.0 User's Guide. U.S.A.: ANSYS, Inc.
- ANSYS Inc. 2016. *ANSYS CFD* [Online]. Available: <http://www.ansys.com/Products/Fluids/ANSYS-CFD> [Accessed 27th May 2016].
- Baik, J.-J. & Kim, J.-J. 2002. On the escape of pollutants from urban street canyons. *Atmospheric Environment*, 36, 527-536.
- Balogun, A., Tomlin, A., Wood, C., Barlow, J., Belcher, S., Smalley, R., Lingard, J. N., Arnold, S., Dobre, A., Robins, A., Martin, D. & Shallcross, D. 2010. In-Street Wind Direction Variability in the Vicinity of a Busy Intersection in Central London. *Boundary-Layer Meteorology*, 136, 489-513.
- Blocken, B., Stathopoulos, T. & Carmeliet, J. 2007. CFD simulation of the atmospheric boundary layer: wall function problems. *Atmospheric Environment*, 41, 238-252.
- Blum, D. 2013. Air Pollution as a Heart Threat. *New York Times*.

- Borsani, A., Maltagliati, S., Martelli, F. & Procino, L. 2008. Test Case Optimization of an Urban Section. *BBAA VI International Colloquium on: Bluff Bodies Aerodynamics & Applications*. Milano, Italy.
- Buccolieri, R., Salim, S. M., Leo, L. S., Di Sabatino, S., Chan, A., Ielpo, P., de Gennaro, G. & Gromke, C. 2011. Analysis of local scale tree–atmosphere interaction on pollutant concentration in idealized street canyons and application to a real urban junction. *Atmospheric Environment*, 45, 1702-1713.
- Buccolieri, R., Sandberg, M. & Di Sabatino, S. 2010. City breathability and its link to pollutant concentration distribution within urban-like geometries. *Atmospheric Environment*, 44, 1894-1903.
- Castro, I. P. & Apsley, D. D. 1997. Flow and dispersion over topography: A comparison between numerical and laboratory data for two-dimensional flows. *Atmospheric Environment*, 31, 839-850.
- Castro, I. P. & Robins, A. G. 1977. The flow around a surface-mounted cube in uniform and turbulent streams. *Journal of Fluid Mechanics*, 79, 307-335.
- Celik, I. B., Ghia, U., Roache, P. J. & Freitas, C. J. 2008. Procedure for Estimation and Reporting of Uncertainty Due to Discretization in CFD Applications. *Journal of fluids Engineering-Transactions of the ASME*, 130.
- Chan, T. L., Dong, G., Leung, C. W., Cheung, C. S. & Hung, W. T. 2002. Validation of a two-dimensional pollutant dispersion model in an isolated street canyon. *Atmospheric Environment*, 36, 861-872.
- Cheng, W. C. & Liu, C.-H. 2011. Large-eddy simulation of turbulent transports in urban street canyons in different thermal stabilities. *Journal of Wind Engineering and Industrial Aerodynamics*, 99, 434-442.
- Cheng, W. C., Liu, C.-H. & Leung, D. Y. C. 2009. On the correlation of air and pollutant exchange for street canyons in combined wind-buoyancy-driven flow. *Atmospheric Environment*, 43, 3682-3690.

- Coccal, O., Goulart, E. V., Branford, S., Glyn Thomas, T. & Belcher, S. E. 2014. Flow structure and near-field dispersion in arrays of building-like obstacles. *Journal of Wind Engineering and Industrial Aerodynamics*, 125, 52-68.
- Craft, T. J. 2011. Wall Functions, TPF E MSc Advanced Turbulence Modelling. The University of Manchester, unpublished.
- Cui, Z., Cai, X. & Baker, C. J. 2004. Large-eddy simulation of turbulent flow in a street canyon. *Quarterly Journal of the Royal Meteorological Society*, 130, 1373-1394.
- Department for Transport 2015. Traffic counts in Westminster.
- Di Sabatino, S., Buccolieri, R., Pulvirenti, B. & Britte, R. E. 2008. Flow and Pollutant Dispersion in Street Canyons using FLUENT and ADMS-Urban. *Environmental Modeling & Assessment*, 13, 369-381.
- Di Sabatino, S., Buccolieri, R., Pulvirenti, B. & Britter, R. 2007. Simulations of pollutant dispersion within idealised urban-type geometries with CFD and integral models. *Atmospheric Environment*, 41, 8316-8329.
- Dixon, N. S., Boddy, J. W. D., Smalley, R. J. & Tomlin, A. S. 2006. Evaluation of a turbulent flow and dispersion model in a typical street canyon in York, UK. *Atmospheric Environment*, 40, 958-972.
- Eliasson, I., Offerle, B., Grimmond, C. S. B. & Lindqvist, S. 2006. Wind fields and turbulence statistics in an urban street canyon. *Atmospheric Environment*, 40, 1-16.
- Endalew, A. M., Hertog, M., Delele, M. A., Baetens, K., Persoons, T., Baelmans, M., Ramon, H., Nicolaï, B. M. & Verboven, P. 2009. CFD modelling and wind tunnel validation of airflow through plant canopies using 3D canopy architecture. *International Journal of Heat and Fluid Flow*, 30, 356-368.
- Erell, E., Pearlmutter, D. & Williamson, T. 2012. *Urban Microclimate: Designing the Spaces Between Buildings*, Taylor & Francis.
- European Commission n.d. Air Quality Standards.

- Fitzpatrick, T. 2014. *Climate change and poverty: A new agenda for developed nations*, Policy Press.
- Fletcher, C. A. J. 1991. *Computational techniques for fluid dynamics*, Berlin, Springer-Verlag.
- Franke, J. & Frank, W. 2008. Application of generalized Richardson extrapolation to the computation of the flow across an asymmetric street intersection. *Journal of Wind Engineering and Industrial Aerodynamics*, 96, 1616-1628.
- Franke, J., Hellsten, A., Schlünzen, H. & Carissimo, B. 2007. *Best practice guideline for the CFD simulation of flows in the urban environment*, COST Office.
- Glover, N. 2015. *Investigate the impact of trees on airflow within street canyons through the use of CFD and field measurements*. Doctor of Philosophy, University College London.
- Gromke, C. & Blocken, B. 2015. Influence of avenue-trees on air quality at the urban neighborhood scale. Part I: Quality assurance studies and turbulent Schmidt number analysis for RANS CFD simulations. *Environmental Pollution*, 196, 214-223.
- Gromke, C., Buccolieri, R., Di Sabatino, S. & Ruck, B. 2008. Dispersion study in a street canyon with tree planting by means of wind tunnel and numerical investigations – Evaluation of CFD data with experimental data. *Atmospheric Environment*, 42, 8640-8650.
- Gromke, C. & Ruck, B. 2007. Influence of trees on the dispersion of pollutants in an urban street canyon—Experimental investigation of the flow and concentration field. *Atmospheric Environment*, 41, 3287-3302.
- Gu, Z.-L., Zhang, Y.-W., Cheng, Y. & Lee, S.-C. 2011. Effect of uneven building layout on air flow and pollutant dispersion in non-uniform street canyons. *Building and Environment*, 46, 2657-2665.
- Guillas, S., Glover, N. & Malki-Epshtein, L. 2014. Bayesian calibration of the constants of the – turbulence model for a CFD model of street canyon flow. *Computer Methods in Applied Mechanics and Engineering*, 279, 536-553.

- Hamlyn, D. & Britter, R. 2005. A numerical study of the flow field and exchange processes within a canopy of urban-type roughness. *Atmospheric Environment*, 39, 3243-3254.
- Hargreaves, D. M. & Wright, N. G. 2007. On the use of the k- model in commercial CFD software to model the neutral atmospheric boundary layer. *Journal of Wind Engineering and Industrial Aerodynamics*, 95, 355-369.
- Hogan, C. M. 2011. Air pollution line source. In: BEYCHOK, M. (ed.) *The Encyclopedia of Earth*.
- Hoydysh, W. G., Griffiths, R. A. & Ogawa, Y. 1974. A scale model study of the dispersion of pollutant in street canyons. *67th annual meeting of the air pollution control association*. Denver, CO.
- Huang, Y., Hu, X. & Zeng, N. 2009. Impact of wedge-shaped roofs on airflow and pollutant dispersion inside urban street canyons. *Building and Environment*, 44, 2335-2347.
- Hunter, L. J., Johnson, G. T. & Watson, I. D. 1992. An investigation of three-dimensional characteristics of flow regimes within the urban canyon. *Atmospheric Environment. Part B. Urban Atmosphere*, 26, 425-432.
- Johnston, I. 2014. UK faces £300m fine over failure to meet air pollution targets by 2010. Independent.
- Jones, W. P. & Launder, B. E. 1973. The calculation of low-Reynolds-number phenomena with a two-equation model of turbulence. *International Journal of Heat and Mass Transfer*, 16, 1119-1130.
- Kader, B. A. 1981. Temperature and concentration profiles in fully turbulent boundary layers. *Heat mass transfer*, 24, 1541-1544.
- Karra, S. 2012. *An investigation of traffic related pollutants dispersion in heterogeneous street canyon*. Doctor of Philosophy, University College London.
- Karra, S., Malki-Epshtein, L. & Neophytou, M. 2011. The Dispersion of Traffic Related Pollutants Across a Non-Homogeneous Street Canyon. *Procedia Environmental Sciences*, 4, 25-34.

- Kastner-Klein, P. 1999. Description of wind tunnel studies on flow field and dispersion characteristics in street canyons at the University of Karlsruhe.
- Kastner-Klein, P., Berkowicz, R. & Britter, R. 2004. The influence of street architecture on flow and dispersion in street canyons. *Meteorology and Atmospheric Physics*, 87, 121-131.
- Kastner-Klein, P., Fedorovich, E. & Rotach, M. W. 2001. A wind tunnel study of organised and turbulent air motions in urban street canyons. *Journal of Wind Engineering and Industrial Aerodynamics*, 89, 849-861.
- Kastner-Klein, P. & Plate, E. J. 1999. Wind-tunnel study of concentration fields in street canyons. *Atmospheric Environment*, 33, 3973-3979.
- Kim, J.-J. & Baik, J.-J. 2003. Effects of inflow turbulence intensity on flow and pollutant dispersion in an urban street canyon. *Journal of Wind Engineering and Industrial Aerodynamics*, 91, 309-329.
- Koutsourakis, N., Bartzis, J. G. & Markatos, N. C. 2012. Evaluation of Reynolds stress, k - ϵ and RNG k - ϵ turbulence models in street canyon flows using various experimental datasets. *Environmental Fluid Mechanics*, 12, 379-403.
- Kovar-Panskus, A., Moulinneuf, L., Savory, E., Abdelqari, A., Sini, J. F., Rosant, J. M., Robins, A. & Toy, N. 2002. A Wind Tunnel Investigation of the Influence of Solar-Induced Wall-Heating on the Flow Regime within a Simulated Urban Street Canyon. *Water, Air and Soil Pollution: Focus*, 2, 555-571.
- Launder, B. E. & Sharma, B. I. 1974. Application of the energy-dissipation model of turbulence to the calculation of flow near a spinning disc. *Letters in Heat and Mass Transfer*, 1, 131-137.
- Launder, B. E. & Spalding, D. B. 1974. The numerical computation of turbulent flows. *Computer Methods in Applied Mechanics and Engineering*, 3, 269-289.
- Le, H., Moin, P. & Kim, J. 1997. Direct numerical simulation of turbulent flow over a backward-facing step. *Journal of Fluid Mechanics*, 330, 349-374.

- Leitl, B. M. & Meroney, R. N. 1997. Car exhaust dispersion in a street canyon. Numerical critique of a wind tunnel experiment. *Journal of Wind Engineering and Industrial Aerodynamics*, 67–68, 293-304.
- London Air Quality Network 2015. Nitrogen Dioxide ($\mu\text{g m}^{-3}$).
- Louka, P., Belcher, S. E. & Harrison, R. G. 2000. Coupling between air flow in streets and the well-developed boundary layer aloft. *Atmospheric Environment*, 34, 2613-2621.
- Meroney, R. N., Pavageau, M., Rafailidis, S. & Schatzmann, M. 1996. Study of line source characteristics for 2-D physical modelling of pollutant dispersion in street canyons. *Journal of Wind Engineering and Industrial Aerodynamics*, 62, 37-56.
- Met Office. 2015. *Southern England: climate* [Online]. Available: <http://www.metoffice.gov.uk/climate/uk/regional-climates/so> [Accessed June 2nd 2016].
- Miao, Y., Liu, S., Zheng, Y., Wang, S. & Li, Y. 2014. Numerical Study of Traffic Pollutant Dispersion within Different Street Canyon Configurations. *Advances in Meteorology*, 2014, 1-14.
- Moonen, P., Gromke, C. & Dorer, V. 2013. Performance assessment of Large Eddy Simulation (LES) for modeling dispersion in an urban street canyon with tree planting. *Atmospheric Environment*, 75, 66-76.
- Oke, T. R. 1988. Street design and urban canopy layer climate. *Energy and Buildings*, 11, 103-113.
- Panagiotou, I., Neophytou, M. K. A., Hamlyn, D. & Britter, R. E. 2013. City breathability as quantified by the exchange velocity and its spatial variation in real inhomogeneous urban geometries: An example from central London urban area. *Science of The Total Environment*, 442, 466-477.
- Patankar, S. V. 1980. *Numerical heat transfer and fluid flow*, USA, Hemisphere Publishing Corporation.
- Pope, S. B. 2000. *Turbulent Flows*, Cambridge, Cambridge University Press.

- Rafailidis, S. 1997. Influence of Building Areal Density and Roof Shape on the Wind Characteristics Above a Town. *Boundary-Layer Meteorology*, 85, 255-271.
- Reid, R. N. 2000. *Roofing & Cladding Systems: A Guide for Facility Managers*, USA, The Fairmont Press, Inc.
- Richards, P. J. & Hoxey, R. P. 1993. Appropriate boundary conditions for computational wind engineering models using the k- ϵ turbulence model. *Journal of Wind Engineering and Industrial Aerodynamics*, 46–47, 145-153.
- Riddle, A., Carruthers, D., Sharpe, A., McHugh, C. & Stocker, J. 2004. Comparisons between FLUENT and ADMS for atmospheric dispersion modelling. *Atmospheric Environment*, 38, 1029-1038.
- Salim, S. M., Cheah, S. C. & Chan, A. 2011. Numerical simulation of dispersion in urban street canyons with avenue-like tree plantings: Comparison between RANS and LES. *Building and Environment*, 46, 1735-1746.
- Salizzoni, P., Marro, M., Soulhac, L., Grosjean, N. & Perkins, R. J. 2011. Turbulent Transfer Between Street Canyons and the Overlying Atmospheric Boundary Layer. *Boundary-Layer Meteorology*, 141, 393-414.
- Salizzoni, P., Soulhac, L., Mejean, P. & Perkins, R. J. 2008. Influence of a Two-scale Surface Roughness on a Neutral Turbulent Boundary Layer. *Boundary-Layer Meteorology*, 127, 97-110.
- Salmond, J. A., Williams, D. E., Laing, G., Kingham, S., Dirks, K., Longley, I. & Henshaw, G. S. 2013. The influence of vegetation on the horizontal and vertical distribution of pollutants in a street canyon. *Science of The Total Environment*, 443, 287-298.
- Schlunzen, K. H., Bachlin, W., Brunger, H., Eichhorn, J., Grawe, D., Schenk, R. & Winkler, C. 2004. An evaluation guideline for prognostic microscale wind field models. In: Ninth International Conference on Harmonisation Within Atmospheric Dispersion Modelling for Regulatory Purposes. *9th Int. Conf. on Harmonisation within Atmospheric Dispersion Modelling for Regulatory Purposes* Garmisch-Partenkirchen, Germany.

- Schmid, K. F. 2014. Concise encyclopedia of construction terms and phrases. *"Slope" def. 1*. New York: Momentum.
- Scungio, M., Arpino, F., Stabile, L. & Buonanno, G. 2013. Numerical Simulation of Ultrafine Particle Dispersion in Urban Street Canyons with the Spalart-Allmaras Turbulence Model. *Aerosol and Air Quality Research*, 13, 1423-1437.
- Sini, J.-F., Anquetin, S. & Mestayer, P. G. 1996. Pollutant dispersion and thermal effects in urban street canyons. *Atmospheric Environment*, 30, 2659-2677.
- Smith, E. G. 1951. *The feasibility of using models for predetermining natural ventilation*, Texas Engineering Experiment Station, College Station, Tex.
- Snyder, W. H. 1972. Similarity criteria for the application of fluid models to the study of air pollution meteorology. *Boundary-Layer Meteorology*, 3, 113-134.
- Solazzo, E., Cai, X. & Vardoulakis, S. 2009. Improved parameterisation for the numerical modelling of air pollution within an urban street canyon. *Environmental Modelling & Software*, 24, 381-388.
- Soulhac, L., Garbero, V., Salizzoni, P., Mejean, P. & Perkins, R. J. 2009. Flow and dispersion in street intersections. *Atmospheric Environment*, 43, 2981-2996.
- Soulhac, L., Perkins, R. & Salizzoni, P. 2008. Flow in a Street Canyon for any External Wind Direction. *Boundary-Layer Meteorology*, 126, 365-388.
- Takano, Y. & Moonen, P. 2013. On the influence of roof shape on flow and dispersion in an urban street canyon. *Journal of Wind Engineering and Industrial Aerodynamics*, 123, Part A, 107-120.
- Tao, W. 2001. *Numerical Heat Transfer*, Xi'an, China, Xi'an Jiaotong University Press [In Chinese].
- Theodoridis, G. & Moussiopoulos, N. 2000. Influence of Building Density and Roof Shape on the Wind and Dispersion Characteristics in an Urban Area: A Numerical Study. *Environmental Monitoring and Assessment*, 65, 407-415.

- Tominaga, Y., Akabayashi, S.-i., Kitahara, T. & Arinami, Y. 2015. Air flow around isolated gable-roof buildings with different roof pitches: Wind tunnel experiments and CFD simulations. *Building and Environment*, 84, 204-213.
- Tominaga, Y., Mochida, A., Yoshie, R., Kataoka, H., Nozu, T., Yoshikawa, M. & Shirasawa, T. 2008. AIJ guidelines for practical applications of CFD to pedestrian wind environment around buildings. *Journal of Wind Engineering and Industrial Aerodynamics*, 96, 1749-1761.
- Tominaga, Y. & Stathopoulos, T. 2007. Turbulent Schmidt numbers for CFD analysis with various types of flowfield. *Atmospheric Environment*, 41, 8091-8099.
- Tu, J., Yeoh, G. H. & Liu, C. 2008. *Computational Fluid Dynamics*, Burlington, MA, Butterworth-Heinemann.
- Uehara, K., Murakami, S., Oikawa, S. & Wakamatsu, S. 2000. Wind tunnel experiments on how thermal stratification affects flow in and above urban street canyons. *Atmospheric Environment*, 34, 1553-1562.
- Vachon, G., Louka, P., Rosant, J. M., Mestayer, P. G. & Sini, J. F. 2002. Measurements of Traffic-Induced Turbulence within a Street Canyon during the Nantes'99 Experiment. *Water, Air and Soil Pollution: Focus*, 2, 127-140.
- van Hooff, T., Blocken, B. & van Harten, M. 2011. 3D CFD simulations of wind flow and wind-driven rain shelter in sports stadia: Influence of stadium geometry. *Building and Environment*, 46, 22-37.
- Vaughan, A. 2015. *Nearly 9,500 people die each year in London because of air pollution – study* [Online]. theguardian. Available: <https://www.theguardian.com/environment/2015/jul/15/nearly-9500-people-die-each-year-in-london-because-of-air-pollution-study> [Accessed June 2nd 2016].
- VDI 2005. Environmental meteorology - Prognostic microscale windfield models - Evaluation for flow around buildings and obstacles. *VDI 3783 Blatt 9* Berlin: Beuth Verlag.
- Versteeg, H. K. & Malalasekera, W. 2007. *An introduction to computational fluid dynamics : the finite volume method*, Harlow, Pearson Prentice Hall.

- Vos, P. E. J., Maiheu, B., Vankerkom, J. & Janssen, S. 2013. Improving local air quality in cities: To tree or not to tree? *Environmental Pollution*, 183, 113-122.
- Walton, H., Dajnak, D., Beevers, S., Williams, M., Watkiss, P. & Hunt, A. 2015. Understanding the Health Impacts of Air Pollution in London. Available: <https://www.kcl.ac.uk/lsm/research/divisions/aes/research/ERG/research-projects/HIAinLondonKingsReport14072015final.pdf>.
- Warhaft, Z. 2000. Passive Scalars in Turbulent Flows. *Annu. Rev. Fluid Mech.*, 32, 203-240.
- Wilcox, D. C. 2006. *Turbulence Modeling for CFD*, DCW Industries.
- World Health Organization. 2014a. *7 million premature deaths annually linked to air pollution* [Online]. Available: <http://www.who.int/mediacentre/news/releases/2014/air-pollution/en/> [Accessed Oct 21th 2014].
- World Health Organization. 2014b. *Ambient (outdoor) air quality and health* [Online]. Available: <http://www.who.int/mediacentre/news/releases/2014/air-pollution/en/> [Accessed Oct 21th 2014].
- Xie, X., Huang, Z. & Wang, J.-s. 2005a. Impact of building configuration on air quality in street canyon. *Atmospheric Environment*, 39, 4519-4530.
- Xie, X., Huang, Z., Wang, J. & Xie, Z. 2005b. The impact of solar radiation and street layout on pollutant dispersion in street canyon. *Building and Environment*, 40, 201-212.
- Yakhot, V. & Orszag, S. A. 1986. Renormalization group analysis of turbulence. I. Basic theory. *Journal of Scientific Computing*, 1, 3-51.
- Yakhot, V., Orszag, S. A., Thangam, S., Gatski, T. B. & Speziale, C. G. 1992. Development of turbulence models for shear flows by a double expansion technique. *Phys. Fluids*, 4, 1510-1520.
- Yamartino, R. J. & Wiegand, G. 1986. Development and evaluation of simple models for the flow, turbulence and pollutant concentration fields within an urban street canyon. *Atmospheric Environment* (1967), 20, 2137-2156.

- Zajic, D., Fernando, H. J. S., Calhoun, R., Princevac, M., Brown, M. J. & Pardyjak, E. R. 2011. Flow and Turbulence in an Urban Canyon. *Journal of Applied Meteorology and Climatology* 50, 203-223.
- Zeman, F. 2012. *Metropolitan Sustainability: Understanding and Improving the Urban Environment*, Elsevier Science.
- Zhang, Y., Gu, Z., Cheng, Y. & Lee, S.-C. 2011. Effect of real-time boundary wind conditions on the air flow and pollutant dispersion in an urban street canyon—Large eddy simulations. *Atmospheric Environment*, 45, 3352-3359.

11 Appendix

11.1 The similarity law for street canyon flow

The similarity law for street canyon flow suggests that when the Reynolds number ($Re=\rho U_0 H/\mu$) and the product of the Reynolds number and the Schmidt number ($Re\cdot Sc$, where $Sc=\mu/\rho I$) are greater than their corresponding critical values, the dimensionless flow properties and concentrations at most positions (except for the positions very close to the walls) are independent of working fluid, inflow velocity and model scale (Snyder, 1972). Here, the Reynolds number and the Schmidt number are defined by density (ρ), free-stream velocity (U_0), building height (H), dynamic viscosity (μ), and molecular diffusion coefficient (I).

Hoydysh et al. (1974) pointed out that for Reynolds number greater than 3,400, the flow in a street canyon is unaffected by viscosity. However, the critical Reynolds number proposed by Snyder (1972) was as large as 11,000, according to a stricter criterion—the invariance of the maximum non-dimensional concentrations on the roof. The critical numbers for buildings other than a cubic shape might be even larger. For example, Smith (1951) found that the critical numbers for sharp-edge buildings were above 20,000. To ensure the flow in a street canyon is fully turbulent, it is better to make the Reynolds numbers in CFD modelling studies larger than 20,000.

The critical number for the production of the Reynolds number and the Schmidt number ($Re\cdot Sc$) was not explicitly mentioned in literature. Nevertheless, Meroney et al. (1996) found that the normalized concentrations were independent of the intensity of the emission source, when the background velocity was larger than 2m/s. This condition corresponded to $Re\cdot Sc>8,300$.

The flow in real street canyons is usually fully-turbulent, as typical wind speed above the buildings is on the order of 1m/s and typical building height is on the order of 10m (e.g. air as the working fluid, $U_0=1\text{m/s}$ and $H=10\text{m}$ give $Re=685,000$, much greater than the critical number of $Re=3,400$ proposed by Hoydysh et al. (1974)). Thus, the dimensionless flow properties should be independent of background wind speed in most cases.

As the mass diffusivities of most gaseous pollutants in air are of the order of $10^{-5}\text{m}^2/\text{s}$, the Schmidt number for pollutant dispersion in air is of the order of 1. As a consequence,

the product of the Reynolds number and the Schmidt number is easy to exceed the critical value 8,300. Hence, the dimensionless concentration in real street canyons should also be independent of background wind speed in most cases.

11.2 Bulk Parameter Data for Chapter 6

Aspect ratio	Roof arrangement	Mean flux ($\text{kg}\cdot\text{m}/\text{s}^2$)	Fluctuating flux ($\text{kg}\cdot\text{m}/\text{s}^2$)	$U_{\text{mix}}/U_{\text{ref}}$	$U_{\text{can}}/U_{\text{ref}}$	$U_{\text{ex}}/U_{\text{ref}}$
AR=0.8	6F	0.55	9.17	0.142	0.129	0.013
	2P2F2P_R1	0.64	8.42	0.147	0.133	0.012
	2P2F2P_R2	0.61	8.29	0.145	0.131	0.012
	2P2F2P_R3	0.40	8.79	0.129	0.117	0.012
	2P1F3P_R1	0.49	8.09	0.145	0.131	0.011
	2P1F3P_R2	0.22	7.48	0.138	0.125	0.010
	2P1F3P_R3	-0.08	7.40	0.117	0.105	0.009
	3P1F2P_R1	0.51	8.75	0.136	0.126	0.012
	3P1F2P_R2	0.56	6.75	0.121	0.109	0.009
	3P1F2P_R3	1.37	3.53	0.114	0.093	0.006
	6P_R1	0.40	8.41	0.135	0.124	0.011
	6P_R2	0.32	5.93	0.116	0.104	0.008
	6P_R3	0.79	2.65	0.103	0.083	0.004
AR=1.0	6F	0.39	7.37	0.134	0.111	0.012
	2P2F2P_R1	0.47	6.74	0.140	0.116	0.012
	2P2F2P_R2	0.44	6.63	0.136	0.113	0.011
	2P2F2P_R3	0.25	6.94	0.117	0.097	0.011
	2P1F3P_R1	0.34	6.44	0.137	0.113	0.011
	2P1F3P_R2	0.13	5.93	0.128	0.106	0.010
	2P1F3P_R3	-0.08	5.74	0.103	0.084	0.009
	3P1F2P_R1	0.38	6.99	0.128	0.109	0.012
	3P1F2P_R2	0.36	5.27	0.110	0.091	0.009
	3P1F2P_R3	0.83	2.61	0.095	0.069	0.005
	6P_R1	0.28	6.67	0.126	0.106	0.011
	6P_R2	0.19	4.55	0.103	0.085	0.007
	6P_R3	0.46	1.91	0.083	0.059	0.004
AR=1.33	6F	0.22	5.88	0.110	0.078	0.013
	2P2F2P_R1	0.28	5.35	0.116	0.082	0.012
	2P2F2P_R2	0.25	5.25	0.112	0.079	0.011
	2P2F2P_R3	0.11	5.35	0.091	0.064	0.011
	2P1F3P_R1	0.19	5.10	0.113	0.080	0.011
	2P1F3P_R2	0.05	4.68	0.104	0.072	0.010
	2P1F3P_R3	-0.07	4.33	0.076	0.054	0.009
	3P1F2P_R1	0.23	5.52	0.105	0.077	0.012
	3P1F2P_R2	0.16	4.02	0.085	0.060	0.008
	3P1F2P_R3	0.39	1.83	0.064	0.039	0.004
	6P_R1	0.16	5.23	0.103	0.074	0.011
	6P_R2	0.07	3.40	0.079	0.055	0.007
	6P_R3	0.20	1.29	0.053	0.032	0.003

Table 11.1: The canyon velocities, mixing velocities, and exchange velocities for all the cases in Chapter 6.

Aspect ratio	Roof arrangement	Normalized c_{can}	Normalized c_{ped}
AR=0.8	6F	26.2	40.7
	2P2F2P_R1	27.9	42.3
	2P2F2P_R2	28.0	42.6
	2P2F2P_R3	26.1	41.4
	2P1F3P_R1	27.9	42.4
	2P1F3P_R2	28.0	43.1
	2P1F3P_R3	26.6	42.9
	3P1F2P_R1	28.2	43.6
	3P1F2P_R2	30.2	47.1
	3P1F2P_R3	27.5	44.6
	6P_R1	28.3	43.9
	6P_R2	30.5	47.9
	6P_R3	28.4	46.6
AR=1.0	6F	32.7	52.3
	2P2F2P_R1	35.1	54.6
	2P2F2P_R2	35.2	55.1
	2P2F2P_R3	32.6	53.6
	2P1F3P_R1	35.1	55.0
	2P1F3P_R2	35.3	55.9
	2P1F3P_R3	33.8	56.4
	3P1F2P_R1	35.5	56.4
	3P1F2P_R2	38.4	61.7
	3P1F2P_R3	36.3	60.7
	6P_R1	35.6	56.7
	6P_R2	39.0	63.1
	6P_R3	38.1	64.9
AR=1.33	6F	45.3	75.4
	2P2F2P_R1	48.8	78.1
	2P2F2P_R2	48.8	78.9
	2P2F2P_R3	46.8	82.4
	2P1F3P_R1	48.8	78.8
	2P1F3P_R2	49.1	81.1
	2P1F3P_R3	50.5	92.2
	3P1F2P_R1	49.4	81.4
	3P1F2P_R2	55.3	93.6
	3P1F2P_R3	57.5	106.7
	6P_R1	49.7	82.4
	6P_R2	56.9	97.9
	6P_R3	63.9	123.6

Table 11.2: The canyon concentrations and pedestrian concentrations for all the cases in Chapter 6.

